SCUOLA INTERNAZIONALE SUPERIORE DI STUDI AVANZATI

PHD COURSE IN ASTROPHYSICS AND COSMOLOGY

Exploring the Universe through the astrophysical gravitational-wave background

CANDIDATE:
Giulia Capurri

SUPERVISORS:
Prof. Carlo Baccigalupi
Prof. Andrea Lapi

ACADEMIC YEAR 2022-2023

DECLARATION OF AUTHORSHIP

I, Giulia Capurri, declare that this Thesis, titled "Exploring the Universe through the astrophysical gravitational-wave background" and the work presented in it are my own. I confirm that:

- This work was done wholly or mainly while in candidature for a the Ph.D. degree at SISSA.
- Where I have consulted the published work of others, this is always clearly attributed.
- Where I have quoted from the work of others, the source is always given. With the exception of such quotations, this thesis is entirely my own work.
- I have acknowledged all main sources of help.
- Where the thesis is based on work done by myself jointly with others, I have made clear exactly what was done by others and what I have contributed myself.

Trieste, 12 December 2023

Giulia Capurri

ABSTRACT

In the last years, the LIGO, Virgo, and KAGRA collaboration (LVK) has reported the detection of 90 gravitational-wave (GW) events resulting from the coalescence of stellar compact binaries. With the ongoing fourth observing run, new events are being discovered daily. This expanding collection of GW observations represents a novel avenue for exploring the physics of binary compact objects, their host galaxies, and the wider Universe. Besides individually resolved events, GW detectors are also searching for the stochastic gravitational-wave background (SGWB), given by the superposition of numerous unresolved GW signals. Several astrophysical and cosmological processes are expected to produce a SGWB. Among these, the SGWB generated by coalescing binaries has notably captured the attention of the scientific community. Just a few months ago, in June 2023, the leading Pulsar Timing Array experiments worldwide announced the groundbreaking detection of a SGWB in the nano Hertz band, likely attributed to coalescing supermassive black-hole binaries. In the frequency range explored by ground-based instruments, ranging between a few and a few hundred Hertz, the SGWB resulting from the merging of stellar compact binaries is expected to be the predominant stochastic signal. While this SGWB has not yet been observed, the LIGO/Virgo data have set upper limits on its amplitude and anisotropies. Studying the SGWB from coalescing stellar compact binaries, which is the central focus of this Thesis, is crucially important. Indeed, the SGWB gives access to the unresolved population of binaries, merging since the beginning of stellar activity. Currently, this unresolved population constitutes the majority. However, even with third-generation interferometers, such as the Einstein Telescope and Cosmic Explorer, which will be able to detect individual events up to very high redshifts, the SGWB will allow us to study those sources that produce fainter GW signals, potentially unveiling distant or sub-dominant families of binaries. Moreover, being by definition a collective signal, the SGWB is an effective tool to study population-level properties of the sources. Finally, the anisotropies of the SGWB reflect those of the large-scale structure (LSS) of the Universe, making the SGWB an interesting cosmological probe as well. For all these reasons, over the last few decades, the SGWB from coalescing stellar compact binaries has been the focus of numerous studies, both theoretical and observational. These studies aimed to characterize both the intensity and the anisotropies of such a signal.

This Thesis is built upon the original scientific publications from my Ph.D. work, aiming to contribute to the current understanding of the properties of both the isotropic and anisotropic components of the SGWB from stellar compact binaries. This involves studying their features both directly and through cross-correlations with other cosmic fields, investigating their detection prospects, and evaluating their effectiveness as observables to constrain the astrophysical and cosmological processes at play. In particular, I devel-

oped a theoretical framework to predict the intensity and anisotropies of the SGWB. This framework is rooted in merger rate predictions that leverage state-of-the-art binary population synthesis codes, complemented by empirical, data-driven descriptions of the galactic environments where these populations form and evolve. An essential aspect for characterizing the SGWB anisotropies is an effective evolution of cosmological perturbations, which I achieved through advanced Boltzmann solvers. Other critical ingredients include models for the GW emission of single binaries, based on their individual properties, and specifications for the scan strategy and sensitivity of the considered GW detectors. By combining all these elements, I generated theoretical predictions for both the frequency spectrum of the SGWB amplitude and the angular power spectrum of the SGWB anisotropies, accounting for various detectors and types of binaries — specifically, binary black holes, binary neutron stars, and neutron star-black hole binaries. Moreover, I characterized the astrophysical SGWB as a tracer of the LSS, providing analytical expressions for its redshift distribution, bias, and magnification bias, subsequently evaluated across multiple scenarios. Expanding upon this established framework, I developed a method to simulate full-sky maps of the SGWB signal, accounting for both its clustering properties and the intrinsic Poissonian nature arising from the discrete distribution of sources in space and time. This approach was useful for evaluating the shot noise, which is an essential factor to take into account for studying the detection prospects for the SGWB anisotropies.

Several studies have shown that cross-correlating the SGWB with other cosmic fields is an effective method to mitigate the impact of shot noise and enhancing the detectability of the common underlying anisotropies induced by the LSS. Therefore, I focused my investigation on the potential of cross-correlating the SGWB from coalescing binaries with the Cosmic Microwave Background (CMB) lensing. After computing the expected cross-correlation angular power spectra, I studied their detection prospects using present and forthcoming GW interferometer networks, both on Earth and in space (e.g., LISA and DECIGO). I conducted these analyses for both stellar compact binaries and extreme/intermediate mass ratio BH binaries, specifically within a newly proposed framework for massive BH seed formation through repeated mergers of stellar remnants, migrating toward the galactic center because of gaseous dynamical friction.

Finally, I recently shifted my focus to studying how different astrophysical and cosmological prescriptions impact the amplitude and shape of the frequency spectrum of the SGWB amplitude. The primary goal was to determine which properties of the source population, as well as the galactic and cosmological environments, can be reverse-engineered from future SGWB measurements. In particular, I developed a theoretical framework to use the high-frequency peak of the SGWB from binary neutron stars as an observable to constrain a selection of astrophysical and cosmological parameters. This involved using a Markov Chain Monte Carlo analysis with a mock data-set of SGWB measurements.

PUBLICATIONS

This Thesis includes the results of the scientific research I conducted as a Ph.D. student in the Astrophysics & Cosmology group at SISSA, under the guidance of Professors Carlo Baccigalupi and Andrea Lapi, working with several collaborators. The contents of the Thesis are mainly based upon the following publications and submitted manuscripts (in chronological order):

[1] G. Capurri, A. Lapi, C. Baccigalupi, L. Boco, G. Scelfo, and T. Ronconi. "Intensity and anisotropies of the stochastic gravitational wave background from merging compact binaries in galaxies." In: *JCAP* (Nov. 2021), p. 032. DOI: 10.1088/1475-7516/2021/11/032. arXiv: 2103.12037.

[2] G. Capurri, A. Lapi, and C. Baccigalupi. "Detectability of the cross-correlation between CMB lensing and stochastic GW background from compact object mergers." In: *Universe* 8.3 (Mar. 2022), p. 160. DOI: 10.3390/universe8030160. arXiv: 2111.04757.

[3] G. Capurri, A. Lapi, L. Boco, and C. Baccigalupi. "Searching for anisotropic stochastic gravitational-wave backgrounds with constellations of space-based interferometers." In: *Astrophys. J.* 943.2, 72 (Feb. 2023), p. 72. DOI: 10.3847/1538-4357/acaaa3. arXiv: 2212.06162.

[4] G. Capurri, A. Lapi, M. Spera, and C. Baccigalupi. "Astrophysical and Cosmological Relevance of the High-Frequency Features in the Stochastic Gravitational-Wave Background." In: *Submitted to Phys. Rev. D* (Oct. 2023). arXiv: 2310.18394.

Other scientific publications, upon some of which this Thesis may be partially based, are:

[5] L. Boco, A. Lapi, A. Sicilia, G. Capurri, C. Baccigalupi, and L. Danese. "Growth of massive black-hole seeds by migration of stellar and primordial black holes: gravitational waves and stochastic background." In: *JCAP* (Oct. 2021), p. 035. DOI: 10.1088/1475-7516/2021/10/035. arXiv: 2104.07682.

[6] G. Capurri, N. Bartolo, D. Maino, and S. Matarrese. "Let Effective Field Theory of Inflation flow: stochastic generation of models with red/blue tensor tilt." In: *JCAP* 11 (2020), p. 037. DOI: 10.1088/1475-7516/2020/11/037. arXiv: 2006.10781.

CONTENTS

LIST OF FIGURES

LIST OF TABLES

LIST OF ABBREVIATIONS

BBH	binary black hole
BBN	Big Bang nucleosynthesis
BNS	binary neutron star
CMB	cosmic microwave background
CE	Cosmic Explorer
DECIGO	DECIhertz interferometer Gravitational-wave Observatory
EPTA	European Pulsar Timing Array
ET	Einstein Telescope

FMR	fundamental metallicity relation
FRW	Friedmann-Robertson-Walker
GW	gravitational waves
IPTA	International Pulsar Timing Array
KAGRA	Kamioka Gravitational Wave Detector
LIGO	Laser Interferometer Gravitational-wave Observatory
LISA	Laser Interferometer Space Antenna
LSS	large-scale structure
LVK	LIGO/Virgo/KAGRA
NANOGrav	North American Nanohertz Observatory for Gravitational Waves
NSBH	neutron star-black hole binary
O_3	third observing run
PLS	power-law integrated sensitivity curve
PPTA	Parkes Pulsar Timing Array
PTA	pulsar timing array
PSD	power spectral density
SFR	star formation rate
SFRF	star formation rate function
SGWB	stochastic gravitational-wave background
SMBBH	supermassive black-hole binary
SMBH	supermassive black hole
SO	Simons Observatory
CMB-S4	Stage-IV network of ground-based observatories
2G	"second generation" detectors
3G	"third generation" detectors

1 STOCHASTIC GRAVITATIONAL-WAVE BACKGROUNDS

The purpose of this opening chapter is to provide a context for my doctoral research project. I will discuss the fundamental concepts concerning stochastic gravitational-wave backgrounds (SGWBs) and offer a concise overview of the current state of research in this field. The chapter is divided in five sections, organized as follows. In Section 1.1, I will introduce stochastic backgrounds, providing different definitions of such signals and a concise overview of the standard mathematical framework used to describe them. In Section 1.2, I will offer a brief description of the main sources of SGWB and their observational properties. In Section 1.3, I will discuss SGWB anisotropies and review the key related results in the literature. In Section 1.4, I will outline the basic concepts about the detection strategies for stochastic backgrounds. In Section 1.5, I will review the main results of current detection efforts and discuss the detection prospects with forthcoming instruments.

1.1 WHAT IS A STOCHASTIC BACKGROUND?

Gravitational waves (GW) are subtle perturbations of the spacetime metric generated by energetic events occurring throughout the Universe. They were predicted by Albert Einstein back in 1916 [1, 2], arising as a natural consequence of his theory of general relativity [3]. A century later, in early 2016, the first direct detection of a GW signal was announced by the Laser Interferometer Gravitational-wave Observatory (LIGO) [4] and Virgo [5] collaborations, marking the inauguration of the GW astronomy era. LIGO consists of two 4 km-long laser interferometers, one located in Hanford, Washington, the other in Livingston, Lousiana, while Virgo is a 3 km-long laser interferometer in Cascina, Italy. This very first signal, named GW150914 after its date of observation in the two LIGO detectors (September 14th, 2015), was also the first observation of a binary black hole merger. This discovery not only confirmed the existence of stellar-mass black hole binaries, but also demonstrated that their merger could occur within the current age of the Universe. A few years later, another milestone was reached through the measurement of the first GW signal produced by a binary neutron star merger, GW170817 [6]. This detection marked the beginning of GW multi-messenger astronomy, with simultaneous observations of the event and its source across the electromagnetic spectrum [7]. By the end of the third observing run, 90 confirmed GW signals were recorded, originating from the final moments of binary black hole and neutron star coalescences (see Figure 1) [8, 9]. Recently, also the japanese Kamioka Gravitational Wave Detector (KAGRA) joined the operational network of ground-based detectors [10]. Many more detections are being announced during the current fourth LIGO/Virgo/KAGRA (LVK) observing run, started in May 2023.

1.1.1 *Standard definition and historical introduction*

All the LVK detections so far have involved coherent measurements of resolved waveforms within the detector data-streams, each originating from a single, point-like source. However, these detections represent only a tiny fraction of the vast GW landscape. The majority consists of unresolved signals arising from extended sources or multiple point sources, too numerous or too faint to be detected individually. All these unresolved sources combine incoherently, leading to the emergence of GW backgrounds. These backgrounds are usually treated as stochastic phenomena due to their non-deterministic strain signals and are commonly referred to as stochastic gravitational-wave backgrounds (SGWBs). Some of them exhibit stochastic properties due to their generation process, such as the SGWB generated by inflationary tensor modes. Others, instead, display stochastic behavior as a result of the limitations of the specific detectors used for their observation, such as the cumulative signal given by the superposition of multiple compact binary coalescences. Notably, a SGWB of this latter nature is a detector-dependent observable, as it intrinsically depends on the detection threshold.

A variety of sources, both astrophysical and cosmological, are expected to produce a SGWB. The most relevant ones will be reviewed in Section 1.2. The main sources of SGWB in the frequency band probed by ground-based interferometers ($\sim 10 - 10^3$ Hz) are coalescing binary systems composed of stellar-origin compact objects, namely binary black holes (BBHs), binary neutron stars (BNSs), and neutron star-black hole binaries (NSBHs). While there has been no detection of such SGWB yet, the LVK collaboration established an upper limit on its amplitude and anisotropies [11, 12]. The only direct measurement of a SGWB so far has been recently announced by the North American Nanohertz Observatory for Gravitational Waves (NANOGrav), European Pulsar Timing Array (EPTA), and Parkes Pulsar Timing Array (PPTA). These pulsar timing array (PTA) experiments search for GWs looking for correlated modulations in the arrival times of radio pulses from a group of galactic millisecond pulsars [13–15]. The origin of the detected signal is still uncertain, but it is most probably due to inspiralling supermassive black hole binaries (SMBBH) in the center of distant galaxies [16]. I will discuss these and other outcomes of current detection efforts in Section 1.5.

1.1.2 *GW strain and Stokes parameters*

When studying the propagation of GWs, it is common to work within the framework of linearized general relativity. In this context, GWs are treated as small perturbations to the Minkowski flat spacetime:

$$g_{\mu\nu} \approx \eta_{\mu\nu} + h_{\mu\nu}, \tag{1}$$

where $g_{\mu\nu}$ is the metric, $\eta_{\mu\nu}$ is the Minkowski metric, and $h_{\mu\nu}$ is the metric perturbation.

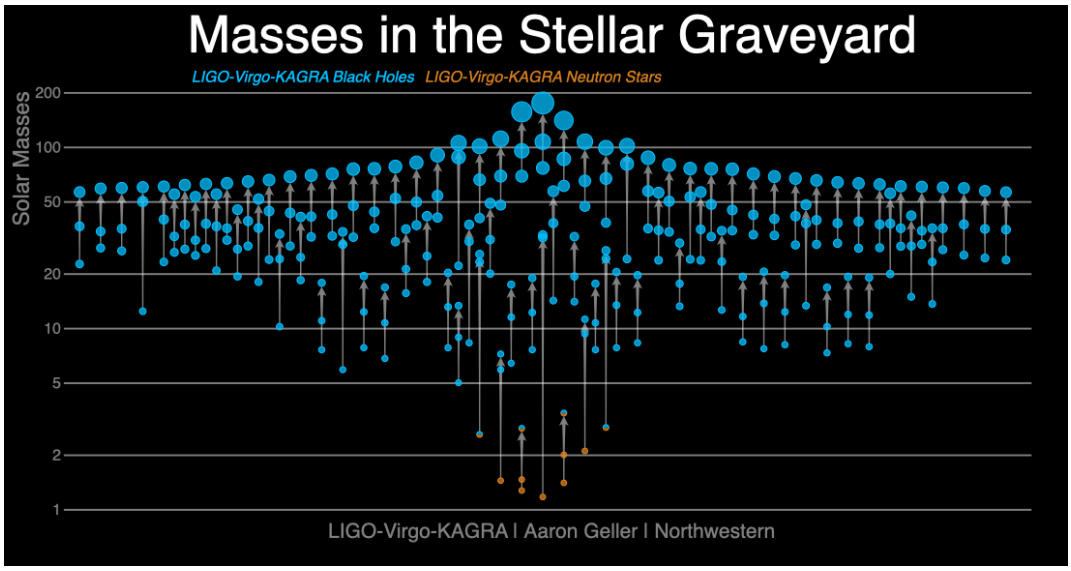

Figure 1: Graphical visualization of the 90 binary mergers observed during the first three LVK observing runs. Credit: LIGO-Virgo-KAGRA/Aaron Geller/Northwestern at https://media.ligo.northwestern.edu/gallery/mass-plot

The production of GWs is a direct consequence of general relativity and can be predicted through the Einstein equations. In particular, GWs are generated when there exists a non-zero second derivative of the mass quadrupole moment with respect to time. GWs carry both energy and momentum, causing energy loss from the emitting system. To first order in the metric perturbations, the vacuum Einstein field equation can be written as a wave equation in the De Donder gauge:

$$\Box\left(h_{\mu\nu} - \frac{1}{2}\eta_{\mu\nu}h^{\alpha}_{\alpha}\right) = 0, \tag{2}$$

where the box operator is the D'Alambert operator, defined as $\Box = \partial_\alpha\partial^\alpha$. The solution of this equation can be expressed as a linear combination of plane waves,

$$h_{\mu\nu} = Ae_{\mu\nu}e^{ik_\alpha x^\alpha}, \tag{3}$$

where $e_{\mu\nu}$ is the normalized polarization tensor, and k_α is the wave four-vector. By inserting this solution back into Equation (2), the dispersion relation $k_\alpha k^\alpha = 0$ is recovered. This implies that GWs travel at the speed of light. Finally, by imposing the transverse-traceless gauge, $h_{\mu\nu}$ is reduced to a purely spatial perturbation, h_{ij}, which carries two physical degrees of freedom. Equivalently, this corresponds to two independent spin-2 polarization states.

Now, returning to our original goal, let's formulate a general expression for the spatial metric perturbation in the context of a stochastic background. The metric perturbations caused by a SGWB at time t and position $\mathbf{x}$ can be writ-

ten as an infinite superposition of plane waves with polarizations P, observed frequencies f, and coming from all directions in the sky $\hat{\mathbf{n}}$ [17]:

$$h_{ij}(t,\mathbf{x}) = \int_{\infty}^{+\infty} df \int_{S^2} d^2\hat{\mathbf{n}} \sum_{P=+,\times} h_P(f,\hat{\mathbf{n}}) e^P_{ij}(\hat{\mathbf{n}}) e^{i2\pi f(t+\mathbf{n}\cdot\mathbf{x}/c)}. \tag{4}$$

In Equation 4, $\hat{\mathbf{n}} = (\sin\theta\cos\phi, \sin\theta\sin\phi, \cos\theta)$, where (θ,ϕ) are the standard angular coordinates on the 2-sphere. The spatial wave vector is explicitly expressed as $\mathbf{k} = 2\pi f\hat{\mathbf{n}}/c$, with c being the speed of light. Since the spatial metric perturbations $h_{ij}(t,\mathbf{x})$ are real, the complex modes in the frequency domain must respect the reality condition $h^\star_P(f,\hat{\mathbf{n}}) = h_P(-f,\hat{\mathbf{n}})$. The provided expression for the stochastic metric perturbation is presented in the linear polarization basis. The orthogonal basis tensors e_P are defined as:

$$e^+ = e^\theta \otimes e^\theta - e^\phi \otimes e^\phi, \tag{5}$$
$$e^\times = e^\theta \otimes e^\phi + e^\phi \otimes e^\theta, \tag{6}$$

where

$$e^\theta = (\cos\theta\cos\phi, \cos\theta\sin\phi, -\sin\theta) \tag{7}$$
$$e^\phi = (-\sin\phi, \cos\phi, 0) \tag{8}$$

are the standard unit vectors tangent to the 2-sphere. In the case of a stochastic background, both the metric perturbations $h_{ij}(t,\mathbf{x})$ and the Fourier amplitudes $h_P(f,\hat{\mathbf{n}})$ are random fields. The statistical properties of the background are determined by the probability distributions associated with these random fields. Most often, it is assumed that the amplitudes are drawn from a Gaussian distribution[1]. This implies that all the statistical properties of the amplitudes are entirely characterized by their second order moments. When dealing with stochastic backgrounds, two other common assumptions are typically made. Firstly, the SGWB is often assumed to be static, meaning that amplitudes at different frequencies are statistically independent. Secondly, it is considered to have no phase coherence across the sky, implying that the phases of the signal originating from different directions are statistically independent. Given these assumptions, the second-order moments of the Fourier amplitudes correspond to the following ensemble averages:

1 This is a good approximation for cosmological backgrounds, as they derive from primordial perturbations, which are adiabatic, Gaussian and nearly scale-invariant in most cosmological models. For a SGWB of astrophysical origin, instead, this assumption may break. However, the central limit theorem guarantees that the Gaussian approximation is valid if the signal is sourced by a sufficiently large number of independent events and any high signal-to-noise outlier has been subtracted from the detector data-stream.

$$\begin{aligned}&\begin{pmatrix}\langle h_+(f,\hat{\mathbf{n}})h_+^\star(f',\hat{\mathbf{n}}')\rangle & \langle h_+(f,\hat{\mathbf{n}})h_\times^\star(f',\hat{\mathbf{n}}')\rangle\\ \langle h_\times(f,\hat{\mathbf{n}})h_+^\star(f',\hat{\mathbf{n}}')\rangle & \langle h_\times(f,\hat{\mathbf{n}})h_\times^\star(f',\hat{\mathbf{n}}')\rangle\end{pmatrix} =\\ &= \delta^2(\hat{\mathbf{n}}-\hat{\mathbf{n}})\delta(f-f')\begin{pmatrix}I(f,\hat{\mathbf{n}})+Q(f,\hat{\mathbf{n}}) & U(f,\hat{\mathbf{n}})-iV(f,\hat{\mathbf{n}})\\ U(f,\hat{\mathbf{n}})+iV(f,\hat{\mathbf{n}}) & I(f,\hat{\mathbf{n}})-Q(f,\hat{\mathbf{n}})\end{pmatrix},\end{aligned} \tag{9}$$

where $I(f,\hat{\mathbf{n}})$ represents the intensity, $Q(f,\hat{\mathbf{n}})$ and $U(f,\hat{\mathbf{n}})$ give the linear polarization, and $V(f,\hat{\mathbf{n}})$ denotes the circular polarization [18]. The quantities I, Q, U and V are known as Stokes parameters and are real functions. They offer a comprehensive description of the signal's polarization, in analogy with the electromagnetic Stokes parameters employed for photons. It's important to note a key distinction: while electromagnetic Q and U Stokes parameters transform as spin-2 quantities under rotation, their counterparts for the GW strain transform as spin-4 quantities. In both cases, intensity behaves as a scalar, while V transforms as a pseudo-scalar. Lastly, another common assumption is that the SGWB is unpolarized. If it is the case, all the Stokes parameters, except for the intensity, vanish, simplifying the previous equation to [19, 20]:

$$\langle h_P(f,\hat{\mathbf{n}})h_{P'}^\star(f',\hat{\mathbf{n}}')\rangle = \delta(P,P')\delta^2(\hat{\mathbf{n}}-\hat{\mathbf{n}}')\delta(f-f')I(f,\hat{\mathbf{n}}). \tag{10}$$

Another quantity commonly used in most SGWB studies that conveys the same information as the intensity $I(f,\hat{\mathbf{n}})$ is the one-sided power spectral density (PSD) of the Fourier modes of the SGWB, denoted as $S_h(f,\hat{\mathbf{n}})$. The PSD is defined through [21–23]

$$\langle h_P(f,\hat{\mathbf{n}})h_{P'}^\star(f',\hat{\mathbf{n}}')\rangle = \frac{\delta(P,P')}{2}\frac{\delta^2(\hat{\mathbf{n}}-\hat{\mathbf{n}}')}{4\pi}\frac{\delta(f-f')}{2}S_h(f,\hat{\mathbf{n}}), \tag{11}$$

so that it is manifest that $S_h(f,\hat{\mathbf{n}}) = 16\pi\, I(f,\hat{\mathbf{n}})$.

Considerations about polarized stochastic backgrounds

For completeness, I conclude this subsection with a few considerations about the polarization in the SGWB. Throughout this Thesis, I will assume that the SGWB is unpolarized, encoding all the information in its intensity. While this assumption is generally justified, as most sources of SGWB are expected to produce a (mostly) unpolarized signal, it is important to note that various physical mechanisms can generate a polarized SGWB or inject polarizations into signals that would be intrinsically unpolarized. Many theoretical scenarios predict the existence of a polarized cosmological SGWB. For example, parity-violating interactions in the early Universe can source a SGWB with a net circular polarization [24–27].However, similar to the cosmic microwave background (CMB), the polarization effect is typically small, and, as a consequence, assuming the absence of polarization is often reasonable for most purposes.

On the other hand, the SGWB given by astrophysical sources is generally expected to be unpolarized. This is because the polarization of the GW signal emitted by each source is averaged out over various inclination angles relative to the observation direction. Nonetheless, some interesting mechanisms could induce a net polarization also in the astrophysical SGWB, possibly detectable by present and forthcoming GW instruments. For instance, a certain level of polarization can be generated in an initially unpolarized SGWB by diffusion through massive structures encountered during propagation [28]. This effect ultimately results from the astrophysical SGWB displaying some level of anisotropy, attributed to different mechanisms discussed in Section 1.3. Similar to the phenomenon in the CMB due to Thomson scattering, the combined effects of SGWB anisotropies and the polarization-dependence of the scattering cross-section are responsible for the generation of polarization. Furthermore, recent studies have shown that the anisotropic distribution of astrophysical sources leads to an effective circular polarization of the astrophysical SGWB [29]. In contrast to the isotropic case, the average over the inclination angle yields a non-zero amount of circular polarization, which coherently sums at low frequencies.

1.1.3 *The energy density parameter*

The standard cosmological framework is based on the assumption of a homogeneous and isotropic spacetime, accurately portraying our Universe on large scales. This is described by the Friedmann-Robertson-Walker (FRW) metric, obtained multiplying the spatial part of a static metric by a time-dependent function called scale factor, denoted as $a(t)$:

$$ds^2 = -dt^2 + a^2(t)\left(\frac{dr^2}{1-Kr^2} + dS^2\right). \tag{12}$$

The constant K characterizes the curvature of spacetime and can take values of $\{-1, 0, 1\}$, corresponding to an open, flat, or closed Universe, respectively. Our Universe can be reasonably approximated as flat, as cosmological measurements indicate that K is consistent with 0. Likewise, the most comprehensive representation of a homogeneous and isotropic stress-energy tensor is given by the following diagonal matrix:

$$T^{\mu}_{\nu} = \begin{pmatrix} \rho(t) & 0 & 0 & 0 \\ 0 & -p(t) & 0 & 0 \\ 0 & 0 & -p(t) & 0 \\ 0 & 0 & 0 & -p(t) \end{pmatrix}, \tag{13}$$

where $\rho(t)$ and $p(t)$ represent the total density and pressure, respectively. These quantities include contributions from all the various energy components

in the Universe. The dynamic of the metric is governed by the Einstein field equations, which, for the FRW metric, reduce to two independent differential equations for the scale factor, known as the Friedmann equations:

$$\left(\frac{\dot{a}(t)}{a(t)}\right)^2 \equiv H^2(t) = \frac{8\pi G}{3}\rho + \frac{Kc^2}{a^2(t)}, \tag{14}$$

$$\frac{\ddot{a}(t)}{a(t)} = -\frac{4\pi G}{3}\left(\rho + \frac{3p}{c^2}\right). \tag{15}$$

Here, $H(t)$ is the Hubble rate, which quantifies the expansion of the Universe, and $G = 6.67 \times 10^{-11}\,m^3 kg^{-1} s^{-2}$ is the universal gravitational constant. Given that $K = 0$, the total energy density today is given by

$$\rho_c = \frac{3H_0^2 c^2}{8\pi G} = 7.8 \times 10^{-9}\,erg\,cm^{-3}, \tag{16}$$

which is know as critical energy density[2]. H_0 is the present value of the Hubble rate, known as the Hubble constant [3]. Another fundamental quantity to be introduced is the cosmological redshift z, which quantifies the change in wavelength of photons received from distant objects due to the Universe's expansion:

$$z = \frac{1}{a(t)} - 1. \tag{17}$$

We now possess all the ingredients to reorganize the Friedmann equations into a more convenient form, which expresses the Hubble rate as a function of time in terms of the energy density contributions from all the species that populate the Universe:

$$H(t) = H_0\left(\Omega_R(1+z)^4 + \Omega_M(1+z)^3 + \Omega_\Lambda\right)^{1/2}, \tag{18}$$

where $\Omega_i \equiv \rho_i/\rho_c$ are the density parameters of each energy component: radiation (R), which includes photons and relativistic neutrinos, matter (M), which includes baryons and cold dark matter, and the cosmological constant (Λ). GWs are incorporated into this equation as a part of the radiation energy density, alongside photons and neutrinos. They are all considered to be carried by massless particles traveling at the speed of light. We can therefore write:

2 Note that the ρ in the Friedman's Equations (14) represents the volumetric mass density. In contrast, here we define ρ_c as a volumetric energy density, which explains the presence of the extra c^2 factor.

3 The measured value of H_0 is approximately $70\,km\,Mpc^{-1}s^{-1}$. However, there is a tension between the values obtained with local measurements (see e.g., Refs [30, 31]) and primordial probes [32]. For a thorough review of the Hubble tension, see Ref. [33]

$$\Omega_R = \Omega_\gamma + \Omega_\nu + \Omega_{gw} + ... \tag{19}$$

The present-day value of the radiation density is very small ($\Omega_R \approx 10^{-4}$). However, Equation (18) shows that at high redshifts, the expansion of the Universe was dominated by radiation. As a consequence, any additional contributions to Ω_R, including those from primordial GWs, would leave an imprint on cosmological probes from the early Universe. These effects are mainly observed in the CMB and the predicted light element abundances from the Big Bang nucleosynthesis (BBN). In the most recent analyses, a combination of CMB and BBN data is integrated with external data-sets such as measurements of the baryon acoustic oscillation scale [34], resulting in

$$\Omega_{gw} < 1.2 \times 10^{-6} \left(\frac{H_0}{100\,\mathrm{km\,s^{-1}\,Mpc^{-1}}} \right)^{-2}. \tag{20}$$

With these stringent constraints on Ω_{gw}, it is reasonable to consider GWs as small perturbations in the Universe, in line with our original assumption. They do not significantly influence the broader cosmological framework but rather adhere to the propagation rules established by the Universe's energy content and structure.

The density parameter appearing in Equations (19) and (20) encapsulates the total energy density of GWs at all frequencies, as it is the quantity that actually determines the expansion rate. However, since all the GW searches focus on particular frequency bands, it is convenient to define a frequency spectrum for the energy density parameter. In particular, the magnitude of the SGWB is usually reported in terms of its energy density per logarithmic frequency[4] interval with respect to the critical energy density of the Universe [20–22, 35]:

$$\Omega_{gw}(f) = \frac{1}{\rho_c} \frac{d\rho_{gw}(f)}{d\ln f}. \tag{21}$$

This quantity refers to the isotropic amplitude of the SGWB over the entire sky. Of course, most stochastic backgrounds feature also some level of anisotropy, which can be taken into account by adding a directional dependence in the previous definition of the energy density parameter:

$$\Omega_{gw}(f, \hat{\mathbf{n}}) = \frac{1}{\rho_c} \frac{d\rho_{gw}(f, \hat{\mathbf{n}})}{d\ln f\, d\hat{\mathbf{n}}}, \tag{22}$$

where $\hat{\mathbf{n}}$ always represents the unit vector along the line of sight.

It is useful to relate the energy density parameter to the intensity Stokes parameter $I(f, \hat{\mathbf{n}})$ and the PSD $S_h(f, \hat{\mathbf{n}})$ defined in Equations (10) and (11), respectively. To this purpose, let's recall that the stress-energy tensor of GWs is given by the Isaacson expression [36]

4 It is important to note that here we are referring to the observed frequency.

$$T_{\mu\nu} = \frac{c^2}{32\pi G} \langle \partial_\mu h_{ij} \partial_\nu h^{ij} \rangle, \tag{23}$$

where h^{ij} is the spatial part of the metric perturbation and the angle brackets denote an average over many wavelengths. The energy density is given by the 00 component:

$$\rho_{gw} = \frac{c^2}{32\pi G} \langle \dot{h}_{ij} \dot{h}^{ij} \rangle. \tag{24}$$

Inserting the plane-wave decomposition of Equation (4) and rewriting the two-point statistics of each plane wave in terms of the intensity parameters in Equation (10), we obtain:

$$\rho_{gw} = \frac{\pi c^2}{2G} \int_0^\infty df \int_{S^2} d\hat{\mathbf{n}}\, f^2 I(f, \hat{\mathbf{n}}). \tag{25}$$

Now, by noticing that Equation (22) implies that

$$\rho_{gw} = \frac{\rho_c}{4\pi} \int_0^\infty \frac{df}{f} \int_{S^2} d\hat{\mathbf{n}}\, \Omega_{gw}(f, \hat{\mathbf{n}}) \tag{26}$$

and comparing the latter expression with the one in Equation (25), it is easily inferred that

$$\Omega_{gw}(f, \hat{\mathbf{n}}) = \frac{4\pi^2 c^2}{\rho_c G} f^3\, I(f, \hat{\mathbf{n}}) = \frac{32\pi^3}{3H_0^2} f^3\, I(f, \hat{\mathbf{n}}). \tag{27}$$

From this equation, given that $S_h(f, \hat{\mathbf{n}}) = 16\pi\, I(f, \hat{\mathbf{n}})$, we also have:

$$\Omega_{gw}(f, \hat{\mathbf{n}}) = \frac{2\pi^2}{3H_0^2} f^3 S_h(f, \hat{\mathbf{n}}). \tag{28}$$

Indeed, the directional expressions in Equations (27) and (28) hold also for the corresponding isotropic quantities integrated or averaged over the sky: $\Omega_{gw}(f)$, $S_h(f)$ and $I(f)$. Another quantity often used to quantify the strength of the expected signal is the characteristic strain defined by

$$h_c(f) = \sqrt{f\, S_h(f)}, \tag{29}$$

so that

$$\Omega_{gw}(f) = \frac{2\pi^2}{3H_0^2} f^2 h_c^2(f). \tag{30}$$

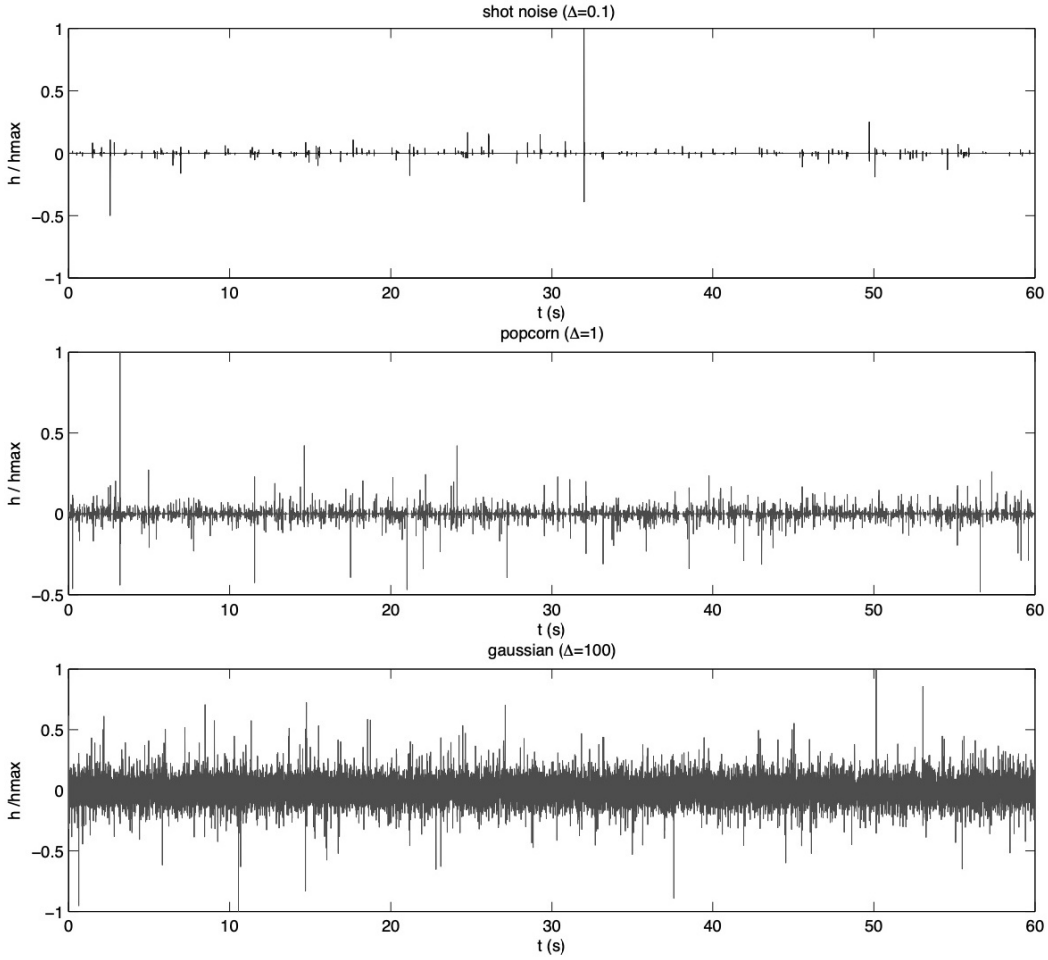

Figure 2: Examples of detector data-streams populated by stochastic backgrounds with different time-domain properties: shot noise (top panel), popcorn (middle panel), and Gaussian (bottom panel). The δ parameter is the duty cycle, the mean ratio between the event duration and the time interval between consecutive events. Credits: Figure 2 of Ref. [37], Regimbau (2011).

1.1.4 *Observational properties of the SGWB*

In Section 1.1, we saw the standard definition according to which a stochastic background is a random GW signal produced by the incoherent superposition of a large number of unresolved events. In this formulation, a random signal means that it can be described only statistically. The characterization can be done using the expectation values of the field variables or, equivalently, the Fourier components of the plane-wave expansion of the metric perturbations of Equation (4). While generally accepted, the above definition could be misleading due to the inclusion of the term "unresolved". Indeed, this term depends on observation details, such as detector sensitivity and total observation time, rather than the intrinsic properties of the SGWB. An alternative, operational definition for the SGWB was introduced in Refs. [23, 38] in the context

of Bayesian inference. According to this definition, a GW signal is stochastic if a Bayesian model selection calculation prefers a stochastic signal model over any deterministic signal model. In contrast, a signal is resolvable if it can be decomposed into separate (e.g., non-overlapping in either time or frequency domains) and individually detectable signals, again in a Bayesian model selection sense. If the SGWB comes from the superposition of signals from numerous astrophysical sources, removing any bright signal above the background is necessary. This action isolates a residual non-deterministic signal with specific statistical properties.

For the backgrounds given by the superposition of several unresolved yet individually defined events, it is possible to identify three observational regimes, represented in Figure 2. These regimes, Poissonian, popcorn and Gaussian, are distinguished by the frequency at which the individual events occur [37]. In the Poissonian or shot noise regime, GWs appear as isolated bursts in the detector time-stream. The number of sources is so reduced that the time interval between events is much longer than the duration of a single event. In the Gaussian or continuous regime, the time-stream is populated by a large number of overlapping signals, so that the central limit theorem applies. The overlapping waveforms create a continuous background that obeys the Gaussian statistic and is completely determined by its spectral properties. The popcorn or intermittent regime, instead, lies somewhere in between the Poissonian and Gaussian ones. In this case, the time interval between events is of the same order of the duration of the single events, so that the waveforms may overlap but the statistic is not Gaussian anymore. The discriminating factor between regimes is encapsulated in the duty cycle, which is the mean ratio of the event duration to the time interval between consecutive events.

1.2 SOURCES OF STOCHASTIC BACKGROUND

Stochastic backgrounds are typically classified into two broad categories according to the nature of their production mechanism: astrophysical or cosmological. In this section, I will present an overview of the various phenomena that can generate a SGWB. I will briefly discuss the most likely SGWB sources and their key observational features (see Ref. [39] for an extensive review). I will particularly emphasize the discussion on stellar compact-object binaries, as they produce the SGWB that constitutes the central focus of this Thesis.

1.2.1 *Cosmological backgrounds*

The first class of stochastic backgrounds is generated by cosmological sources, typically during the early Universe. Most of these primordial backgrounds arise from stochastic processes, resulting in inherently stochastic signals, like for example the SGWB generated by the evolution of vacuum fluctuations during inflation. However, cosmological backgrounds can also exhibit stochastic behavior due to the overlapping of multiple signals, as in the case of cosmic

strings. Moreover, the majority of cosmological backgrounds are assumed to be unpolarized since the underlying stochastic processes do not favor a specific reference frame in most instances. In the following, I will offer a concise overview of the primary sources of cosmological backgrounds. For a more in-depth exploration, I refer the interested reader to the comprehensive review presented in Ref. [40].

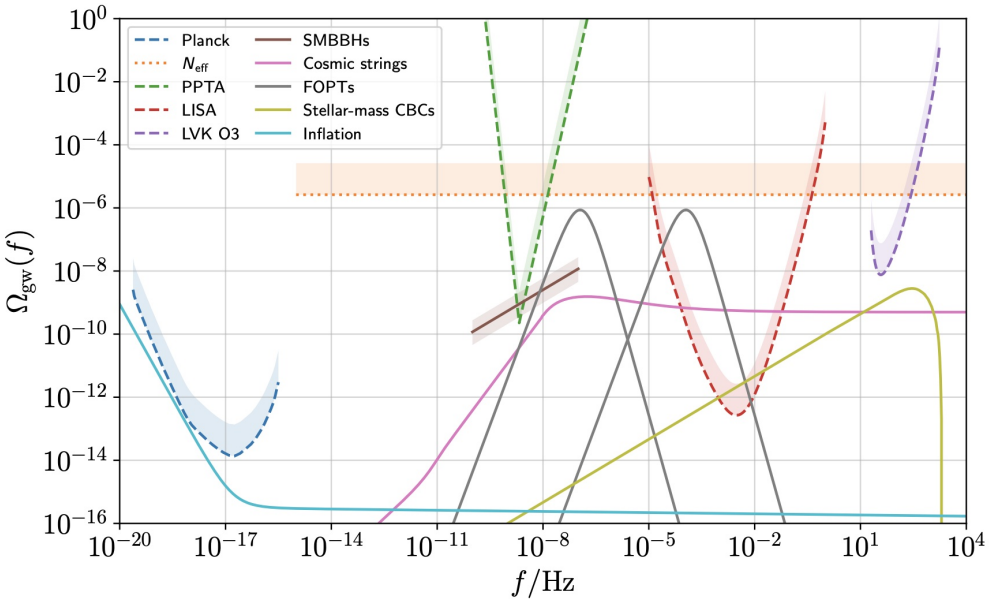

Figure 3: An overview of the most probable SGWB sources across the frequency spectrum. The light blue curve shows the prediction for single-field slow-roll inflation with a canonical kinetic term. The pink curve shows a SGWB from Nambu–Goto cosmic strings. The brown curve shows a SGWB from inspiralling SMBBHs. The two grey curves show the SGWB generated by first-order phase transitions at two different energy scales. The yellow curve shows a GWB generated by stellar-mass compact binaries. The dashed and dotted lines are the sensitivity curves and observational constraints from present and forthcoming detectors, as described further in Sections 1.4 and 1.5. Credits: Figure 7 of Ref. [41], Renzini et al. (2022).

Cosmic inflation and reheating

One of the most significant sources of a cosmological SGWB is undoubtedly cosmic inflation. A fundamental prediction of any inflationary model is the generation of an irreducible stochastic background, the detection of which would be a smoking-gun probe of inflation [42]. In the standard single-field, slow-roll inflationary scenario, tensor fluctuations of the metric are adiabatic,

Gaussian, and approximately scale-invariant, resulting in a SGWB with similar properties. In this case, the energy density Ω_{gw} will be approximately frequency independent for $f \gg H0 \approx 10^{-18}$ Hz and will be primarily characterized by its amplitude[5]. The amplitude of the SGWB produced during inflation is usually described through the tensor-to-scalar ratio (r), defined as the ratio between the amplitudes of the power spectra of tensor and scalar perturbations of the metric. These primordial perturbations are also expected to imprint a pattern of B-modes in the polarization of the CMB, which has not been detected yet. However, the current best upper limit for r comes from the joint analysis of Planck and BICEP/Keck data, which yields $r < 0.032$ at 95% C.L. at the pivot scale $k_\star = 0.05\,\mathrm{Mpc}^{-1}$ [43]. This corresponds to a present time energy density of $\Omega_{gw} \lesssim 10^{-16}$ at $f \approx 10^{-17}$ Hz, a level well below the reach of present or planned GW detectors. A crucial point is that, even in the simplest, single-field framework, different inflationary scenarios predict different values of r. The study of observational signatures of the primordial SGWB thus provide a way to discriminate among specific models. Moreover, if we move beyond single-field inflation, even more specific signatures can be generated. In presence of additional fields besides the inflaton, an extra SGWB can be produced [44–46]. The scalar density perturbations generated during inflation may also source GWs: this may occur either at second order in perturbation theory [47] or by acting as seeds for primordial black holes [48, 49].

Interestingly, classical generation of GWs is also possible during the reheating phase [50]. Therefore, primordial stochastic background also opens a potential window on the reheating mechanisms, and related parameters. It has been shown that the Laser Interferometer Space Antenna (LISA) [51] will be able to probe inflationary scenarios beyond the irreducible vacuum tensor modes expected from any inflationary background. [52]. However, the prevailing consensus within the scientific community is that precision measurements of the CMB remain the best chance to obtain definitive evidence of inflation and to differentiate between various inflationary models. Notably, a number of present and forthcoming CMB experiments are specifically aimed at B-mode detection [53–57].

Phase transitions

After inflation, a cosmological SGWB may have been generated as a consequence of phase transitions. In particular, first-order phase transitions would proceed via the nucleation of true-vacuum bubbles. In this scenario, the production of GWs is due to three processes: bubble collisions [58–60], and the resulting magnetohydrodynamic turbulence [61, 62] and propagation of sound waves in the primordial plasma [63, 64]. The characteristic power spectrum of a SGWB formed by bubble collisions presents a sharp peak at the frequency related to the energy scale at which the transition occurred. Several theoretical

5 Note that for lower frequencies there is an increase in the predicted energy density of the SGWB as perturbations from the early Universe that were frozen out (being larger than observable size of the Universe) re-enter and propagate again as GWs.

scenarios involving first-order phase transitions could give rise to a SGWB that might be detectable by LISA, as discussed in Ref. [65].

Cosmic strings

Phase transitions can also lead to the creation of stable topological defects, with cosmic strings being a prominent example. These line-like topological defects are generated through spontaneous symmetry breaking during the early Universe. Once formed, their dynamical evolution results in a dense network of cosmic string loops, oscillating at relativistic speeds and producing abundant GWs that collectively contribute to a robust SGWB [66]. Additionally, when cosmic strings intersect, they form cusps and kinks, generating bursts of GWs. The superposition of all these GW bursts over the history of the Universe contributes to an overall SGWB [67–69]. Figure 3 shows an overview of the SGWB sources discussed in this Section across the frequency spectrum.

1.2.2 *Astrophysical backgrounds*

The second category of stochastic backgrounds, the astrophysical ones, arises from the superposition of many unresolved GW signals generated by astrophysical sources, both galactic and extragalactic. All sources that are too faint or numerous to be individually resolved contribute collectively to the generation of a diffuse, incoherent background. This background can be considered stochastic in the limit where the number of sources is very large. If the sources are extragalactic, the resulting signal exhibits a nearly homogeneous distribution all over the sky, with minimal anisotropies associated to the large-scale structure (LSS) distribution of matter in the Universe. Moreover, assuming that the orientation of individual sources is random, these SGWB are generally expected to be unpolarized, as the polarizations of the single GW signals emitted by the various sources is averaged out over the different inclination angles relative to the direction of observation.

Merging binaries

Perhaps the most studied SGWB signal in the literature is the one sourced by merging compact-object binary systems. These include black hole binaries, neutron star binaries, white dwarf binaries, and systems given by a mixed pair of these objects. Black hole binaries in particular are a vast category of sources, as the mass of each black hole in the binary ranges between $5\,M_\odot$ and $10^{10}\,M_\odot$.[6] Specifically, a black hole is considered massive for $M_{BH} = 10^5 \div 10^{10} M_\odot$, intermediate for $M_{BH} = 10^2 \div 10^5 M_\odot$, and stellar mass for $M_{BH} = 5 \div 10^2 M_\odot$. The binaries where the two objects fall within the same

6 The lower mass of $5M_\odot$ refers to the lack of BHs between the Tolman–Oppenheimer–Volkoff limit, which sets the maximum mass of a neutron star to $2.9M_\odot$ [70], and $5M_\odot$, as seen in low-mass X-ray binary observations [71, 72]. This possibily prohibited region in the mass space is known as *lower mass gap* [73].

mass category have a mass ratio close to one. On the other hand, there are binaries where the two objects belong to different families, leading in some cases to extremely low values of the mass ratio. The GW events associated to these objects are called extreme mass ratio inspirals (EMRI).

The intrinsic astrophysical features defining a binary system, such as its total mass, mass ratio, and spin, significantly influence the properties of the GW emission. In particular, the total mass of a binary impacts the characteristic amplitude of the GW signal and the maximum frequency it reaches. Nevertheless, across the mass spectrum, the GW power spectra exhibit similar characteristics. During the early stages of binary evolution, known as the *inspiral* phase, the energy emission increases adiabatically as the binary orbit gradually shrinks and is well-approximated by a power-law behavior, as explained in Subsection 1.2.3. Subsequently, a powerful burst of energy accompanies the *merger* event, followed by a sudden decline in GW emission during the *ringdown* phase as the newly formed compact object stabilizes. These three phases are also reflected in the peculiar shape of the SGWB produced by merging binaries, as it is shown in Figure 4. Notably, the peak of the GW emission associated with the merger event occurs at higher frequencies for lighter binary systems. This determines the frequency band at which specific classes of binaries are typically observed. For instance, the SGWB produced by stellar binaries is expected to dominate the frequency range accessible to ground-based interferometers ($10 - 10^3$ Hz). In the lower frequency range, within the LISA band ($10^{-3} - 10^{-2}$ Hz), the SGWB from massive black holes and EMRIs become observable, along with the confusion-limited background generated by double white dwarfs within the Milky Way [74]. Lastly, the SGWB produced by merging supermassive black holes (SMBHs) occupies the extreme low-frequency regime ($10^{-9} - 10^{-8}$ Hz), which is explored by PTA experiments. Additional details on the detection techniques at the different frequency bands, along with insights into ongoing and forthcoming experiments, will be provided in Sections 1.4 and 1.5.

The SGWB is a collective signal, whose properties are given by the features of the population of binaries contributing to it. Specifically, the binary mass distribution and event rate, both varying with redshift, have a significant influence on the amplitude and shape of the resulting SGWB. It is possible to reconstruct the mass distribution and redshift history from the SGWB through meticulous modeling and combination with direct measurements of individual events, as shown in Ref. [75], for example. When using such phenomenological approaches, however, it's important to acknowledge that the selection effects of the detector can introduce limitations in fully sampling the parameter space. Alternative approaches involve probing the redshift-dependent event rate through a detailed modeling of the specific astrophysical conditions favoring the formation and merger of stellar compact binaries. For instance, empirical constraints for the galaxy star formation and chemical enrichment, combined with prescriptions for compact binary mergers obtained through stellar evolution simulations, can provide a well-grounded theoretical framework for predicting the expected GW emission, as seen in Refs. [76, 77]. This kind of

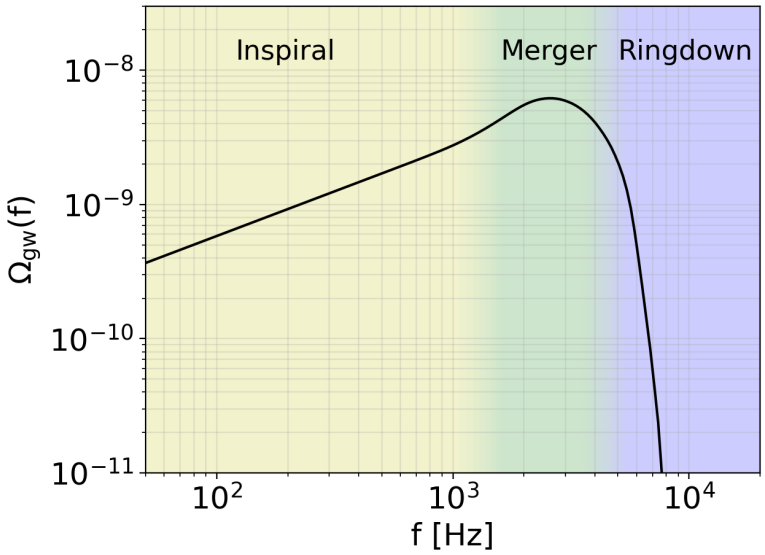

Figure 4: Typical frequency behavior of the energy density as a function of the observed frequency for a SGWB produced by merging compact binaries. The power-law, peak and exponential cutoff regimes correspond to the inspiral, merger and ringdown phases, respectively, as explained in the text. This specific plot shows the SGWB produced by merging BNSs, computed as explained in Subsection 1.2.3, according to the astrophysical prescriptions presented in Chapter 2.

approach forms the foundation of the results presented in this Thesis and will be extensively discussed in the following chapters.

Unmodeled bursts

Additional astrophysical sources of SGWB encompass asymmetric supernova explosions [78–80] and rotating neutron stars that do not exhibit perfect spherical symmetry [81, 82]. It is important to note that these sources are considered minor contributors in comparison to coalescing compact binaries, mainly due to their weaker characteristic signals and the greater complexity required to model them (indeed, they are often referred to as unmodeled bursts). On the other hand, this latter fact implies that these secondary sources will inevitably become subjects of a stochastic search, which can also be viewed as a generic, "unmodeled" approach to detect GW power, making it suitable for identifying signals from these less predictable astrophysical sources.

1.2.3 *The SGWB from coalescing binaries*

Since the SGWB generated by coalescing compact binaries is the primary focus of this Thesis, this subsection will be dedicated to deriving the expression for

its energy density parameter.[7] Specifically, I will summarize the various equivalent methodologies outlined in several previous works [37, 83–90]. Let's start by performing a useful manipulation of the definition of the energy density parameter, introduced in Equation (21):

$$\Omega_{gw}(f) = \frac{1}{\rho_c}\frac{d\rho_{gw}}{d\ln f} = \frac{f}{\rho_c}\frac{d\mathcal{E}_{gw}}{dVdf} = \frac{f}{\rho_c c}\frac{d\mathcal{E}_{gw}}{dSdtdf}, \tag{31}$$

where $\mathcal{E}_{gw}$ is the total energy carried by the stochastic background, so that $d\mathcal{E}_{gw}/dSdtdf$ is the total energy flux per unit time and frequency in the observer frame. At this point, we can expand the previous equation as follows:

$$\Omega_{gw}(f) = \frac{f}{\rho_c c}\int dz d\theta\, p(\theta)\, F(f,z|\theta)\,\frac{d\dot{N}}{dz}(z|\theta). \tag{32}$$

In Equation (32), $p(\theta)$ is the probability distribution of the astrophysical parameters θ that characterize the sources (e.g. chirp mass, mass ratio, spin, etc.). $F(f,z|\theta)$ is the averaged energy flux per unit observed frequency emitted by merging compact binaries located at redshift z and characterized by the intrinsc astrophysical parameters θ:

$$F(f,z|\theta) = \frac{1}{4\pi d_L^2}\frac{dE_{gw}}{df}(f|\theta) = \frac{1}{4\pi r^2(1+z)}\frac{dE_{gw}}{df_s}(f_s|\theta), \tag{33}$$

where dE_{gw}/df is the emitted gravitational spectral energy and $f_s = f(1+z)$ is the frequency in the source frame. $d_L(z)$ and $r(z)$ are the luminosity distance and the proper distance, respectively, and depend on the adopted cosmology. The last element of the integral in Equation (32) is the rate of mergers per unit redshift interval. This quantity can be expressed in terms of the intrinsic merger rate per unit comoving volume, $\mathcal{R}(z|\theta)$, as follows:

$$\frac{d\dot{N}}{dz}(z|\theta) = \mathcal{R}(z|\theta)\frac{dV}{dz}, \tag{34}$$

with

$$\frac{dV}{dz} = \frac{4\pi c\, r^2(z)}{H(z)}, \tag{35}$$

where $H(z) = H_0 h(z)$ is the Hubble rate. By combining everything together, we arrive at the well-known expression for the SGWB energy density parameter, as reported in [37, 83–90]:

7 Using the parameter Ω_{gw} to describe the energy density of GWs emitted by astrophysical events may seem unconventional as, historically, it is considered a cosmological quantity. Nevertheless, over the years, it has become a well-established convention, enabling practical cross-disciplinary comparisons among researchers.

$$\Omega_{gw}(f) = \frac{8\pi G f}{3H_0^3 c^2} \int dz d\theta \, p(\theta) \frac{dE_{gw}}{df_s}(f_s(z)|\theta) \frac{\mathcal{R}(z|\theta)}{(1+z)h(z)}. \tag{36}$$

As it will become clear in the next chapters, this equation holds particular significance within this Thesis, as it serves as a foundational tool for calculating the SGWB energy density across different scenarios. Throughout my research, I extensively used this expression to estimate $\Omega_{gw}(f)$ for various astrophysical sources, within distinct theoretical frameworks. This involved the incorporation of different prescriptions for the merger rates $\mathcal{R}(z|\theta)$, the emitted energy spectra dE_{gw}/df, and even the adopted cosmology, which enters in the value of H_0 and the expression of $h(z)$.

Let's now explore a practical example involving the inspiral of binaries in circular orbit. In the Newtonian limit, a circular binary system with component masses m_1 and m_2 that merges due to gravitational-radiation loss emits the following energy spectrum (see e.g. Ref. [83]):

$$\frac{dE_{gw}}{df_s} = \frac{(\pi G)^{2/3}}{3} \mathcal{M}_c^{5/3} f_s^{-1/3}, \tag{37}$$

where $\mathcal{M}_c$ is the *chirp mass* of the binary system, given by

$$\mathcal{M}_c = \frac{(m_1 m_2)^{3/5}}{(m_1 + m_2)^{1/5}}. \tag{38}$$

If we assume for our example that the population of binaries is defined only by their chirp masses, then the total merger rate per unit comoving volume can be written as:

$$\mathcal{R}(z) = \int_{\mathcal{M}_{c,min}}^{\mathcal{M}_{c,max}} d\mathcal{M}_c \, \mathcal{R}(z|\mathcal{M}_c), \tag{39}$$

where the integration extremes depend on the specific features of the source population. Substituting everything into Equation (36) and rearranging the terms, we obtain:

$$\Omega_{gw}^{insp}(f) = \frac{8(\pi G)^{5/3} f^{2/3}}{9H_0^3 c^2} \int_0^{z_{max}} dz \int_{\mathcal{M}_{c,min}}^{\mathcal{M}_{c,max}} d\mathcal{M}_c \, \frac{p(\mathcal{M}_c) \, \mathcal{M}_c^{5/3} \, \mathcal{R}(z|\mathcal{M}_c)}{(1+z)^{4/3} h(z)}. \tag{40}$$

Equation (40) provides a simple spectral dependence for $\Omega_{gw}^{insp}(f)$, which may be condensed in

$$\Omega_{gw}^{insp}(f) = \Omega_{gw}^{insp}(f_{ref}) \left(\frac{f}{f_{ref}} \right)^{2/3}, \tag{41}$$

where $\Omega_{gw}^{insp}(f_{ref})$ is the energy density evaluated at a reference frequency f_{ref}. This power-law behavior captures the actual trend of the SGWB produced by a realistic population of binaries in the frequency range where all the contributing binaries are in their inspiral phase, as it can be seen in the low-frequency region in Figure 4. During the merger and ringdown phases, instead, the energy output changes substantially with respect to the simple expression reported in Equation (37), leading to a different behavior also for the resulting SGWB, as it can be seen Figure 4 at higher frequencies.

1.3 ANISOTROPIES

My Ph.D. project was primarily focused on theoretical modeling and detection prospects for the anisotropies of the SGWB produced by binary mergers. In this section, I will provide a general introduction to anisotropies and an overview of the related literature, aiming to contextualize my research. I will briefly discuss different theoretical models and computation strategies for the anisotropic stochastic background and its cross-correlation with other cosmic fields. The fundamental concepts about directional searches and observational constraints will be outlined in Sections 1.4 and 1.5. In most cases, the SGWB is nearly uniform with small fluctuations. Anisotropy in stochastic signals can be attributed to three main causes. First, it may derive from inhomogeneities in the generation mechanisms, such as a specific distribution of sources, inevitably resulting in an anisotropic signal. Second, as GWs propagate, they accumulate line-of-sight effects by crossing the matter density field that is unevenly distributed throughout the Universe. Third, the motion of the observer with respect to the rest frame of the SGWB sources produces an anisotropic distortion of the signal, caused by the Doppler effect. In the case of astrophysical backgrounds, the spatial distribution of GW sources is a biased tracer of the underlying matter distribution. Conversely, primordial backgrounds show anisotropies related to processes during the early Universe.

1.3.1 *Introduction to SGWB anisotropies*

To describe the SGWB anisotropies, let's recall the definition of fractional energy density parameter per unit solid angle, introduced in Equation (22):

$$\Omega_{gw}(f,\hat{\mathbf{n}}) = \frac{1}{\rho_c}\frac{d\rho_{gw}(f,\hat{\mathbf{n}})}{d\ln f\, d\hat{\mathbf{n}}}. \tag{42}$$

Using this expression, we can compute the full-sky average of the anisotropic SGWB, commonly known as the *monopole*[8]:

$$\overline{\Omega}_{gw}(f) = \frac{1}{4\pi}\int_{S^2} d\hat{\mathbf{n}}\, \Omega_{gw}(f, \hat{\mathbf{n}}). \tag{43}$$

It is useful to split the energy density parameter in two parts: an isotropic one, which depends only on frequency and corresponds to the full-sky average, and an anisotropic one, which depends also on the direction of observation:

$$\Omega_{gw}(f, \hat{\mathbf{n}}) = \overline{\Omega}_{gw}(f) + \delta\Omega_{gw}(f, \hat{\mathbf{n}}). \tag{44}$$

In analogy with the formalism used for CMB temperature and polarization fluctuations and galaxy clustering, we can also define the *energy density contrast*[9]:

$$\delta_{gw}(f, \hat{\mathbf{n}}) = \frac{\Omega_{gw}(f, \hat{\mathbf{n}}) - \overline{\Omega}_{gw}(f)}{\overline{\Omega}_{gw}(f)} = \frac{\delta\Omega_{gw}(f, \hat{\mathbf{n}})}{\overline{\Omega}_{gw}(f)}. \tag{45}$$

At first order, the energy density contrast can be expanded into three contributions that represent three different causes of anisotropy:

$$\delta_{gw} \approx \delta^{s}_{gw} + \delta^{l.o.s.}_{gw} + \mathcal{D}\, \hat{\mathbf{n}} \cdot \hat{\mathbf{v}}_{obs}. \tag{46}$$

In Equation (46), δ^{s}_{gw} is the source term related to the intrinsic inhomogeneities in the distribution of the SGWB emitters. $\delta^{l.o.s.}_{gw}$ is the propagation term that contains all the accumulated line-of-sight effects [91]. $\mathcal{D}\, \hat{\mathbf{n}} \cdot \hat{\mathbf{v}}_{obs}$ is the kinematic dipole induced by the observer's peculiar velocity $\boldsymbol{v}_{obs}$ with respect to the rest frame of the SGWB sources [92, 93]. Interestingly, the propagation term has contributions similar to those of CMB anisotropies, including the Sachs–Wolfe effect, caused by the local curvature at the source position, and the integrated Sachs–Wolfe effect, caused by the curvature perturbations encountered during propagation along the line-of-sight [94], a Doppler term, due to the peculiar motion of the sources, and higher order effects such as gravitational lensing and redshift-space distortions. All these terms have been the subject of intense study in the last years. I will summarize the main different approaches in Subsection 1.3.2.

Most works in the literature assume that $\delta_{gw}(f, \hat{\mathbf{n}})$ behaves like a zero mean Gaussian random field. Under this assumption, the energy density contrast is fully characterized by its two-point correlation function:

8 Many works in the literature use a different notation, where $\overline{\Omega}_{gw}$ represents the total SGWB energy density integrated over the sky. This notation differs from the one adopted here by a factor 4π.

9 The energy density contrast is a normalized quantity, which is insensitive to the adopted notation for $\overline{\Omega}_{gw}$. Hence, it can be used for unambiguous comparisons of different results.

$$C_{2P}(f,\theta) = \langle \delta_{gw}(f,\hat{\mathbf{n}})\delta_{gw}(f,\hat{\mathbf{n}}')\rangle, \tag{47}$$

where the angle brackets represent the average over all direction pairs $(\hat{\mathbf{n}}, \hat{\mathbf{n}}')$ with given separation angle $\theta = \cos^{-1}(\hat{\mathbf{n}}\cdot\hat{\mathbf{n}}')$. The first moment $\langle\delta_{gw}\rangle$ is zero by definition, and all the higher order moments either vanish or can be expressed in terms of $C_{2P}(f,\theta)$ [95]. The statistical isotropy of the Universe implies that the two-point correlation function depends only on the relative angle θ. In particular, $C_{2P}(f,\theta)$ is larger for the values of θ that correspond to more pronounced spatial correlations in the sky. It is common practice to perform a multipole expansion of $C_{2P}(f,\theta)$:

$$C_{2P}(f,\theta) = \sum_{\ell=0}^{\infty} \frac{2\ell+1}{4\pi} C_\ell(f) P_\ell(\cos\theta), \tag{48}$$

where $P_\ell(\cos\theta)$ are the Legendre polynomials of degree ℓ. The coefficients $C_\ell(f)$, known as *angular power spectrum*, contain all the information about the statistics of the SGWB anisotropies. An explicit expression for $C_\ell(f)$ can be obtained by inverting Equation (48):

$$C_\ell(f) = 2\pi \int_{-1}^{1} d\cos\theta\, C_{2P}(f,\theta) P_\ell(\cos\theta), \tag{49}$$

which can be constrained empirically from the two-point correlation function of a measured SGWB map. Roughly speaking, the value of the angular power spectrum C_ℓ evaluated at different multipoles ℓ represents the magnitude of the SGWB fluctuations on angular scales of about π/ℓ. In particular, the quantity $\ell(\ell+1)C_\ell/2\pi$ is approximately the contribution to the variance of δ_{gw} per logarithmic bin in ℓ, as can be seen by considering [93, 96]:

$$\sigma^2_{\delta_{gw}} = C_{2P}(\theta=0) = \sum_{\ell} \frac{2\ell+1}{4\pi} C_\ell \approx \int d\ln\ell\, \frac{\ell(\ell+1)}{2\pi} C_\ell. \tag{50}$$

Hence, the quantity $\ell(\ell+1)C_\ell/2\pi$ is often shown in plots instead of simply C_ℓ. As an alternative, the angular power spectrum can also be estimated directly from multiple realizations of the SGWB map. For instance, let's consider a map of the SGWB energy density contrast at a given frequency f. We can decompose it into spherical harmonic components

$$\delta_{gw}(f,\hat{\mathbf{n}}) = \sum_{\ell=0}^{\infty} \sum_{m=-\ell}^{+\ell} \delta_{gw,\ell m}(f) Y_{\ell m}(\hat{\mathbf{n}}), \tag{51}$$

and then estimate the angular power spectrum as:

$$C_\ell(f) = \frac{1}{2\ell+1} \sum_{m=-\ell}^{+\ell} \langle (\delta_{gw,\ell m}(f))^2 \rangle, \tag{52}$$

where the angle brackets represent the ensemble average over multiple random realizations of $\delta_{gw}(f, \hat{\mathbf{n}})$.

The angular power spectrum of Equations (49) and (52) refers to the energy density contrast δ_{gw}. Hence, it does not depend on the overall amplitude of the SGWB, but only on the relative strength of the fluctuations with respect to the monopole $\overline{\Omega}_{gw}$. To quantify the absolute amplitude of the SGWB anisotropies, it is useful to introduce the angular power spectrum of the fluctuation $\delta\Omega_{gw}$, defined in Equation (44). In this case, we start from the two-point correlation function for $\delta\Omega_{gw}$ [96]:

$$C^{\Omega}_{2P}(f, \theta) = \langle \delta\Omega_{gw}(f, \hat{\mathbf{n}}) \delta\Omega_{gw}(f, \hat{\mathbf{n}}') \rangle, \tag{53}$$

and, following the same steps, we obtain the angular power spectrum of the energy density fluctuation. Since $\delta\Omega_{gw} = \overline{\Omega}_{gw}\, \delta_{gw}$, we have

$$C^{\Omega}_{\ell}(f) = \overline{\Omega}^2_{gw} C_\ell(f). \tag{54}$$

1.3.2 *Theoretical models in the literature: an overview*

In recent years, significant effort has been dedicated to the theoretical characterization of the SGWB anisotropies. To give a context for my own research, I will provide a brief overview of the main approaches. Since I mostly worked on the astrophysical SGWB from merging compact binaries, I will focus on the frameworks to compute the anisotropies of this type of background. Nevertheless, some of the approaches I will discuss already include the cosmological stochastic background and can be easily adapted to other types of astrophysical stochastic backgrounds.

The anisotropies of the cosmological stochastic background retain precious information about the primordial mechanisms generating GW emissions and the early-time characteristics of the Universe, such as its geometry and particle content. Numerous studies in the literature focus on calculating the angular power spectrum of the anisotropies resulting from various cosmological generation processes like, e.g., Refs. [97–101]. The computation of the anisotropies of the astrophysical SGWB, instead, relies on (i) the underlying cosmology, (ii) the large-scale structure of the Universe and its effect on GW propagation, and (iii) the local astrophysics on galactic and sub-galactic scales.

A Boltzmann approach

The first formalism to calculate an explicit theoretical expression for the SGWB anisotropies, both cosmological and astrophysical, was proposed in Ref. [91],

Contaldi (2017). In analogy with CMB calculations, the author adopts a Boltzmann approach to describe the perturbations in the distribution function of the tensor modes propagating the energy flux of the SGWB. Furthermore, the author uses a line-of-sight method to calculate the angular power spectrum of the SGWB anisotropies. Indeed, the anisotropies are induced not only by inhomogeneities in the source distribution but also by those encountered during the SGWB propagation through the large-scale structure of the Universe. The main result is a general expression for the SGWB anisotropies, which consists of a time integral of a Legendre-expanded source function. All the contributions to the SGWB source function are attributed to well-understood physical effects, which have counterparts in the CMB source function as well. These contributions include a density term resulting from the inhomogeneous distribution of the emitters, the Sachs-Wolfe effect, the Integrated Sachs-Wolfe effect, and a Doppler term originating from the peculiar velocities of the GW emitters. An important difference from the CMB case is that the photons reach the observer from a constant-time hypersurface, while the sources of the SGWB have a non-trivial redshift distribution. The obtained expression is finally used to provide preliminary estimates of the anisotropies for the primordial SGWB generated during inflation and the astrophysical SGWB from merging compact binaries. The initial findings presented in Ref. [91] paved the way for subsequent analyses, where more accurate descriptions of the astrophysical source mechanisms for anisotropies were incorporated.

A coarse-graining approach

The first theoretical expression for the energy density anisotropies for the astrophysical SGWB was derived in Refs. [102, 103], Cusin et al. (2017,2018). The authors use a "coarse-graining" approach, distinguishing the three physical scales in the problem: cosmological, galactic and subgalactic. The largest scale is the one of the cosmic flow, which controls the evolution of the matter density contrast and peculiar velocity. Galaxies are then assumed to be a biased tracer of matter, and are associated with an effective GW luminosity. This GW luminosity takes into account the contribution of different astrophysical sources to the total GW emission from each galaxy, which is characterized by a selection of astrophysical parameters, such as mass and metallicity. As their main result, the authors present a covariant expression for the SGWB anisotropies valid in any spacetime, as well as its application to a perturbed FRW Universe. Using this framework, the first predictions of the power spectrum of the SGWB anisotropies have been presented in Ref. [96], for the contribution of binary black holes mergers at frequencies in the LVK band. The influence of various astrophysical prescriptions on the angular power spectrum was investigated in Ref. [104] and extended to the LISA band in Ref. [105].

Further approaches and a comparison

Building upon the formalism outlined in Cusin et al. (2017,2018), at least two other frameworks have been proposed to compute the anisotropies of the astrophysical SGWB. One was introduced in Ref. [93], Jenkins et al. (2018), initially applied to cosmic strings and then extended to merging compact binaries in Refs. [95, 106]. The angular power spectrum of the SGWB anisotropies has been determined using two complementary approaches: an analytical approach featuring simple expressions for the galaxy number density and galaxy-galaxy two-point correlation function, and a detailed numerical study using an all-sky mock galaxy catalogue from the Millennium simulation [107]. It has been pointed out in the literature [108, 109] that there is a tension between the predictions of Refs. [95, 106] and those of Refs. [96, 104]. The discrepancy between the two estimates probably depends on various factors, including different treatments of sources at very low redshift, of non-linear clustering at small scales and of shot noise, which results from the discreteness of the sources in both space and time.

Finally, the second approach based on Cusin et al. (2017,2018) was presented in Refs. [110, 111], Bertacca et al. (2020) and Bellomo et al. (2022), where a new derivation of the SGWB anisotropies in a cosmological context was proposed. In these works, the angular power spectrum is computed accounting for all the projection effects intervening between the source and the observer. The authors, in particular, argue the presence of additional effects in their result, not previously taken into account in the literature. One such effect is a "Kaiser projection term", arising from peculiar velocity Doppler shifts.

All the mentioned results for the expression of the astrophysical SGWB anisotropies were compared in Ref. [112], Pitrou et al. (2020). The authors show that the various predictions are essentially equivalent when appropriate matching of terms and integration by parts are performed. Indeed, all the formulations contain the same well-known cosmological effects, implying that discrepancies can only emerge in the treatment of galactic and sub-galactic physics.

1.3.3 *Shot noise and cross-correlations*

Unlike cosmological stochastic backgrounds, typically originating from extended sources, the astrophysical SGWB is given by the superposition of a large yet finite number of unresolved events. These sources are discrete in both space and time. Therefore, the Poissonian fluctuations in this finite population of sources induce a white shot noise component in the angular power spectrum. The shot noise is very large [113–116], and the intrinsic anisotropies induced by the LSS are often concealed beneath it. One possible solution to reduce the impact of shot noise is to cross-correlate the SGWB anisotropies with other cosmic fields that trace the LSS. In this way, it is possible to enhance the intrinsic anisotropies due to the LSS. Cross-correlations of the astrophsyical SGWB with galaxy number counts, galaxy lensing, CMB anisotropies have

been extensively studied in the literature . Of course, the same principle applies to cosmological backgrounds, which typically do not suffer from shot noise. Cross-correlations with CMB temperature anisotropies offer an effective way to amplify the power of anisotropies in the cosmological SGWB as a probe of the early Universe [117–121]. Lastly, the detection of intrinsic anisotropies in the SGWB is further complicated by the presence of instrumental noise. This noise contribution, often larger than the shot noise, must be considered in all detectability studies. The angular power spectrum of instrumental noise for various networks of detectors mapping the SGWB was calculated in Ref. [122], Alonso et al. (2020). The calculation took into account the network configuration, individual detector noise properties, and scan strategy.

1.3.4 *Kinematic anisotropies*

Aside from the intrinsic anisotropies discussed in the previous subsection, there are also kinematic anisotropies due to the peculiar motion of our detectors with respect to the rest frame of the SGWB. This process results in a dipole in the SGWB, with the Doppler enhancement of the intensity of the GW sources we are moving towards and a corresponding reduction in the intensity of the sources we are receding from. The kinematic dipole is a well-known effect that has already been measured with high precision in other cosmological observables, such as the CMB temperature fluctuations [123], or the number counts of quasars and radio galaxies [124]. Notably, measuring the kinematic dipole in the SGWB could potentially provide insights into the existing tension between the dipole measured from the CMB and the number counts of radio sources [125].

Within the SGWB, the Doppler boost generates kinematic anisotropies from the rest-frame monopole. Furthermore, it causes the modulation and aberration of existing rest-frame anisotropies [92]. Notably, these kinematic effects are amplified when the SGWB is characterized by sizeable tilts in its rest-frame energy density $\Omega_{gw}(f)$ or intrinsic anisotropies. As a result, Doppler effects offer complementary probes of the SGWB frequency profile and its intrinsic, rest-frame anisotropies. Kinematic anisotropies are one of the guaranteed features of the SGWB and are expected to be quite strong, possibly the first ones to be measured, provided that the corresponding monopole has a sufficiently high signal-to-noise ratio. Recent detection studies for the kinematic dipole using present and forthcoming GW instruments have been put forth for both the astrophysical SGWB [126–128] and resolved sources [129]. Specifically, the Einstein Telescope (ET) is potentially able to detect a dipole anisotropy at the level of $C_{\ell=1} \sim 10^{-24}$, which is the size of the kinematic dipole expected from a SGWB component on the edge of being detected by LVK at O5 sensitivity. LISA, on the other hand, will have better sensitivity to detecting a quadrupole (i.e., $\ell = 2$) than for the dipole (i.e., $\ell = 1$). The SGWB energy density required to observe the kinematic dipole induced by the motion of the LISA detector with

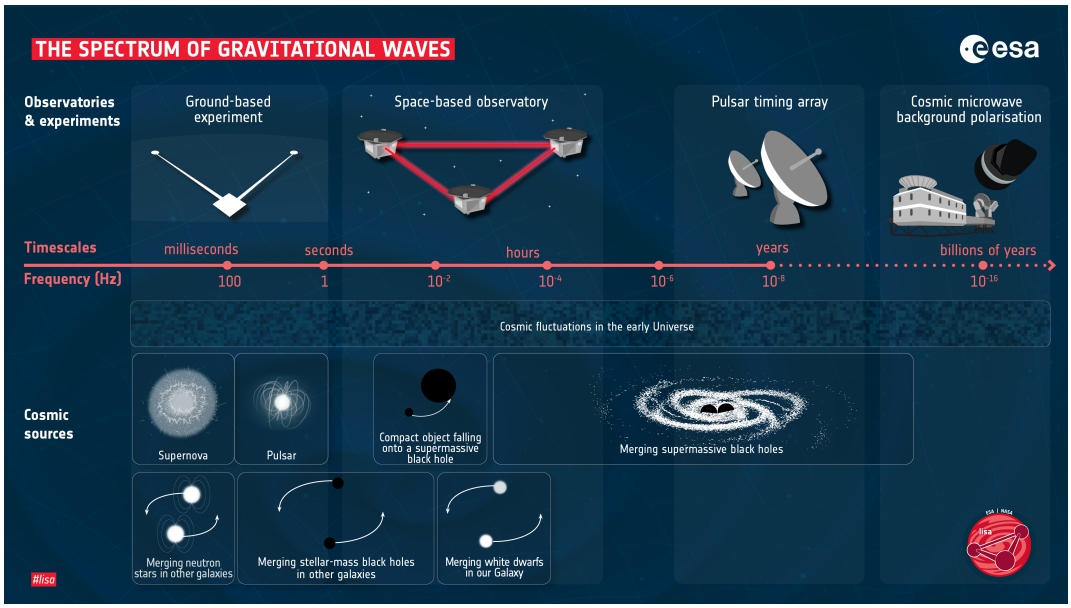

Figure 5: The GW spectrum with the main sources and detectors in the various frequency bands. Credits: ESA https://www.esa.int.

respect to the SGWB rest frame is $\Omega_{\rm gw} \sim 2 \times 10^{-11}$. In contrast, the sensitivity to the quadrupole is a factor $\sim 10^3$ larger than that to the dipole [130].

1.4 DETECTION STRATEGIES

In this section, I will give a general overview of the most common detection strategies for stochastic searches. The discussion is mostly based on the comprehensive and pedagogical review of current and proposed detection methods provided in Ref. [23], Romano&Cornish (2017).

1.4.1 *Searches across the GW spectrum*

As we already discussed in Section 1.2, there are many different astrophysical and cosmological sources of stochastic backgrounds. These sources emit GWs within specific frequency ranges. Indeed, different instruments and detection techniques are needed to access signals in different frequency bands. An illustration of the GW frequency spectrum, together with potential sources and relevant detectors, is shown in Figure 5. In the following, I will highlight a few important GW experiments, both operational and planned.

Ground-based interferometers

Ground-based laser interferometers search for GWs between 10 Hz and a few kHz. Gravity gradient and seismic noise are the limiting noise sources below 10 Hz, and photon shot noise above a couple of kHz. At these frequencies, the main sources of GWs are the coalescences of stellar binary systems. The

current "second generation" (2G) ground-based detectors are L-shaped laser interferometers with arms spanning a few kilometers in length. The 2G detector network includes four operational facilities: the two detectors of the Laser Interferometer Gravitational-wave Observatory in the United States [4], the Virgo detector in Italy [5], and the Kamioka Gravitational Wave Detector in Japan [10]. KAGRA joined the other three detectors only recently for their fourth observing run (O4). To these, we can add the GEO600 detector in Germany, which, however, does not have comparable sensitivity to the others given its smaller size [131]. The individual collaborations behind these detectors have joined efforts under the LIGO/Virgo/KAGRA collaboration. In the future, the Indian Initiative in Gravitational-wave Observations plans to set up more experimental facilities, such as LIGO India [132]. Beyond these, the next phase of advancements involves the so-called "third generation" detectors (3G), such as the ET in Europe [133–135] and the Cosmic Explorer (CE) in the United States [136, 137]. 3G detectors will provide an improvement in sensitivity by one order of magnitude and a significant enlargement of the bandwidth. The current design of 3G detectors is based on several innovative concepts. For instance, ET is planned as a single underground observatory to drastically reduce seismic noise. In the current concept, it has a triangular shape with three nested detectors, allowing for a null stream to act as a veto against disturbances and enabling the resolution of GW polarizations. Within each of the three detectors, a "xylophone" configuration will be employed, featuring two interferometers tuned to different frequency bands.

Spaced-based interferometers

In the frequency range between 10^{-4} Hz and 10^{-1} Hz, corresponding to timescales from hours to minutes, planned space-based interferometers such as the Laser Interferometer Space Antenna (LISA) will explore a variety of GW sources [51, 74]. These include (i) SMBBHs with masses $\sim 10^6$ $M_\odot$, (ii) extreme mass ratio inspirals, and (iii) the stochastic confusion noise generated by white-dwarf binaries within our Galaxy. Interestingly, LISA will also be able to detect coalescing stellar binaries, eventually entering in the LVK band within a few years, thus paving the way for multi-band GW astronomy [138]. The current configuration of LISA involves three satellites in an equilateral triangle formation, with arm length of 2.5 million km. Each satellite will house two lasers, two telescopes, and two test masses. This particular design is a variation of the original LISA concept, and was officially selected by the European Space Agency (ESA) in February 2017 to be their third major mission in the Cosmic Vision Program. The earliest launch date for LISA is 2034. A test mission named LISA Pathfinder was launched in December 2015, successfully meeting or surpassing all requirements for a crucial subset of the LISA technologies [139]. At higher frequencies, between 0.1 Hz and 10 Hz, corresponding to periods between 10 s and 0.1 s, there are proposals for 2G space-based instruments: the Big-Bang Observer (BBO) [140] and the DECIhertz interferometer Gravitational-wave Observatory (DECIGO) [141]. Such detectors would bridge

the frequency gap between LISA and ground-based interferometers. The primary sources in this band are intermediate-mass (10^3–10^4 $M_\odot$) BBHs, galactic and extra-galactic BNSs, and cosmological stochastic backgrounds.

Pulsar timing arrays

At frequencies between 10^{-9} Hz and 10^{-7} Hz, corresponding to periods of order years to decades, pulsar timing arrays (PTAs) can be used to search for GWs. This is done by carefully monitoring the arrival times of radio pulses from an array of galactic millisecond pulsars, looking for correlated modulations in the arrival times induced by a passing GW [142, 143]. The major current PTA experiments include the North American Nanohertz Observatory for Gravitational Waves (NANOGrav) [144], the Parkes Pulsar Timing Array (PPTA) [145], the European Pulsar Timing Array (EPTA) [146], and the consortium of these collaborations known as the International Pulsar Timing Array (IPTA) [147, 148]. Over the years, these searches have continuously enhanced their sensitivity by upgrading instrument back-ends and discovering more millisecond pulsars that were added to the arrays. These improvements have progressively placed tighter upper limits on the amplitude of the SGWB, until the first evidence for a stochastic signal was announced by the NANOGrav, ETPA and PPTA collaborations in July 2023 [13–15]. The origin of this signal is still uncertain, but the leading hypothesis is a SGWB formed from the incoherent superposition of signals produced by the inspiral of SMBBHs in the center of distant galaxies [16].

CMB experiments

At the extreme low-frequency end of the spectrum, corresponding to GW periods of order the age of the Universe, numerous CMB experiments are looking for evidence of the primordial SGWB in the B-mode component of CMB polarization maps [149, 150]. Numerous ground-based experiments are currently scanning the microwave sky in search of the primordial B-modes, including the BICEP2/Keck Array [151], the POLARBEAR/Simons Array [152, 153], the Atacama Cosmology Telescope [154], and the South Pole Telescope [155]. Furthermore, the next decade will see a great increase in the detection efforts with a new generation of experiments including the Simons Observatory (SO) [57] and the Stage-IV network of ground-based observatories (CMB-S4) [156]. As for space-borne experiments, the Japan Aerospace Exploration Agency has selected the LiteBIRD [157] as the second strategic large-class mission. In 2014, BICEP2 announced the detection of relic GWs from inflation [158], but it was later shown that the observed B-mode signal was due to contamination by intervening dust in the galaxy [159, 160]. So at present, these experiments have been able to only set upper limits on the amount of GWs in the early Universe [43]. These constraints severely limit the possibility of detecting the relic gravitational-wave background with any of the higher-frequency detec-

tion methods, unless its spectrum features characteristic bumps or increases with frequency [161].

1.4.2 *Stochastic search methods*

In the following, I will give an overview of the stochastic search methods, mainly focusing on cross-correlation methods for ground-based detectors.

Cross-correlation methods

Stochastic GW signals are indistinguishable from instrumental noise in a single detector, but are correlated between pairs of detectors in ways that differ, in general, from instrumental noise. Cross-correlation methods basically use the random output of one detector as a template for the other, taking into account the physical separation and relative orientation of the two detectors. To understand the basic idea, let's consider the simple case of a pair of co-located and co-aligned detectors attempting to measure a SGWB. The data-streams from those detectors will be:

$$\begin{aligned} d_1(t) &= s(t) + n_1(t), \\ d_2(t) &= s(t) + n_2(t), \end{aligned} \tag{55}$$

where $s(t)$ is the common GW signal, and $n_1(t)$ and $n_2(t)$ are the detector noises, with $n_1, n_2 \gg s$. A straightforward way to obtain the GW signal is to cross-correlate the outputs of the two detectors:

$$\begin{aligned} \langle d_1(t) d_2(t) \rangle &= \langle s^2(t) \rangle + \langle s(t) n_1(t) \rangle + \langle s(t) n_2(t) \rangle + \langle n_1(t) n_2(t) \rangle \\ &\approx \langle s^2(t) \rangle, \end{aligned} \tag{56}$$

where the angle brackets represent the time average. Since it is assumed that the noise in each detector is statistically independent from one another, and also from the stochastic background, the cross-correlation of the two data-streams is just the variance of the stochastic signal. However, in practical scenarios, the two detectors will be displaced from one another, resulting in slightly different detected signals. The implications of this will be discussed further below. Cross-correlation methods can be applied when using two or more detectors that respond to a common GW signal. On the other hand, when dealing with a single detector, or multiple detectors with correlated noise (such as LISA or ET), stochastic searches require alternative methods to distinguish the signal from the noise. This distinction might be achieved through differences between the spectra of the noise and the GW signal, or the modulation of an anisotropic signal due to the motion of the detector (as expected for the confusion noise from galactic white-dwarf binaries for LISA).

Detector response

Since GWs are weak, the detector's output $s(t)$ is linear in the metric perturbations $h_{ij}(t,\mathbf{x})$ and can be written as the convolution of $h_{ij}(t,\mathbf{x})$ with a filter function known as detector response $R_{ij}(t,\mathbf{x})$:

$$s(t) = (\mathbf{R} * \mathbf{h})(t,\mathbf{x}) = \int_{\infty}^{+\infty} d\tau \int d^3\mathbf{y}\, R^{ij}(\tau,\mathbf{y})\, h_{ij}(t-\tau,\mathbf{x}-\mathbf{y}), \tag{57}$$

where $\mathbf{x}$ is the location of the measurement at time t. In terms of a plane-wave expansion of the metric perturbations introduced in Equation (4), we have:

$$s(t) = \int_{\infty}^{+\infty} df \int_{S^2} d\hat{\mathbf{n}} \sum_{P=+,\times} h_P(f,\hat{\mathbf{n}})\, R^{ij}(f,\hat{\mathbf{n}})\, e^P_{ij}(\hat{\mathbf{n}})\, e^{i2\pi ft}, \tag{58}$$

or, in the frequency domain,

$$\tilde{s}(f) = \int_{S^2} d\hat{\mathbf{n}} \sum_{P=+,\times} h_P(f,\hat{\mathbf{n}})\, R^{ij}(f,\hat{\mathbf{n}})\, e^P_{ij}(\hat{\mathbf{n}}), \tag{59}$$

where

$$R^{ij}(f,\hat{\mathbf{n}}) = e^{i2\pi f\hat{\mathbf{n}}\cdot\mathbf{x}/c} \int_{\infty}^{+\infty} d\tau \int d^3\mathbf{y}\, R^{ij}(t,\mathbf{x})\, e^{-2i\pi(\tau+\hat{\mathbf{n}}\cdot\mathbf{y}/c)}. \tag{60}$$

Further specifications of the response function depend on the specific detector under consideration. Indeed, the functional form of $R^{ij}(f,\hat{\mathbf{n}})$ is determined by the detection strategy implemented by the instrument, such as laser interferometry or pulsar timing, as well as the geometry and orientation of the detector. For a derivation of the response function for various types of detectors, I refer the interested reader to Ref. [23].

Overlap reduction function

We saw that a SGWB manifests itself as a non-vanishing correlation between the data taken by two or more detectors. This correlation differs, in general, from that due to instrumental noise, allowing us to distinguish between a SGWB signal and other noise sources. To quantify the expected correlation due to a SGWB, let's consider the simple case of two detectors, labeled as I and J. In the presence of a GW signal, the data acquired by the two detectors will have the form

$$\begin{aligned} d_I(t) &= s_I(t) + n_I(t), \\ d_J(t) &= s_J(t) + n_J(t). \end{aligned} \tag{61}$$

Assuming that the instrumental noises of the two detectors are uncorrelated, the expected correlation of the data-streams is just the correlation of the detector responses to the GW signal, $\langle d_I d_J \rangle = \langle s_I s_J \rangle$. If we also assume that the GW signal is due to a stationary, Gaussian, isotropic, and unpolarized SGWB, then

$$\langle s_I(t) s_J(t') \rangle = \frac{1}{2} \int_{-\infty}^{+\infty} df\, e^{i2\pi f(t-t')}\, \Gamma_{IJ}(f)\, S_h(f), \tag{62}$$

where $S_h(f)$ is the PSD of the SGWB strain, defined in Equation (11), and

$$\Gamma_{IJ}(f) = \frac{1}{8\pi} \int_{S^2} d^2\hat{n} \sum_{P=+,\times} R_I^P(f,\hat{n})\, R_J^{P*}(f,\hat{n}) \tag{63}$$

is the so-called overlap reduction function of the two detectors, written in terms of the response function projected onto the polarization basis tensors:

$$R^P(f,\hat{n}) = R^{ij}(f,\hat{n}) e^P_{ij}(\hat{n}). \tag{64}$$

In the frequency domain, Equation (63) becomes

$$\langle \tilde{s}_I(f)\, \tilde{s}_J(f') \rangle = \frac{1}{2} \delta(f-f')\, \Gamma_{IJ}(f)\, S_h(f), \tag{65}$$

from which we can see that $\Gamma_{IJ}(f)$ plays the role of a transfer function between the PSD of the SGWB strain, $S_h(f)$, and the cross-correlation of the detector outputs, $\langle \tilde{s}_I(f)\, \tilde{s}_J(f') \rangle$. Therefore, the overlap function can be interpreted as the reduction in sensitivity of the cross-correlation of the detector outputs due to the non-trivial response of the detectors and their separation and orientation relative to one another. Indeed, in the expression for the overlap reduction function in Equation (63), four length scales are involved: the lengths of the two detectors, L_1 and L_2, which appear in the response functions $R_I^P(f,\hat{n})$ and $R_J^P(f,\hat{n})$; the separation of the detectors, $l = |\mathbf{x}_I - \mathbf{x}_J|$, which appears in the exponential factor; and the wavelength of the GW signal, $\lambda = c/f$. It is often convenient to define a normalized overlap reduction function $\gamma_{IJ}(f)$ by requiring that $\gamma_{IJ}(0) = 1$ for two co-located and co-aligned detectors. For two identical equal-arm Michelson interferometers, this leads to the relation

$$\gamma_{IJ}(f) = \frac{5}{\sin^2\beta} \Gamma_{IJ}(f), \tag{66}$$

where β is the opening angle between the two arms [23]. For example, $\beta = 90°$ for LIGO and $\beta = 60°$ for LISA. In the formalism outlined above, we have ignored any time-dependence in the detector response resulting from the detectors' motion relative to the GW source. In reality, this time-dependence is always present: for ground-based instruments, it is caused by the Earth's revolution around the Sun, while for space-borne instruments, it arises from their own motion along the orbit. Overall, this relative motion induces a modulation in both the amplitude and the phase of the response function.

Isotropic search methods

Let's now examine a cross-correlation search for a Gaussian, stationary, unpolarized, isotropic background using two detectors, I and J, with uncorrelated noise. Let T be the total observation time. In the frequency domain, the measurements are given by the complex-valued cross-correlation:

$$C_{IJ}(f) = \tilde{d}_I(f)\tilde{d}_J(f), \tag{67}$$

where $\tilde{d}_I(f)$ and $\tilde{d}_J(f)$ are the Fourier transforms of the time-series output of the two detectors reported in Equation (61). Since we assumed uncorrelated noise between detectors, the expectation value of the cross-correlation is:

$$\langle C_{IJ}\rangle = \frac{T}{2}\Gamma_{IJ}(f)S_h(f), \tag{68}$$

which is the same result of Equation (65), where we have replaced the $\delta(f - f')$ by its finite-time version $\delta_T(f - f') = T\,\mathrm{sinc}(\pi(f - f')T)$, which equals T for $f = f'$. In the weak-signal limit, which is typically verified for ground-based interferometers, the covariance matrix of the correlated measurement is dominated by the diagonal terms:

$$\begin{aligned} C_{ff'} &= \langle C_{IJ}(f)C^*_{IJ}(f')\rangle - \langle C_{IJ}(f)\rangle\langle C^*_{IJ}(f')\rangle \\ &\approx \langle n_I(f)n^*_I(f')\rangle\langle n_J(f)n^*_J(f')\rangle \\ &= \frac{T}{4}P_{nI}(f)\,P_{nJ}(f)\delta(f - f'), \end{aligned} \tag{69}$$

where $P_{nI}(f)$ and $P_{nJ}(f)$ are the noise PSDs in the two detectors:

$$\langle n(f)n^*(f')\rangle = \frac{1}{2}P_n(f)\delta(f - f'). \tag{70}$$

There are numerous methods for searching for an isotropic stochastic background. Many of them rely on the cross-correlation statistics discussed earlier. Below, I will briefly overview the optimal filtering technique. Let's suppose we are searching for a stochastic background with a power-law spectrum

$$\Omega_{gw}(f) = \Omega_{ref}\left(\frac{f}{f_{ref}}\right)^{\alpha}, \tag{71}$$

where Ω_{ref} is the value of the energy density parameter at the frequency f_{ref}. Then, according to Equation (28),

$$S_h(f) = \frac{3H_0^2}{2\pi^2}\frac{\Omega_{ref}}{f_{ref}^3}\left(\frac{f}{f_{ref}}\right)^{\alpha-3} = \Omega_{ref}H_\alpha(f), \tag{72}$$

where

$$H_{ref}(f) = \frac{3H_0^2}{2\pi^2}\frac{1}{f_{ref}^3}\left(\frac{f}{f_{ref}}\right)^{\alpha-3}. \tag{73}$$

At this point, it is possible to use the cross-correlation statistic presented in Equations (68) and (69) to write down an optimal filter to apply to the data and draw out an estimate for the amplitude Ω_α (see Refs. [20, 23, 39, 162] for different derivations):

$$\hat{\Omega} = N\int_{-\infty}^{+\infty} df \frac{\Gamma_{IJ}(f)H_\alpha(f)}{P_{nI}(f)P_{nJ}(f)}\tilde{d}_I(f)\tilde{d}_J^*(f), \tag{74}$$

where

$$N = \left[\frac{T}{2}\int_{-\infty}^{+\infty} df \frac{\Gamma_{IJ}^2(f)H_\alpha^2(f)}{P_{nI}(f)P_{nJ}(f)}\right]^{-1}. \tag{75}$$

The variance and signal-to-noise ratio of the estimator $\hat{\Omega}_\alpha$ are:

$$\sigma^2_{\hat{\Omega}_\alpha} = \left[T\int_{-\infty}^{+\infty} df \frac{\Gamma_{IJ}^2(f)H_\alpha^2(f)}{P_{nI}(f)P_{nJ}(f)}\right]^{-1} = \frac{N}{2}, \tag{76}$$

and

$$\rho = \sqrt{T}\left[\int_{-\infty}^{+\infty} df \frac{\Gamma_{12}^2(f)S_h^2(f)}{P_{nI}(f)P_{nJ}(f)}\right]^{1/2}. \tag{77}$$

All in all, the expression

$$\tilde{Q}(f) = N\frac{\Gamma_{IJ}(f)H_\alpha(f)}{P_{nI}(f)P_{nJ}(f)} \tag{78}$$

is the standard optimal filter used also in the official isotropic stochastic searches of the LVK collaboration [11, 163, 164].

Anisotropic search methods

The estimator of Equation (74) works well with a Gaussian, isotropic, stationary, and unpolarized stochastic background. However, for more general searches, it is possible to create estimators by considering if one (or more) of these assumptions does not hold. Indeed, to map the SGWB, one needs to relax the isotropic assumption, allowing the signal to have preferred directions

in the sky. Then, to reconstruct the angular information, one may use equal-time correlations of data from different detectors and the motion of individual detectors with respect to the signal's rest frame.

There are several methods for searching for anisotropic SGWBs, starting with the seminal paper of Ref. [17], Allen&Ottewill (1997), which laid the foundation for subsequent strategies. This first approach consists in searching for modulations in the correlated output of a network of detectors, focusing on harmonics of the rotational or orbital frequency of the detectors (e.g., daily rotational motion for ground-based detectors, or yearly orbital motion for space-based detectors). This method assumes a known distribution of the SGWB intensity $I(f, \hat{n})$ (see Equation (10)), and filters the data in order to maximize the signal-to-noise ratio of the correlated signal's harmonics. One class of approaches uses cross-correlated data from a network of detectors to construct maximum-likelihood estimates of the SGWB intensity across the sky, disregarding any time-domain phase information present in the data. These methods produce full-sky maps of $I(f, \hat{n})$, similar to how maps of the CMB temperature anisotropies are created [19, 165–168][10]. Other approaches aim to measure both the amplitude and phase of the stochastic background at every point in the sky, making minimal assumptions about the signal's statistical properties. This "phase-coherent" approaches result in full-sky maps of the real and imaginary components of the random fields $h_P(f, \hat{n})$, where $P = \{+, \times\}$ [171–173]. A detailed analysis of all these methods can be found, e.g., in Ref. [23].

1.4.3 *Sensitivity curves*

When discussing the detectability of GW signals using current or planned detectors, a typical approach is to plot the characteristic strain $h_c(f)$ of the predicted signal $h_c(f) = \sqrt{f\, S_h(f)}$, as defined in Equation (29), and compare it to sensitivity curves of different detectors [21]. A standard way to build the sensitivity curve is by taking the ratio of the detector's noise PSD $P_n(f)$ to its sky- and polarization-averaged response to a GW signal $\mathcal{R}(f)$, defining an effective characteristic strain of the noise amplitude:

$$h_{\rm eff} = \sqrt{f \frac{P_n(f)}{\mathcal{R}(f)}} = \sqrt{f S_n(f)}, \tag{79}$$

where $\mathcal{R}(f) = \Gamma_{II}(f)$ is obtained by setting $I = J$ in Equation (63) and represents the transfer function between the GW signal's PSD $S_h(f)$ and the detector response auto-power:

$$\langle \tilde{s}(f) \tilde{s}^*(f') \rangle = \frac{1}{2} \delta(f - f') \mathcal{R}(f) S_h(f). \tag{80}$$

10 These works are specifically applied to ground-based interferometers. See Refs. [169, 170] for intensity mapping methods applied to PTAs.

For deterministic signals, if the characteristic strain $h_c(f)$ lies above the detector sensitivity curve, then the signal has signal-to-noise ratio $\rho > 1$. Stochastic backgrounds, on the other hand, are typically searched for by cross-correlating data from two or more detectors. Therefore, it is appropriate to adjust the height of a sensitivity curve to account for the total observation time. For uncorrelated detector noise, the expected signal-to-noise ratio of a cross-correlation search for frequencies between f and $f + \delta f$ scales like $\sqrt{T\delta f}$ [174]. Therefore, the effective characteristic strain of the noise h_{eff} should be multiplied by a factor of $(T\delta f)^{-1/4}$. Also, instead of the characteristic strain, most analyses show directly the SGWB energy density $\Omega_{\text{gw}}(f) \propto f^2 h_c(f)$, as in Equation (30). Even with this rescaling, however, the standard sensitivity curves do not grasp the fact that stochastic searches also benefit for the broadband nature of the signal. Indeed, the integrated signal-to-noise ratio of Equation (77) scales like $\sqrt{N_{\text{bins}}} = \sqrt{\Delta f/\delta f}$, where N_{bins} is the number of frequency bins of width δf in the total bandwidth Δf. The specific value of the proportionality constant depends not only on the detector geometry, but also on the spectral shape of the stochastic background. Moreover, every stochastic search must involve at least two detectors, so that the sensitivity to the background depends also on the configuration of the detector network under consideration, whereas standard sensitivity curves are referred to one single detector.

To overcome all these issues, an alternative form of sensitivity curve that incorporates multiple detectors and the integrated nature of the detection statistic was proposed in Ref. [174]. These sensitivity curves, known as power-law integrated sensitivity curves (PLSs), are defined as the envelope of the limits that can be placed on power-law stochastic backgrounds with different spectral indices at a fixed value of the signal-to-noise ratio. Thus, any line (on a log-log plot) that is tangent to the power-law integrated sensitivity curve corresponds to a stochastic background power-law spectrum with an integrated signal-to-noise ratio of $\rho = \rho_{\text{fix}}$ by construction. This implies that if the predicted background, characterized by $\Omega_{\text{gw}}(f)$, consistently lies below the sensitivity curve, then it possesses $\rho < \rho_{\text{fix}}$. Conversely, if the curve representing a predicted power-law background with $\Omega_{\text{gw}}(f) \propto f^{\alpha}$ lies above the sensitivity curve, it will be observed with an expected signal-to-noise ratio $\rho = \Omega_{\alpha}^{\text{pred}}/\Omega_{\alpha} > 1$. Here, $\Omega_{\alpha}^{\text{pred}}$ represents the value of the predicted power-law spectrum evaluated at a certain f_{ref}, while Ω_{α} represents the value of the power-law spectrum with the same index α that is tangent to the sensitivity curve, always at $f = f_{\text{ref}}$.

1.5 CURRENT AND FORTHCOMING DETECTION EFFORTS

I will conclude this opening chapter with an overview of the current and upcoming detection efforts. First, I will provide a brief review of the results from the stochastic searches conducted by the LVK collaboration and the recent detection announced by PTA experiments, representing the first-ever direct measurement of a SGWB. Then, I will discuss the possibilities of measuring the

stochastic background using the main forthcoming GW observatories: the 3G ground-based detectors ET and CE, and the space-borne interferometer LISA.

1.5.1 *Results of the LVK stochastic searches*

The most recent stochastic search results from the LVK collaboration are obtained using data from the third observing run (O3) of the "second generation" detectors (2G) detectors LIGO and Virgo, combined with data from the first two observing runs, O1 and O2. In the following, I will briefly summarize the results of the LVK analyses, that were carried out for both an isotropic and anisotropic stochastic background [11, 12].

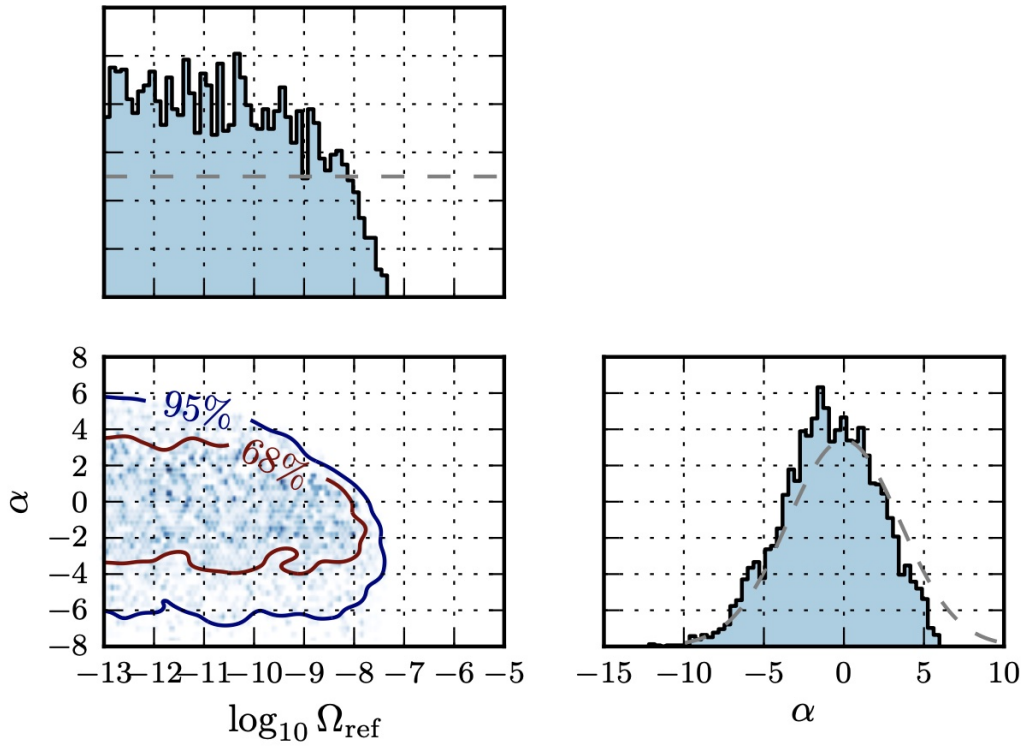

Figure 6: Posteriors for the amplitude $\Omega_{\rm ref}$ and spectral index α for a power-law SGWB obtained with the LIGO/Virgo O3 data. The dashed gray lines indicate the prior distributions. Credits: Figure 4 from Ref. [11].

Isotropic searches: upper limits on the SGWB

The latest LVK isotropic stochastic search consists in the application of the cross-correlation technique outlined in Subsection 1.4.2 to the data taken during O3 by the LIGO Hanford, LIGO-Livingston, and Virgo detectors. The anal-

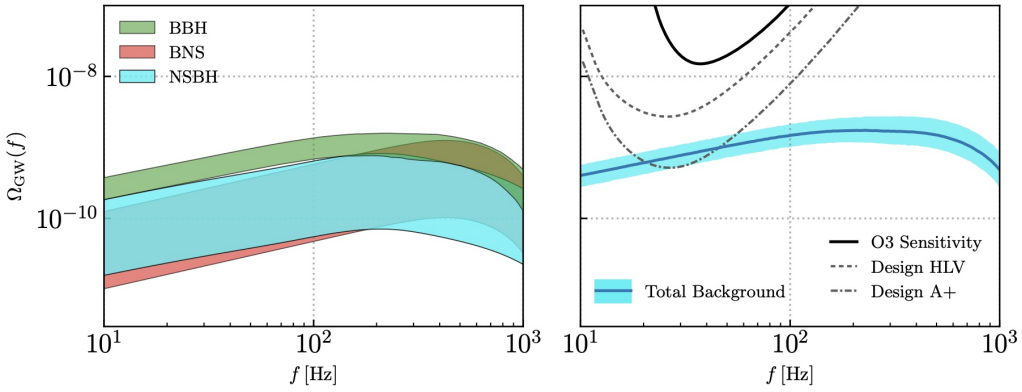

Figure 7: Forecast of the SGWB due to compact binary coalescence obtained from LIGO/Virgo O3 data. *Left panel*: Individual contributions expected from BBH, BNS, and NSBH coalescences. *Right panel*: Expected amplitude of the total SGWB, as well as the LIGO/Virgo O3 PLS curve [11, 174]. The expected sensitivities of the LIGO/Virgo network at design sensitivity and the anticipated LIGO A+ configuration are also reported for comparison (see https://dcc.ligo.org). Credits: Figure 23 from Ref. [9].

ysis searches for the existence of a Gaussian, stationary, unpolarized, isotropic background by applying the optimal filter defined in Equation (78) to the cross-correlation of the data from three distinct baselines: Hanford–Livingston (HL), Hanford–Virgo (HV), and Livingston–Virgo (LV). The optimal filter is built for a power-law SGWB with energy density

$$\Omega_{gw}(f) = \Omega_{ref}\left(\frac{f}{f_{ref}}\right)^{\alpha}, \tag{81}$$

where $f_{ref} = 25$ Hz, which is approximately the start of the most sensitive frequency band for the isotropic search [164]. The results of the search are consistent with uncorrelated noise, hence there is no clear evidence of a SGWB. Therefore, the LVK analysis sets upper limits on the SGWB amplitude for three fixed spectral indices: $\alpha = 0$, typically associated with a scale-invariant cosmological background, for example, from cosmic strings and slow-roll inflation [40]; $\alpha = 2/3$, describing a population of inspiralling compact binaries (see Equation (41)); and $\alpha = 3$, corresponding to a flat strain power that approximately describes certain astrophysical sources such as supernovae [175]. At a 95% confidence level and using a log-uniform prior, the analysis concluded that Ω_{ref} is less than 5.8×10^{-9} for $\alpha = 0$, 3.4×10^{-9} for $\alpha = 2/3$, 3.9×10^{-10} for $\alpha = 3$, and 6.6×10^{-9} when marginalizing over α. The posterior in the $\Omega_{ref} - \alpha$ plane is shown in Figure 6. The observations from LIGO/Virgo O3 have significantly increased our knowledge of the compact binary population. Therefore, the latest LVK stochastic search analysis also provides an updated forecast of the SGWB due to compact binaries, aligning with the most recent observations and their adopted fiducial astrophysical prescriptions [11, 163, 164].

The left panel of Figure 7 shows the LVK forecasts for the individual contributions from binary black hole (BBH), binary neutron star (BNS), and neutron star-black hole binary (NSBH) to the astrophysical SGWB. The uncertainties for BNSs and NSBHs stem from Poisson uncertainties in their merger rates, while the forecast for BBHs also accounts for systematic uncertainties associated with their imperfectly known mass distribution [9]. The blue band in the right panel of Figure 7 represents the LVK estimate of the total SGWB resulting from the superposition of these three source types. For comparison, the solid black curve is the LIGO/Virgo O3 sensitivity to the SGWB [11, 174]. While the estimate for the SGWB amplitude is currently below the detection threshold, it may become accessible with future detectors, such as the planned "A+" LIGO configuration.

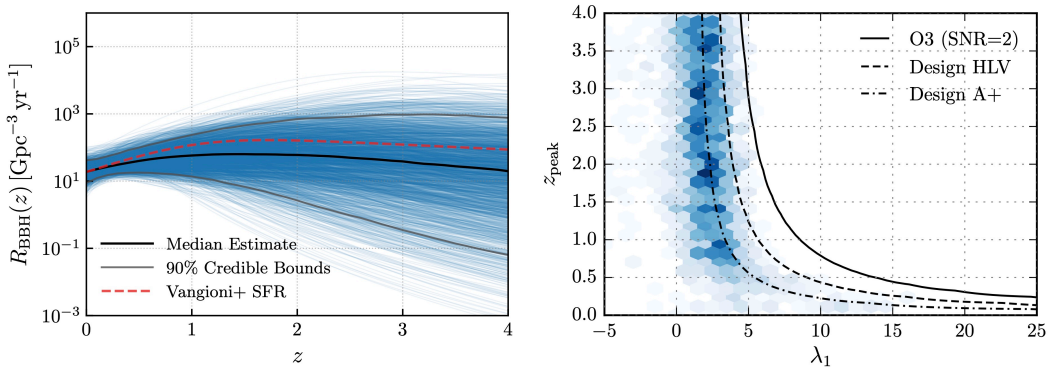

Figure 8: *Left panel*: Posterior constraints on the BBH merger rate combining LVK stochastic search results and direct BBH detections. The black line shows the median estimate of $R_{\rm BBH}(z)$, while grey lines are the 90% credible bounds. The dashed red line is proportional to the cosmic star formation rate used in the analysis [176]. *Right panel*: 2D posterior on the parameters λ_1 and $z_{\rm peak}$ describing $R_{\rm BBH}(z)$. While the stochastic measurements from LIGO/Virgo O3 alone (solid line) are not competitive, those from future observing runs (dashed lines) may impose tighter constraints on these parameters. Credits: Figures 6 and 7 from Ref. [11].

Constraining the BBH merger rate

Figure 7 presents LVK current best estimates for the SGWB based on an astrophysically plausible model for the merger rate $R_{\rm BBH}(z)$ of stellar BBHs. However, one can attempt to directly measure $R_{\rm BBH}(z)$ by combining individual detections of compact binaries with upper limits on the SGWB. This approach was initially presented in Ref. [75] and then applied to the latest LVK results in Ref. [11]. The analysis assumes a broken power law form for the mass distribution of BBH mergers [9] and a phenomenologically-parametrized form for their merger rate:

$$R_{\rm BBH}(z) = \mathcal{C}(\lambda_1, \lambda_2, z_{\rm peak}) \frac{R_0 (1+z)^{\lambda_1}}{1 + \left(\frac{1+z}{1+z_{\rm peak}}\right)^{\lambda_1+\lambda_2}}. \tag{82}$$

Under this form, the merger rate evolves as $R_{\rm BBH}(z) \approx (1+z)^{\lambda_1}$ at $z \lesssim z_{\rm peak}$ and $R_{\rm BBH}(z) \approx (1+z)^{-\lambda_2}$ at $z \gtrsim z_{\rm peak}$. Using the individual BBH detections from LIGO/Virgo O3 in combination with the latest LVK stochastic search results, the parameters governing both the mass and redshift distributions of BBH mergers are jointly inferred. The resulting constraints on the BBH merger rate as a function of redshift are shown in Figure 8. Each blue line represents a single draw from the obtained posteriors on the BBH mass distribution and merger rate history. The black and gray curves are the median estimated merger rate and central 90% credible bounds, respectively. The BBH merger rate approximately traces star formation, but it seems to increase more slowly with redshift, consistently with a non-vanishing time delay distribution between binary formation and merger. The constraints on the behavior of $R_{\rm BBH}(z)$ at $z < 0.5$ are primarily driven by individual detections rather than stochastic results. This is elucidated in the right panel of Figure 8, showing the joint $\lambda_1 - z_{\rm peak}$ posterior, marginalized over the remaining parameters governing the BBH mass and redshift distributions. The solid black contour shows the values of λ_1 and $z_{\rm peak}$ that would yield a SGWB detection with SNR = 2 in O3. Hence, values to the right of this contour can be excluded based on SGWB non-detection. Conversely, individual BBH detections allow for a measurement of λ_1, but are not expected to significantly constrain $z_{\rm peak}$, likely extending beyond the LIGO/Virgo horizon. However, with continued data collection, the non-detection (or potential detection) of the SGWB may provide informative constraints on λ_1 and $z_{\rm peak}$. Indeed, as additional individual BBH detections occur, the constraints on λ_1 will continue to improve, revealing an increasingly narrow, nearly-vertical contour in the $\lambda_1 - z_{\rm peak}$ plane. In parallel, ongoing time integration in stochastic searches will exclude a growing portion of this plane, ruling out large values for both λ_1 and $z_{\rm peak}$.

Directional searches: upper limits on the angular power spectrum

The latest LVK searches for anisotropic stochastic backgrounds use data from the first three LIGO/Virgo observing runs and rely on the cross-correlation techniques presented in Ref. [23]. In particular, three different analyses are applied to the data: (i) the broadband radiometer analysis (BBR) [165], targeting a small number of resolvable, persistent point sources emitting GWs over a wide frequency band; (ii) the spherical harmonic decomposition (SHD) [167], seeking extended sources by reconstructing the harmonic coefficients of the GW power across the sky; and (iii) the narrowband radiometer analysis (NBR) [177], studying frequency spectra from three astrophysically relevant sky locations: Scorpius X-1, Supernova 1987A, and the Galactic Center [12]. None

of the three analyses shows evidence for anisotropic GWs, setting direction-dependent upper limits on the GW emission. Figure 9 shows the upper limits on the power spectrum of anisotropies, defined in Equation (52) at each angular scale ℓ. These limits were determined using the spherical harmonic decomposition analysis on the combined LIGO/Virgo data from O1, O2, and O3. They correspond to a power-law SGWB with the three distinct spectral indices α discussed in the previous subsection.

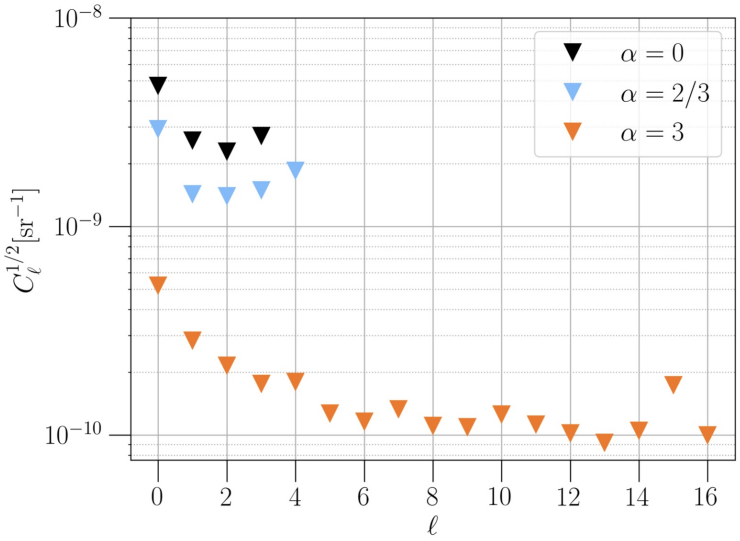

Figure 9: Upper limits at 95% confidence level on the angular power spectrum using the spherical harmonic decomposition analysis on O1+O2+O3 combined LIGO/Virgo data. The results are obtained for a power-law SGWB with three different spectral indices α. Credits: Figure 4 of Ref. [12].

1.5.2 *Results of stochastic searches with PTAs*

PTA experiments monitor the time of arrival of light pulses emitted by a group of galactic millisecond pulsars to detect the passage of a GW signal. Pulsars are highly magnetized rotating neutron stars emitting beams of electromagnetic radiation from their magnetic poles. Some pulsars, known as millisecond pulsars, have rotation periods of the order of 10^{-3} s. Due to their extraordinarily stable rotation, millisecond pulsars can be used as clocks rivaling the stability of the best atomic clocks on Earth. The fact that pulsars are such accurate clocks enables precise measurements of their rotational, astrometric, and binary parameters based on the times of arrival of their pulses. In 1983, Hellings and Downs suggested that correlations between the time-of-arrival perturbations of multiple pulsars could reveal a GW signal buried in pulsar

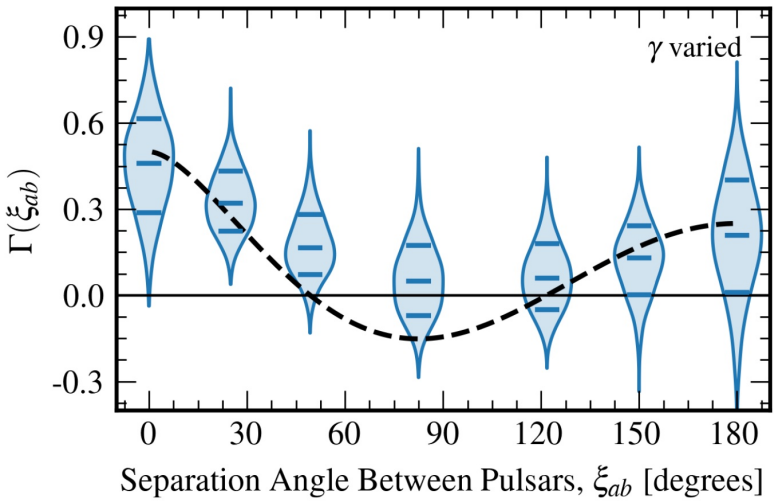

Figure 10: Bayesian reconstruction of the correlations between pulsars, modeled as a cubic spline within a power-law model with variable spectral index. The violins represent the marginal posterior densities (with median and 68% credible values) of the correlations at the knots. The knot positions are chosen on the basis of the features of the Hellings–Downs correlation curve (dashed black line). Credits: Figure 2 of Ref. [13].

noise [143]. From a statistical inference standpoint, the problem of detecting GWs with PTAs is analogous to GW searches with earth- or space-based interferometers. Two crucial differences are (i) irregular observation times, which are better analyzed in the time-domain rather than in the Fourier-domain, and (ii) noise sources (intrinsic pulsar noise, frequency-dependent fluctuations due to the interstellar medium, and timing model errors) correlated on the same timescales of GWs. This requires that GW signal and noise are estimated jointly. Thus, standard analyses are performed within a Bayesian framework that represents all noise sources as Gaussian processes and relies on model comparison to establish a detection [178]. PTAs are geared towards detecting stochastic backgrounds rather than deterministic GW signals. Indeed, as PTA datasets grow in extent and sensitivity, the SGWB is expected to manifest as an excess residual power observed across multiple pulsars. In 2020, after years of null results and progressively decreasing upper limits on the SGWB amplitude, such an observation was reported for the NANOGrav 12.5 yr dataset [179] and later validated through analogous analyses on PPTA [180], EPTA [181], and IPTA [182] datasets. However, such an excess of power could originate from intrinsic pulsar processes or a common systematic noise, and it could not be automatically attributed to an SGWB. Confirming a SGWB detection requires identifying phase-coherent interpulsar correlations with the characteristic pattern predicted by Hellings and Downs. In Refs. [13–15], the NANOGrav, EPTA and PPTA collaborations announce the detection of a stochastic signal correlated among their monitored pulsars. The correlations between the pulsars follow the expected Hellings–Downs pattern. The Bayesian reconstruction of the

correlations between 67 pulsars in the NANOGrav 15-year dataset is shown in Figure 10. The presence of a SGWB with a power-law spectrum is strongly favored over a model considering only independent pulsar noises, with a Bayes factor[11] of 10^{14}. These PTA detections mark the first-ever direct measurement of a SGWB. The principal results of the PTA analyses are referred to a fiducial power-law spectrum of characteristic GW strain

$$h_c(f) = A_{GWB}\left(\frac{f}{f_f}\right)^{\alpha}. \tag{83}$$

However, the analysis is performed in terms of the timing-residual cross-power spectral density

$$S_{ab}(f) = \Gamma_{ab}\frac{A^2_{GWB}}{12\pi^2}\left(\frac{f}{f_{ref}}\right)^{-\gamma_{GWB}} f^{-3}_{ref}, \tag{84}$$

where $\gamma_{GWB} = 3 - 2\alpha$ and $\Gamma_{ab} = \Gamma(\xi_{ab})$ is the overlap reduction function describing the average correlations between two pulsars a and b as a function of their separation angle ξ_{ab}. For an isotropic SGWB, Γ_{ab} is given by the Hellings-Downs curve. The posterior distributions for A_{GWB} and γ_{GWB} are shown in Figure 11. The value $\gamma_{GWB} = 13/3$ (corresponding to $\alpha = 2/3$), expected for binary coalescences, is only marginally compatible with the obtained posterior. Several astrophysically motivated models of supermassive black-hole binary (SMBBH) populations are able to reproduce the observed SGWB. However, retrieving the measured SGWB amplitude requires either a large number of model parameters to be at the edges of expected values, or a small number of parameters to be notably different from standard expectation [16]. In conclusion, even though SMBBHs are the most probable source of SGWB in the nHz band, the NANOGrav results highlight the importance of accurately modeling binary evolution for reproducing realistic SGWB spectra.

1.5.3 *Stochastic searches with 3G detectors*

Third-generation (3G) laser interferometers, including the Einstein Telescope (ET) [133–135] and Cosmic Explorer (CE) [136, 137], are expected to come online before the end of the 2030s. These observatories will outperform the sensitivity of current 2G detectors by several orders of magnitude, extending the detection horizon for BBH mergers to $z \sim 10$ [183]. This suggests that 3G detectors will have the capacity to resolve over 99.9% of all stellar BBHs in the Universe [184]. Therefore, only a small fraction of BBHs will remain unresolved, contributing to the SGWB. The situation is quite different for BNS mergers, as individual events will only be resolvable up to $z \sim 1$ [134]. Indeed, 3G detectors will have an extraordinary sensitivity to stochastic backgrounds. The

11 The Bayes factor is the ratio of the marginal likelihoods of two competing statistical models, used to quantify the support for one model over the other.

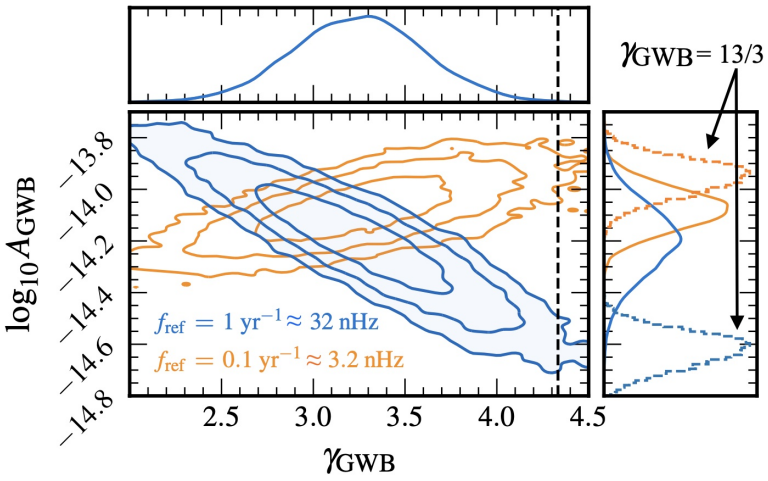

Figure 11: Posterior distributions of the SGWB amplitude and spectral index, with 68%, 95%, and 99% credible regions. The dashed black line represents the value $\gamma_{GWB} = 13/3$, expected for a SGWB due to binary mergers. This value is inside the 99% credible region. The dashed curves in the $\log_{10} A_{GWB}$ subpanel show its marginal posterior density for a $\gamma_{GWB} = 13/3$ model. All the posteriors are computed at the reference frequencies $f_{ref} = 1\,yr^{-1}$ (blue) and $0.1\,yr^{-1}$ (orange). Credits: Figure 2 of Ref. [13].

power-law integrated sensitivity curves PLS [174] for various 3G network configurations, compared with the LIGO/Virgo O3 sensitivity, are shown in Figure 12. In this plot, the PLS curves for ET are computed based on the current triangular design, as described in Subsection 1.4.1. However, alternative configurations for ET involving two L-shaped interferometers have been proposed recently [135]. In the context of stochastic backgrounds, the triangular configuration performs better at higher frequencies. On the other hand, configurations with two L-shaped interferometers are preferred for lower frequencies, up to several tens of Hz, but only when the detectors are co-aligned. This comparison is made clear in Figure 13, taken from Ref. [135], where the sensitivity curves of various ET configurations are presented. This plot also shows the three main targets stochastic searches with 3G detectors: the search of population III stars, the study of star formation history and BBH formation channels, and the residual background from BNSs. As we saw in Equation (41), the low-frequency part of the SGWB spectrum is proportional to $f^{2/3}$, as most of the contributing binaries are in their inspiral phase. This power-law behavior is common to all binary types, whereas the position and shape of the peak, associated to the frequencies where the sources stop emitting GWs (see Figure 4), depend on the features of the specific populations. Therefore, the distinct signatures of specific populations on the SGWB manifest as deviations from the $f^{2/3}$ behaviour. The peak of the SGWB from BBHs is expected to fall in the 100-1200 Hz frequency range. The main factors influencing the shape and the position of the peak are the star formation history, the evolution of the metallicity of the galactic environment and the different binary formation channels

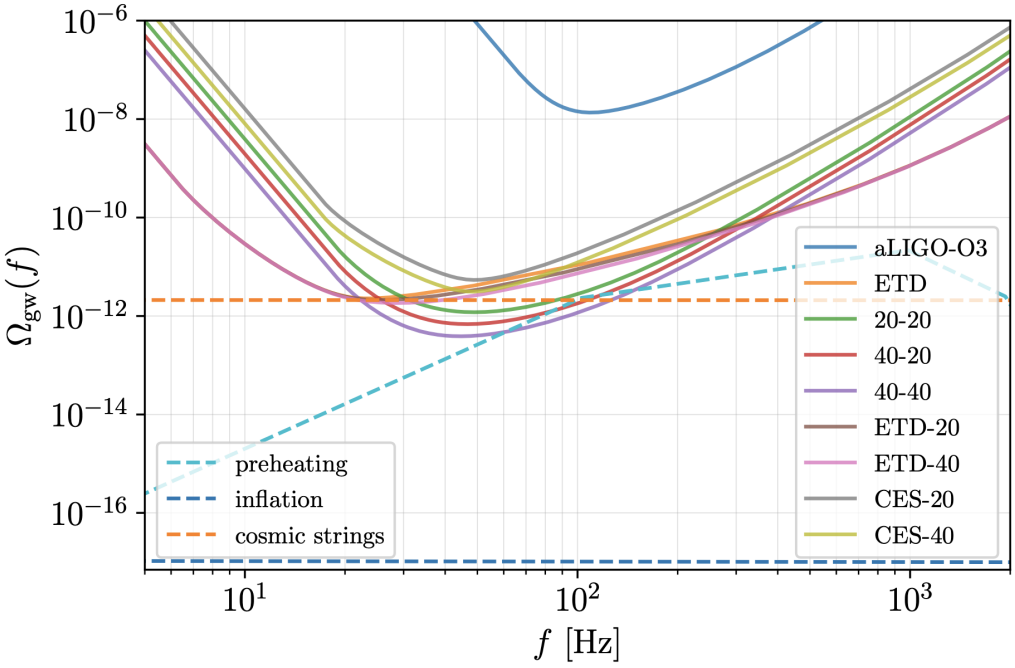

Figure 12: Power-law integrated sensitivity curves (PLS) [174] for different 3G detector networks. The labels 20–20, 40–20 and 40–40 correspond to two Cosmic Explorers (CE) in the US, with the numbers indicating the arm length in km. ETD, ETD–20, and ETD–40 denote the sensitivity of Einstein Telescope (ET) alone and combined with a CE in the US. Likewise, CES–20 and CES–40 correspond to the sensitivity of a 20-km CE in Australia combined with a 20- or 40-km CE in the US. A SGWB with energy density $\Omega_{\rm gw}(f_{\rm ref} = 300{\rm Hz})$ intersecting these curves would be detected with a signal-to-noise ratio of 3 after one year of observation. Dashed lines show the expected SGWB for cosmic strings, preheating, and standard slow-roll inflation, computed according to reasonable models described in the caption of the original plot. Credits: Figure 5.4 of Ref. [137].

[183, 185]. Therefore, the detection of this signature from 3G detectors would be a new powerful probe of for stellar and galaxy formation and evolution. The signature from population III stars [186] is expected to emerge in the 5-200 Hz frequency range [187–189]. Indeed, the remnants of these ancient, metal-free stars are predicted to be very massive and to merge at lower frequencies compared to other types of binaries. Moreover, the merger rate density of population III remnants is expected to reach its maximum value at very high redshifts, $z \sim 8-16$, further shifting the SGWB peak at lower frequencies [190, 191]. Finally, as previously mentioned, 3G detectors will detect the majority of BBHs. However, a significant portion of BNSs will remain unresolved, resulting in a strong SGWB. The detection of this background will be a key tool in studying the features of the BNS population in the Universe [187]. Other potential sources of SGWB that could be observed with 3G detectors are primordial black holes. Indeed, the merger rate of primordial BBHs is predicted to steadily increase towards redshifts $z \gtrsim 50$ [192], creating a high-redshift source

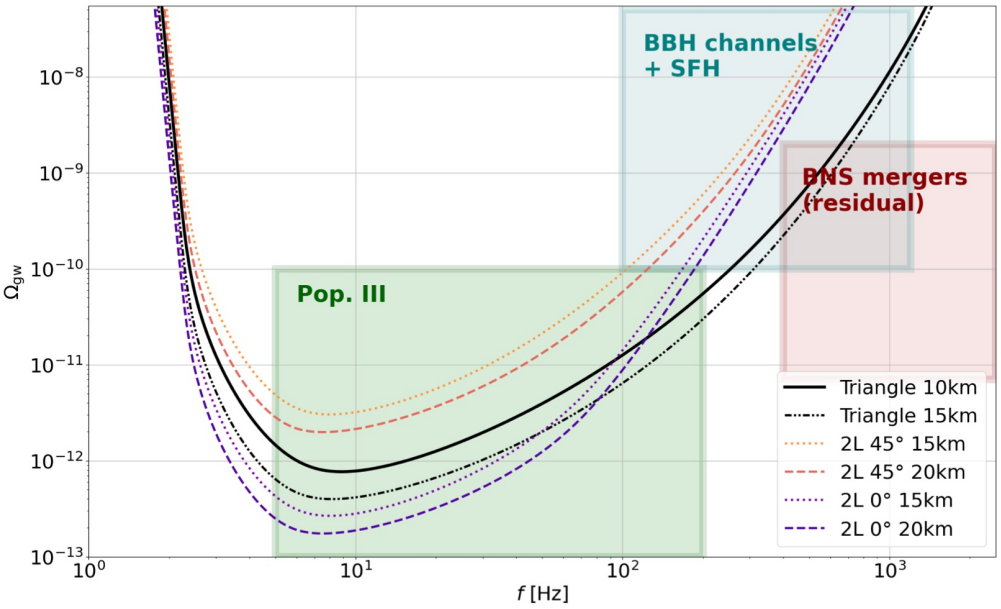

Figure 13: Power-law integrated sensitivity curves (PLS) [174] for various proposed configurations of the Einstein Telescope (ET): triangular configuration and two L-shaped interferometers, with different arm-lengths and mutual orientations. The plot also shows the three main targets for stochastic searches with 3G detectors: the star formation history and the different BBH formation channels, the residual SGWB from BNSs, and Population III stars. Credits: Figure 32 of Ref. [135].

of stochastic background. Furthermore, after subtracting the signals from resolved and unresolved compact binary coalescences, the attention can also be directed towards cosmological backgrounds.

The response of 3G detectors to anisotropic stochastic backgrounds has been extensively studied [128, 193–196]. All these studies converge on the conclusion that, in the best-case scenario, only the first few multipoles of the angular power spectrum will be accessible. In particular, ET and CE are potentially able to detect a dipole anisotropy at the level of $C_{\ell=1} \approx 10^{-24}$, which is the size of the kinematic dipole expected from a SGWB on the edge of being detected by LVK at design sensitivity [92]. For ET, it has been shown that the configurations featuring two L-shaped detectors have a better sensitivity to odd multipoles compared to the standard triangular configuration. This improvement is attributed to the different baselines. Indeed, the baseline of the three nested interferometers is equivalent to the length of one arm (10 or 15 km), whereas the two L-shaped detectors have a substantially larger baseline. Consequently, the overlap reduction function for the triangular configuration is predominantly even under parity, resulting in poor sensitivity to odd multipoles [135]. The situation is expected to improve when SGWB anisotropies are combined with electromagnetic observations. One of the primary targets for future detectors is to cross-correlate both resolved events and stochastic

backgrounds with galaxy catalogues, CMB anisotropies, and other tracers of the LSS.

1.5.4 *Stochastic searches with LISA*

Stochastic searches with LISA face different challenges compared to ground-based interferometers and PTAs. The cross-correlation techniques discussed in Section 1.4 are unfeasible because LISA is considered a single instrument, consisting of a triangular constellation of three spacecraft orbiting the Sun. However, as each spacecraft exchanges laser beams with the others, it is possible to synthesize multiple interferometry signals using the data from these six laser links [197]. One particular combination of data, called the T channel, approximately corresponds to a null channel, and is relatively insensitive to GWs. Other combinations, such as the so-called A and E channels [198], are much more sensitive to GW signals. Using the T channel to measure the instrumental noise, the relative power levels in the $\{A, E, T\}$ channels can be used to separate a stochastic signal from the noise [199]. Working within this framework, known as time-delay interferometry (TDI), the computation of LISA's sensitivity to both stochastic backgrounds and deterministic GW sources is discussed in several studies, such as Refs. [200, 201].

One of the major challenges for LISA data analysis will be that of component separation, as a large variety of long-lasting signals will contribute to the same frequency band overlapping in time [202]. In particular, LISA will be sensitive to multiple stochastic backgrounds, including an anisotropic confusion-limited background from galactic white-dwarf binaries [203], a nearly isotropic background originating from BNSs and either primordial or stellar-origin BBHs [204], massive BBHs [205, 206] and extreme mass ratio inspirals [207]. Moreover, LISA may also detect primordial backgrounds arising from inflation [52], first-order phase transitions [65], and cosmic strings [69].

Anisotropic stochastic searches with LISA use the motion of the LISA constellation around the Sun to map the signal in the rest frame of the solar system's center of mass. The approach presented in Ref. [208] maintains a fixed noise model, simulates mock data, and uses a maximum-likelihood technique to assess the mapping capabilities of LISA. The study reveals that, under the best-case scenario where the signal dominates with a high signal-to-noise ratio at frequencies around 0.1 Hz, the angular resolution would be $\ell_{\rm max} \approx 15$. Another method, proposed in Ref. [209], addresses the mapping issue by setting priors on the spherical harmonic components of the signal and then solving for their amplitudes in a Bayesian framework, using a single TDI channel. This approach is particularly valuable when the sky distribution of the signal is well-known, as for the galactic white dwarf binary background. The angular response of LISA to various multipoles for a statistically isotropic SGWB were computed in Ref. [130]. Using the $\{A, E, T\}$ TDI basis, the authors compute the angular response as a function of frequency for both channel auto-correlations (AA, EE, and TT) and cross-correlations (AE and AT = ET). Due to its configu-

ration being even under parity, LISA has a better response to even multipoles. Specifically, the sensitivity to the quadrupole ($\ell = 2$) is better than that for the dipole ($\ell = 1$). The authors also quantify the minimum energy density required to observe the kinematic dipole (quadrupole) induced by the motion of LISA with respect to the rest frame of the SGWB, which is $\Omega_{gw} \sim 2 \times 10^{-11}$ (10^{-8}) for the dipole (quadrupole). Finally, the authors perform a forecast to assess the detectability of the lowest multipoles of the SGWB angular power spectrum through a Fisher matrix analysis.

2 INTENSITY AND ANISOTROPIES OF THE SGWB FROM MERGING COMPACT BINARIES IN GALAXIES

This Chapter is based on the following publication:

G. Capurri, A. Lapi, C. Baccigalupi, L. Boco, G. Scelfo, T. Ronconi
Intensity and anisotropies of the stochastic gravitational wave background from merging compact binaries in galaxies
JCAP 11.032 (Nov 2021), arXiv:2103.12037

In this chapter, I will discuss the methods and results of the initial study I carried out as part of my PhD project, forming the foundation for much of the subsequent work.

2.1 INTRODUCTION AND MOTIVATION

In this first work, we establish a phenomenological framework to characterize both the isotropic and the anisotropic parts of the stochastic gravitational-wave background (SGWB) given by stellar compact-object binary coalescences. Our analysis is built on empirical, data-driven prescriptions for galactic physics, and the outcome of state-of-the-art binary population synthesis codes. We derive predictions for the isotropic SGWB energy density as a function of frequency, distinguishing the contribution of different binary types, namely binary black holes (BBH), neutron star-black hole binaries (NSBH), and binary neutron stars (BNS). We present our predictions for two distinct networks of ground-based interferometers: the current network of second-generation (2G) instruments, LIGO, Virgo, and KAGRA (LVK), and the forthcoming third-generation (3G) detector Einstein Telescope (ET). Since the binaries that produce the SGWB generally reside inside galaxies, and galaxies trace the underlying dark matter distribution, the anisotropies of the SGWB are themselves a tracer of matter. Thus, as a first step towards a robust theoretical modeling of the SGWB anisotropies, we characterize the SGWB energy density as a tracer of the large-scale structure (LSS). Then, we compute the angular power spectrum of the SGWB anisotropies using the Boltzmann solver `CLASS` [210, 211]. Finally, we develop a methodology to simulate a full-sky map of the SGWB, taking into account both the intrinsic Poisson nature of the signal as well as its clustering properties.

The Chapter is structured as follows: in Section 2.2, I describe the empirical prescriptions that we used to characterize the binary population; in Section 2.3, I present our predictions for the isotropic SGWB energy density; in Section 2.4, I discuss the characterization of the SGWB energy density as a tracer of the LSS; in Section 2.5, I describe our treatment of SGWB anisotropies and compute

their angular power spectrum; in Section 2.6, I present our nover framework to produce simulated full-sky maps of the expected SGWB signal; finally, in Section 2.7, I draw the conclusions of this first work.

Throughout this work, the standard flat ΛCDM cosmology with parameter values from the Planck 2018 legacy release is adopted, with Hubble rate today corresponding to $H_0 = 67.4$ km s^{-1} Mpc^{-1}, Cold Dark Matter (CDM) and baryon abundances with respect to the critical density corresponding to $\Omega_{CDM}h^2 = 0.120$ and $\Omega_b h^2 = 0.022$, respectively, reionization optical depth $\tau = 0.054$, amplitude and spectral index of primordial scalar perturbations corresponding to $\ln(10^{10}A_S) = 3.045$ and $n_S = 0.965$, respectively [32].

2.2 CHARACTERIZATION OF THE BINARY POPULATION

We characterize the population of coalescing compact binaries and compute their merger rates following the approach outlined in Boco et al. (2019, 2021) [76, 77]. The merger rate per unit comoving volume V and chirp mass $\mathcal{M}_c$ can be computed as:

$$\frac{d^2\dot{N}}{dVd\mathcal{M}_c}(t) = \int dt_d \int dZ \frac{d^3N}{dM_{SFR}\,d\mathcal{M}_c\,dt_d}(\mathcal{M}_c, t_d|Z)\frac{d^2\dot{M}_{SFR}}{dVdZ}(Z, t - t_d), \quad (85)$$

where t is the cosmic time, equivalent to redshift, M_{SFR} is the star-formed mass, t_d is the delay time between the formation of the progenitor binary and the merging of the compact-object binary, and Z is the galaxy metallicity [212, 213]. The first term in the integral is related to stellar and binary evolution and represents the number of binary mergers per unit of star-forming mass per chirp mass and time delay bin. It can be decomposed into three factors:

$$\frac{d^3N}{dM_{SFR}\,d\mathcal{M}_c\,dt_d}(Z) = \frac{dN}{dM_{SFR}}(Z)\,\frac{dp}{d\mathcal{M}_c}(Z)\,\frac{dp}{dt_d}, \quad (86)$$

where dN/dM_{SFR} is the number of merging binaries per unit of mass formed in stars at metallicity Z, $dp/d\mathcal{M}_c$ is the metallicity-dependent chirp mass distribution, and dp/dt_d is the normalized distribution of delay times between the formation of the progenitor binary and the merger. For the first two factors, we rely on the results of the `StarTrack` population synthesis simulations[1] [214, 215]. In principle, the `StarTrack` code could also provide a delay time distribution, which would be a function of both chirp mass and metallicity. However, several studies based on both simulations and observations suggest that the dependence on these two parameters is weak [214–218]. The delay time distribution is often found to be proportional to t_d^{-1}, normalized to unity between a minimum value $t_{d,min} \sim 10^7 - 10^8$ yr and the age of the Universe (see e.g., Refs. [215, 216] for `StarTrack`). The value of $t_{d,min}$ and the subsequent normalization of the distribution is highly uncertain since it strongly depends on the model prescriptions. Therefore, we assume $dp/dt_d \propto t_d^{-1}$ with $t_{d,min} = 50$

1 We use simulation data publicly available at https://www.syntheticuniverse.org/, specifically the 'reference B' model in Refs. [214, 215].

Myr, independently on metallicity and binary type. Still, we must emphasize that this is an approximation, albeit supported by the aforementioned works. In principle, we should use the distribution retrieved from the code.

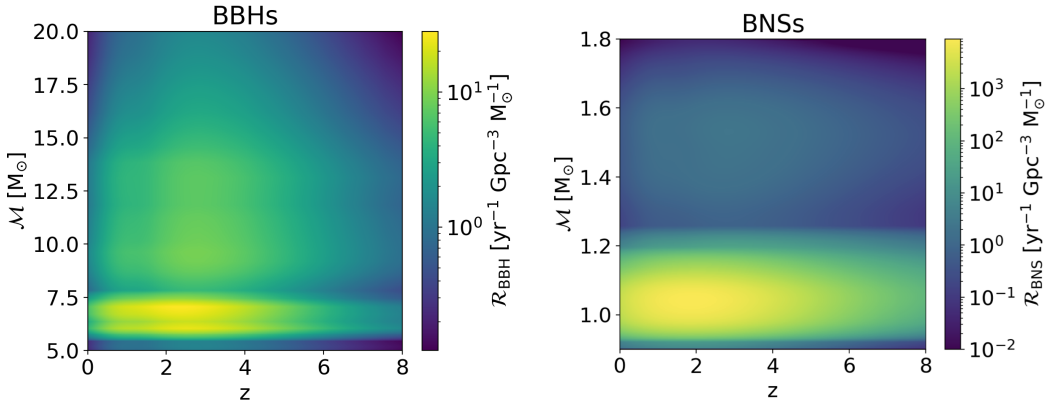

Figure 14: Differential merger rates $\mathcal{R} = d^2\dot{N}/dV\, d\mathcal{M}_c$ as a function of redshift and chirp mass for BBHs and BNSs, obtained combining the output of the `StarTrack` population synthesis code with the empirical galactic prescriptions described in Ref. [77]. Both the merger rates are normalized to the local values inferred by LIGO/Virgo during the second observing run [219, 220].

The second term in the integral of Equation (85) is related to galaxy evolution and represents the star-forming mass per unit time, comoving volume and metallicity. We compute it using semi-empirical prescriptions. Following the procedure presented in Boco et al. (2021) [77], we use the star formation rate function (SFRF) as galaxy statistics and the fundamental metallicity relation (FMR) to assign metallicity to galaxies. The SFRF $d^2N/d\log\psi/dV$ represents the galaxy number density per logarithmic bin of star formation rate (SFR). We use the empirical prescription for the SFRF derived in Ref. [221]. This prescription is based on galaxy luminosity functions measured at various redshifts across the Ultra-Violet (UV), Infra-Red (IR), submm, and radio bands. The gas phase metallicity Z of the interstellar medium is derived using the empirical FMR, as discussed in Refs. [222–225]. The FMR is a three-parameter relation among the stellar mass of the galaxy ($M_\star$), the SFR (ψ), and the gas-phase metallicity (Z). Since galaxies are parametrized and counted through the SFRF statistics, we need to relate the SFR to $M_\star$ in order to derive a metallicity. We do so using the main sequence (MS) of star forming galaxies, an observational redshift dependent power law relationship between the stellar mass and the SFR [226–232]. Even though the galaxy main sequence is a relation followed by most of the star-forming objects, there is a non negligible population of galaxies, known as starbursts, which lies above the main sequence:

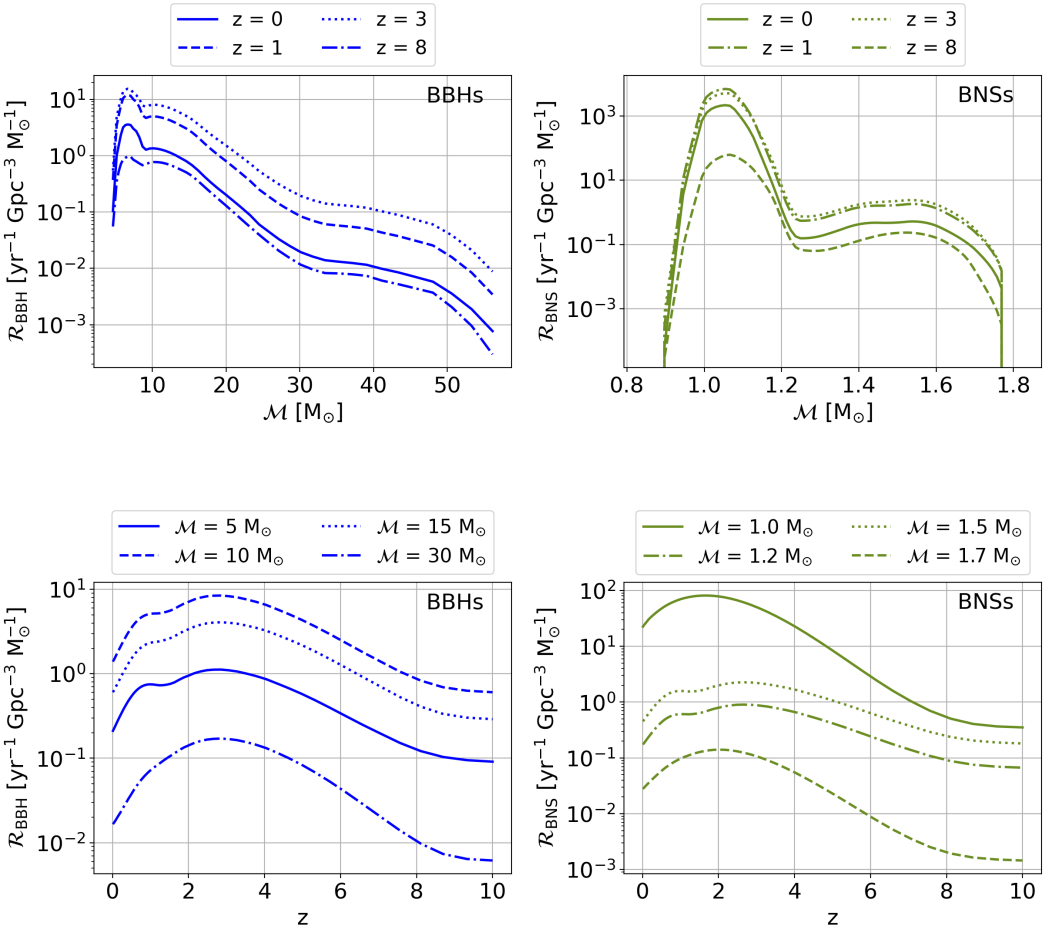

Figure 15: *Upper panels*: Differential merger rate as a function of redshift at fixed chirp mass for BBHs (left) and BNSs (right). *Lower panels*: Differential merger rate as a function of chirp mass at fixed redshift for BBHs (left) and BNSs (right).

their SFR is higher with respect to the SFR predicted by the main sequence at a given mass. In order to model this population, we follow Ref. [77], which provides a $M_\star$ distribution $dp/dM_\star(M_\star|z,\psi)$ for galaxies at fixed value of SFR. Combining together all these ingredients, we can compute the galactic term of Equation (85) as:

$$\frac{d^2\dot{M}_{SFR}}{dV dZ}(Z|z) = \int d\log\psi\,\psi \frac{d^2N}{dV\,d\log\psi}\int dM_\star \frac{dp}{dM_\star}(M_\star|z,\psi)\times \\ \times \left.\frac{dp}{dZ}\right|_{FMR}(Z|Z_{FMR}(M_\star,\psi))\,, \tag{87}$$

where $dp/d\log Z|_{FRM} \propto \exp[-(\log Z - \log Z_{FMR}(M_\star,\psi))^2/2\sigma^2_{FMR}]$ is a log normal distribution around the logarithmic metallicity value set by the FMR at fixed stellar mass and SFR.

The resulting merger rates are in good agreement with the local estimates by LIGO and Virgo, as shown in Ref. [77]. The overall normalization of the

merger rates is the result of many different and complex physical processes related to stellar evolution that could in principle depend on the binary type (e.g., binary fraction, common envelope development and survival, natal kicks, mass transfers). In order to reduce the impact of the huge uncertainties in the modeling of these processes, we decide to rescale our results to match the LIGO/Virgo local merger rates estimations, as already done in previous works [233–235]. Incidentally, in this way we also partially reabsorb the effect of adopting the approximated delay time distribution $dp/dt_d \propto t_d^{-1}$. The original values of the local rates are $32\,\mathrm{Gpc^{-3}\,yr^{-1}}$ for BBHs, $150\,\mathrm{Gpc^{-3}\,yr^{-1}}$ for BNSs, and $13\,\mathrm{Gpc^{-3}\,yr^{-1}}$ for NSBHs. This values are compatible with the LIGO/Virgo estimations[2] [219, 220]: $23.9^{+14.9}_{-8.6}\,\mathrm{Gpc^{-3}\,yr^{-1}}$ for BBHs, $320^{+490}_{-240}\,\mathrm{Gpc^{-3}\,yr^{-1}}$ for BNSs and $45^{+75}_{-33}\,\mathrm{Gpc^{-3}\,yr^{-1}}$ for NSBHs. The rescaled merger rates as a function of redshift and chirp mass for BBHs and BNSs are shown in Figure 14. The plots in Figure 15 show explicitly the redshift (upper panels) and chirp mass (lower panels) dependence of the merger rates. The redshift distribution of the merger rates is highly influenced by the star formation history of the host galaxies: most of the BBH events come from $z \sim 2-3$, whereas most of the BNS ones come from slightly lower redshifts, $z \sim 2$. The chirp mass dependence, instead, is mainly determined by the stellar prescriptions and the derived binary mass function, which is largely uncertain in the high mass end, since in that regime different formation channels may enter into play complicating the evolutionary scenario [236]. All in all, the features of the merger rates strongly depend on the adopted astrophysical prescriptions.

Finally, I emphasize that our method for computing the merger rates offers a twofold benefit. On the one hand, the galactic part is totally empirical and does not rely on the results of any cosmological simulation or semi-analytic framework. Therefore, employing empirical prescriptions allows us to circumvent the issue of selecting one among various competing astrophysical models. While the empirical relations we use come with their observational errors, they establish a robust and well-motivated astrophysical scenario in a field characterized by significant theoretical uncertainties. On the other hand, using the SFRF as galaxy statistics, we are able to assess the contribution of galaxies with different properties to the overall binary merger rate and subsequent GW emission. The fundamental notions of galaxy statistics and evolution used for the works presented in this Thesis can be found in Appendix A.

2.3 THE ISOTROPIC COMPONENT OF THE SGWB

The SGWB is usually described through the energy density parameter defined in Equation (22):

$$\Omega_{gw}(f,\hat{\mathbf{n}}) = \frac{1}{\rho_c}\frac{d\rho_{gw}(f,\hat{\mathbf{n}})}{d\ln f\, d\hat{\mathbf{n}}}, \tag{88}$$

2 Note that these are the LIGO/Virgo estimates from the second observing run, which were the latest results available at the time of publication. Specifically, we normalize to the mode value given by LIGO/Virgo.

where $\rho_c = 3H_0^2c^2/8\pi G$ is the critical density, introduced in Equation (16), and ρ_{gw} is the SGWB energy density observed at frequency f, coming from the direction $\hat{\mathbf{n}}$ in the sky. The energy density parameter can be split into an isotropic term $\overline{\Omega}_{gw}(f)$ and a directional energy density contrast $\delta\Omega_{gw}(f,\hat{\mathbf{n}})$:

$$\Omega_{gw}(f,\hat{\mathbf{n}}) = \overline{\Omega}_{gw}(f) + \delta\Omega_{gw}(f,\hat{\mathbf{n}}). \tag{89}$$

The term $\overline{\Omega}_{gw}$ is the average energy density per unit solid angle at the observed frequency f. The total energy density across the sky is given by:

$$\Omega_{gw}(f) = \int_{S^2} d\hat{\mathbf{n}}\, \Omega_{gw}(f,\hat{\mathbf{n}}) = 4\pi\, \overline{\Omega}_{gw}(f), \tag{90}$$

assuming that the density contrast $\delta\Omega_{gw}(f,\hat{\mathbf{n}})$ is a zero-mean field. Since results for isotropic models of the SGWB are usually expressed in terms of the total energy density in the literature, we are going to express our results in terms of $\Omega_{gw}(f)$.[3]

2.3.1 *Theoretical modeling*

Let's now focus on the isotropic component of the SGWB energy density. The SGWB is given by the superposition of all the unresolved GW signals coming form coalescing binaries. The intensity of such signals mainly depends on the chirp mass and redshift of the source binary. Indeed, the waveform of a GW produced by a coalescing binary is proportional to:

$$\tilde{h}(f) \propto \mathcal{M}_z^{5/6}\, D_L^{-1}(z)\, F(f)\,, \tag{91}$$

where $\mathcal{M}_z = \mathcal{M}_c(1+z)$, $D_L(z)$ is the binary luminosity distance, and $F(f)$ is a function of frequency that depends on the orbital evolution phase and is typically computed using post-Newtonian approximations or numerical relativity codes. The isotropic part of the SGWB energy density is directly related to the binary merger rates and the energy spectrum of the GW signal generated by each source, as we saw in Equation (36) of Chapter 1. In reality, it also depends on the detector's sensitivity: instruments with higher sensitivity resolve a larger fraction of GW signals, reducing the overall SGWB intensity. All in all, the isotropic energy density of the SGWB is given by [37, 83–90]:

$$\Omega_{gw}(f) = \frac{8\pi G f}{3H_0^3c^2} \int dz \int d\mathcal{M}_c \frac{\mathcal{R}(z|\mathcal{M}_c)}{(1+z)h(z)} \frac{dE}{df}(f_e(z)|\mathcal{M}_c) \int_0^{\bar{\rho}} d\rho P_\rho(\rho|\mathcal{M}_c, z), \tag{92}$$

where:

3 Notice that here I adopted a different notation with respect to the published work, Ref. [116], where $\overline{\Omega}_{gw}(f)$ denotes the integrated energy density instead of the sky-averaged one.

- $\mathcal{R}(z|\mathcal{M}_c) = d^2\dot{N}/dVd\mathcal{M}_c$ is the intrinsic merger rate per unit comoving volume and per unit chirp mass, as computed in Section 2.2;
- $h(z) = [\Omega_M(1+z)^3 + 1 - \Omega_M]^{1/2}$ is the redshift evolution of the Hubble parameter for a flat ΛCDM cosmology;
- $dE/df(z|\mathcal{M}_c)$ is the energy spectrum of the GW emitted by a coalescing binary with chirp mass $\mathcal{M}_c$ at redshift z;
- $f_e = (1+z)f$ is the frequency in the rest frame of the source;
- $P_\rho(\rho|\mathcal{M}_c, z)$ is the sky-averaged distribution of the signal-to-noise ratio ρ. It represents the signal-to-noise ratio at which a GW from a binary with chirp mass $\mathcal{M}_c$ merging at redshift z would be detected by a specific detector.

The idea behind Equation (92) is to sum the contributions from all GW events with a signal-to-noise ratio below the assumed detection threshold of $\bar{\rho} = 8$.[4]. In this way, we compute the energy density of the *residual background*, coming from unresolved events only. The *total background*, including both resolved and unresolved events, can be calculated by setting $\bar{\rho} = \infty$ in Equation (92). This sets the signal-to-noise ratio integral to unity, considering the contribution of all events. Following the formalism presented in Refs. [237, 238], we compute the sky-averaged distribution of signal-to-noise ratio as

$$P_\rho(\rho|\mathcal{M}_c, z) = P_\Theta(\Theta_\rho)\frac{\Theta_\rho}{\rho}, \tag{93}$$

in terms of the orientation function

$$\Theta = \frac{\rho}{8}\frac{D_L(z)}{R_0}\left[\frac{1.2M_\odot}{(1+z)\mathcal{M}_c}\right]^{5/6}\frac{1}{\sqrt{\zeta_{ISCO}+\zeta_{insp}+\zeta_{merg}+\zeta_{ring}}}, \tag{94}$$

and its distribution function

$$P_\Theta = \begin{cases} 5\Theta(4-\Theta)^3/256 & \text{for } 0 < \Theta < 4, \\ 0 & \text{otherwise.} \end{cases} \tag{95}$$

The quantity R_0 in Equation (94) is the detector characteristic distance parameter given by

$$R_0^2 = \frac{5}{192}\sqrt{N_{det}}\frac{M_\odot^2}{\pi c^3}\left(\frac{3G}{20}\right)^{5/3}x_{7/3}, \tag{96}$$

4 This is a reasonable value for ground based interferometers. See e.g. Ref. [219].

where N_{det} is the number of co-located detectors, and $x_{7/3}$ is the auxiliary quantity

$$x_{7/3} = \int_0^\infty \frac{df}{(\pi M_\odot)^{1/3} f^{7/3} S(f)}, \tag{97}$$

with $S(f)$ being the noise spectral density. The functions ζ_{ISCO}, ζ_{insp}, ζ_{merg} and ζ_{ring} specify the overlap of the waveform with the observational bandwidth during the inspiral, merger and ring-down phases of the event [239]. They are given by:

$$\begin{aligned}
\zeta_{ISCO} &= \frac{1}{(\pi M_\odot)^{1/3}\, x_{7/3}} \int_0^{2f_{ISCO}} \frac{df}{S(f)} \frac{1}{f^{7/3}}, \\
\zeta_{insp} &= \frac{1}{(\pi M_\odot)^{1/3}\, x_{7/3}} \int_{2f_{ISCO}}^{f_{merg}} \frac{df}{S(f)} \frac{1}{f^{7/3}}, \\
\zeta_{merg} &= \frac{1}{(\pi M_\odot)^{1/3}\, x_{7/3}} \int_{f_{merg}}^{f_{ring}} \frac{df}{S(f)} \frac{1}{f^{4/3} f_{merg}}, \\
\zeta_{ring} &= \frac{1}{(\pi M_\odot)^{1/3}\, x_{7/3}} \int_{f_{ring}}^{f_{cut}} \frac{df}{S(f)} \frac{1}{f_{ring}^{4/3} f_{merg}} \left[1 + \left(\frac{f - f_{ring}}{\sigma/2}\right)^2\right]^{-2},
\end{aligned} \tag{98}$$

where f_{merge}, f_{ring}, f_{cut} and σ are phenomenological waveform parameters and f_{ISCO} is the redshifted frequency at the innermost stable circular orbit (ISCO):

$$f_{ISCO} \simeq \frac{2198}{1+z} \left(\frac{M_{tot}}{M_\odot}\right)^{-1} \text{Hz}, \tag{99}$$

with M_{tot} being the total mass of the binary in solar masses. Finally, the energy spectrum emitted by the binary is taken as [88, 239]:

$$\frac{dE}{df}(z|\mathcal{M}_c) \simeq \frac{(\pi G)^{2/3} \mathcal{M}_c^{5/3}}{3} \times \begin{cases} f^{-1/3} & f < f_{merg} \\ f_{merg}^{-1} f^{2/3} & f_{merg} \leqslant f < f_{ring} \\ \dfrac{f_{merg}^{-1} f_{ring}^{-4/3} f^2}{\left[1 + \left(\dfrac{f - f_{ring}}{\sigma/2}\right)^2\right]^2} & f_{ring} < f \leqslant f_{cut} \end{cases} \tag{100}$$

2.3.2 *Predicted SGWB amplitude*

We compute the SGWB energy density for BBHs, BNSs, and NSBHs using Equation (92) within the astrophysical setup described in Section 2.2. In particular, we consider the merger rates normalized to the local values inferred by

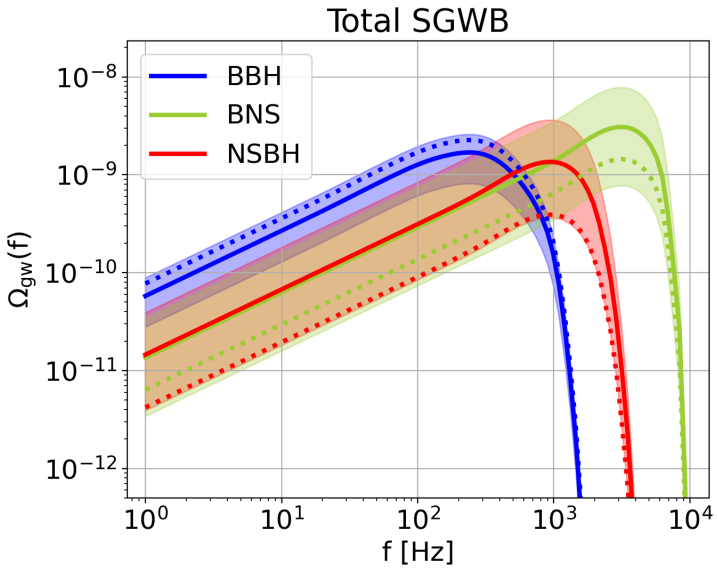

Figure 16: Energy density parameter of the total SGWB generated by all the events, resolved and unresolved, as a function of the observed frequency. The curves are based on the astrophysical prescriptions described in Section 2.2, using Equation (92) with $\bar{\rho} = \infty$. The colors represent the SGWB produced by different types of merging binaries: BBHs (blue), NSBHs (red), and BNSs (green). We show both the predictions obtained normalizing the merger rates to the local rates inferred by LIGO/Virgo [219, 220] (solid lines), and those obtained using the original rates as computed in Equation (85) (dotted lines). The two families of curves are both within the range of amplitudes defined by the error bars of the LIGO/Virgo estimates, represented by the shaded areas.

LIGO/Virgo. For completeness, in Figure 16, we also plot the curves obtained with the original (non-normalized) rates and we show that they lie within the range of amplitudes defined by the LIGO/Virgo error bars. We present our results for both the total background, which includes all events (resolved and unresolved), and the residual background, obtained by excluding the events resolved by the detector. For the residual background, we consider the 2G detector network LIGO/Virgo at design sensitivity and the forthcoming 3G detector Einstein Telescope. The results for the total and residual background are shown in Figure 16 and 17, respectively.

All the curves in Figures 16 and 17 feature the typical shape expected for a SGWB given by the superposition of signals produced by coalescing binaries, already discussed in Chapter 1. At low frequencies, the dominating contribution comes from the inspiral phase and the energy density is proportional to $f^{2/3}$. As the frequency increases, the contribution from the merger phase becomes more and more important, and energy density reaches a peak. The frequency of the SGWB peak is related to the typical mass of the considered binary systems. Lower chirp masses result in higher merger frequencies, causing the SGWB from BBH mergers to peak at lower frequencies compared to

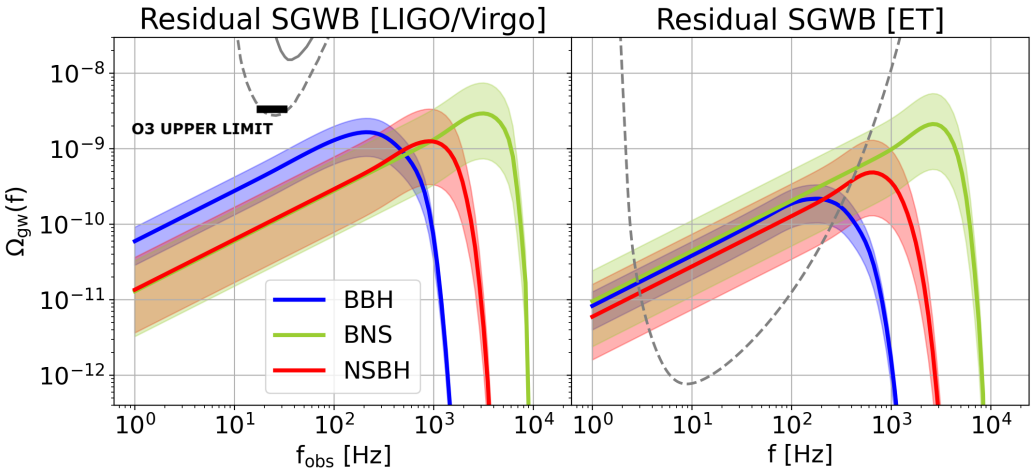

Figure 17: Energy density parameter of the residual SGWB for LIGO/Virgo (left panel) and Einstein Telescope (right panel) computed using Equation (92) within the astrophysical set-up described in Section 2.2, using $\bar{\rho} = 8$. The color code is the same as in Figure 16. The shaded areas represent the range of amplitudes defined by the error bars of the LIGO/Virgo estimations. The dashed grey lines represent the power-law integrated sensitivity curves for the considered detectors at design sensitivity. In the LIGO/Virgo panel, we also show the sensitivity during the third observing run (solid grey curve) and the current upper limit on the isotropic SGWB: $\Omega_{gw} \leqslant 3.4 \times 10^{-9}$ at 25 Hz for a power-law background with a spectral index of 2/3 [11].

that from BNS mergers. At higher frequencies, the energy density behavior is dominated by the ringdown phase, characterized by a rapid exponential decrease. The substantial impact of various astrophysical prescriptions on the energy density makes it difficult to directly compare our results with previous studies. Nevertheless, we can observe that both the shape and amplitude of our detector-independent spectra in Figure 16 align with the findings in Refs. [37, 89, 90, 240]. The relative amplitudes of the backgrounds coming from different types of binaries depend on several factors, including the merger rates, the typical strengths of the emitted GW, and the fraction of events resolved by the detector. In our astrophysical framework, BNS binary systems have the largest merger rate density, followed in order by NSBH and BNS. On the other hand, binary systems with higher chirp mass produce louder GWs, so that BBH events are the most intense, followed by NSBH and BNS. Without considering the detector, these two effects combine together so that the BBH systems produce the SGWB with the largest amplitude, followed by BNS and NSBH. For LIGO/Virgo this order is preserved since the fraction of resolved events is very low. The situation is quite different for ET, which is expected to detect most of BBH systems up to $z \sim 10$ and most of the BNS systems up to $z \sim 1$, as we will discuss in more detail in the next section. Therefore, for ET, the stochastic backgrounds produced by BBHs and NSBHs are slightly lower than the one produced by BNSs. The higher sensitivity of ET leads to a lower observed energy density compared to LIGO/Virgo. This is because ET will be able detect

a larger number of events, resulting in fewer unresolved events contributing to the SGWB.

Finally, we compare the predicted SGWB amplitudes with the sensitivities of the considered detectors. The dashed grey lines in Figure 17 represent the power-law integrated sensitivity curves [174] for LIGO/Virgo and ET. ET will have greater sensitivity and will cover a wider frequency range compared to 2G detectors like LIGO and Virgo. The expected signal for LIGO/Virgo is approximately one order of magnitude below the upper limit obtained from the first half of the third observing run, which stands at $\Omega_{gw} \leqslant 3.4 \times 10^{-9}$ at 25 Hz for a power-law background with a spectral index of $2/3$. However, the exceptional sensitivity of ET will ensure the detection of the astrophysical SGWB, despite its reduced amplitude due to the large number of resolved GW events. Both LIGO/Virgo and ET have a better sensitivity to SGWBs within the frequency range between ~ 10 Hz and a few hundreds of Hz. For the rest of the analysis, we will focus on an intermediate reference frequency $f_{ref} = 65$ Hz.

2.3.3 *Total and residual background*

Filtering out the resolved events to obtain the residual background not only dampens the overall amplitude of $\Omega_{gw}(f)$, as a consequence of the reduced number of events that contribute to the background, but also shifts the position of the high-frequency peak and slightly changes its shape. These effects are clearly visible in Figure 18, where the total and residual backgrounds for LIGO/Virgo and ET are directly compared. The modification of the peak reflects the fact that the population of unresolved binaries contributing to the residual background has different properties compared to the total population. Specifically, it has overall higher redshifts and masses, as both very nearby and very massive events are more easily detected individually. Indeed, the extent to which the properties of the unresolved population of binaries differs from that of the total population depends on the sensitivity and configuration of the considered network of detectors.

In this work, we consider only compact remnants of Population I/II stars. Their merger rate peaks at $z \sim 2-3$, and their individual masses hardly go over $100\,M_\odot$. For this reason, the overall shape of $\Omega_{gw}(f)$ for the residual background remains a power-law $\propto f^{2/3}$, followed by a single peak and an exponential decay. Other studies, such as Ref. [187], include in their analysis also Population III stars. These stars are a hypothetical population of very ancient, metal-poor stars formed in the young Universe, just at the onset of stellar activity. They are characterized by high masses, contributing to the SGWB at low frequencies. Since binaries of Population III remnants would be very distant in redshift, their GW signals are not only highly redshifted, but also extremely faint. Therefore, they would be buried under the signals of younger, closer binaries when considering the total background. However, they could be observable in the residual background within next-generation ground-based detectors, such as ET, which will be able to resolve the majority of BBH up to

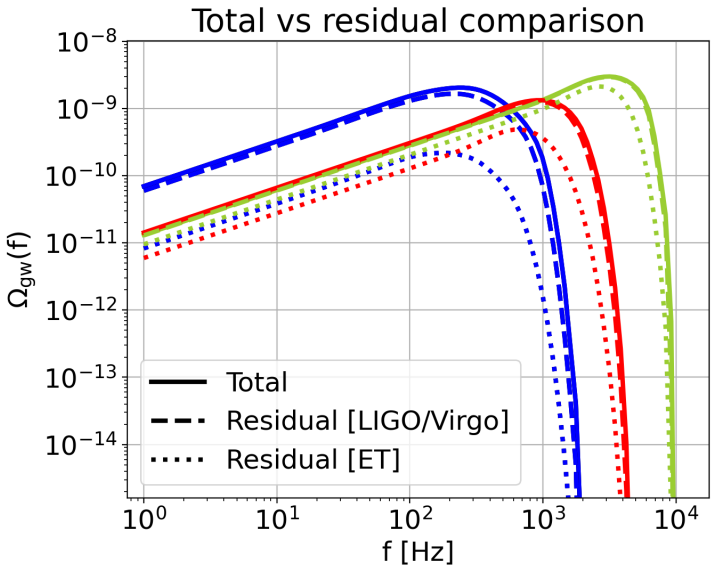

Figure 18: Comparison of total and residual SGWB. Filtering out the resolved events not only reduces the amplitude of $\Omega_{gw}(f)$, but also changes the position and the shape of its high-frequency peak. The color code is the same as in the previous figures.

high redshifts. If this is the case, Population III binaries would show up as a secondary peak in the $\Omega_{gw}(f)$ of the residual background, located at lower frequencies compared to the peak associated with Population I/II stars.

2.4 CHARACTERIZING THE SGWB AS A TRACER OF THE LSS

In this work, we are studying the SGWB given by the superposition of GW signals emitted by coalescing binaries. Most of the stellar compact-object binaries in the Universe reside within galaxies. Since the large-scale distribution of galaxies trace the total matter distribution, the SGWB energy density is also a tracer of matter. In this Section, we characterize the astrophysical SGWB as a tracer of the large-scale structure (LSS). There are four physical quantities that fully characterize a cosmic field as tracer of the LSS:

- the *redshift distribution*, which quantifies the contribution from sources at different redshifts;
- the *bias*, which expresses the mismatch between the distribution of the tracer and the underling dark matter distribution;
- the *magnification bias*, which quantifies the change in the observed field density induced by gravitational lensing;
- the *evolution bias*, which reflects the fact that the number of sources is not necessarily conserved across different redshift due to the possible formation of new objects.

In the following, we derive all these quantities for the SGWB energy density from scratch. Then, we evaluate them numerically within the astrophysical framework we described in Section 2.2.

Redshift distribution

By definition, we can express the energy density Ω_{gw} as:

$$\Omega_{gw} = \int dz \, \frac{d\Omega_{gw}}{dz} \, . \tag{101}$$

Thus, the redshift distribution can be easily computed from Equation (92) by removing the integral over redshift:

$$\frac{d\Omega_{gw}}{dz}(z, f) = \frac{8\pi G f}{3H_0^3 c^2} \frac{1}{(1+z)h(z)} \int d\mathcal{M}_c \frac{d^2\dot{N}}{d\mathcal{M}_c dV}(z|\mathcal{M}_c) \frac{dE}{df}(f_e(z)|\mathcal{M}_c) \times \\ \times \int_0^{\bar{\rho}} d\rho \; P_\rho(\rho|\mathcal{M}_c, z) \, . \tag{102}$$

Indeed, the redshift distribution is a function of the observed frequency, but in the following we focus on a reference frequency, $f_{ref} = 65$ Hz, which lies more or less at the center of the frequency band where both LIGO/Virgo and ET are more sensitive to SGWB (see the sensitivity curves in Figure 17). In Figure 19, we plot $d\Omega_{gw}/dz$ as a function of redshift at the reference frequency. We show the results for the total background ($\bar{\rho} = \infty$ in Equation (102)) and the residual background ($\bar{\rho} = 8$ in Equation (102)), for both LIGO/Virgo and ET. The distribution $d\Omega_{gw}/dz$ for the total background is almost flat up to $z \lesssim 1$ due to a compensation between the increasing number of mergers and the dilution of the GW flux. At $z \gtrsim 1$, $d\Omega_{gw}/dz$ starts to decrease because the merging rates flatten at those redshifts, not compensating anymore for flux dilution. At even higher redshifts, $d\Omega_{gw}/dz$ decreases rapidly due to the absence of merging binaries. The curves for the residual background reflect the fact that an real detector will resolve a substantial number of nearby events, particularly BBHs. As a result, these resolved events do not contribute to the SGWB. Hence, the redshift distributions for LIGO/Virgo and ET decline at low redshifts, so that intermediate redshifts are the ones that contribute most to the SGWB energy density. This effect is more evident for ET, which has a better sensitivity than LIGO/Virgo and is expected to resolve the majority of BBH events up to $z \lesssim 10$ and BNS events up to $z \lesssim 1$. As a consequence, ET will observe a residual SGWB whose energy density mainly comes from events located at $1 \lesssim z \lesssim 3$.

Bias

The bias b_Ω quantifies the mismatch between the distribution of the SGWB energy density and the total matter distribution. Since we are considering the SGWB produced by coalescing binaries inside galaxies, the bias of its energy

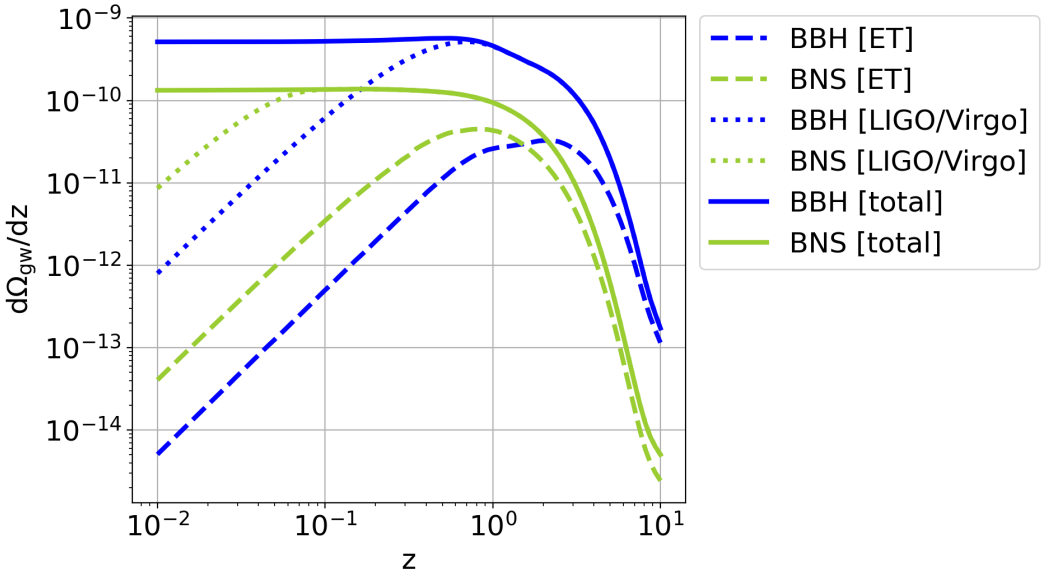

Figure 19: Redshift distributions $d\Omega_{gw}/dz$ for BBH (solid) and BNS (dashed) events at $f_{ref} = 65$ Hz. The solid curves are the redshift distributions of the energy density for the total background. The dotted and dashed curves are the redshift distributions of the energy density for the residual background for LIGO/Virgo and ET, respectively.

density is directly related to the bias of the host galaxies. To derive an expression for b_Ω, we start from the bias $b(z,\psi)$, associated to a galaxy at a given redshift z with given star formation rate (SFR) ψ. Following the procedure presented in Ref. [241], we associate the SFR of each galaxy to the mass of its dark matter halo through an abundance matching technique. Then, we assign to a galaxy with SFR ψ the bias of the corresponding halo. The abundance matching is a standard method to derive a monotonic relationship between the galaxy and the halo properties. This is done by matching the corresponding number densities in the following way:

$$\begin{aligned}&\int_{\log_{10}\psi}^{\infty} d\log_{10}\psi' \frac{d^2N}{d\log_{10}\psi' dV} = \\ &= \int_{-\infty}^{\infty} d\log_{10} M_H' \frac{d^2N}{d\log_{10} M_H' dV} \frac{1}{2} \mathrm{Erf}\left[\frac{\log_{10}(M_H(\psi))/M_H'}{\sqrt{2}\tilde{\sigma}}\right],\end{aligned} \tag{103}$$

where $\mathrm{Erf}[\cdot]$ is the error function, $d^2N/d\log_{10}\psi'/dV$ is the star formation rate function (SFRF) and $d^2N/d\log_{10} M_H'/dV$ is the galaxy halo mass function, i.e., the mass function of those halos that are hosting one individual galaxy (see Appendix A for further details). $M_H(\psi)$ is the relation we are looking for and $\tilde{\sigma} = \sigma d\log_{10} M_H/d\log_{10}\psi$ is the scatter around that relation (we set $\sigma_{\log_{10}\psi} \simeq 0.15$). Once $M(\psi)$ is determined, we assign to each galaxy the bias corresponding to the halo associated with its SFR, i.e, $b(z,\psi) = b(z, M_H(z,\psi))$, where $b(z, M_H)$ is computed as in Ref. [242] and approximated as in Ref. [243].

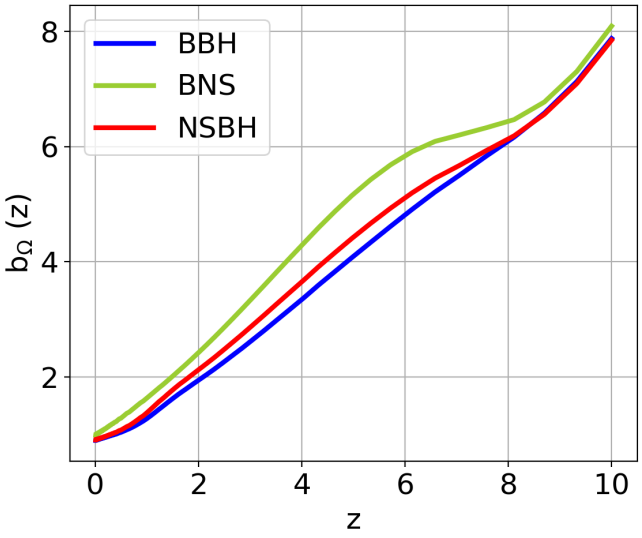

Figure 20: Bias of the SGWB energy density for BBH, BNS and NSBH as a function of redshift at $f_{ref} = 65$ Hz for ET.

In order to assign a redshift-dependent bias to the SGWB energy density, we weight the galaxy bias $b(z, \psi)$ with the energy density per unit redshift and SFR, which keeps into account the contribution of GWs coming from galaxies with different SFRs. The energy density per unit redshift and SFR can be computed in the same way as the redshift distribution of Equation (102), using the merger rate per unit volume, chirp mass and SFR, $d^2\dot{N}/d\mathcal{M}_c dV d\log_{10}\psi$, instead of the merger rate per unit volume and chirp mass. All in all, the bias of the SGWB energy density is given by:

$$b_\Omega(z, f) = \frac{\int d\log_{10}\psi \frac{d^2\Omega_{gw}}{dz d\log_{10}\psi}(z, \psi, f)\, b(z, \psi)}{\int d\log_{10}\psi \frac{d^2\Omega_{gw}}{dz d\log_{10}\psi}(z, \psi, f)}. \tag{104}$$

In Figure 20, we show the bias of the SGWB energy density for BBH, BNS and NSBH binaries as a function of redshift at $f_{ref} = 65$ Hz for ET. Since it mainly reflects the behavior of the galaxy bias, the $b_\Omega(z)$ increases with redshift for all binary types. However, the bias for BBHs and NSBHs is smaller than the one for BNSs because black holes need a lower metallicity to form. An environment with lower metallicity, in turn, requires a lower SFR. Since low-SFR galaxies have a smaller bias at all redshifts, the SGWB produced by coalescing binaries containing at least one black hole comes from galaxies with smaller biases, on average.

Magnification bias

Let's now focus on the effect of gravitational lensing on the SGWB. In the geometrical-optics limit, a gravitational lens with a magnification factor μ en-

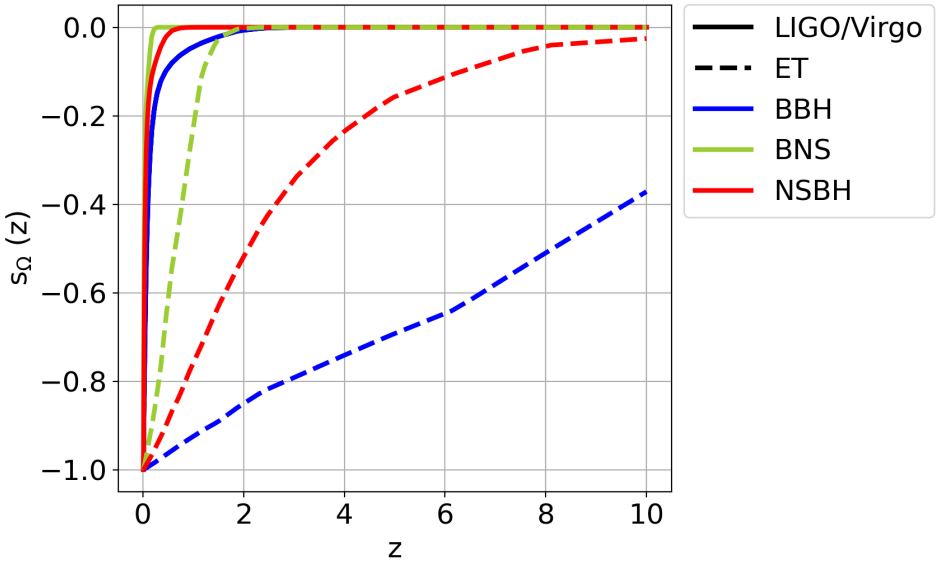

Figure 21: Magnification bias of the SGWB energy density for BBHs, BNSs, and NSBHs as a function of redshift at $f_{ref} = 65$ Hz for LIGO/Virgo (solid lines) and ET (dashed lines).

hances the signal-to-noise ratio ρ of a GW signal by a factor of $\sqrt{\mu}$, without altering the shape of the observed waveform. For what concerns strong lensing, we verified that the effect of lenses with magnification $\mu > 2$ on the SGWB energy density is negligible. Instead, weak lensing can affect the SGWB in two ways: by boosting the amplitude of some events through magnification and by reducing the received GW flux due to volume dilution. The overall effect, given by the interplay of these two factors, is encoded in the magnification bias. Adapting the general derivation that is found in the appendix of Ref. [244] to the case of SGWB, we define the magnification bias s_Ω of the SGWB energy density through

$$\frac{d\Omega_{gw}^{lensed}}{dz} = \frac{d\Omega_{gw}}{dz}\left[1 + \kappa(5s_\Omega - 2)\right], \tag{105}$$

where κ is the lensing convergence. After some manipulation, we obtain the explicit expression

$$s_{\Omega,\bar{\rho}}(z,f) = -\frac{1}{5}\frac{d\log_{10}\left(\frac{d\Omega_{gw}(f,z,<\rho)}{dz}\right)}{d\log_{10}\rho}\bigg|_{\rho=\bar{\rho}}. \tag{106}$$

This expression for the magnification bias is similar to the one derived in Refs. [245, 246] for resolved GW events: a crucial difference is that we are now considering only the GW events that are below the detection threshold $\bar{\rho}$. When we compute the SGWB considering all events, resolved and unresolved, the two

effects of weak lensing - growth of energy density due to magnification and dilution of flux - balance each other. Therefore, weak lensing does not affect the anisotropies of the SGWB in this case, as already shown in Ref. [110]. For this reason, we set the magnification bias to 0.4, i.e., the value for which the two competing effects cancel out. The situation is different when we account for the detector sensitivity by subtracting the resolved GW events from the energy budget. In this case, the lensing magnification boosts some events above the detection threshold, so that they are resolved by the detector and do not contribute to the energy density. This is reflected by a negative magnification bias, as it can be seen in Figure 21, where we plot $s_\Omega(z)$ for LIGO/Virgo and ET. The magnification bias is different from zero where there is a considerable amount of events with a signal-to-noise ratio close to the detection threshold. Accordingly, for BBHs it goes to zero at higher redshifts than for NSBHs and BNSs, since BBH events are more energetic and can be resolved up to higher redshifts. For the same reason, the magnification bias for the extremely sensitive ET is lower than zero up to very high redshifts, especially for BBHs.

Evolution Bias

Finally, the evolution bias takes into account that new sources are continuously formed throughout cosmic history, so that the number of sources is not necessarily conserved in redshift. Adapting the definition for resolved GW events presented in Ref. [246], the evolution bias of the SGWB energy density can be written as:

$$f_\Omega^{\rm evo} = \frac{d\ln\left(\frac{d\Omega_{\rm gw}}{dz\,d\hat{\mathbf{n}}}\right)}{d\ln a}\,, \tag{107}$$

where a is the scale factor. As we will see in Equations (110) and (111), the evolution bias appears only in sub-leading contributions in the computation of the SGWB anisotropies.

2.5 THE SGWB ANISOTROPIES

Now that we have characterized the SGWB energy density as a tracer of the LSS, we are ready to compute its anisotropies. As discussed in Chapter 1, these anisotropies are due to the inhomogeneous distribution of sources in the Universe and the propagation effects that GWs experience as they travel from the source to the observer.

2.5.1 *Theoretical modeling*

Similar to the isotropic term $\Omega_{\rm gw}(f)$, the anisotropic term $\delta\Omega_{\rm gw}(f,\hat{\mathbf{n}})$ is influenced by the local astrophysical conditions at both galactic and sub-galactic scales, as well as the underlying cosmology. However, the anisotropies are also affected by the LSS and its impact on the distribution of sources and the propagation of GWs. Analytic expressions for the anisotropies of the astrophysical

SGWB, derived from the mentioned ingredients, are already present in the literature (see, e.g., [91, 93, 110, 112]). In Section 2.4, we characterize the SGWB energy density as a tracer of the LSS. This allows us to use the Boltzmann solver `CLASS` [210, 211] to compute the angular power spectrum of the SGWB anisotropies. Indeed, the formalism for computing the SGWB anisotropy angular power spectrum is similar to the one used for computing the power spectrum of galaxy number counts. We can therefore use the `CLASS` routines dedicated to number counts [247] also in our case. Despite the analogy in the two formalisms, it is crucial to handle the conceptual differences with care. Indeed, the physics of number counts is intrinsically tomographic, whereas the physics of SGWB is somehow blind to the location in redshift space of the sources, since the superposition of all the unresolved events is calculated integrating along z. Therefore, in order to adapt the number count formalism to the SGWB, we must reduce the analysis to a single redshift bin that spans from $z = 0$ up to a certain z_{max}, beyond which the GW contributions are negligible. In this way, all the events in the considered redshift range are integrated together and contribute to the angular power spectrum of the energy density contrast:

$$C_\ell = \frac{2}{\pi}\int \frac{dk}{k}\, P(k) \left[\frac{\delta\Omega_\ell(k)}{\Omega_{gw}}\right]^2 , \tag{108}$$

where

$$\delta\Omega_\ell(k) = \int_0^{z_{max}} dz\, \frac{d\Omega_{gw}}{dz} W(z|z_{max}/2)\, \delta\Omega_\ell(k,z)\,. \tag{109}$$

In Equation (108), $P(k)$ is the primordial matter power spectrum as a function of wavenumber k, $d\Omega_{gw}/dz$ is the redshift distribution of the SGWB energy denasity, as defined in Equation (102). The window function $W(z|z_{max}/2)$, is a top hat function centred at $z_{max}/2$, designed to equally weigh all the events occurring the redshift range. Finally, $\delta\Omega_\ell(k,z)$ is the relativistic angular fluctuation of the density of the tracer, which is determined by density (den), velocity (vel), lensing (len) and gravity (gr) effects [246, 248, 249]:

$$\delta\Omega_\ell(k,z) = \delta\Omega_\ell^{den}(k,z) + \delta\Omega_\ell^{vel}(k,z) + \delta\Omega_\ell^{len}(k,z) + \delta\Omega_\ell^{gr}(k,z)\,. \tag{110}$$

The significance of each of these terms varies based on the specific configuration, such as redshift bins and window functions. However, the main contribution typically comes from the density term. The full expressions of the relativistic effects in the fluctuation $\delta\Omega_\ell$ are:

$$\begin{aligned}
\delta\Omega_\ell^{den}(k,z) &= b_\Omega\, \delta(k,\tau_z) j_\ell \\
\delta\Omega_\ell^{vel}(k,z) &= \frac{k}{\mathcal{H}} j_\ell'' V(k,\tau_z) + \\
&+ \left[(f_\Omega^{evo} - 3)\frac{\mathcal{H}}{k} j_\ell + \left(\frac{\mathcal{H}'}{\mathcal{H}^2} + \frac{2-5s_\Omega}{r(z)\mathcal{H}} + 5s - f_\Omega^{evo}\right) j_\ell'\right] V(k,\tau_z),
\end{aligned} \tag{111}$$

$$
\begin{aligned}
\delta\Omega_\ell^{\rm len}(k,z) &= \ell(\ell+1)\frac{2-5s_\Omega}{2}\int_0^{r(z)} dr \frac{r(z)-r}{r(z)r}\big[\Phi(k,\tau_z)+\Psi(k,\tau_z)\big] j_\ell(kr)\,,\\
\delta\Omega_\ell^{\rm gr}(k,z) &= \Bigg[\Big(\frac{\mathcal{H}'}{\mathcal{H}^2}+\frac{2-5s_\Omega}{r(z)\mathcal{H}}+5s_\Omega-f_\Omega^{\rm evo}+1\Big)\Psi(k,\tau_z)+\\
&\quad +(5s_\Omega-2)\Phi(k,\tau_z)+\mathcal{H}^{-1}\Phi'(k,\tau_z)\Bigg] j_\ell+\\
&\quad +\int_0^{r(z)} dr \frac{2-5s_\Omega}{r(z)}\big[\Phi(k,\tau)+\Psi(k,\tau)\big] j_\ell(kr)+\\
&\quad +\int_0^{r(z)} dr\Big(\frac{\mathcal{H}'}{\mathcal{H}^2}+\frac{2-5s_\Omega}{r(z)\mathcal{H}}+5s_\Omega-f_\Omega^{\rm evo}\Big)\big[\Phi'(k,\tau)+\Psi'(k,\tau)\big] j_\ell(kr)\,,
\end{aligned}
\tag{27}
$$

where b_Ω, s_Ω, and $f_\Omega^{\rm evo}$ are the bias, magnification bias, and evolution bias of the SGWB energy density, introduced in Section 2.4. Moreover, r is the conformal distance on the light cone, $\tau = \tau_0 - r$ is the conformal time, $\tau_z = \tau_0 - r(z)$, j_ℓ, j_ℓ' and j_ℓ'' are the Bessel functions and their derivatives evaluated at $y = kr(z)$ if not explicitly stated, $\mathcal{H}$ is the conformal Hubble parameter, the prime symbol stands for derivatives with respect to conformal time, δ is the density contrast in the comoving gauge, V is the peculiar velocity, Φ and Ψ are Bardeen potentials.

2.5.2 *Angular power spectrum*

The anisotropies of the SGWB from astrophysical sources has been studied in recent works [95, 96, 104, 106, 114]. Discrepancies in the results obtained in these works have been observed and discussed in Refs. [108, 109]. There, the authors suggest that the discrepancies could arise from variations in the astrophysical modeling and treatment of galaxy clustering. The goal here is to present the predicted signal within the astrophysical framework introduced in Section 2.2, which features new descriptions of both stellar and galactic physics. In the following, I will discuss our results and analyze the phenomenology of our predictions.

We compute the angular power spectrum of the SGWB anisotropies using the Boltzmann solver `CLASS`. In particular, we consider the redshift bin $z_{\rm bin} = [0, 8]$, using a top-hat window function in order to weight all the events equally. One drawback of using `CLASS` is that it allows only one bias and magnification bias value for each redshift bin. This limitation is significant because bias and magnification bias change noticeably with redshift, as shown in Figures 20 and 21. To overcome this issue, we use a weighted mean of $b_\Omega(z)$ and $s_\Omega(z)$

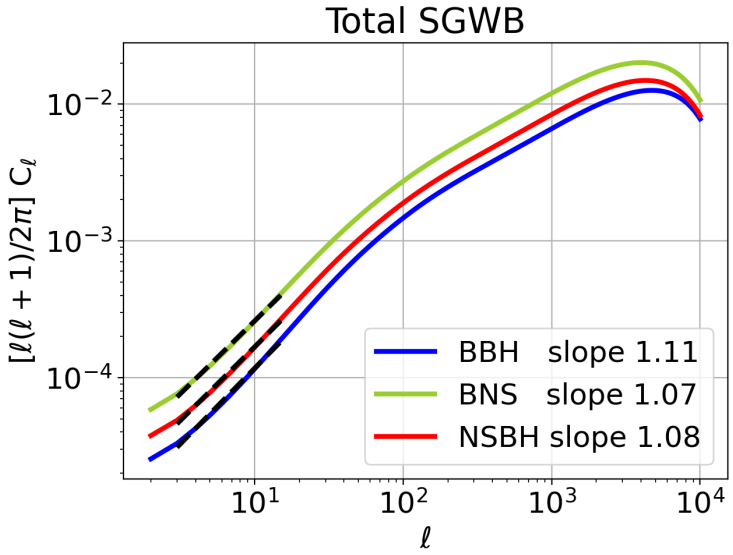

Figure 22: Angular power spectrum of the anisotropies of the total SGWB produced by BBHs, BNSs, and NSBHs at $f_{ref} = 65$ Hz. The black dotted lines represent the power-law fit at large angular scales, whose slopes are also reported.

in the considered redshift interval, where the weight is given by the redshift distribution of the SGWB energy density:

$$\langle b_\Omega \rangle = \frac{\int dz \frac{d\Omega_{gw}}{dz} b_\Omega(z)}{\int dz \frac{d\Omega_{gw}}{dz}} \quad \text{and} \quad \langle s_\Omega \rangle = \frac{\int dz \frac{d\Omega_{gw}}{dz} s_\Omega(z)}{\int dz \frac{d\Omega_{gw}}{dz}} \tag{28}$$

Considering the strong redshift dependence of both bias and magnification bias, relying on this approximation should be avoided in the future. Indeed, modifying `CLASS` to incorporate redshift-dependent bias and magnification bias would lead to more accurate results. As an initial step, we computed the angular power spectrum of the anisotropies in the total background, given by the superposition of all events, both resolved and unresolved. It's important to emphasize again that the SGWB measured by a real detector is given by the unresolved events only. Nevertheless, analyzing the anisotropies in the total background is interesting for two main reasons:

1. The total SGWB provides a detector-independent estimate of the expected signal amplitude;

2. Working with the total SGWB enables a comparison of our results with other predictions in the literature.

In Figure 22, we show the angular power spectrum of the anisotropies in the total SGWB for BBHs, BNSs, and NSBHs at $f_{ref} = 65$ Hz. Independently on the binary type, the spectra behave as a power-law at large angular scales and bend at smaller scales, reaching a peak at $l \sim 5 \times 10^3$. The slope of the power-law is close to 1, which means that $C_\ell \propto 1/\ell$ approximately, as it was also found in Refs. [96, 104].

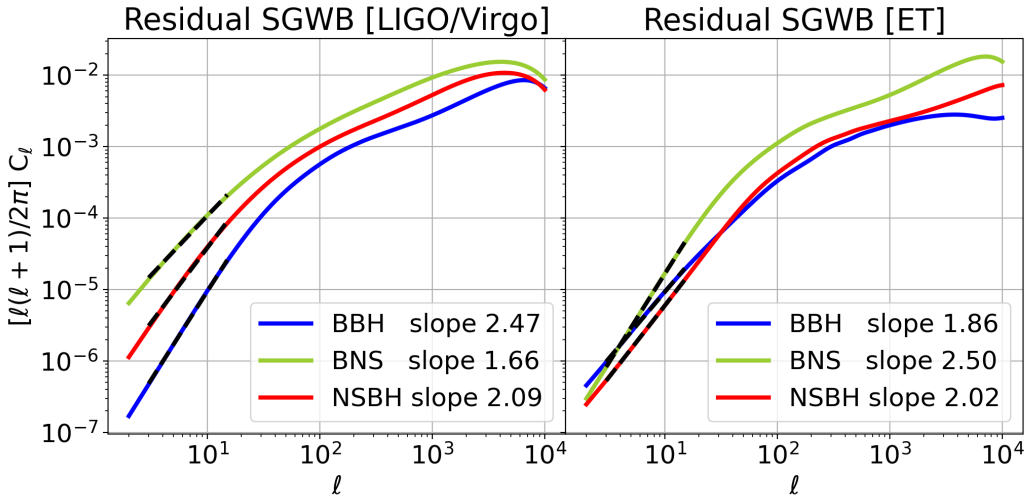

Figure 23: Angular power spectrum of the anisotropies of the residual SGWB produced by BBHs, BNSs, and NSBHs at $f_{ref} = 65$ Hz. Here, the SGWB is obtained integrating only the unresolved GW signals, for LIGO/Virgo (left) and ET (right). The black dotted lines represent the power-law fit at large scales.

One important innovation of this work is the analysis of the statistical properties of the anisotropies in the residual SGWB, as potentially measured by real detectors, i.e., considering only the unresolved GW events. The angular power spectrum of the SGWB anisotropies at $f_{ref} = 65$ Hz for LIGO/Virgo and ET are shown in Figure 23. For both detectors and for all binary types, the angular power spectrum behaves as a power law at large angular scales, as we also found when considering the total background. In this case, however, the power law is steeper and its slope is close to 2. Indeed, the value of the slope is slightly different for different binary types and detectors. We investigated the frequency behavior of the angular power spectra analyzing the anisotropies of the SGWB also at $f = 33, 65, 105$ and 209 Hz. We found that the slopes at large angular scales are constant with frequency. This feature could be used to distinguish the contribution of the various type of coalescing binaries from future measurements.

We compare our results with the current LIGO/Virgo upper limit obtained from the data of the first three observing runs. In Ref. [12], these upper limits are presented in terms of $\tilde{C}\ell^{1/2} = \overline{\Omega}_{gw} C\ell^{1/2}$, and the associated 95% upper limit at 25 Hz is $\tilde{C}\ell^{1/2} \lesssim 1.9 \times 10^{-9}$ sr^{-1} for $1 \leqslant \ell \leqslant 4$, assuming an isotropic background with a spectral index of $2/3$. Based on our results for $\Omega_{gw} = 4\pi\overline{\Omega}_{gw}$ and $C\ell$ at $f_{ref} = 65$ Hz, we obtain $\tilde{C}_\ell^{1/2} \simeq 3 \times 10^{-14}$ sr^{-1} at $\ell = 2$ for both BBHs and BNSs, which is significantly below the current upper limit. Regarding ET, in Ref. [193], the amplitude required for the $\ell = 2$ multipole to produce a S/N = 1 in one year of observation with two ET detectors is reported as $\tilde{C}\ell^{1/2} \lesssim 1.5 \times 10^{-14}$ sr^{-1} at 10 Hz, assuming an isotropic background with

a spectral index of 0. Our results for ET at $f_{ref} = 65$ Hz yield $\tilde{C}_\ell^{1/2} \simeq 6 - 8 \times 10^{-15}$ sr^{-1} for the $\ell = 2$, slightly below the minimum value found in Ref. [193].

2.5.3 *A tomographic approach*

Interestingly, our framework yields different predictions for different sources and detector types. This is the result of the complex interplay between various factors in the calculation, including the redshift distribution of the sources, their bias, and their magnification bias. In the following, I will provide a qualitative interpretation of these features, with a particular emphasis on the large angular scales. From Figures 22 and 23, it is apparent that the main difference between the power spectra of total and residual backgrounds is a steeper slope at large angular scales. The interpretation of this feature is not trivial because of the integrated nature of the SGWB. The SGWB, indeed, is given by the incoherent superposition of GW events up to a typical maximum redshift z_{max}. Hence, there is no direct relation between wavenumbers and angular scales. Instead, a given wavenumber contributes to all multipoles $\ell \lesssim \ell_{max}(k)$, where $\ell_{max}(k)$ is related to z_{max} through

$$\ell_{max}(k) = k\left[\tau_0 - \tau(z_{max})\right], \tag{29}$$

where $\tau(z)$ is the conformal time and $\tau_0 = \tau(0)$. Still, it is possible to identify the contributions of events at different redshifts using a tomographic approach. The results must then be interpreted taking into account the redshift distribution of the energy density. The tomographic analysis consists in computing the angular power spectrum of the SGWB anisotropies in the redshift bins $z_{bin} = [0, 1], [1, 3]$ and $[3, 8]$ and to compare them with the results in the total redshift interval $z_{bin} = [0, 8]$ presented in Section 2.5. In Figure 24, we show the power spectra of the SGWB anisotropies in these redshift bins for BBHs and BNSs and for both the total and residual backgrounds. We focus on the shape of the curves and do not consider their amplitude, which is typically higher for thinner redshift bins.

The upper panels of Figure 24 show the results of the tomographic analysis for the total SGWB. Remarkably, the power spectra have similar behaviors for both BBHs and BNSs. In both cases, the power-law slope at large angular scales is approximately ≈ 1 for the redshift bin $z_{bin} = [0, 1]$, while it steepens to approximately ≈ 2 for the redshift bins $z_{bin} = [1, 3]$ and $z_{bin} = [3, 8]$. This pattern leads us to deduce that the power-law slope is correlated with the distance of the considered sources. Specifically, the slope tends to be milder when the dominant contribution comes from sources at lower redshifts, whereas it steepens when the primary contribution comes from high-redshift sources. This observation is consistent with the fact that nearby events mostly contribute to the SGWB anisotropies at large angular scales. As we already saw in Figure 19, the redshift distribution of the total SGWB remains relatively flat up to $z \sim 1$ for both BBHs and BNSs. Therefore, the energy density of the total SGWB is predominantly shaped by nearby events, from which we receive the most intense

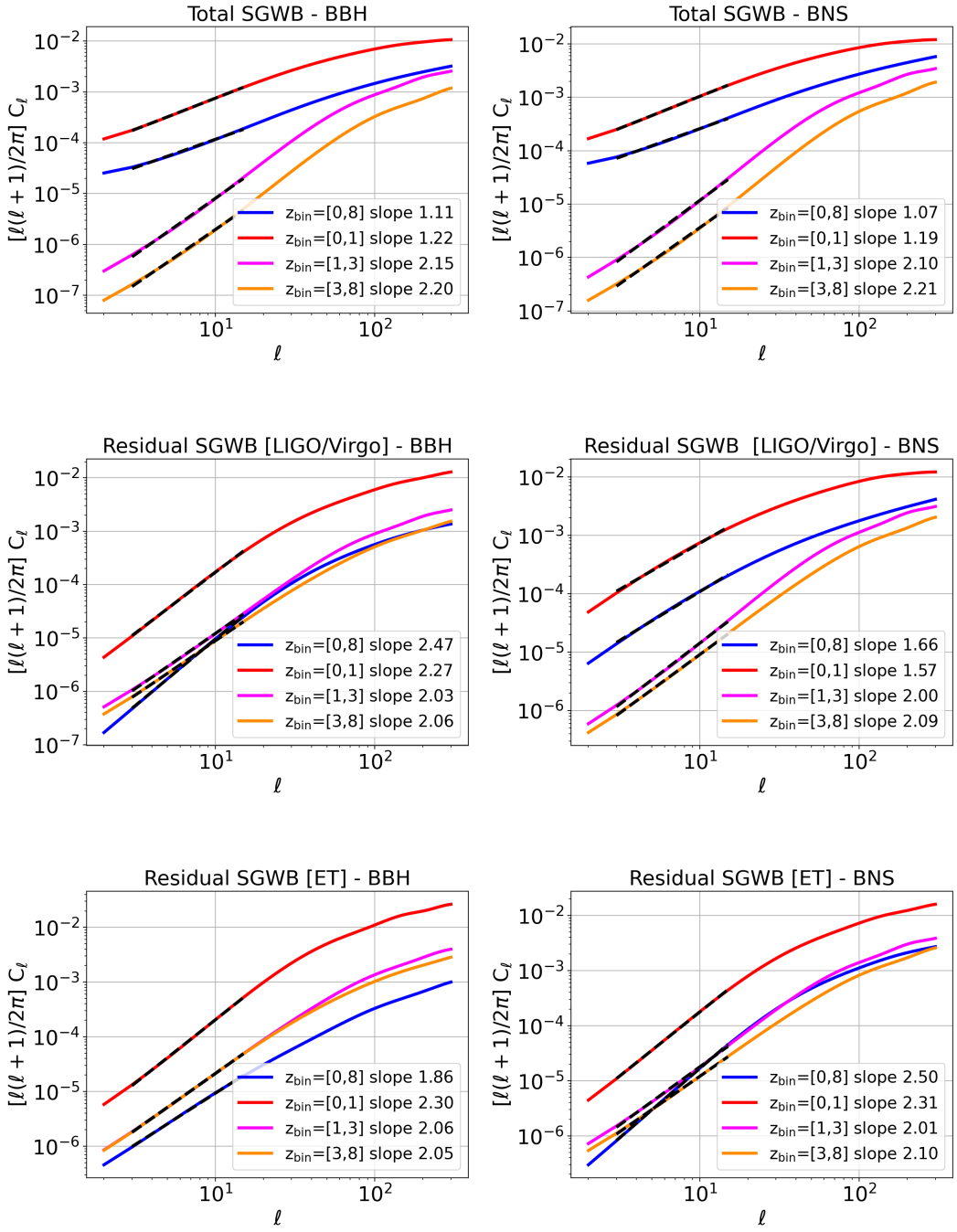

Figure 24: Tomographic analysis of the SGWB anisotropies for BBH and BNS coalescing binaries at $f_{ref} = 65$ Hz. We consider the total SGWB (upper panels), and the residual SGWB for LIGO/Virgo (middle panels) and ET (lower panels).

GW signals. This is the reason why the overall signal, integrated within the redshift bin $z_{bin} = [0, 8]$, features a mild slope (≈ 1) for both BBHs and BNSs.

The middle panels of Figure 24 show the results of the tomographic analysis for the residual SGWB for LIGO/Virgo. In this scenario, the detectors resolve

many nearby events, leading to a suppression of the contribution from low-redshift sources, particularly pronounced for BBH events (as shown by the blue curves in Figure 19). As a consequence, the power spectra have different behaviors at large scales for BBHs and BNSs. In the case of BNS events, the power spectra features a steeper slope (≈ 2) for the redshift bins $z_{\rm bin} = [1, 3]$ and $z_{\rm bin} = [3, 8]$, while a milder slope (≈ 1.5) is observed for $z_{\rm bin} = [0, 1]$. In contrast, for BBHs, the slope remains ≈ 2 across all redshift bins. This is because even for $z_{\rm bin} = [0, 1]$, the main contribution comes from events at $z \gtrsim 0.5$, given that many nearby BBH events are resolved by the detector. These observations clarify why the power spectra of the anisotropies of the residual SGWB over the total redshift interval $z_{\rm bin} = [0, 8]$ generally display a steeper profile at large angular scales compared to the total SGWB. Furthermore, we infer that the power spectrum for BNSs has a milder slope than that for NSBHs and BBHs because the signal is given by a higher number of low-redshift unresolved BNS events, contributing significantly at larger angular scales. As previously highlighted, the specific behavior of each curve is the result of the interplay of numerous factors. However, for LIGO/Virgo, the SGWB energy density is mainly given by a population of events at relatively low redshifts. Therefore, the complexities associated with the LSS and gravitational lensing are mitigated, allowing for a qualitative interpretation of the different slopes observed for different sources.

Finally, the lower panels of of Figure 24, show the results for ET. In this case, the slope at larger angular scales remains ≈ 2 across all redshift bins, regardless of the binary type. This behavior stems from the fact that ET will be able to resolve all nearby events, including both BBHs and BNSs, as shown by the redshift distributions in Figure 19. This explains why all the power spectra feature steep slopes (≈ 2) for ET. However, this alone does not provide a complete interpretation of the slightly different slopes observed for different binary types (as also shown in Figure 23). Compared to LIGO/Virgo, ET is sensitive to a SGWB generated by a population of events situated at higher redshifts. Therefore, accurately capturing all the intricate effects associated with the LSS and gravitational lensing, which significantly influence the computation of the power spectrum, becomes more challenging.

2.6 A FRAMEWORK TO SIMULATE FULL-SKY MAPS OF THE SGWB

In this Section, I introduce a technique to simulate full-sky maps of the expected SGWB density contrast, $\delta_{\rm gw}(f, \hat{\mathbf{n}})$. The peculiarity of the astrophysical SGWB with respect to other backgrounds, such as the CMB, is that it is given by the superposition of numerous unresolved point sources, instead of a single extended source. Since these sources are discrete in space and time, the SGWB statistics will follow a Poisson distribution. In order to simulate a realistic signal, we therefore need to develop a framework that produces maps with a poissonian statistic and the cosmological clustering expected for the GW emitters. To this purpose, we adapt the procedure presented in Ref. [250] to the

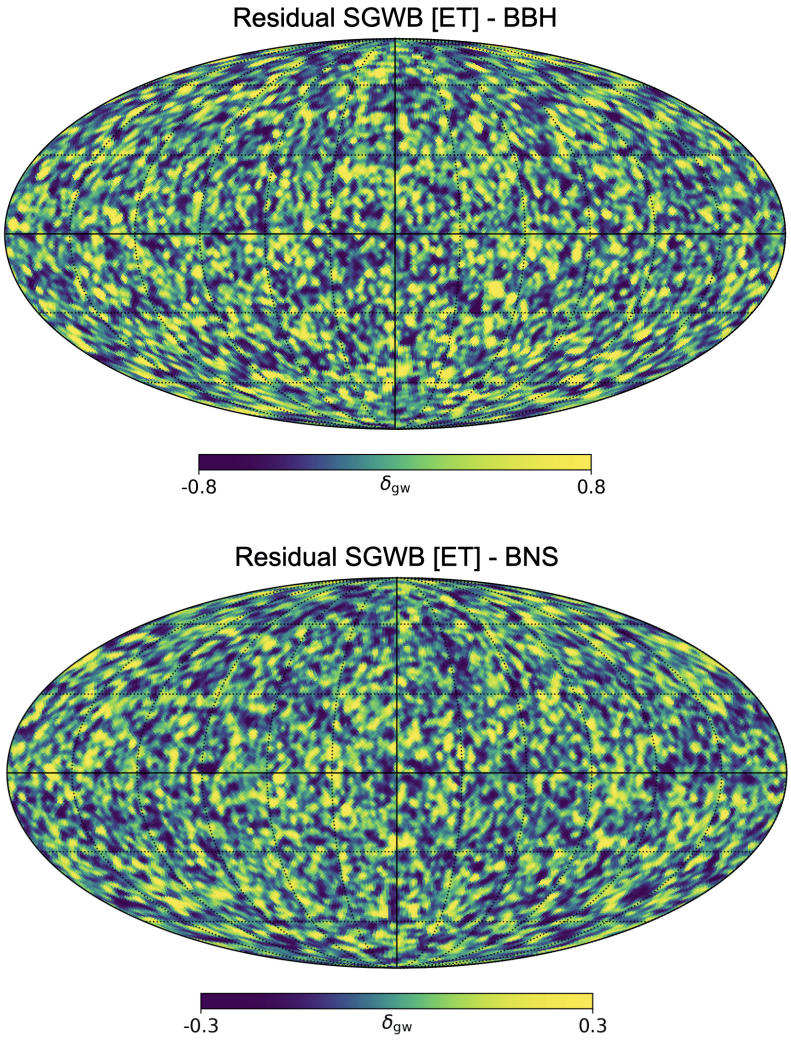

Figure 25: Simulated full-sky map of the SGWB generated by BBH and BNS binaries at $f_{ref} = 65$ Hz. As an example, we show the residual SGWB for ET after T = 1 yr of observation. Both plots have been realized with the HEALPix package, using $N_{side} = 64$, which corresponds to an angular resolution of $\theta_{pix} = 55'$. In order to remove the ringing effect arising when manipulating the harmonic coefficients, the maps have been smoothed with a Gaussian filter corresponding to $\sigma = \theta_{pix}$.

case of the SGWB. A preliminary step is to produce a purely poissonian map of the energy density contrast, without any clustering. First, we compute the mean number of unresolved events per unit time in each pixel:

$$\langle \dot{N}_{pix} \rangle = \frac{4\pi}{N_{pix}} \int dz \int d\mathcal{M}_c \frac{d^3\dot{N}}{d\hat{n}\, dz\, d\mathcal{M}_c} \int_0^{\bar{\rho}} d\rho\, P_\rho(\rho|z, \mathcal{M}_c)\,. \tag{30}$$

In Equation (30), N_{pix} is the number of pixels in the map and $d\dot{N}/d\hat{n}\, dz\, d\mathcal{M}_c$ is the merger rate per unit redshift, solid angle and chirp mass, which can be easily obtained from the differential merger rate of Equation (85) through:

$$\frac{d^3\dot{N}}{d\hat{n}dzd\mathcal{M}_c} = \frac{d^2\dot{N}}{dVd\mathcal{M}_c}\frac{c\,r(z)}{H_0\,h(z)}\,, \tag{31}$$

where $r(z)$ is the comoving distance. We then create a map assigning to each pixel a number of events per unit time extracted from a Poisson distribution with mean $\langle\dot{N}_{pix}\rangle$. We assign to each event in each pixel a chirp mass and a redshift that we generate randomly from a 2D probability distribution obtained from the differential merger rate $d\dot{N}/dz\,d\mathcal{M}_c$. In this way, we can compute the energy density in each pixel summing the contributions from all the events:

$$\Omega_{gw}^{Poiss} = \frac{8\pi G f}{3H_0^3c^2}\frac{1}{T}\sum_i \frac{dE/df(z_i,\mathcal{M}_{c\,i})}{4\pi(1+z_i)r^2(z)}\,, \tag{32}$$

where T is the considered observing time (T = 1 yr, in our case). At this stage, we have a map of the SGWB energy density which follows a pure Poisson statistics, without any clustering. In order to inject the clustering induced by the LSS, we first compute the energy density contrast of the purely poissonian map:

$$\delta_{gw}^{Poiss} = \frac{\Omega_{gw}^{Poiss} - \langle\Omega_{gw}\rangle}{\langle\Omega_{gw}\rangle}\,. \tag{33}$$

Then, using the HEALPix[5] package [251, 252], we compute the harmonic coefficients $a_{\ell m}^{Poiss}$ of the density contrast map. At this point, we can introduce the correlation given by the angular power spectrum C_ℓ^{CLASS} obtained with `CLASS` in the following way:

$$a_{\ell m} = a_{\ell m}^{Poiss}\frac{\sqrt{C_\ell^{Poiss} + C_\ell^{CLASS}}}{\sqrt{C_\ell^{Poiss}}}\,. \tag{34}$$

Finally, by performing an inverse harmonic transform, we obtain the clustered density contrast δ_{gw}, from which the energy density at each pixel can be easily computed as $\Omega_{gw} = \langle\Omega_{gw}\rangle(1+\delta_{gw})$. In Figure 25, we show a full-sky realization of the SGWB energy density contrast produced by BBH and BNS coalescing binaries at $f_{ref} = 65$ Hz. For simplicity, we focus on the residual SGWB for ET. In Figure 26, we plot the angular power spectra of the two maps, together with the theoretical power spectra obtained with `CLASS` and the power spectra of the purely poissonian maps (no clustering). As expected, the angular power spectrum of the shot noise is flat across all multipoles and its amplitude is related to the chosen integration time. Increasing T, the number N of events in each pixel increases and the shot noise amplitude decreases as $1/\sqrt{N}$. We find

5 http://healpix.sourceforge.net

that, for T = 1 yr, the shot noise dominates over the signal, especially for BBHs. For BNSs, the shot noise is relatively lower due to the higher merger rate, as seen in Figures 14 and 15. Accordingly, the number of merging BNSs per year in each pixel, is higher than the number BBHs, and the resulting shot noise is lower. All in all, it is clear that being able to remove the shot noise is crucial to obtain an estimate of the intrinsic angular power spectrum of the SGWB from real data. Recent studies addressed this issue, finding that the effect of shot noise can be reduced cross-correlating the signal with other probes [102, 104, 113–115, 118, 253, 254].

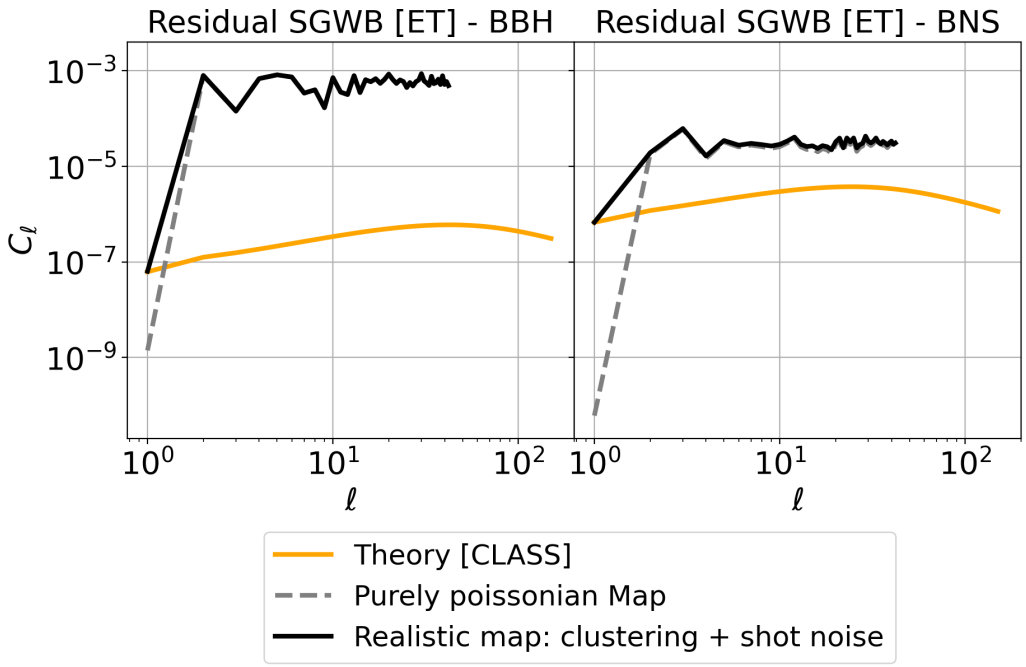

Figure 26: Comparison of the angular power spectra of the simulated SGWB map (solid black) and the purely poissonian map (dashed grey) with the theoretical angular power spectrum of SGWB anisotropies obtained with `CLASS` (orange). The power spectrum of shot noise is flat across all multipoles and it dominates over the signal at most scales. The shot noise is lower for BNSs, since the merger rate is higher than for BBHs.

2.7 DISCUSSION AND CONCLUSIONS

In this chapter, I discussed a theoretical characterization of the SGWB generated by the superposition of unresolved GW signals produced by binary coalescences in galaxies. This SGWB is expected to be the dominant contribution in the frequency band of ground-based interferometers. The significant amount of astrophysical and cosmological information encoded in this particular SGWB

makes its characterization one of the primary goals for the GW community. Our predictions rely on an empirical, data-driven approach to galactic astrophysics, which allows us to track the evolution of individual galaxies. We also use the outcomes of population synthesis codes to model stellar and binary evolution.

We have characterized the energy density parameter of the SGWB as a tracer of LSS. This involved computing its redshift distribution, bias, and magnification bias. We then used the Boltzmann solver `CLASS` to calculate the angular power spectrum of SGWB anisotropies. We presented our predictions for the isotropic energy density and the angular power spectrum of anisotropies of the residual SGWB for LIGO/Virgo and ET. In this context, we filtered out events with expected signal-to-noise ratios that would enable LIGO/Virgo or ET to resolve them individually. Additionally, we also analyzed the scenario in which all GW events, both resolved and unresolved, contributed to the SGWB. This allowed us to compare our findings with existing literature. We presented our results for all binary types – namely, BBHs, NSBHs, and BNSs. We also performed a tomographic analysis in order to isolate the contribution of sources located at different redshifts. Finally, we have introduced a framework for simulating realistic full-sky maps of the SGWB. This framework accounts for both the poissonian nature of the signal and the cosmological clustering properties. With this technique, we were able to estimate the amplitude of the shot noise caused by the discreteness of sources in space and time. Our findings show that the shot noise dominates over the pure clustering signal, especially in the case of the SGWB generated by BBH events, given their lower merger rate compared to BNS events.

In the following chapters, I will present our subsequent works, in which we extend the results presented in this chapter in several different ways. First, we employ our pipelines to cross-correlate the SGWB with other cosmic fields. Cross-correlations are highly effective in mitigating the impacts of shot noise and instrumental noise, as discussed in Chapter 3. In Chapter 4, I will show how we expanded our analysis to include other sources of SGWB and various detectors. Finally, in Chapter 5, I will investigate how different astrophysical and cosmological models affect our results concerning the isotropic SGWB.

CROSS-CORRELATION WITH CMB LENSING: THEORY AND DETECTION PROSPECTS

3

This chapter is based on the following publication:

G. Capurri, A. Lapi, C. Baccigalupi
Detectability of the cross-correlation between CMB lensing and stochastic GW background from compact object mergers
Universe 8.3 (Mar. 2022) , arXiv:2111.04757

The anisotropies of the stochastic gravitational-wave background (SGWB) produced by stellar compact binaries coalescences constitute a new probe of the large-scale structure (LSS). However, the shot noise caused by the discreteness of the GW sources in space and time and the limited angular resolution of GW instruments hamper the detection of the intrinsic anisotropies induced by the LSS. In this chapter, I will investigate the potential of cross-correlating forthcoming high precision measurements of the SGWB energy density and the Cosmic Microwave Background (CMB) lensing convergence to mitigate the effect of shot noise.

3.1 INTRODUCTION AND MOTIVATION

The SGWB generated by stellar compact binary coalescences has garnered significant interest in the scientific community [37, 84–90, 187, 240]. Indeed, it anticipated to be the dominant stochastic background in the frequency range explored by ground-based detectors (f $\sim$ Hz-kHz). Although it has not been measured yet, existing data from the LIGO/Virgo network have already placed upper bounds on both its amplitude and anisotropies [11, 12]. The binaries that produce this SGWB are the outcomes of stellar evolution and are primarily located inside galaxies. As a consequence, the SGWB anisotropies reflect the distribution of galaxies in the Universe and constitute themselves a tracer of the LSS, as we discussed in Chapter 2. Therefore, the anisotropic SGWB has been extensively studied in recent years, with a significant focus on theoretical modeling [91, 95, 96, 102–104, 106, 110–112, 116], observational searches [193, 208, 255–258], and data analysis techniques [18, 167, 168, 171, 173, 259, 260].

The two main challenges in detecting SGWB anisotropies in the Hz-kHz band are the limited angular resolution of GW detectors and the shot noise. The former issue is associated with the noise characteristics of the detector, their projection onto the sky, as well as the network configuration and scan strategy. [23, 122]. In contrast, shot noise arises because the SGWB consists of the superposition of individual events that are discrete in both space and time, leading to a high level of uncertainty in the predicted SGWB energy

density. Several recent studies have addressed the shot noise issue, showing that its expected amplitude is orders of magnitude higher than the clustering induced by the LSS [113–116]. Cross-correlation with other tracers of the LSS has been proposed as a potential solution to mitigate the impact of shot noise. Specifically, cross-correlations with galaxy number counts, weak lensing, and CMB temperature fluctuations have already been investigated [102, 104, 118, 119, 253, 254, 261].

In this chapter, I discuss the cross-correlation between the astrophysical SGWB and the CMB lensing convergence[1]. The aim of the study is to investigate whether cross-correlation with another cosmic field, tracing the same underlying dark matter distribution, can reveal the intrinsic SGWB anisotropies in the presence of both shot noise and instrumental noise. We chose to work with CMB lensing convergence, which is as an integrated tracer of the LSS, like the SGWB, and will be constrained with high precision by future CMB experiments. Starting from the detailed models of stellar and binary evolution [214, 215] and galaxy astrophysics [76, 77], described in Chapter 2, we compute the anisotropies of the SGWB for binary black holes (BBH), binary neutron stars (BNS) and neutron star-black hole binaries (NSBH). We also consider different present and forthcoming ground-based detectors: the LIGO/Virgo/KAGRA network (LVK) [4, 5, 10], the Einstein Telescope (ET) [134, 135, 264], and Cosmic Explorer (CE) [136, 137]. Using the framework for distributing GW emitters across the sky and simulating a full-sky map of the SGWB developed discussed in the last section of Chapter 2, we estimate the shot noise. Finally, we explore the potential of the cross-correlation with upcoming high-precision measurements of CMB lensing by the Simons Observatory (SO) [57]. SO is a powerful future probe that will observe arcminute-scale CMB anisotropies with high sensitivity, allowing us to characterize the lensing signal with unprecedented precision and use it to enhance sensitivity to cosmological GWs [265].

The chapter is structured as follows: in Section 3.2, I will review the characterization of the CMB lensing as a tracer of the LSS through its kernel, and I derive an analogous quantity for the SGWB as well. In Section 3.3, I will provide an overview of the theory behind the cross-correlation of two cosmic fields. In Section 3.4, I will present our results for the cross-correlation angular power spectra and study the detectability of such signals with present and forthcoming instruments. Finally, in Section 3.5 I will discuss the results and draw the conclusions.

Throughout this work, we assume the standard flat ΛCDM cosmology with parameter values from the Planck 2018 legacy release [32], with Hubble rate today corresponding to $H_0 = 67.4$ km s^{-1} Mpc^{-1}, Cold Dark Matter (CDM) and baryon abundances with respect to the critical density corresponding to $\Omega_{\rm CDM}h^2 = 0.120$ and $\Omega_b h^2 = 0.022$, respectively, reionization optical depth

1 Although the cross-correlation of CMB lensing with resolved GW sources was already employed as a probe of general relativity and dark energy [262, 263], this is the first time to our knowledge that CMB lensing is cross-correlated with the SGWB, exploiting the fact that both cosmic fields are tracers of the underlying dark matter distribution.

$\tau = 0.054$, amplitude and spectral index of primordial scalar perturbations corresponding to $\ln(10^{10}A_S) = 3.045$ and $n_S = 0.965$, respectively.

3.2 SGWB AND CMB LENSING AS TRACERS OF MATTER

In this section, I provide a review the standard CMB lensing description, closely following Refs. [266, 267]. Then, I recall the characterization of the SGWB as a tracer of the LSS presented in Chapter 2, and we use this characterization to derive an expression of a kernel for the SGWB energy density.

3.2.1 *The lensing kernel*

The LSS between the last-scattering surface and the observer gravitationally deflects CMB photons. This process leaves small imprints on the observed temperature and polarization fluctuations of the CMB. Specifically, the effect of gravitational lensing on CMB photons can be described as a remapping of the unlensed temperature anisotropies $\Theta(\hat{\mathbf{n}})$ by a two-dimensional vector field in the sky, known as the deflection field $\mathbf{d}(\hat{\mathbf{n}})$ [268]:

$$\begin{aligned}\tilde{\Theta}(\hat{\mathbf{n}}) &= \Theta(\hat{\mathbf{n}} + \mathbf{d}(\hat{\mathbf{n}})) \\ &= \Theta(\hat{\mathbf{n}} + \nabla\phi(\hat{\mathbf{n}})) \\ &= \Theta(\hat{\mathbf{n}}) + \nabla^i\phi(\hat{\mathbf{n}})\nabla_i\Theta(\hat{\mathbf{n}}) + \mathcal{O}(\phi^2),\end{aligned} \tag{35}$$

where $\tilde{\Theta}(\hat{\mathbf{n}})$ is the lensed temperature fluctuation and $\phi(\hat{\mathbf{n}})$ is the CMB lensing potential:

$$\phi(\hat{\mathbf{n}}) = -2\int_0^{z_\star} \frac{c\,dz}{H(z)} \frac{r_\star - r(z)}{r_\star r(z)} \Psi(r(z)\hat{\mathbf{n}}, z). \tag{36}$$

In Equation (36), $r(z)$ is the comoving distance to redshift z, $r_\star$ is the comoving distance to the last-scattering surface at $z_\star \approx 1090$, $H(z)$ is the Hubble parameter, and $\Psi(r(z)\hat{\mathbf{n}}, z)$ is the three-dimensional gravitational potential at the point on the photon path given by $r(z)\hat{\mathbf{n}}$. The deflection field is defined as $\mathbf{d}(\hat{\mathbf{n}}) = \nabla\phi(\hat{\mathbf{n}})$, where ∇ is the the two-dimensional gradient on the sphere. Since the lensing potential is an integrated measure of the gravitational potential, it is convenient to describe the CMB lensing by means of the lensing convergence, which is proportional to the two-dimensional Laplacian of the lensing potential and can be written as a weighted integral over redshift of the projected dark matter density contrast δ [269]:

$$\kappa(\hat{\mathbf{n}}) = -\frac{1}{2}\nabla^2\phi(\hat{\mathbf{n}}) = \int_0^{z_*} W^\kappa(z)\delta(r(z)\hat{\mathbf{n}}, z). \tag{37}$$

The weight inside the integral is known as *lensing kernel* and describes the lensing efficiency of the matter distribution. The lensing kernel is given by:

$$W^{\kappa}(z) = \frac{3\Omega_m}{2c}\frac{H_0^2}{H(z)}(1+z)r(z)\frac{r_* - r(z)}{r_\star}, \tag{38}$$

where Ω_m and H_0 are the present-day values of the matter density and the Hubble parameter, respectively.

3.2.2 *Derivation of the SGWB energy density kernel*

As usual, we describe the SGWB using the energy density parameter:

$$\Omega_{gw}(f,\hat{\mathbf{n}}) = \frac{1}{\rho_c}\frac{d^3\rho_{gw}(f,\hat{\mathbf{n}})}{d\ln f\, d^2\hat{\mathbf{n}}} = \frac{8\pi G f}{3H_0^2c^2}\frac{d^3\rho_{gw}(f,\hat{\mathbf{n}})}{df\, d^2\hat{\mathbf{n}}}, \tag{39}$$

where $\rho_c = 3H_0^2c^2/8\pi G$ is the critical density and ρ_{gw} is the SGWB energy density at the observed frequency f, arriving from the unit solid angle centred around the observed direction $\hat{\mathbf{n}}$. The energy density parameter can be split into an isotropic term and a directional fluctuation:

$$\Omega_{gw}(f,\hat{\mathbf{n}}) = \overline{\Omega}_{gw}(f) + \delta\Omega_{gw}(f,\hat{\mathbf{n}})\,. \tag{40}$$

In this work, we consider the astrophysical SGWB given by the incoherent superposition of GW signals produced during the coalescence of stellar compact-object binaries inside galaxies. Assuming that the SGWB, as well as the galaxies that host the coalescing binaries, traces the peaks of the underlying dark matter distribution, the energy density contrast $\delta_{gw} = \delta\Omega_{gw}/\overline{\Omega}_{gw}$ can be expressed as a line-of-sight integral of the dark matter density contrast:

$$\delta_{gw}(f,\hat{\mathbf{n}}) = \int_0^{z_\star} W^{\Omega}(f,z)\delta(r(z)\hat{\mathbf{n}},z), \tag{41}$$

where the SGWB kernel $W^{\Omega}(f,z)$ is the sum of two terms:

$$W^{\Omega}(f,z) = \frac{b_\Omega(f,z)\dfrac{d\Omega_{gw}}{dz}(f,z)}{\left(\int dz'\frac{d\Omega_{gw}}{dz'}\right)} + \mu(f,z). \tag{42}$$

The first term is the product of the bias b_Ω, which quantifies the mismatch between the distribution of the SGWB and the total matter density, and the SGWB redshift distribution $d\Omega_{gw}/dz$. The second term takes into account the effect of weak lensing on the observed SGWB energy density and is given by:

$$\begin{aligned}\mu(f,z) =& \frac{3\Omega_m}{2c}\frac{H_0^2}{H(z)}(1+z)r(z)\times \\ &\times\int_z^{z_\star} dz'\left(1-\frac{r(z)}{r(z')}\right)\left(s_\Omega(f,z)-1\right)\frac{\dfrac{d\Omega_{gw}}{dz}(f,z)}{\left(\int dz'\frac{d\Omega_{gw}}{dz'}\right)},\end{aligned} \tag{43}$$

where s_Ω is the magnification bias. We derived and discussed the expressions of the redshift distribution $d\Omega_{gw}/dz$, the bias b_Ω and the magnification bias s_Ω in Chapter 2. For this work, we adopt the same framework to describe the SGWB, with only minor modifications that I discuss in Appendix B. The redshift distribution, bias and magnification bias of the SGWB can be evaluated once specific models for stellar and binary evolution and galaxy astrophysics have been chosen. In this work, we adopt the same prescriptions outlined in Section 2.2, originally presented in Refs. [76, 77]. We use the merger rates obtained combining the results of the `StarTrack` population synthesis code[2], specifically the 'reference B' model in Refs. [214, 215], with data-driven prescriptions for the host galaxies. In particular, we use the merger rates computed employing the empirical star formation rate function (SFRF) as galaxy statistics and the fundamental metallicity relation (FMR) to assign metallicity to galaxies[3] (see Figures 15 and 14). To reduce the impact of the uncertainties in the astrophysical modeling, we re-scale the merger rates to match the local values measured by LIGO and Virgo during the second observing run[4] [219, 220]: $23.9^{+14.9}_{-8.6}\,\mathrm{Gpc^{-3}\,yr^{-1}}$ for BBHs, $320^{+490}_{-240}\,\mathrm{Gpc^{-3}\,yr^{-1}}$ for BNSs and $45^{+75}_{-33}\,\mathrm{Gpc^{-3}\,yr^{-1}}$ for NSBHs.

3.3 CROSS-CORRELATION OF TWO COSMIC FIELDS

In this section, I will provide an overview of the theoretical background for the cross-correlation of two cosmic fields, closely following Refs. [266, 267]. All the formulas will be specific for the SGWB and the CMB lensing convergence, but they can be easily adapted to other cosmic fields as well. The kernels of both the considered cosmic fields, CMB lensing and SGWB, are broad functions of redshift, as we will verify in Section 3.4. Therefore, we can compute the cross-correlation angular power spectrum using the Limber approximation [270]:

$$C_\ell^{\kappa\Omega} = \int_0^{z_\star} \frac{dz}{c}\frac{H(z)}{r^2(z)} W^\kappa(z) W^\Omega(z)\, P\left(k = \frac{l}{r(z)}, z\right), \tag{44}$$

where $P(k,z)$ is the matter power spectrum, which we compute using `CLASS`[5] [210, 211]. The nonlinear evolution of the matter power spectrum is taken into account using the `HALOFIT` prescription [271]. Assuming that both the SGWB and the CMB lensing behave as Gaussian random fields[6], the variance of $C_\ell^{\kappa\Omega}$ is given by:

2 Simulation data publicly available at https://www.syntheticuniverse.org.

3 See Appendix A for an overview of galaxy statistics and evolution.

4 Please note that these were the most recent estimates at the time of publication. Currently, the most up-to-date estimates are the ones obtained during the third observing run, which are slightly different [9].

5 The Cosmic Linear Anisotropy Solving System, available at http://class-code.net.

6 We saw in Chapters 2 and 2 that this is not always true for the SGWB. Indeed, in the frequency band of ground-based interferometers, the discreteness of sources in space and time causes a large shot noise, which dominates over the intrinsic LSS-driven anisotropies and follows a poissonian statistics. Nevertheless, the angular power spectrum still offers a valuable tool to study the properties of the SGWB anisotropies and serves as a good starting point.

$$\left(\Delta C_\ell^{\kappa\Omega}\right)^2 = \frac{\left(C_\ell^{\kappa\Omega}\right)^2 + \left(C_\ell^{\kappa\kappa} + N_\ell^{\kappa\kappa}\right)\left(C_\ell^{\Omega\Omega} + S_\ell^{\Omega\Omega} + N_\ell^{\Omega\Omega}\right)}{(2\ell+1) f_{\rm sky}}, \tag{45}$$

where $f_{\rm sky}$ is the sky fraction covered by both the SGWB and the CMB lensing surveys, $N_\ell^{\kappa\kappa}$ is the lensing noise, $S_\ell^{\Omega\Omega}$ and $N_\ell^{\Omega\Omega}$ are the SGWB shot noise and instrumental noise, respectively. For our analysis, we employ the Simons Observatory lensing noise curves [57] and we adopt the fiducial Large Aperture Telescope value $f_{\rm sky}^{\kappa} = 0.4$ for the sky fraction. Since GW experiments cover the full sky (i.e. $f_{\rm sky}^{\Omega} = 1$), we use the limiting value $f_{\rm sky} = f_{\rm sky}^{\kappa}$ for the cross-correlation. As for the SGWB, we compute the instrumental noise curves for different detector network configurations using the software `schNell`[7] [122], while we evaluate the SGWB shot noise contribution through the novel map-making technique developed in [116] and discussed in Section 2.6. The signal-to-noise ratio (S/N) at each multipole ℓ is then given by:

$$\left(\frac{S}{N}\right)_\ell^2 = \frac{\left(C_\ell^{\kappa\Omega}\right)^2}{\left(\Delta C_\ell^{\kappa\Omega}\right)^2} = \frac{(2\ell+1) f_{\rm sky}\left(C_\ell^{\kappa\Omega}\right)^2}{\left(C_\ell^{\kappa\Omega}\right)^2 + \left(C_\ell^{\kappa\kappa} + N_\ell^{\kappa\kappa}\right)\left(C_\ell^{\Omega\Omega} + S_\ell^{\Omega\Omega} + N_\ell^{\Omega\Omega}\right)}, \tag{46}$$

and the cumulative S/N for multipoles up to $\ell_{\rm max}$ is

$$\left(\frac{S}{N}\right)(\ell < \ell_{\rm max}) = \sqrt{\sum_{\ell=\ell_{\rm min}}^{\ell_{\rm max}} \left(\frac{S}{N}\right)_\ell^2}. \tag{47}$$

The auto-correlation angular power spectra for both the SGWB and CMB lensing can be calculated in a similar manner. For the SGWB, we have:

$$C_\ell^{\Omega\Omega} = \int_0^{z_\star} \frac{dz}{c} \frac{H(z)}{r^2(z)} \left[W^{\Omega}(z)\right]^2 P\left(k = \frac{l}{r(z)}, z\right). \tag{48}$$

The associated S/N is given by

$$\left(\frac{S}{N}\right)_\ell^2 = \frac{(2\ell+1)}{2} \frac{\left(C_\ell^{\Omega\Omega}\right)^2}{\left(C_\ell^{\Omega\Omega} + S_\ell^{\Omega\Omega} + N_\ell^{\Omega\Omega}\right)^2}, \tag{49}$$

where $S_\ell^{\Omega\Omega}$ and $N_\ell^{\Omega\Omega}$ are the shot noise and the instrumental noise, respectively. Notice that for SGWB searches we have $f_{\rm sky}^{\Omega} = 1$. The angular power spectrum in Equation (48) is the same quantity we examined in Chapter 2. For this work, however, we use a different formulation involving the kernels derived in the previous subsection and the Limber approximation, whereas in

7 The package is public available at https://github.com/damonge/schNell.

our previous work did a full computation using the Boltzmann solver CLASS. With CLASS, we were able to take into account all the relativistic effects, while the kernel of Equation 42 contains only the clustering and the lensing terms. We verified that the angular power spectra calculated using the two pipelines differ by a factor of order unity. Indeed, relativistic effects play a subdominant role in comparison to clustering and lensing. This is shown, for instance, in Ref. [110], where the maximum contribution is estimated to be around 10%, encompassing the Kaiser term that can be eliminated through integration by parts, as detailed in Ref. [112]. Hence, we choose to prioritize the simplicity gained through a fully analytical approach[8], even at the cost of neglecting relativistic effects. This decision also considers the substantial impact of shot noise and instrumental noise, in addition to the significant uncertainties in the astrophysical modeling. These factors have a much larger effect than the error incurred by neglecting the subdominant relativistic terms. Nonetheless, a comprehensive estimation of SGWB anisotropies should incorporate all the relativistic effects, particularly as our understanding of the astrophysical modeling becomes more precise and we approach the detection threshold. In that case, even a small deviation of a few percentage points is relevant.

Finally, the auto-correlation power spectra can be evaluated as:

$$C_\ell^{\kappa\kappa} = \int_0^{z_\star} \frac{dz}{c} \frac{H(z)}{r^2(z)} \left[W^\kappa(z)\right]^2 P\left(k = \frac{l}{r(z)}, z\right), \tag{50}$$

with an associated S/N given by:

$$\left(\frac{S}{N}\right)^2_\ell = \frac{(2\ell+1)}{2} f^\kappa_{\rm sky} \frac{\left(C_\ell^{\kappa\kappa}\right)^2}{\left(C_\ell^{\kappa\kappa} + N_\ell^{\kappa\kappa}\right)^2}. \tag{51}$$

where $N_\ell^{\kappa\kappa}$ is the lensing noise and $f^\kappa_{\rm sky}$ is sky fraction covered by the considered CMB survey. Notice that differently from the S/N for the SGWB of Equation (49), in Equation (51) the shot noise is not present, as the CMB lensing is a continuous field.

3.4 DETECTION PROSPECTS FOR THE CROSS-CORRELATION SIGNAL

We study the cross-correlation between the astrophysical SGWB and the CMB lensing convergence in two different scenarios. First, we examine the case where all GW events are taken into account when computing the SGWB energy density. Second, we consider the residual SGWB as potentially measured by a specific detector network, i.e. we only take into account the contribution of the unresolved events. The events that can be resolved individually are filtered out by means of a signal-to-noise threshold, which we fix at the reference

8 Moreover, within this analytic approach, we can utilize redshift-dependent values for bias and magnification bias. This flexibility was not possible with CLASS, which requires a single value of bias and magnification bias per redshift bin.

value of $\bar{\rho} = 8$ (see Appendix B for more details). We include in our analysis the present and forthcoming ground-based GW detectors LIGO, Virgo, and KAGRA (LVK) [4, 5, 10], Einstein Telescope (ET) [135] and Cosmic Explorer (CE) [136]. In Table 1, we report the detector coordinates and orientation angles that we plug into the `schNell` to compute the noise curves for specific network configurations. In particular, for the anisotropies of the residual SGWB detected by LVK, we consider a network composed of the first four interferometers in Table 1 and the associated noise curves. Instead, to investigate the detectability of the anisotropies of the residual SGWB measured by ET or CE, we consider a network composed of LVK and ET or CE, respectively. In all cases, we consider an integration time of $T = 1$ yr. Finally, we also consider an extended network given by all the detectors taken into account in this work. We use the noise curves of this extended network for $T = 1$ yr and $T = 10$ yr to study the detectability of the total background, given by all resolved and unresolved events. We work at the reference frequency of $f_{ref} = 65$ Hz, which falls in the middle of the sensitivity bands of all the considered detectors.

Detector	**Latitude** (deg)	**Longitude** (deg)	**Orientation** (deg)
LIGO Hanford	46.6	-119.4	171.8
LIGO Livingston	30.7	-90.8	243.0
Virgo	43.6	10.5	116.5
KAGRA	36.3	137.2	225.0
ET*	40.1	9.0	90.0
CE*	40.8	-113.8	90.0

Table 1: Location coordinates and orientation angles of the detectors considered in this work. For the forthcoming 3G detectors Einstein Telescope and Cosmic Explorer, we adopted arbitrary locations and orientations, assuming that the detectors will be built in one of the proposed sites: Sardinia (Italy) and Utah (USA), respectively. See [122] for further details on the definition of the coordinates and the orientation angles.

3.4.1 *SGWB kernel for different detector networks*

In Figure 27, we show the SGWB kernel for different binary types (BBHs, NSBHs, and BNSs) and detector networks (LVK, LVK+ET, and LVK+CE), which was computed using Equation (42). For comparison, we also show the lensing kernel, computed according to Equation (38). The lensing kernel is a broad function of redshift. It reaches its peak at around $z \simeq 2$ and gradually decreases

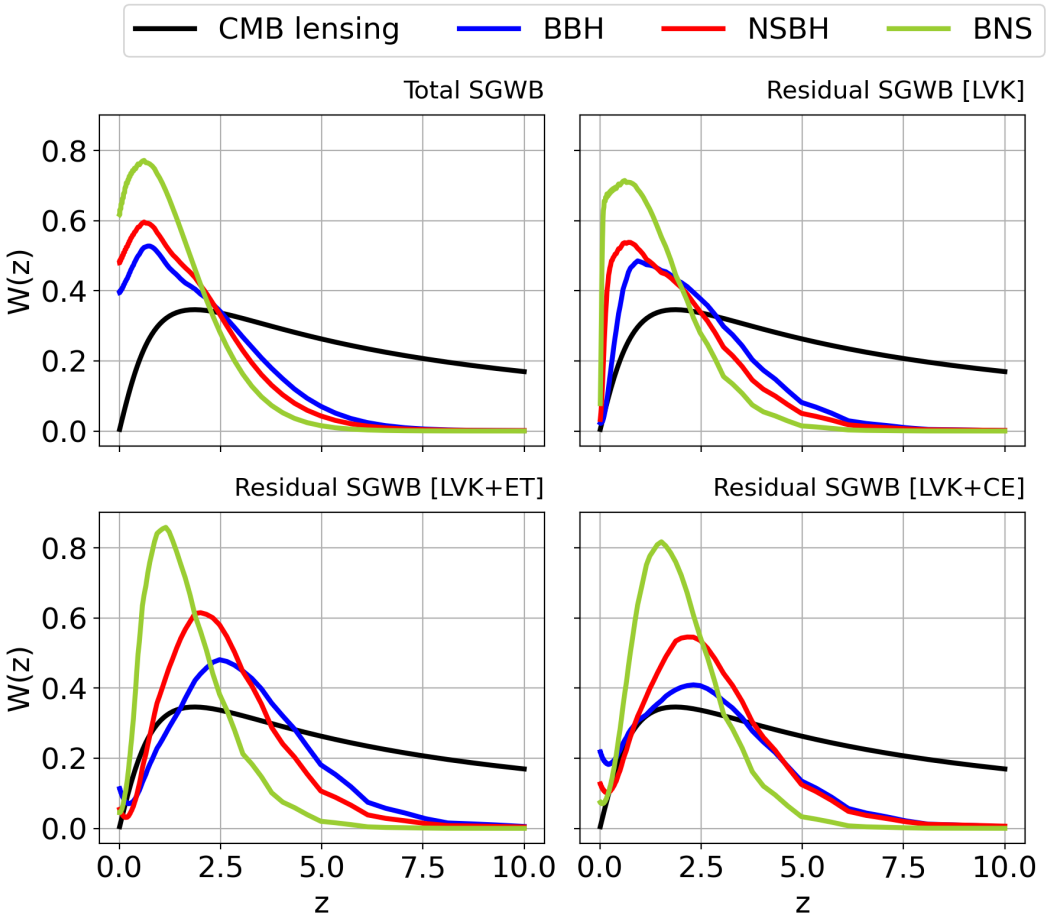

Figure 27: SGWB kernel for BBHs, NSBHs, and BNSs (in blue, red and green, respectively) at $f_{ref} = 65$ Hz. The black curve is the lensing kernel. In the upper left panel, we consider the total SGWB given by both resolved and unresolved events. In the other three panels, instead, we consider the residual SGWB for the considered detector networks (LVK, LVK+ET, and LVK+CE).

at higher redshifts, making the CMB lensing convergence a powerful probe of LSS up to the last-scattering surface. In the upper-left panel of Figure 27, we consider the total SGWB obtained by integrating all GW events, both resolved and unresolved. In this case, the SGWB kernel has a broad shape and peaks around $z \lesssim 1$ for all types of binaries. The exact position of the peak and the shape of the kernel result from the intricate interplay among three factors: the merger rate, the energy carried by each GW event, and the SGWB bias. On the one hand, the shape of the redshift distribution, $d\Omega_{gw}/dz$, reflects the fact that the merger rate peaks in conjunction with the cosmic star formation rate at around $z \simeq 2$ and then rapidly declines at higher redshifts (see Figure 19). On the other hand, closer GW events contribute more to the total energy density because their GW flux is less diluted. Moreover, the SGWB bias is an increasing function of redshift (as shown in the upper panels of Figure 20), which

means that it gives more weight to more distant objects. The kernel for BBHs is slightly broader than that for NSBHs and BNSs because BBHs have a greater chirp mass and produce more energetic GW signals, contributing significantly up to higher redshifts. In the upper-right panel of Figure 27, we show the kernels of the residual SGWB for the LVK detector network. The residual SGWB is obtained by filtering out individually resolved events. Notably, this operation removes many nearby events, giving a proportionally higher weight to more distant events. As a result, the kernels are broader and peak at slightly higher redshifts compared to the total SGWB. From the lower panels of Figure 27, it is apparent that these effects are even more pronounced when 3G detectors are involved. Both ET and the CE will be able to individually resolve most BBH mergers up to $z \simeq 10$, and most NSBH and BNS mergers up to $z \simeq 1-2$. Consequently, the kernels are significantly broader compared to previous cases and peak at higher redshifts. It is also apparent that these kernels have a more extensive overlap with the lensing kernel. As we will discuss in the following subsection, this overlap has a substantial impact on the cross-correlation results. The non-monotonic behavior characterizing the SGWB kernels at low redshifts for ET and CE is a consequence of the lensing term in Equation (42). As explained in Chapter 2, the effect of lensing is to reduce the SGWB energy density, elevating some events above the detection threshold, enabling direct resolution by the instrument. This could be the origin of the small dip at $z \simeq 0.2-0.3$.

3.4.2 *Cross-correlation angular power spectra*

In Figure 28, we show the auto- and cross-correlation power spectra for all binary types and detector networks. Although we perform the calculations in the Limber approximation, the SGWB auto-correlation power spectra are in good agreement[9] with the previous results obtained with `CLASS` [210, 211] and presented in Chapter 2. At large angular scales, most of the spectra behave as a power-law whose slope depends on the source type and detector network. For networks including ET and CE, the large-scale behavior is significantly affected by the magnification bias and the power-law is broken. As expected, the $\Omega \times \kappa$ cross-correlation power spectrum always lies between the two auto-correlation power spectra. The fact that the cross-correlation is strong is quite remarkable and constitutes one of the most important findings of this paper since it proves that the large-scale distribution of late-time objects such as merging compact binaries is well correlated with the linear structures probed by CMB lensing.

9 In this work we opted for a simpler analytic treatment with respect to the one adopted in [116], neglecting some of the relativistic effect that are instead taken into account using `CLASS` to compute the power spectra. However, we verified that the results obtained with the two pipelines are compatible within a factor of order unity, which do not affect our overall results.

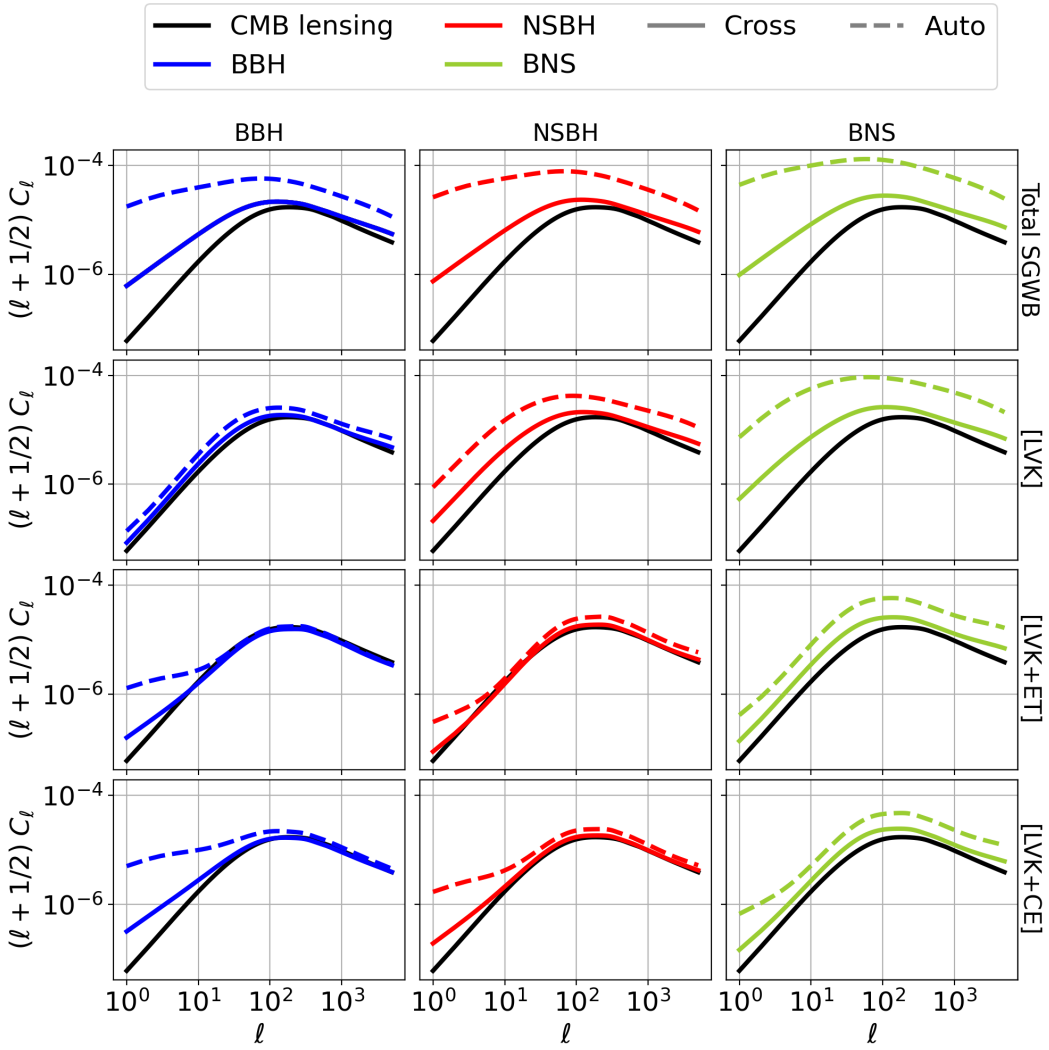

Figure 28: In each panel, we show the auto-correlation angular power spectrum of the SGWB as dashed lines and the cross-correlation angular power spectrum of $\Omega_{gw} \times \kappa$ as solid lines. The panels correspond to different sources (BBHs, NSBHs, or BNSs) and detector networks (LVK, LVK+ET, LVK+CE), as well as the detector-independent case (i.e., the total SGWB). For reference, the lensing convergence auto-correlation angular power spectrum is also plotted.

3.4.3 *Detectability with a network of 3G detectors*

The subtle SGWB anisotropies produced by the LSS, described by the power spectra in Figure 28, coexist with the much larger ones caused by the spatial and temporal discreteness of the GW sources. Indeed, the shot noise power spectrum exceeds the SGWB auto-correlation power spectrum by several orders of magnitude (see, e.g., Figure 26). The instrumental noise is an even more significant obstacle for measuring intrinsic SGWB anisotropies. For all the considered detector networks, the noise curve N_ℓ is orders of magnitude

larger than the shot noise power spectrum S_ℓ. For these reasons, as we can see in Figure 29, the S/N of the auto-correlation power spectra are far smaller than unity for all sources and detector configurations.

The cumulative S/N of the $\Omega \times \kappa$ cross-correlation, displayed in Figure 30, shows that cross-correlating with CMB lensing convergence is an effective way to mitigate the impact of instrumental and shot noise: indeed, it is around three orders of magnitude larger than the one of auto-correlation. The cross-correlation with another tracer of the same underlying dark matter distribution actually enhances the SGWB anisotropies induced by the LSS. However, the instrumental noise is too high and this substantial improvement is not sufficient to guarantee a direct detection of the cross-correlation signal.

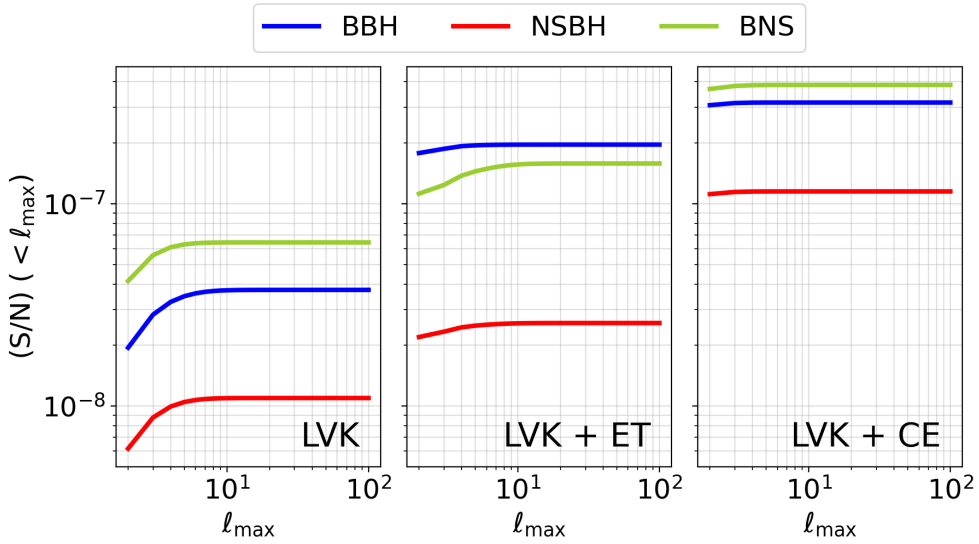

Figure 29: Cumulative S/N as a function of ℓ_{max} for the SGWB auto-correlation angular power spectrum. The curves have been evaluated summing the equation 29 from $\ell_{min} = 1$ up to ℓ_{max}.

As a final step, we try to increase as much as possible the S/N using a network with the five instruments considered in this work to detect the total SGWB. Combining the outputs of more detectors is an effective way to reduce the noise curve N_ℓ, whereas considering the total background enhances the signal because the amplitude of the monopole is higher than for the residual background. Moreover, we also explore the benefits of measuring the GW signal for a longer integration time, $T = 10$ yr. In Figure 31 we show the results of this analysis. The left panel showz the noise curves for $T = 1$ yr and $T = 10$ yr together with the shot noise and auto-correlation power spectra. The enhanced sensitivity of the extended network enables the observation of a flat shot noise power spectrum. However, the amplitude of the intrinsic anisotropies is well below the noise level, as we can see in the right panels: despite a two-orders-

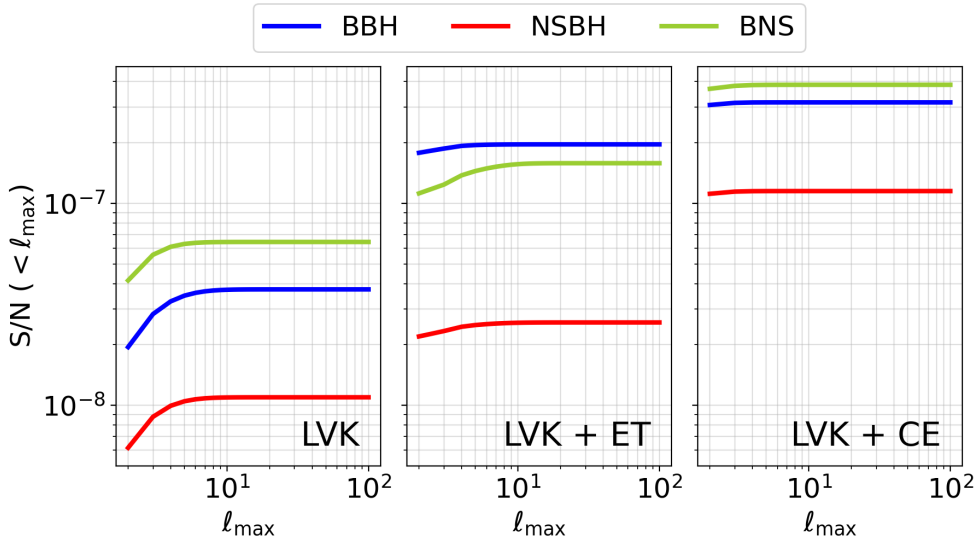

Figure 30: Cumulative S/N for $\Omega \times \kappa$ cross-correlation angular power spectrum as a function of ℓ_{max}. The curves are evaluated by means of equations 46 and 47 starting from $\ell_{min} = 1$.

of-magnitude enhancement, the cumulative S/N of the cross-correlation is still too low to allow a direct detection even for $T = 10$ yr.

3.5 DISCUSSION AND CONCLUSIONS

The anisotropies of the SGWB produced by merging binaries in galaxies hold valuable information about the physical properties of GW emitters, including their distribution in redshift and their position in the sky. However, the signal is covered under the shot noise caused by the spatial and temporal discreteness of GW emitters. Moreover, the limited angular resolution of GW interferometers is a significant obstacle to the detection of SGWB anisotropies. Recent works have already shown that cross-correlating the SGWB with other cosmological probes can effectively mitigate the impact of shot noise. In this chapter, we explored the potential of cross-correlating the SGWB with CMB lensing. We provided forecasts for the cross-correlation of upcoming high-precision measurements of the SGWB energy density and CMB lensing convergence. Our analysis specifically considered the detector network LVK at design sensitivity, the Einstein Telescope, and Cosmic Explorer, along with the Simons Observatory for CMB measurements

Starting from detailed models of stellar and galactic astrophysics, based on simulations and data-driven prescriptions, we characterized the SGWB energy density as a tracer of LSS, derived its kernel and compared it with the CMB lensing kernel. We computed the auto- and cross-correlation angular power spectra in the Limber approximation for BBHs, BNSs, and NSBHs. Notably, we found a strong correlation between the two cosmic fields for each binary type and detector network. This result is non-trivial, as it implies a meaningful

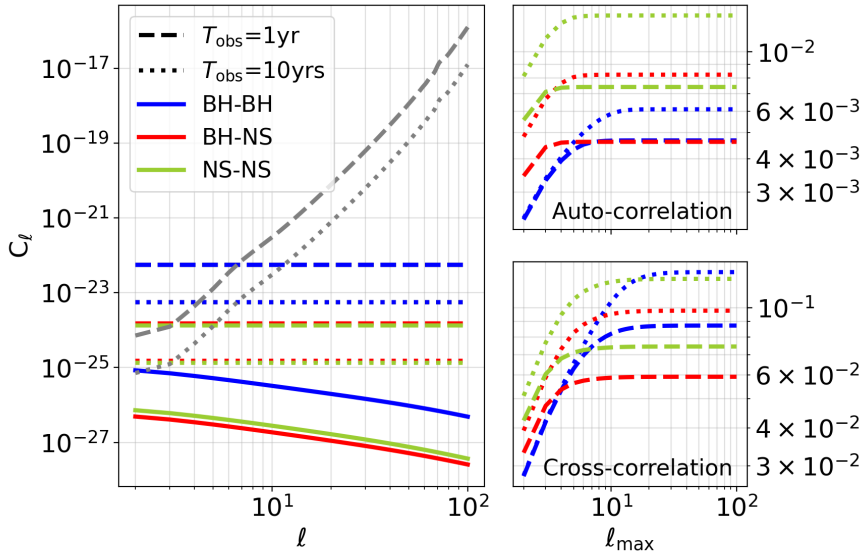

Figure 31: *Left panel*: the grey lines represent the noise curves N_ℓ for the extended network given by LIGO/Virgo/Kagra + ET + CE, for two different integration times: T = 1 yr (dashed) and T = 10 yr (dotted). The noise curves are compared with the shot noise power spectrum S_ℓ for the two different integration times and the auto-correlation power spectrum C_ℓ for the anisotropies of total SGWB. *Right panels*: auto- and cross-correlation cumulative S/N. The colour code is the same as in the previous figures.

correlation between the distribution of merging binaries, as traced by SGWB anisotropies, and the linear structures probed by CMB lensing. Finally, we computed the S/N for both the auto- and the cross-correlation power spectra. To this purpose, we used the shot noise estimation naturally provided by the novel framework for distributing GW emitters in the sky, as presented in Section 2.6. We also computed the instrumental noise using the public package `schNell` [122].

We found that the cumulative S/N for the auto-correlation is very low. This is primarily because the instrumental noise surpasses in amplitude both the signal and the shot noise by several orders of magnitude, even when considering the 3G detectors ET and CE. While cross-correlating the SGWB with CMB lensing effectively boosts the S/N by at least three orders of magnitude, this improvement is not enough to guarantee the detection of the intrinsic SGWB anisotropies induced by the LSS. On a more positive note, our findings suggest that combining all the instruments considered in this work into a single network, at the very least, help constrain the shot noise that still contains valuable information about the total number of events contributing to the signal throughout the observation time.

In conclusion, we found that cross-correlating the astrophysical SGWB with CMB lensing significantly enhances the S/N. However, our analysis has shown that instrumental noise remains a major limiting factor for the S/N of both

auto- and cross-correlation. Nonetheless, this study provides a useful framework for computing SGWB cross-correlations and estimating the associated S/N, providing valuable insights that directly impact our understanding of SGWB anisotropies generated by the LSS.

SEARCHING FOR SGWB ANISOTROPIES WITH CONSTELLATIONS OF DETECTORS

4

This Chapter is based on the following publication:

G. Capurri, A. Lapi, L. Boco, C. Baccigalupi
Searching for anisotropic stochastic gravitational-wave backgrounds with constellations of space-based interferometers
ApJ 943,72 (Feb. 2023), arXiv:2212.06162

Recent studies have shown that the angular resolution of ground-based detectors is too poor to characterize the anisotropies of the stochastic gravitational-wave background (SGWB) except from the largest angular scales. In this Chapter, we ask ourselves if a constellation of space-based instruments could be more effective for measuring the SGWB anisotropies. We consider three possible detector configurations: i) the Laser Interferometer Space Antenna (LISA), ii) a constellation of multiple LISAs in orbit around the Sun, and iii) the Decihertz Interferometer Gravitational-wave Observatory (DECIGO). We examine the SGWB generated by two astrophysical sources: stellar compact binary coalescences, and a recently proposed scenario for supermassive black-hole (SMBH) seed formation through repeated mergers of stellar remnants.

4.1 INTRODUCTION AND MOTIVATION

Measuring the anisotropies of the astrophysical SGWB faces two main challenges: the limited angular resolution of GW detectors to a diffuse SGWB mapping and the presence of shot noise. The angular resolution primarily depends on the noise properties of the detector and how they project onto the sky. It is also influenced by the configuration of the detector under consideration [122]. On the other hand, the shot noise arises because the astrophysical SGWB results from the superposition of numerous unresolved events, which are discrete in both space and time. Recent studies have addressed the issue of shot noise, revealing that its power spectrum exceeds that of the intrinsic SGWB anisotropies induced by the large-scale structure (LSS) by orders of magnitude [113–116]. To mitigate the impact of shot noise, cross-correlations with other tracers of the LSS have been proposed. Several studies have explored cross-correlations with galaxy number counts [115, 253, 254, 261] and CMB temperature fluctuations [118, 119, 272]. These studies have shown that the limited angular resolution of ground-based instruments hinders the measurement of the angular power spectrum of SGWB anisotropies beyond the first few multipoles, even if the cross-correlation with other probes alleviate the impact of instrumental and shot noise.

This led us to inquire whether a constellation of space-based detectors might be more effective in measuring the SGWB anisotropies. The large separation among the instruments forms a long interferometric baseline that should result in a sensibly improved angular resolution. Specifically, we focused on two instruments: the Laser Interferometer Space Antenna (LISA) [51, 273, 274] and the Deci-hertz Interferometer Gravitational-wave Observatory (DECIGO) [141, 275, 276]. As a case study, we explore two distinct astrophysical sources of SGWB. First, we investigate the detection prospects for the anisotropies of the SGWB generated by stellar binary coalescences [11, 12, 37, 91, 95, 96, 102–104, 106, 110–112, 116]. Additionally, we study the anisotropies of the SGWB produced by intermediate and extreme mass ratio BH binaries formed in the cores of dusty star-forming galaxies due to the migration towards the center of compact stellar remnants. This process, induced by the dynamical friction with the gaseous environment, constitutes a potential formation mechanism for SMBH seeds [277, 278].

The plan of the Chapter is the following: in Section 4.2, we describe the considered detectors, with particular interest on the computation of their angular sensitivity. In Section 4.3, we review the astrophysical processes that produce the stochastic backgrounds that we include in the analysis presented in this work. In Section 4.4, we discuss the detection prospects for the isotropic amplitude of the SGWB. In Section 4.5, we present the results for the SGWB anisotropies. In particular, we compute their amplitude and discuss their detection prospects. In Section 4.6, we show the results concerning the cross-correlation between the SGWB and the CMB lensing. Finally, in Section 4.7, we comment our results and draw our conclusions.

Throughout this work, we adopt the standard flat ΛCDM cosmology with parameter values from the Planck 2018 legacy release, with Hubble rate today corresponding to $H_0 = 67.4$ km s^{-1} Mpc^{-1}, Cold Dark Matter (CDM) and baryon abundances with respect to the critical density corresponding to $\Omega_{CDM}h^2 = 0.120$ and $\Omega_b h^2 = 0.022$, respectively, reionization optical depth $\tau = 0.054$, amplitude and spectral index of primordial scalar perturbations corresponding to $\ln(10^{10}A_S) = 3.045$ and $n_S = 0.965$, respectively [32].

4.2 DETECTOR CONSTELLATIONS

In this section, we provide a general overview of the instruments we consider in this work: the Laser Interferometer Space Antenna (LISA) and the Deci-hertz Interferometer Gravitational-wave Observatory (DECIGO). After a brief description of the main features of these detectors, we focus on a more detailed report of the specific prescriptions for the noise curves and the angular sensitivity we used for our analyses.

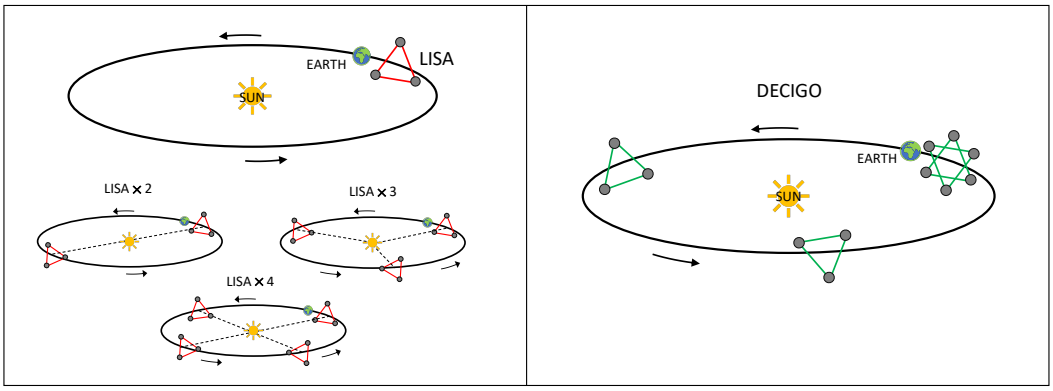

Figure 32: Cartoon representation of the proposed configurations LISA (left) and DECIGO (right), described in the text. We also show the three different constellations of multiple LISAs we use for this work.

4.2.1 *LISA*

LISA is a space-based GW observatory selected to be one of the three projects of the European Space Agency's long-term plan, addressing the scientific theme of the Gravitational Universe [51, 273, 274]. LISA will consist of three spacecraft trailing the Earth around the Sun in a triangular configuration, with a mutual separation between spacecraft pairs of about 2.5 million kilometers, as shown by the cartoon representation in the left panel of Figure 32. The laser beams that connect the three satellites combine via time-delay interferometry. Because of its long arm length, LISA will be most sensitive in the millihertz frequency regime. The proposed launch year for LISA is 2037, and the mission lifetime is four years, with a possible six-year extension. A test mission - called LISA pathfinder [139, 279] - was launched in 2015 to test the technology necessary for LISA. The goal of LISA pathfinder was to demonstrate a noise level 10 times worse than the one needed for LISA, but it exceeded this goal by a large margin, approaching the LISA requirement noise levels. The scientific goals of LISA are numerous since the instrument sensitivity window is extremely rich in GW sources. Among them, we mention: studying the formation and the evolution of compact binary stars in our galaxy; tracing the origin, growth, and merger history of massive BHs across cosmic ages; probing the dynamics of dense nuclear clusters using extreme mass ratio inspirals; understanding the astrophysics of stellar BHs; exploring the fundamental nature of gravity; measuring the rate of expansion of the Universe; understanding stochastic backgrounds and their implications for the early Universe; searching for GW bursts and unforeseen sources.

For this work, we calculate the LISA sensitivity curve using the parametric expression reported in Ref. [200], assuming the nominal mission lifetime of four years. To compute the noise angular power spectrum (N_ℓ), we use the public code `schNell` [1], developed to calculate the angular power spectrum of

1 Publicly available at https://github.com/damonge/schNell.

the instrumental noise in interferometer networks mapping the SGWB [122]. The code already contains the detector specifications to compute the angular sensitivity of LISA. We modified the code to evaluate the angular sensitivity of a network of multiple LISA-like observatories in orbit around the Sun, spaced apart at equal distances along the orbit. We show the specific configurations we consider for this work in the left panel of Figure 32. Multiple LISAs operating together as a detector network have a better angular sensitivity because of the larger interferometric baseline. Indeed, according to the Rayleigh criterion, the angular resolution of a GW detector is proportional to $\delta\theta \propto \lambda/D\rho$, where λ is the GW wavelength, ρ is its signal-to-noise ratio of the GW event, and D is the aperture of the interferometric baseline (see Ref. [280] for example). A large aperture can be synthesized by having more than one detector operating simultaneously with a separation of a significant fraction of an astronomic unit, as it is the case for the configurations shown in Figure 32. In the lower right panel of Figure 33, we plot the ratio between the N_ℓ for different constellations of LISAs and the ones for a single LISA. We find that using two LISAs improves the angular sensitivity quite remarkably, especially for the even multipoles favored by the parity of the LISA antenna pattern. The angular sensitivity improves further by adding more detectors, even though the highest contribution results from adding the second LISA. Indeed, when we pass from one to two LISAs, the effective aperture of the network increases from a few million km to around two astronomic units. Instead, the aperture remains of the same order of magnitude when we add more than two clusters around the orbit. For this reason, there is a spectacular sensitivity improvement when adding a second LISA cluster and a modest one when adding more. As a consequence, we will report only the results of the analysis with a constellation with two LISAs.

4.2.2 *DECIGO*

DECIGO is the planned Japanese space GW antenna [141, 275, 276]. It will target Gs produced by astrophysical and cosmological sources in the 0.1 - 10 Hz frequency range. In this sense, DECIGO aims to bridge the frequency gap between LISA and ground-based detectors. A key advantage of DECIGO specializing in this frequency band is that the expected confusion noise, caused by irresolvable GW signals such as the ones from galactic white dwarf binaries, is low above 0.1 Hz. Moreover, DECIGO can serve as a follow-up for LISA by observing inspiralling sources that have moved above the mHz band or as a predictor for ground-based instruments by detecting inspiralling sources that have not yet moved into the 10 Hz - kHz band. DECIGO will consist of four clusters of observatories in heliocentric orbit: two of them will be in the same position, whereas the other two will be evenly distributed around the Sun, as shown in the right panel of Figure 32. Each cluster consists of three spacecraft, which form an equilateral triangle with a side of $\sim$ 1000 km (the exact values of the parameters are still debated). Each instrument has a drag-free system and contains two mirrors floating inside the satellite as proof masses. DECIGO will

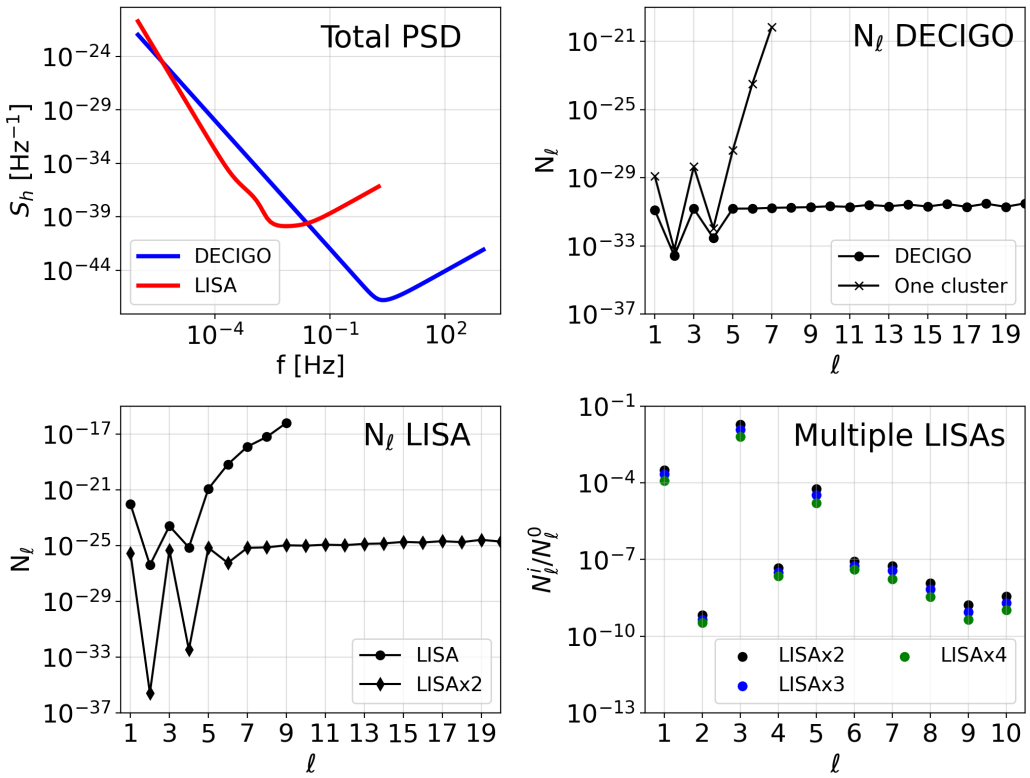

Figure 33: *Upper left*: LISA's and DECIGO's sensitivity curves expressed as total power spectral density. *Upper right*: noise angular power spectra for DECIGO (four clusters) and a single cluster. *Lower left*: noise angular power spectra for LISA and constellation of two LISAs in orbit around the Sun. *Lower right*: relative improvement of the N_ℓ of a constellation of several LISA detectors with respect to LISA's ones for the various multipoles.

measure the change in the distance caused by a passage of a GW between the two mirrors by employing a Fabry–Pérot cavity. Once launched, the mission lifetime of DECIGO will be at least three years. Before that, the DECIGO working group plans to launch the scientific pathfinder B-DECIGO in the 2030s to demonstrate the technologies required for DECIGO. The most relevant goal for DECIGO is to detect primordial GWs. However, there are many other scientific targets, such as probing the acceleration and expansion of the Universe, testing the accuracy of general relativity, examining the symmetry between the two polarizations of GWs, and determining to which extent primordial BHs contribute to dark matter [281]. Finally, DECIGO could reveal the formation mechanism of SMBHs in the center of distant galaxies by detecting GWs coming from entreme/intermediate mass ratio BH binaries. Of course, the present work has relevance concerning this latter scientific objective. For more information about DECIGO's scientific targets, we remand the interested reader to Ref. [141].

For this work, we compute DECIGO's sensitivity curve, including radiation pressure noise, shot noise, internal thermal noise, and gas thermal noise, fol-

lowing the prescriptions discussed in Refs. [282, 283]. In particular, we employ the detector parameters[2] presented in Ref. [283]. For the angular sensitivity, instead, we modified the public code `schNell` to compute the angular power spectrum of the instrumental noise. Specifically, we included an additional class of objects apt to describe a single DECIGO cluster. We then obtained the complete detector as a network of four clusters oriented and positioned around the orbit as depicted in the right panel of Figure 32. In the upper right panel of Figure 33, we show the noise angular power spectrum for a single DECIGO cluster and the complete DECIGO configuration (four clusters).

4.3 SGWB SOURCES

We choose two astrophysical GW sources as our case studies. First, we consider the SGWB produced by stellar binary coalescences, specifically binary black holes (BBH) and neutron stars (BNS). As we will see in more detail in Section 4.4, these sources emit GWs in a broad frequency band. Even if the bulk of the signal resides in the Hz-kHz range, we expect the SGWB produced by merging compact binaries to constitute one of the most relevant components also in the deci-Hz band. Second, we choose the SGWB produced during one of the possible formation processes for SMBH seeds. This particular scenario envisages multiple mergers of stellar remnants that sink toward the galactic center dragged by gaseous dynamical friction. Since the chirp mass and the mass ratio of the binaries involved in this scenario span a broad range of values, the SGWB frequency spectrum is very extended and includes the sensitivity bands of both LISA and DECIGO.

4.3.1 *Coalescing stellar compact binaries*

We characterize the population of coalescing stellar binaries and compute their merger rates following the approach presented in Refs. [76, 77]. There, the authors combine the results of stellar population synthesis codes with different observationally derived prescriptions for the host galaxies. For our analysis, we adopt the merger rates computed using the empirical Star Formation Rate Function as galaxy statistics and the Fundamental Metallicity Relation to assign metallicity to galaxies, combined with the results of the `StarTrack` simulations[3], specifically the 'reference' model in [214, 215] (see Figure 8 of Ref. [77]). This state-of-the-art method to compute the merger rates presents a twofold benefit. On the one hand, the galactic part is entirely observational-based, not relying on the results of any cosmological simulation or semi-analytic framework. On the other hand, since it uses the Star Formation Rate Function as galaxy statistics, one can assess the contribution of galaxies with different properties to the overall merger rate. Indeed, such empirical approaches also have

2 Notice that the values of those parameters are not definitive and are still to be confirmed by the DECIGO working group.

3 Simulation data publicly available at https://www.syntheticuniverse.org/

their downsides. Mainly, the observational uncertainties affect all the final predictions, especially at high redshift. The resulting merger rates are in good agreement with the recent local determination by the LVK collaboration, as shown in Refs. [77, 116]. The redshift distribution of the merger rates highly depends on the star formation history of the host galaxies. Most of the BBH events come from $z \sim 2-3$, whereas most of the BNS ones come from slightly lower redshifts, $z \lesssim 2$. The chirp mass dependence, instead, is mainly determined by the stellar prescriptions and the derived binary mass function, which is largely uncertain in the high-mass regime, where different formation channels may enter into play, complicating the evolutionary scenario (see Ref. [236] for an example). All in all, the particular features of the merger rates strongly depend on the adopted astrophysical prescriptions: we refer the interested reader to Ref. [77] for a more in-depth treatment. The overall normalization of the merger rates results from many different and complex physical processes related to stellar evolution that, in principle, could depend on the binary type (binary fraction, common envelope development/survival, natal kicks, mass transfers, etc.). In order to reduce the impact of the uncertainties in the astrophysical modeling, we decide to re-scale all the merger rates per unit comoving volume to match the values measured by LIGO and Virgo as reported in [9]: $17.9-44\,\mathrm{Gpc^{-3}\,yr^{-1}}$ at $z=0.2$ for BBHs, and $10-1700\,\mathrm{Gpc^{-3}\,yr^{-1}}$ at $z=0$ for BNSs, where the intervals are a union of 90 % credible intervals for the different methods used in the paper. Specifically, we calculate the logarithmic mean of the 90 % intervals and normalize our merger rates to retrieve those values at $z=0.2$ for BBHs and $z=0$ for BNSs. In this way, we maintain the redshift and chirp mass dependencies that we obtain with the methods described above but re-scale all the results to match the measured local values. Indeed, such a normalization directly affects all the results presented in this paper. Nonetheless, we stress that the local values of the merger rates we get with our calculations are inside the error bars of the LVK estimates, as it is shown in Figure 16.

4.3.2 *SMBH seeds formation process*

The recent observations of high redshift quasars ($z \gtrsim 7$) powered by SMBHs with $M > 10^9 M_\odot$ have created tension between the estimated age of the Universe at those redshifts and the typical timescales of SMBH growth [284–287]. Indeed, at $z \gtrsim 7$, the age of the Universe was shorter than $\lesssim 0.8$ Gyr, whereas the accretion timescale driven by the gas disk (Eddington-like) is $\gtrsim 0.75$ Gyr. There are two classes of possible solutions to relieve this tension. The first way out invokes super-Eddington accretion rates, whereas the second involves mechanisms able to rapidly produce heavier BH seeds ($M \gtrsim 10^3 - 10^5 M_\odot$), reducing the time required to attain the final billion solar masses by standard Eddington accretion. In Refs. [277, 278], the authors submit a new scenario to form heavy BH seeds, alternative or at least complementary to the other mechanisms. Specifically, they propose that BH seeds grow in the inner, gas-rich regions of dusty star-forming galaxies via multiple mergers with stellar com-

pact remnants that migrate toward the center because of gaseous dynamical friction. Indeed, the dynamical drag subtracts energy and angular momentum from the moving object, making it sink toward the galactic center. The process is particularly efficient in dusty star-forming galaxies because they feature high star formation rates and huge molecular gas reservoirs concentrated in a compact region of a few kiloparsecs. These conditions foster the efficient sinking of numerous compact remnants toward the galactic nucleus via gaseous dynamical friction. In Ref. [277], the authors show that this mechanism can grow heavy BH seeds of masses $10^4 - 10^6 M_\odot$ within some 10^7 yr, so possibly alleviating the problem of SMBH formation at high redshift. With an accurate modeling of the gas distribution and the dynamical friction force, the authors of Ref. [277] derive a fitting formula for the dynamical friction timescale. Consequently, they exploit the expression for the dynamical friction timescale to compute the merging rate of compact remnants at different galactic ages, so evaluating the contribution of this process to the growth of the central SMBH seed. A more detailed description of this accretion mechanism can be found in Appendix C. Of course, the repeated mergers of stellar BHs with the central growing seed would produce GW emission, whose detection could be a smoking gun test for this scenario. In particular, the superposition of the unresolved GW events constitutes an SGWB that extends over a wide range of frequencies, as we will see in the following.

4.4 DETECTION PROSPECTS FOR THE MONOPOLE

Stochastic gravitational-wave backgrounds are usually described through their energy density parameter $\Omega_{gw}(f, \hat{n})$. We have already derived and discussed the expression of the isotropic component ($\Omega_{gw}(f) = 4\pi\overline{\Omega}_{gw}(f)$, aka the monolope), in Sections 1.2.3 and 2.3.1. In Chapter 2, we described the emitting binaries through their chirp mass, without considering other binary parameters like the mass ratio or the spin. This approximation was reasonable because the chirp mass is the parameter that most significantly influences the features of the SGWB. Moreover, the stellar binaries observed by LIGO and Virgo typically have a mass ratio close to one. However, for the binaries involved in the formation of SMBH seeds, this approximation is no longer valid, as the mass ratio could assume significantly small values. Therefore, it becomes necessary to incorporate the mass ratio into the expression of $\Omega_{gw}(f)$, which now appears as follows:

$$\Omega_{gw}(f) = \frac{8\pi G f}{3H_0^3 c^2} \int dz \frac{1}{(1+z)h(z)} \int d\mathcal{M}_c \, \frac{d^2\dot{N}}{dV d\mathcal{M}_c} \times \\ \times \int dq \, \frac{dp}{dq}(q|\mathcal{M}_c, z) \frac{dE}{df}(f_e(f,z)|\mathcal{M}_c, q), \tag{52}$$

where $\mathcal{M}_c$ is the chirp mass, $f_e = (1+z)f$ is the source frequency, $d^2\dot{N}/dVd\mathcal{M}_c$ is the intrinsic merger rate per unit comoving volume and chirp mass, $h(z) =$

$[\Omega_M(1+z)^3+1-\Omega_M]^{1/2}$, and $dE/df(f_e(z)|\mathcal{M}_c, q)$ is the energy spectrum of the signal emitted by a single binary [239]. With the previous expression, we can evaluate the intensity of the total SGWB, given by the superposition of all the events, resolved and unresolved. It is also possible to compute the residual SGWB by subtracting the contributions of GW signals that lie above the detection threshold. The residual SGWB has a different frequency dependence and a globally lower amplitude (see Ref. [116] for coalescing stellar binaries and Ref. [278] for SMBH seeds formation). In this work, however, we focus on the total SGWB since it has a higher amplitude and is more likely to be detected.

In Figure 34, we plot the isotropic energy density parameter of the two astrophysical SGWBs analyzed in this paper as a function of the observed frequency. The blue and green curves represent the monopole for merging BBHs and BNSs, respectively. At lower frequencies, as expected, the GWs emitted during the inspiral phase dominate the signal, and the energy density parameter behaves as a power-law $\propto f^{2/3}$. At higher frequencies, the contribution from the merger phase becomes more and more relevant. After peaking at $f \sim 10^2 - 10^3$ Hz, the curves undergo an exponential drop related to the suppression of GW emission after the ringdown. The SGWB produced by coalescing stellar binaries has the largest amplitude in the frequency band of ground-based detectors. This signal will probably be observed for the first time at those frequencies, where it constitutes the dominant contribution to the total SGWB given by all possible sources. Still, the SGWB produced by coalescing stellar binaries also has great relevance for the space-based interferometers that operate at lower frequencies. The dashed and dotted grey curves in Figure 34 represent the power-law integrated sensitivity curves (PLS) for LISA and DECIGO, respectively. The PLS is a graphic representation of the detector sensitivity for SGWBs that considers the increase in sensitivity that comes from integrating over frequency other than time [174]. This representation is strictly valid for SGWBs characterized by a power-law frequency dependence in the sensitivity band of the detectors, but it is usually employed to assess the ability of an instrument to measure a SGWB. Specifically, an SGWB whose energy density parameter is tangent to the PLS has a signal-to-noise ratio equal to one. It follows that LISA can marginally detect the monopole of the SGWB produced by coalescing stellar binaries, whereas DECIGO can measure it with very high significance. The black curve in Figure 34 represents the frequency spectrum of the SGWB amplitude for the SMBH seeds formation process. The signal extends over a broad range of frequencies, including the sensitivity bands of both LISA and DECIGO. This is because the chirp masses of the involved binaries can have very different values. Indeed, at the beginning of the process, the central object is still very light, and the chirp mass has 'stellar' values. As the central BH grows, the chirp mass increases and reaches values up to 10^6 solar masses. High-mass mergers are more numerous and populate the low-frequency regime, whereas low-mass ones contribute at higher frequencies. In particular, the SGWB amplitude peaks around $10^{-6} - 10^{-5}$ Hz, where there

is a lack of planned GW detectors[4]. However, the amplitude remains more or less flat up to 10^{-1} Hz before experiencing a gradual decrease followed by an exponential drop at $f \gtrsim 10^3$ Hz, which corresponds to the lower possible chirp masses involved in the process. Comparing the SGWB monopole amplitude with the PLSs, it follows that both LISA and DECIGO should be able to measure it with high significance. Because of its remarkable intensity in a frequency band where other SGWBs are less relevant, this signal - if detected - could be a smoking-gun probe of its origin process.

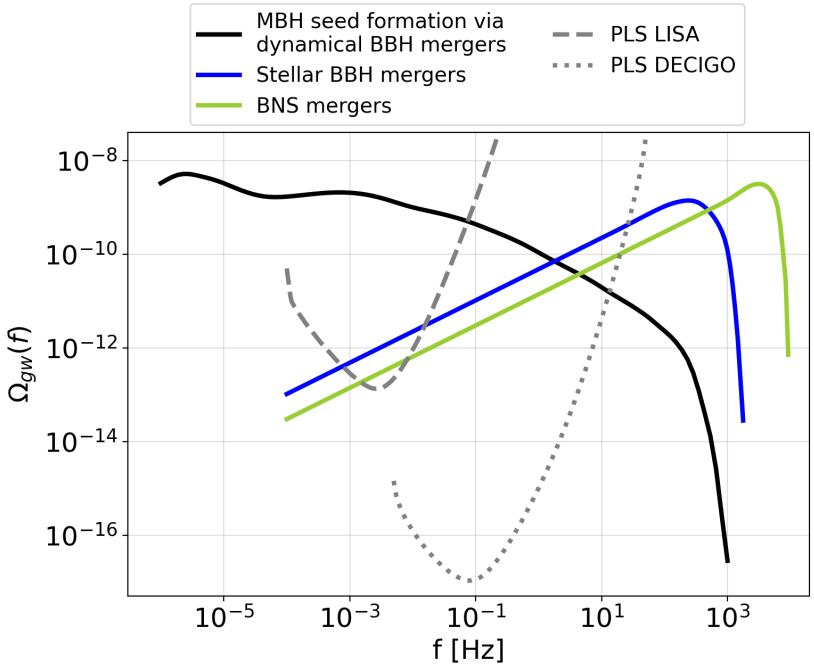

Figure 34: SGWB energy density for the SMBH seed formation process (black), stellar BBHs (blue) and BNSs (green). The grey lines represent the PLS curves for LISA (dashed) and DECIGO (dotted), computed assuming total observing times of four and three years, respectively.

4.5 DETECTION PROSPECTS FOR ANISOTROPIES

In this work, we calculate the angular power spectrum of the SGWB anisotropies according to the framework presented in Chapter 3, which we briefly sketch hereafter (see also Chapter 3). Assuming that the SGWB is a biased tracer of the underlying dark matter distribution, we can express the energy density

4 Actually, Refs. [288, 289] show that the μHz gap could be filled by searching for deviations in the orbits of stellar and planetary binary systems caused by their resonant interaction with GWs.

contrast $\delta_{gw} = \delta\Omega_{gw}/\overline{\Omega}_{gw}$ as a line-of-sight integral of the dark matter density contrast $\delta(r(z)\hat{\mathbf{n}}, z)$:

$$\delta_{gw}(f, \hat{\mathbf{n}}) = \int_0^{z_\star} dz\, W^{\Omega}(f, z)\delta(r(z)\hat{\mathbf{n}}, z), \tag{53}$$

where $r(z)$ is the comoving distance to redshift z and $z_\star \approx 1090$ is redshift at the last-scattering surface. The kernel $W^{\Omega}(f, z)$ is the sum of two terms:

$$W^{\Omega}(f, z) = \frac{b_{\Omega}(f, z)\frac{d\Omega_{gw}}{dz}(f, z)}{\left(\int dz' \frac{d\Omega_{gw}}{dz'}\right)} + \mu(f, z). \tag{54}$$

The first term is the product of the linear bias b_{Ω}, which quantifies the mismatch between the distribution of the SGWB and the total matter density, and the SGWB redshift distribution $d\Omega_{gw}/dz$. We compute b_{Ω} and $d\Omega_{gw}/dz$ as discussed in Section 2.4. The second term accounts for the effect of weak gravitational lensing on the observed SGWB energy density. In this work, however, we consider only the total background that does not perceive any net impact from the weak lensing because its two effects - growth of energy density due to magnification and dilution of flux - balance each other in the absence of a detection threshold [110, 116]. For this reason, we will neglect the lensing term μ from now on. The left panels of Figures 35 and 36 show the kernel of the SGWB produced by the SMBH seed formation mechanism and coalescing stellar binaries, respectively, evaluated at various frequencies of interest. Even though the two processes are different and produce different SGWB signals (see Figure 34), the kernels look similar because both the processes produce more GW events in concurrence with the peak of the cosmic star formation rate at $z \sim 2$. At higher redshifts, the kernels rapidly decrease because stellar remnants, which populate both kind of binaries, are less and less numerous. Since the kernel W_{Ω} is a broad function of redshift for both the SGWB sources we consider for this work, we compute the angular power spectrum using the Limber approximation [270] in the following way:

$$C_{\ell}^{\Omega} = \int_0^{z_\star} \frac{dz}{c}\frac{H(z)}{r^2(z)}\left[W^{\Omega}(z)\right]^2 P\left(k = \frac{l}{r(z)}, z\right), \tag{55}$$

where c is the speed of light and $P(k, z)$ is the matter power spectrum, which we computed using the `CLASS`[5] public code [210, 211]. We account for the non-linear evolution of the matter power spectrum by using the `HALOFIT` prescription [271]. The right panels of Figures 35 and 36 show the angular power spectrum of the anisotropies for the SGWB produced by the two processes. We evaluate the power spectra (and the kernels) at the frequencies $f = 1$ mHz and $f = 0.1$ Hz, optimal for a survey with LISA and DECIGO, and at the frequency

5 The Cosmic Linear Anisotropy Solving System, available at `http://class-code.net`

where the two processes produce the signal with the largest amplitude. For SMBH seed formation, this frequency is $f = 5 \times 10^{-6}$ Hz, whereas for merging compact binaries, we use $f = 65$ Hz.

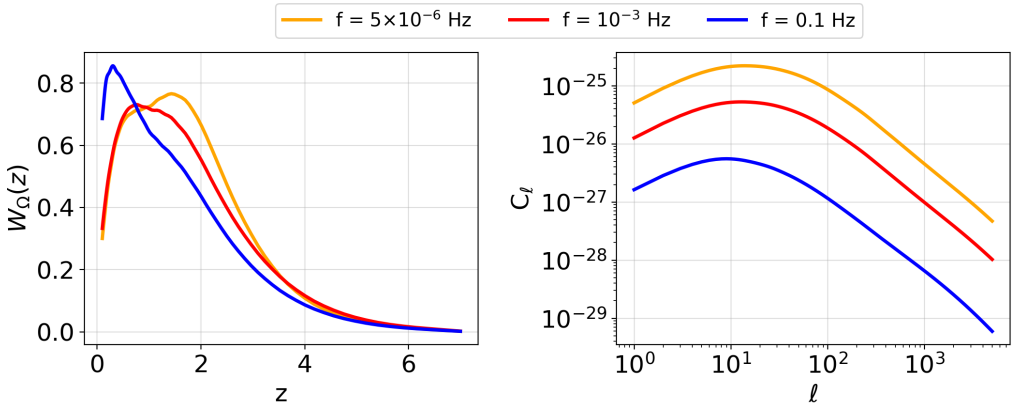

Figure 35: *Left panel*: Kernel of the SGWB produced by the SMBH seed formation process evaluated at three frequencies of interest. *Right panel*: Angular power spectrum of the anisotropies of the SGWB produced by the same process.

Assuming that the SGWB behaves as a Gaussian random field, the signal-to-noise ratio (S/N) of the C_ℓ^Ω is given by:

$$\left(\frac{S}{N}\right)^2_\ell = \frac{(2\ell+1)}{2} \frac{\left(C_\ell^\Omega\right)^2}{\left(C_\ell^\Omega + S_\ell^\Omega + N_\ell^\Omega\right)^2}, \tag{56}$$

where S_ℓ^Ω and N_ℓ^Ω are the shot noise and the instrumental noise, respectively. We evaluate the shot noise by exploiting the map-making technique discussed in Chapter 2, which includes both Poisson statistics and clustering properties. For the instrumental noise, instead, we use the prescriptions described in Section 4.2. All in all, the three main ingredients for the computation of the S/N are the angular power spectrum of the SGWB anisotropies C_ℓ (aka the signal), the shot noise S_ℓ and the instrumental noise N_ℓ. To visually compare the contributions of signal, shot noise and instrumental noise, in the left panels of Figures 37 and 38, we plot these quantities at the various multipoles for our two sources (coalescing stellar binaries and SMBH seeds formation) and for the three considered detector configurations (LISA, constellation of two LISAs and DECIGO). Throughout this work, we will assess the potential detectability of the various signals by using the cumulative S/N for multipoles up to ℓ_{max}, which is given by:

$$\left(\frac{S}{N}\right)(\ell < \ell_{max}) = \sqrt{\sum_{\ell=\ell_{min}}^{\ell_{max}} \left(\frac{S}{N}\right)^2_\ell}. \tag{57}$$

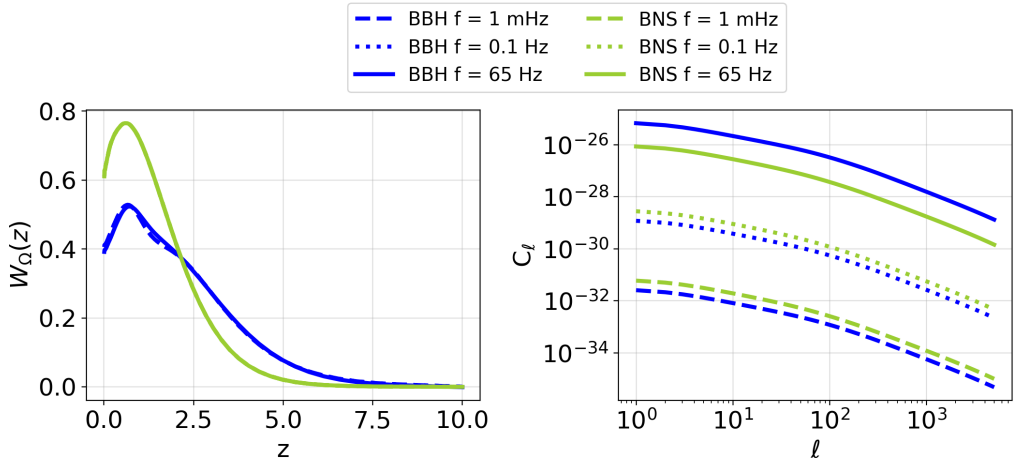

Figure 36: *Left panel*: Kernel of the SGWB produced by stellar BBHs (blue) and BNSs (green) evaluated at three frequencies of interest. *Right panel*: Angular power spectrum of the anisotropies of the SGWB produced by coalescing compact binaries.

We show the cumulative S/N for the various considered cases in the right panels of Figures 37 and 38. For the SGWB produced during the formation of SMBH seeds, it turns out that the auto-correlation of the anisotropies is not detectable in both LISA's and DECIGO's frequency bands. Around $f = 1$ mHz, both the shot noise and the LISA instrumental noise are too high compared to the angular power spectrum of the anisotropies, even if we consider the optimistic scenario of two LISAs operating for ten years. At DECIGO's frequencies, instead, the signal is higher than the instrumental noise, but the shot noise constitutes a killing factor for the overall S/N. Such a high shot noise depends on the small number of merger events contributing at $f = 0.1$ Hz. Indeed, the merger events that contribute to those high frequencies have a relatively low chirp mass ($\mathcal{M}_c \lesssim 10^3 M_\odot$) and are a tiny fraction of the total (see Figure 3 in Ref. [278]). The results for the SGWB produced by coalescing stellar binaries are only slightly better. A general comment is that the anisotropies of the SGWB produced by BBHs are more intense than the ones for BNSs because the overall amplitude of the SGWB is higher. Nevertheless, the shot noise is sensibly lower for BNSs than for BBHS since the BNS merger rate is around two orders of magnitude higher (see Section 2.2). Consequently, a detector will measure much more BNSs mergers during a given observation time, leading to a lower shot noise. All in all, the S/N for BNSs is higher than the S/N for BBHs. As we already commented in Section 4.4, in both LISA's and DECIGO's frequency range, the SGWB produced by merging binaries has a power-law behavior $\propto f^{2/3}$. Therefore, at $f = 1$ mHz, the signal is too low to be detected even by two LISAs. Instead, at $f = 0.1$ Hz, the SGWB is slightly more intense: this, together with the incredibly low DECIGO's instrumental noise, causes the S/N to be higher. In particular, for an observation time $T = 10$ yr, the S/N for BNSs reaches the threshold value of one for $\ell_{max} \sim 10$.

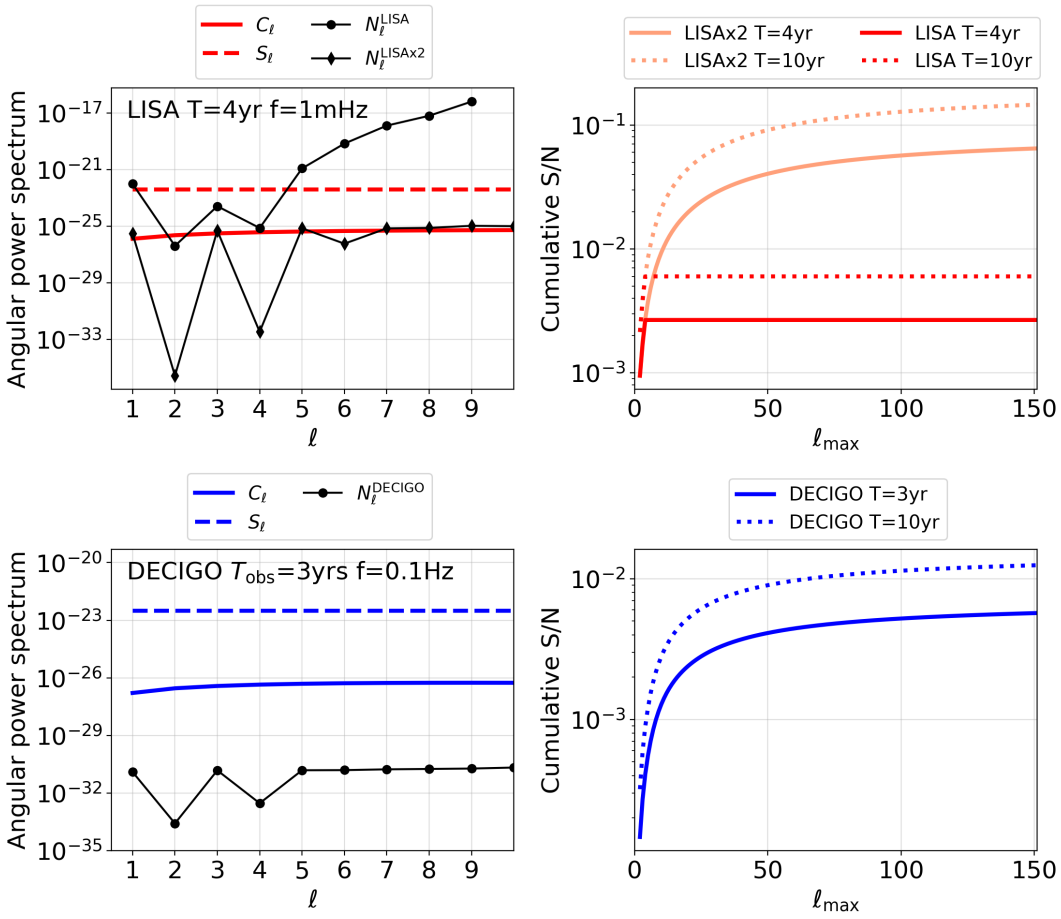

Figure 37: Results for the auto-correlation of the SGWB produced through the SMBH seed formation process. *Upper left*: Angular power spectrum of the SGWB anisotropies, shot noise, and instrumental noise for an observation time T=4 yr with LISA (or a constellation of two LISAs) at f=1 mHz. *Upper right*: Signal-to-noise ratio for the nominal LISA lifetime of four years (solid) and for an extended observation time of ten years (dashed). We show the results for LISA alone (red) and for two LISAs (orange). *Lower left*: Angular power spectrum of the SGWB anisotropies, shot noise, and instrumental noise for an observation time T=3 yr with DECIGO at f=0.1 Hz. *Lower right*: Cumulative signal-to-noise ratio for the nominal DECIGO lifetime for three years (solid) and for an extended observation time of ten years (dashed).

4.6 CROSS-CORRELATION WITH CMB LENSING

The take-home message from the previous Section is that a measurement of the SGWB anisotropies is very challenging even with a constellation of space-based interferometers. The combined effects of instrumental and shot noise make the task extremely arduous, even with a long observation time. As already suggested in many works, a possible way to enhance the intrinsic SGWB anisotropies is the cross-correlation with another tracer of the LSS. Previous works discuss the benefits of cross-correlating the astrophysical SGWB with galaxy number counts [115, 253, 254, 261], weak lensing [102, 104], and CMB

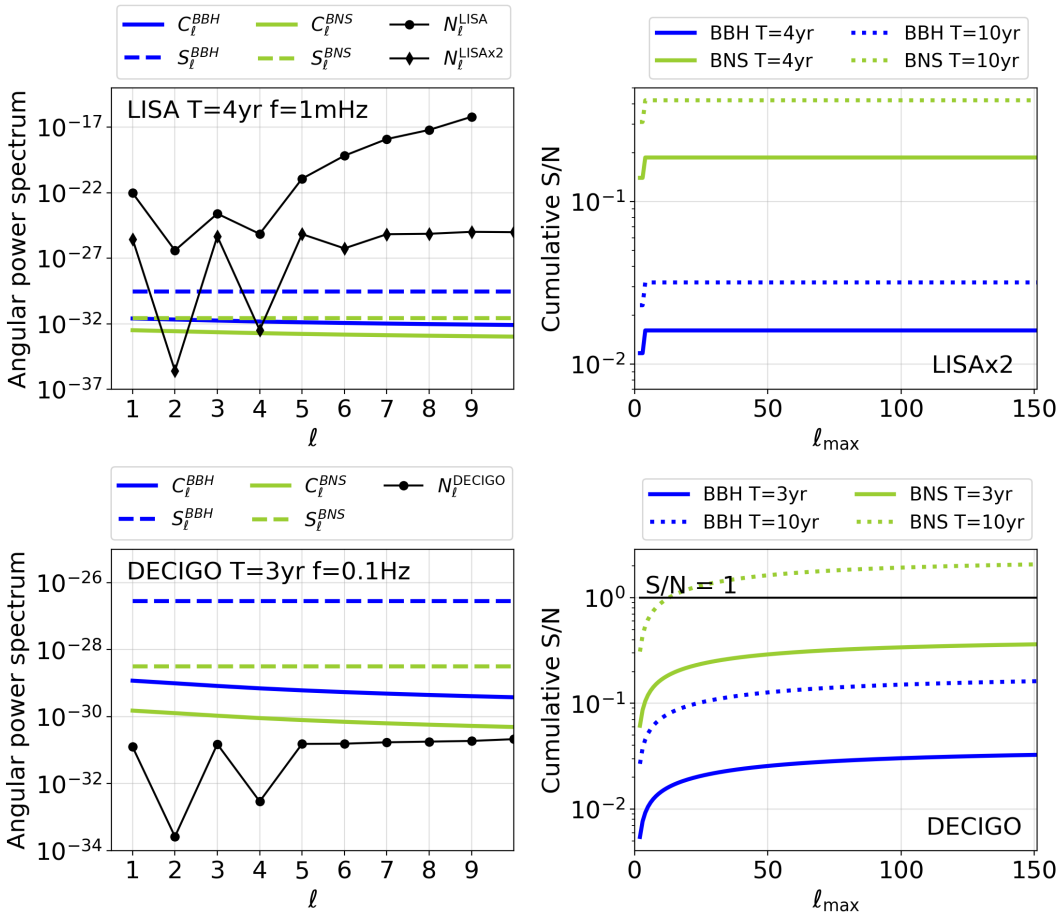

Figure 38: Results for the auto-correlation of the SGWB produced by coalescing stellar binaries, specifically BBHs (blue) and BNSs (green). *Upper left*: Angular power spectrum of the SGWB anisotropies, shot noise, and instrumental noise for T=4 yr with LISA (or a constellation of two LISAs) at f=1 mHz. *Upper right*: Signal-to-noise ratio for the nominal LISA lifetime of four years (solid) and for an extended observation time T=10 yr (dashed). We only show the results for a constellation composed of two LISAs. *Lower left*: Angular power spectrum of the SGWB anisotropies, shot noise, and instrumental noise for an observation time of T=3 yr with DECIGO at f = 0.1 Hz. *Lower right*: Cumulative signal-to-noise ratio for the nominal DECIGO lifetime of three years (solid) and for an extended observation time of ten years (dashed).

temperature and polarization fluctuations [118, 119, 272]. Here, we re-propose the cross-correlation with the CMB lensing convergence. We characterize CMB lensing as a tracer of the LSS following the approach presented in Chapter 3, which - in turn - is inspired to Refs. [266, 267]. The CMB lensing convergence κ is defined as the laplacian of the lensing potential ϕ, and we can express it as a weighted integral over redshift of the projected dark matter density contrast δ:

$$\kappa(\hat{\mathbf{n}}) = -\frac{1}{2}\nabla^2\phi(\hat{\mathbf{n}}) = \int_0^{z_*} dz\, W^{\kappa}(z)\delta(r(z)\hat{\mathbf{n}}, z), \tag{58}$$

where $r(z)$ is the comoving distance to redshift z, and $z_\star = 1090$ is the redshift at the last-scattering surface. The weight inside the integral is the lensing kernel W^{κ}, which describes the lensing efficiency of the matter distribution and is given by

$$W^{\kappa}(z) = \frac{3\Omega_m}{2c}\frac{H_0^2}{H(z)}(1+z)r(z)\frac{r_* - r(z)}{r_\star}, \tag{59}$$

where $r_\star$ is the comoving distance to the last-scattering surface and Ω_m and H_0 are the present-day value of the matter density and the Hubble parameter, respectively. Similarly to what we did for the auto-correlation, we compute the angular power spectrum of the cross-correlation as:

$$C_\ell^{\kappa\Omega} = \int_0^{z_\star} \frac{dz}{c}\frac{H(z)}{r^2(z)} W^{\kappa}(z) W^{\Omega}(z)\, P\left(k = \frac{l}{r(z)}, z\right). \tag{60}$$

Assuming that also the CMB lensing is a Gaussian field, the S/N of the cross-correlation is given by:

$$\left(\frac{S}{N}\right)^2_\ell = \frac{(2\ell+1) f_{sky}\left(C_\ell^{\kappa\Omega}\right)^2}{\left(C_\ell^{\kappa\Omega}\right)^2 + \left(C_\ell^{\kappa} + N_\ell^{\kappa}\right)\left(C_\ell^{\Omega} + S_\ell^{\Omega} + N_\ell^{\Omega}\right)}. \tag{61}$$

In the previous expression, f_{sky} is the sky fraction covered by both the SGWB and the CMB surveys, C_ℓ^{κ} is the auto-correlation angular power spectrum of the CMB lensing convergence and N_ℓ is the lensing noise. Notice that in the lensing-related terms in the denominator (aka the cross-correlation and the lensing convergence auto-correlation), we have only the contribution from cosmic variance since the shot noise is absent when considering a diffuse field such as the lensing convergence. For our analysis, we employ the lensing noise curves for CMB-S4 [290, 291] and the Simons Observatory (SO) [57]. For both surveys, we adopt the Large Aperture Telescope configuration sky fraction $f_{sky}^{\kappa} = 0.4$. Since GW experiments cover the entire sky (i.e. $f_{sky}^{\Omega} = 1$), we use the limiting value $f_{sky} = f_{sky}^{\kappa}$ for the cross-correlation. In the following, we will show only the results for CMB-S4 for a matter of simplicity. Indeed, it has lower noise, and the final S/N does not strongly depend on the adopted lensing noise curve. Moreover, the Simons Observatory will be active in a few years, while CMB-S4 is likely to be more contemporary to the GW detectors we are considering for this work.

In Figure 39, we show the S/N of the cross-correlation angular power spectrum for the SGWB produced during the formation of SMBH seeds. As discussed in the previous Section, the shot noise in the DECIGO band is too high

and compromises the S/N even if we cross-correlate the SGWB with CMB lensing. In the mHz band, instead, the situation is more promising. As expected, LISA alone is not able to resolve the signal, but with a constellation of two LISAs[6], the cross-correlation S/N reaches unity at $\ell_{max} \sim 50$ for $T = 4$ yr and at $\ell_{max} \sim 30$ for $T = 10$ yr. In principle, this means that one should be able to probe the signal by summing the contributions from enough multipoles. However, we still don't know if the large noise contributions will allow us to obtain the C_ℓ from the raw maps up to such high ℓ_{max}. In Figure 40, we show the results for the cross-correlation between the CMB lensing convergence and the SGWB produced by coalescing stellar binaries. In the LISA band, the SGWB amplitude is too low to access the signal, even with the help of cross-correlations. In the DECIGO band, instead, there are more chances to measure the cross-correlation signal. For the nominal mission lifetime of $T = 3$ yr, the S/N reaches unity at $\ell_{max} \sim 20$ for BNSs, while it always stays below one for BBHs. However, if we consider a longer observation time $T = 10$ yr, the S/N will reach unity at $\ell_{max} \lesssim 10$ for BNSs and $\ell_{max} \lesssim 40$ for BBHs.

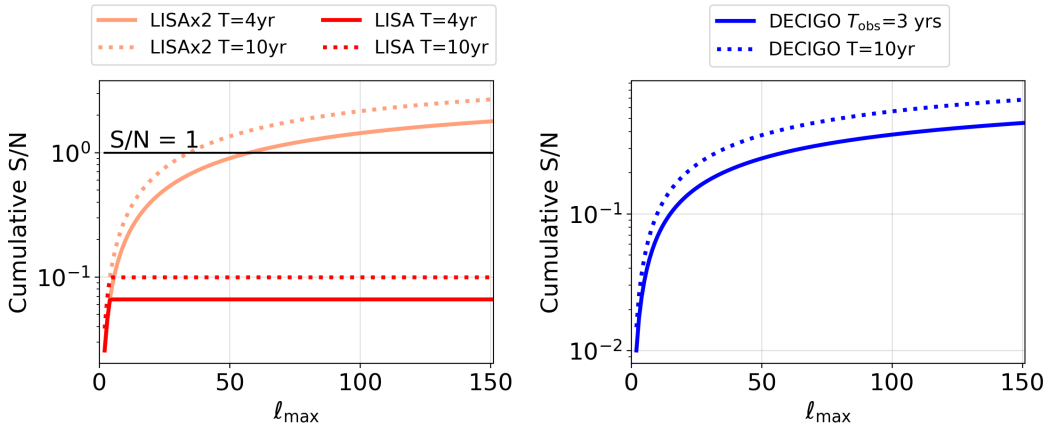

Figure 39: Cumulative S/N of the cross-correlation between the SGWB produced by SMBH seed formation process and the CMB lensing convergence, measured with CMB-S4. *Left panel*: S/N with LISA (red) and a constellation of two LISAs (orange) observing for four (solid) and ten (dotted) years. The black line corresponds to S/N = 1. *Right panel*: S/N for DECIGO observing for three (solid) and ten (dotted) years.

6 We performed the analysis also for the constellations of three and four LISAs depicted in Figure 32. The results improve only slightly (less than 1%) with respect to the configuration with two LISAs. Indeed, the N_ℓ are only a few times lower (see Figure 33) and, in any case, smaller than the C_ℓ and S_ℓ evaluated at the multipoles that contribute most to the S/N ($\ell = 2$ and $\ell = 4$, see the left panels of Figures 37 and 38).

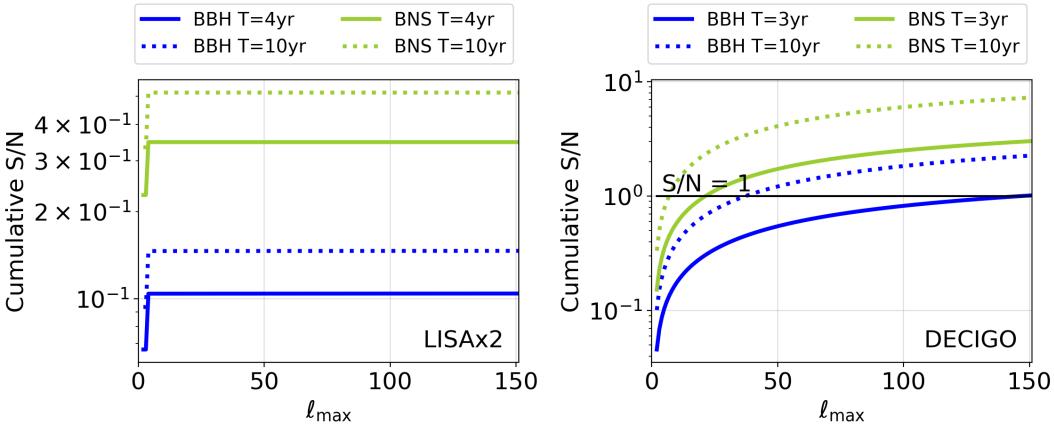

Figure 40: Cumulative S/N of the cross-correlation between the SGWB produced by coalescing stellar binaries (BBHs in blue and BNSs in green) and the CMB lensing convergence, measured with CMB-S4. *Left panel*: S/N with a constellation of two LISAs for four (solid) and ten (dotted) years of observing time. *Right panel*: S/N for DECIGO observing for three (solid) and ten (dotted) years. The black line corresponds to S/N = 1.

4.7 DISCUSSION AND CONCLUSIONS

In this Chapter, we investigated the possibility of probing the anisotropies of the astrophysical SGWB by using constellations of space-based interferometers. For our analysis, we considered a network composed of multiple LISAs and the planned Japanese mission DECIGO, which is already a constellation of four detector clusters. We tested these detector configurations with two different anisotropic SGWBs of astrophysical origin. First, we considered the SGWB produced by merging stellar compact binaries: even though this signal is dominant in the Hz-kHz band, its contribution is also relevant in the mHz and deci-Hz bands. Second, we considered the SGWB produced during a newly proposed scenario for SMBH seed formation through consecutive mergers of stellar remnants brought into the galactic center by gaseous dynamical friction. This process, recently developed in Refs. [277, 278], produces an SGWB in an extended frequency band, ranging from 10^{-7} Hz up to 1 Hz, making it a potential target for space-based interferometers. Following the formalism presented in Chapter 3, we computed the angular power spectrum of the SGWB anisotropies for both sources, the shot noise, and the instrumental noise for all the considered detector configurations. We then used these ingredients to evaluate the S/N for the auto-correlation power spectra. As expected, we found that measuring the SGWB anisotropies alone is very challenging even with a constellation of space-based interferometers. A possible exception holds for the SGWB produced by merging binary neutron stars, observed with DECIGO for at least ten years. In this case, the cumulative S/N reaches unity at $\ell_{\rm max} \lesssim 10$ with our prescriptions. Indeed, there are large uncertainties in the astrophysical modeling, and the exact amplitude of the signal could be very different

from the one we computed with our prescriptions. The detection prospects sensibly improve when considering cross-correlations with other tracers of the LSS. In particular, we cross-correlated our SGWB signals with the CMB lensing convergence. We computed the S/N of the cross-correlation power spectrum by including the lensing noise curves for CMB-S4 and the Simons Observatory. We found that a constellation of two LISAs operating for ten years can marginally probe the cross-correlation between CMB lensing and the SGWB produced during the formation of SMBH seeds. Specifically, the S/N reaches unity at $\ell_{\rm max} \sim 30$. Moreover, we found that DECIGO can instead probe the cross-correlation between CMB lensing and the SGWB produced by merging compact binaries. For an observation time of ten years, the S/N reaches unity at $\ell_{\rm max} \lesssim 10$ for BNSs and $\ell_{\rm max} \lesssim 40$ for BBHs. All in all, the anisotropies of the SGWB contain a large amount of astrophysical and cosmological information that makes them a sought-after target for present and future GW observatories. However, there is the possibility the numerous observational challenges might hinder their exploration using ground-based interferometers, particularly beyond the initial multipoles. Through this preliminary analysis, we showed that using a constellation of space-based interferometers could substantially enhance the angular sensitivity, potentially enabling the investigation of SGWB anisotropies, especially through cross-correlations with other cosmic fields such as CMB lensing.

ASTROPHYSICAL AND COSMOLOGICAL RELEVANCE OF THE HIGH-FREQUENCY FEATURES IN THE SGWB

5

This Chapter is based on the following manuscript:

G. Capurri, A. Lapi, M. Spera, C. Baccigalupi
Astrophysical and Cosmological Relevance of the High-Frequency Features in the Stochastic Gravitational-Wave Background
Submitted to Phys. Rev. D, arXiv:2310.18394

The SGWB produced by merging neutron stars features a peak in the kHz frequency band. In this chapter, I discuss e new theoretical framework to exploit such a distinguishing feature through a Markov Chain Monte Carlo analysis using a simulated data-set of SGWB measurements within this frequency band. The aim is to use the peak of the SGWB as an observable to constrain a selection of astrophysical and cosmological parameters describing the SGWB.

5.1 INTRODUCTION AND MOTIVATION

The SGWB coming from compact binary coalescences is one of the main targets of present and forthcoming GW observatories. Indeed, such a signal (i) comes from all merging binaries since the beginning of stellar activity, and hence contains information about the entire population of sources; (ii) it is a tracer of the large-scale structure, as its anisotropies reflect those of the underlying dark matter distribution; (iii) it is dominant within the frequency band probed by ground-based interferometers. As a consequence, an effective modeling of this specific component is needed to isolate other SGWB sources that might be present in the signal. As we discussed in the previous chapters, the amplitude and shape of the energy density $\Omega_{gw}(f)$ are influenced by several astrophysical factors. Another intriguing and largely unexplored characteristic of the SGWB from compact binary coalescences is its sensitivity to a set of cosmological parameters, including the Hubble parameter H_0. Relying on a robust set of astrophysical and cosmological parameters is fundamental to provide an accurate description of the SGWB signal. On the other hand, the measurement of SGWB amplitude across multiple frequencies gives the opportunity to constrain these parameters. The majority of the binary coalescences building up the SGWB are in their inspiral phase between 10 Hz and a few hundred Hz, and the energy density parameter follows a power-law behavior with a fixed slope, $\Omega_{gw}(f) \propto f^{2/3}$. Hence, in this regime, there is a strong degeneracy between the astrophysical and cosmological parameters that characterize the SGWB, as their complex interplay shows up only as variations in the amplitude of the power-law. As a consequence, constraining the different parameters sep-

arately is impossible in this regime. In contrast, the scenario is different above a few hundred Hz. In this high-frequency regime, an increasingly larger portion of binaries evolves towards the merger and ringdown phases. Thus, the energy density parameter $\Omega_{gw}(f)$ features a distinctive peak, as shown in Figure 41. The shape of the peak is influenced by a combination of astrophysical factors, such as the mass and redshift distribution of the merging binaries, as well as cosmological factors, including the value of the Hubble parameter H_0, the matter content of the Universe, and the effective equation of state of dark energy. Therefore, the kHz range might contain additional information to better constrain the astrophysical and cosmological parameters describing the SGWB signal.

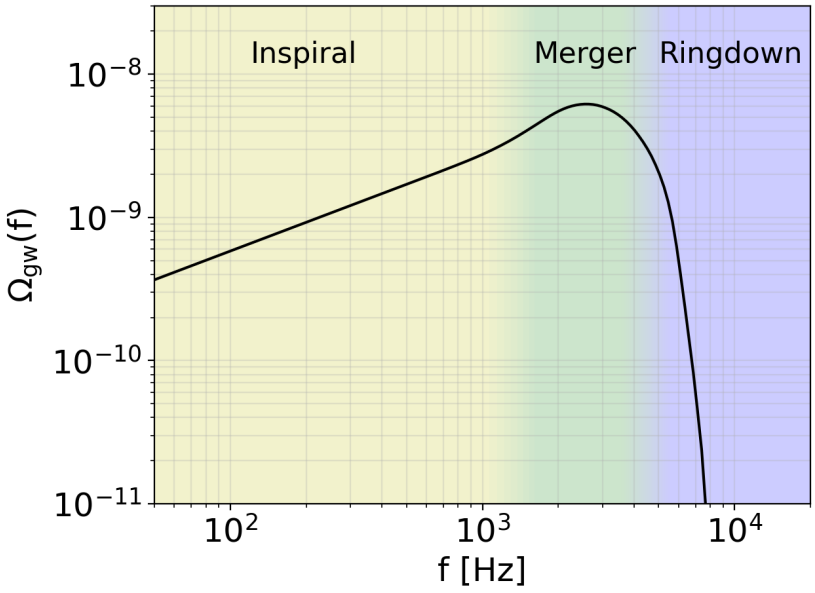

Figure 41: Frequency behavior of the energy density parameter. The power-law, peak and exponential cutoff regimes correspond to the inspiral, merger and ringdown phases, as explained in the text. This plot shows the SGWB produced by merging BNS, computed as described in Chapter 2 according to the astrophysical prescriptions presented in Refs. [76, 77].

The aim of this chapter is to study the information concealed in the peak of the SGWB. I will investigate how different sets of astrophysical and cosmological parameters affect the amplitude and shape of $\Omega_{gw}(f)$ in the high-frequency regime. Furthermore, I will show how a series of measurements within the kHz range can help to constrain these parameters. Finally, I will give some insights on the required sensitivity in the high-frequency regime needed to measure the H_0 parameter and possibly shed light on the Hubble tension [33]. There are alternative methods to estimate the value of the Hubble constant using GWs as,

for example, with resolved signals. Each measurement provides the luminosity distance to the source, while the corresponding redshift can be obtained using various approaches, including the redshifted masses and a galaxy catalog [134, 135, 292]. The value of H_0 is then inferred from the $d_L - z$ relation. The method presented in this chapter represents a completely independent approach.

This chapter is organized as follows. In Section 5.2, I briefly recall the derivation of the SGWB energy density parameter for binary coalescences. Then, I identify a set of astrophysical and cosmological parameters suitable for describing a specific family of coalescing binaries (i.e., BNSs) and study how different values of such parameters affect $\Omega_{gw}(f)$. In Section 5.3, I describe our methodology for exploiting the high-frequency features of the SGWB through a Markov Chain Monte Carlo analysis using a simulated data set of SGWB measurements. In Section 5.4, I study how well different input values of the astrophysical and cosmological parameters are retrieved with the MCMC analysis. Finally, I discuss the results and draw the conclusions in Section 5.5.

5.2 STUDY OF PHYSICAL DEPENDENCIES

In this section, I give an overview of the astrophysical and cosmological dependencies of the SGWB energy density parameter. Following Refs. [37, 83–90, 293], $\Omega_{gw}(f)$ can be re-written as[1]:

$$\Omega_{gw}(f) \equiv \frac{1}{\rho_c}\frac{d\rho_{gw}(f)}{d\ln f} = \frac{f}{\rho_c}\frac{d^2\mathcal{E}_{gw}}{dVdf} = \frac{f}{\rho_c c}\frac{d^3\mathcal{E}_{gw}}{dSdtdf}, \tag{62}$$

where $\mathcal{E}_{gw}$ is the total energy carried by the stochastic background, so that $d^3\mathcal{E}_{gw}/dSdtdf$ is the total energy flux per unit time and frequency in the observer frame. By expanding Equation (62), we get

$$\Omega_{gw}(f) = \frac{f}{\rho_c c}\int dz d\theta_a \, p(\theta_a)\, F(f, z|\theta_a)\, \frac{d\dot{N}}{dz}(z|\theta_a). \tag{63}$$

In Equation (63), $p(\theta_a)$ is the probability distribution of the source astrophysical parameters, θ_a. $F(f, z|\theta_a)$ is the averaged energy flux per unit observed frequency emitted by coalescing binaries located at redshift z and characterized by the astrophysical parameters θ_a:

$$F(f, z|\theta_a) = \frac{\frac{dE_{gw}}{df}(f|\theta_a)}{4\pi d_L^2(z|\theta_c)} = \frac{\frac{dE_{gw}}{df_s}(f_s|\theta_a)}{4\pi r^2(z|\theta_c)(1+z)}, \tag{64}$$

where dE_{gw}/df is the emitted gravitational spectral energy and $f_s = f(1+z)$ is the frequency in the source frame. $d_L(z|\theta_c)$ and $r(z|\theta_c)$ are the luminosity

1 Here I derive the expression of $\Omega_{gw}(f)$ following exactly the same steps of the derivation reported in Section 1.2.3. However, here I hightlight more explicitly the dependence on the astrophysical and cosmological parameters.

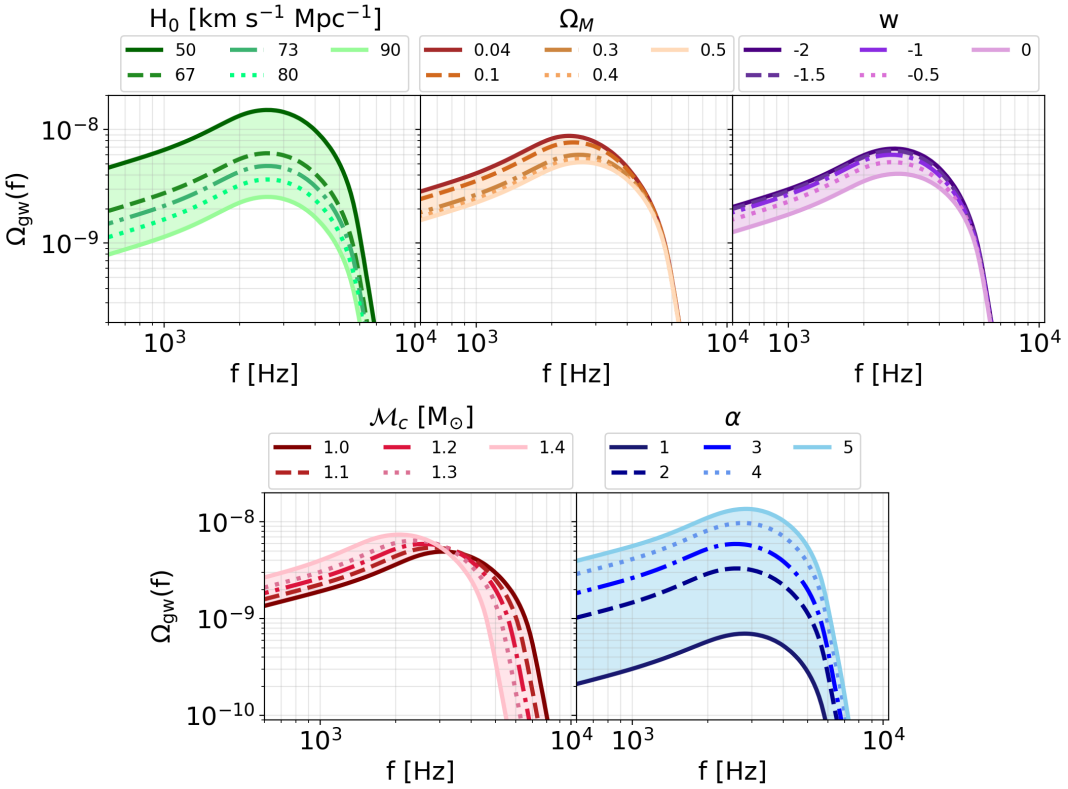

Figure 42: The energy density of the SGWB produced by merging BNS systems exhibits different behaviors for different values of the cosmological and astrophysical parameters considered in our analysis: $\theta_c = \{H_0, \Omega_M, w\}$ and $\theta_a = \{\mathcal{M}_c, \alpha\}$. In each panel, we explore the effect of varying a single parameter while keeping the others fixed at their reference values: $H_0^{ref} = 67$ km s^{-1}Mpc^{-1}, $\Omega_M^{ref} = 0.31$, $w^{ref} = -1$, $\mathcal{M}_c^{ref} = 1.25\ M_\odot$, and $\alpha^{ref} = 3.8$.

distance and the proper distance, respectively, and depend on the adopted cosmology, defined by the cosmological parameters θ_c. The last term of the integral in Equation (63) is the rate of mergers per redshift interval. This quantity can be expressed in terms of the intrinsic merger rate per unit comoving volume, $R(z|\theta_a)$, as follows:

$$\frac{d\dot{N}}{dz}(z|\theta_a) = \mathcal{R}(z|\theta_a)\frac{dV}{dz}, \tag{65}$$

with

$$\frac{dV}{dz} = \frac{4\pi c\, r^2(z|\theta_c)}{H(z|\theta_c)}, \tag{66}$$

where $H(z|\theta_c) = H_0 h(z|\theta_c)$ is the Hubble rate. By combining everything together, we obtain the well-known expression for the SGWB energy density parameter, as reported in Refs. [37, 83–90, 293]:

$$\Omega_{gw}(f) = \frac{8\pi G f}{3H_0^3 c^2} \int dz d\theta_a \, p(\theta_a) \, \frac{dE_{gw}}{df_s}(f_s, z|\theta_a) \frac{\mathcal{R}(z|\theta_a)}{(1+z)h(z|\theta_c)}. \tag{67}$$

The adopted cosmological model affects $\Omega_{gw}(f)$ through the H_0 parameter. Furthermore, it influences the behavior of $h(z|\theta_c)$, which has distinct functional forms depending on the adopted cosmological scenario. Here, we use a standard flat cosmology, with the Hubble parameter H_0, the matter density parameter Ω_M, and the dark energy equation of state w as free parameters. In this scenario, the expression for $h(z|\theta_c)$, with $\theta_c = \{H_0, \Omega_M, w\}$, is:

$$h(z|\theta_c) = \sqrt{\Omega_M (1+z)^3 + \Omega_\Lambda (1+z)^{3(1+w)}}, \tag{68}$$

where $\Omega_\Lambda = 1 - \Omega_M$ for the flatness requirement. The top panels of Figure 42 show the dependence of $\Omega_{gw}(f)$ on the set of cosmological parameters. From Figure 42, it is apparent that the SGWB energy density is most sensitive to H_0, as $\Omega_{gw} \propto H_0^{-3}$. This means that higher values of H_0 result in a reduced SGWB amplitude because a faster cosmic expansion leads to a more significant dilution of the energy density. However, assessing the sensitivity of a SGWB measurement to the Hubble parameter using $\Omega_{gw}(f)$ may not be the most suitable approach. Notably, a substantial dependence on H_0 arises from the presence of ρ_c in the definition of $\Omega_{gw}(f)$. As a consequence, instead of relying on $\Omega_{gw}(f)$, we will use the spectral density $S_h(f)$, which is directly measured measured by GW detectors. Indeed, a detector produces an output of the measured GW strain, $h(t)$. From the correlation of the outputs of two detectors one can measure the root mean square of the strain, h^2_{rms}, or, equivalently, the power spectral density (PSD) $S_h(f)$, which is defined through (see e.g. Refs. [21, 23]):

$$h^2_{rms} = \left\langle \sum_{ij} h_{ij} h_{ij} \right\rangle = \int_0^\infty df S_h(f). \tag{69}$$

The PSD and the energy density parameter are related through

$$S_h(f) = \frac{3H_0^2}{2\pi^2 f^3} \Omega_{gw}(f), \tag{70}$$

so that

$$S_h(f) = \frac{4G}{\pi H_0 c^2} f^{-2} \int dz d\theta_a \, p(\theta_a) \, \frac{dE_{gw}}{df_s}(f_s, z|\theta_a) \frac{\mathcal{R}(z|\theta_a)}{(1+z)h(z|\theta_c)}. \tag{71}$$

The astrophysical dependencies of $\Omega_{gw}(f)$ are embedded within the merger rate and the GW spectral energy, and are more complex than the cosmological ones. Indeed, the intricate interplay of numerous processes, spanning from

the physics of stars and binary systems to that of the host galaxies, decisively shapes the formation, evolution and merger of compact binaries. As a consequence, capturing all the involved processes with a limited set of parameters is challenging. The difficulty is particularly pronounced in the case of BBHs, as their mass and redshift distributions show complex and distinctive features, heavily influenced by a multitude of astrophysical factors, including the evolution of massive stars (e.g. pair instability, core collapse, natal kicks, etc.), different binary formation channels (e.g. isolated, dynamical, etc.), binary evolution processes (e.g. stable mass transfer, common envelope, etc.), and the metallicity and star formation rate of the galactic environment (see, e.g, Refs. [76, 77, 236, 294–296] for a comprehensive description of relevant physics at play). For BNSs, the complexity level is significantly reduced. Firstly, uncertainties concerning the galactic environment are smaller compared to the BBH case. Indeed, BNS systems are minimally affected by metallicity variations, with their evolution mainly depending on the galaxy main sequence (i.e the relation between stellar mass and star formation rate), which is empirically well-constrained [230, 297]. Secondly, though there are larger uncertainties on the stellar side, the mass spectrum of neutron stars sharply peaks around 1.3 $M_\odot$ [298, 299]. For our analysis, therefore, we have decided to work with the SGWB produced by BNS systems, which can be described with a reasonable number of astrophysical parameters. Specifically, we focus on the stellar domain and characterize the BNS population through two key astrophysical parameters, $\theta_a = \{\mathcal{M}_c, \alpha\}$, where $\mathcal{M}_c$ represents the value at which the chirp mass distribution peaks, and α denotes the common envelope efficiency parameter [217, 300]. On the galactic side, instead, given the increasing confidence in forthcoming observational constraints, we rely on empirical, data-driven prescriptions, based on multi-band measurements of the galaxy main sequence and metallicity. In particular, we establish a fixed fiducial scenario for metallicity and main sequence, the B18 FMR model in Ref. [296]. In the lower panel of Figure 42, we show how $\Omega_{gw}(f)$ depends on the parameters θ_a. Notably, different values of $\mathcal{M}_c$ cause a shift in the peak's position, as BNS populations with different masses merge at different typical frequencies. Conversely, varying α leads to a significant change in the amplitude of the SGWB, as it directly affects the number of merging BNS binaries.

5.3 METHODS: MARKOV CHAIN MONTE CARLO ANALYSIS

In this work, we characterize the SGWB using its PSD, $S_h(f)$, which is linked to the energy density parameter, $\Omega_{gw}(f)$, through Equation (70). As already mentioned, we adopted this approach for two reasons: *i)* $\Omega_{gw}(f)$ introduces a further dependence on H_0, potentially affecting the relationship between the SGWB amplitude and the Hubble parameter, and *ii)* the PSD is more directly related to the GW strain, the quantity measured by detectors. However, since the results about the SGWB are usually expressed in terms of $\Omega_{gw}(f)$, we also present our results in terms of $\Omega_{gw}(f)$ instead of $S_h(f)$. As a preliminary step,

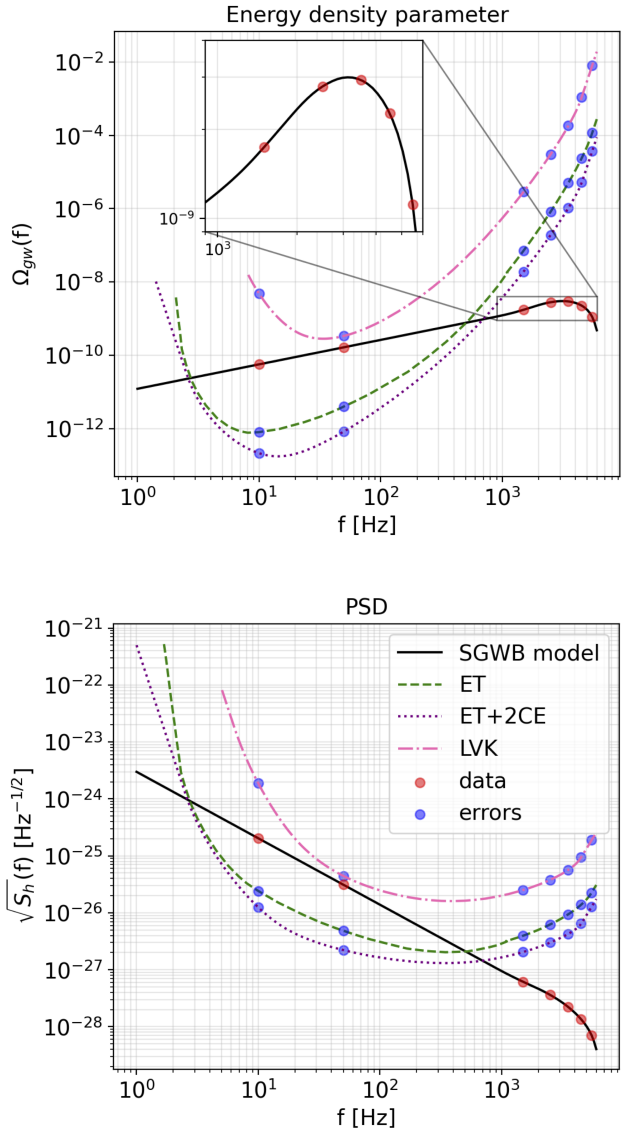

Figure 43: The solid line in the left (right) panel represents our model of $\Omega_{gw}(f)$ ($\sqrt{S_h}(f)$) for the SGWB produced by coalescing BNSs. The coloured lines are the PLS curves of LIGO-Virgo-KAGRA (LVK), Einstein Telescope (ET), and ET in combination with two Cosmic Explorers, one in the US and one in Australia. The red and blue points represent a hypothetical data-set with the corresponding errors, as explained in the text.

we calculate the PSD at different frequencies in the range [10 Hz-5.5 kHz], considering different sets of astrophysical and cosmological parameters. The PSD values are our mock measurements, and we also associate an error to each of them. The error is calculated by computing the 1σ power-law integrated sensitivity curve (PLS) [174] for a specific network of detectors, assuming an observation time $T = 1$ yr. The value of the 1σ-PLS at each frequency represents the amplitude of a power-law SGWB with a signal-to-noise ratio of 1, providing a reasonable estimation of the error for our measurements. Once

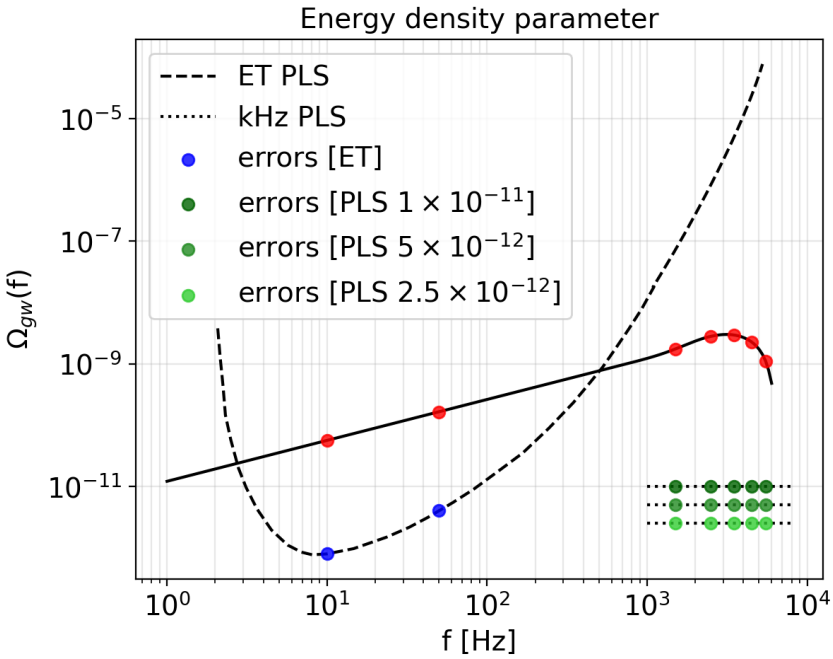

Figure 44: Example of the mock data-set that we actually use for our analysis. $\Omega_{gw}(f)$ is computed using a specific set of input values for our parameters θ_a and θ_c (see Table 2). The data points, in red, are obtained sampling $\Omega_{gw}(f)$ at seven distinct frequencies. The associated errors are fixed to the ET 1σ-PLS in the 1-100 Hz regime (blue points), and at progressively low arbitrary values in the kHz regime (green points).

we have our data-set with errors, we perform a Markov Chain Monte Carlo (MCMC) analysis to retrieve the input values of the astrophysical and cosmological parameters that we used to generate the data. We use the code `emcee`, which is an MIT licensed pure-Python implementation of Goodman & Weare's Affine Invariant MCMC Ensemble sampler [301].

In Figure 43, we show a collection of mock data points along with their corresponding errors, computed in the context of a detection with three different networks: (i) the current network of second-generation instruments, LIGO, Virgo, and KAGRA (LVK) [4, 5, 10] at design sensitivity (post-O5), (ii) the third-generation detector Einstein Telescope (ET) [134, 135], and (iii) an extended network composed of ET and two Cosmic Explorer (CE) detectors [136, 137], one in the US and one in Australia. The left panel of Figure 43 shows the expected $\Omega_{gw}(f)$ based on our fiducial values of the astrophysical and cosmological parameters, as reported in Table 2. We also show our mock data (red points), which are given by the expected values of $\Omega_{gw}(f)$ at specific frequencies where measurements are assumed to be taken at: $f = 10$ Hz, 50 Hz, 1.5×10^3 Hz, 2.5×10^3 Hz, 3.5×10^3 Hz, 4.5×10^3 Hz, and 5.5×10^3 Hz. The first two frequencies are strategically chosen within the region where LVK, ET, and CE have maximum sensitivity to stochastic backgrounds. These data points are crucial for constraining the amplitude of the SGWB. Instead, the five

data points in kHz range are essential to characterize the peak of the SGWB, as it is shown in the zoomed-in region in the left plot of Figure 43. The errors of our mock measurements (blue points) match the values of the PLS of the considered detector network at the observed frequencies. In the right panel of Figure 43, we present the same quantities as in the left panel, but expressed in terms of the PSD using Equation (70). From Figure 43, it is apparent that LVK at design sensitivity will only marginally detect the SGWB. In contrast, the improved sensitivity of ET will allow the detection of the SGWB in the frequency range from a few Hz to a few hundred Hz. Moreover, the PLS shown in the plot refers to the current expectations for ET sensitivity. Once online, the detector will undergo continuous upgrades, similar to LVK, that will improve the sensitivity band to possibly reach the SGWB peak. In particular, pushing the performances of ET in the kHz regime in future implementations, for example through ad-hoc optical configuration of the ET-HF interferometer, would be beneficial to this purpose. Finally, combining ET with other third-generation detectors, such as CE, will enhance the overall sensitivity and may help to give further insights on the high-frequency features of the SGWB.

The primary objective of this paper is to build up a science case to assess whether the SGWB measured in the kHz band can serve as a reliable observable to constrain cosmological and astrophysical parameters. To accomplish this goal, we manually fix the sensitivity in the kHz band so to reach a good level of constraining power on the astrophysical and cosmological parameters. Figure 44 shows a typical data-set that we used for our theoretical analysis, with manually fixed errors in the kHz band (green points). For the first two data points, we use the errors associated with ET. We generate different data-sets using the fiducial values of the parameters θ_c and θ_a, as reported in Table 2. The real values of $\mathcal{M}_c$, α and w are highly uncertain, thus we randomly pick their fiducial values inside the prior ranges typically used in the literature [217, 300, 302–305]. In contrast, for H_0 and Ω_M, we take the latest values obtained by Planck [32]. For H_0, we also consider an additional fiducial value, corresponding to the local measurement from Cepheid variables and Type Ia supernovae [31]. All the priors distributions are flat, except that of $\mathcal{M}_c$, which is a Gaussian with $\sigma_{\mathcal{M}_c} = 0.2\,M_\odot$ centered around $1.2\,M_\odot$. We then perform an MCMC to retrieve the input values of our parameters. Finally, we study the amplitude of the posterior contours for different choices of the kHz PLS, which give an estimate of the constraining power of our observable.

Finally, we emphasize that following this preliminary science case, we plan to apply our methodology to more advanced scenarios. For example, the description of BNS systems could be enhanced by including the dependence on the neutron star equation of state. The equation of state affects the masses of the binary components and the GW waveforms, both contributing to the SGWB energy density. We also plan to extend our study to BBHs, which are expected to produce a SGWB with a peak at lower frequencies (a few hundred Hz). As mentioned earlier, the BBH case requires a larger number of parameters to be described because the properties and evolution of such systems heavily

Parameter	Fiducial value(s)	Prior interval	Units
$\mathcal{M}_c$	1.25	[1,1.5]	$M_\odot$
α	3.8	[1,5]	/
H_0	67.4 73	[50,90]	km s^{-1}Mpc^{-1}
Ω_M	0.315	[0.04, 0.5]	/
w	-1.5	[-2,0]	/

Table 2: Fiducial values and prior intervals for our astrophysical and cosmological parameters. All the priors are flat, except from the one for $\mathcal{M}_c$, which is assumed to be a Gaussian with $\sigma_{\mathcal{M}_c} = 0.2$ centered around $\bar{\mathcal{M}}_c = 1.2$.

depend on the metallicity and various formation channels. Furthermore, since the next-generation GW detectors will resolve the majority of coalescing BBHs, implementing our methodology for such systems will involve considering the residual SGWB, obtained by excluding all resolved events from the energy density computation.

5.4 RESULTS: CONSTRAINTS ON A SELECTION OF PARAMETERS

In Figure 45, we show the joint constraints (68% and 95% confidence regions) and marginalized posterior distributions on $\mathcal{M}_c$, α and H_0 for two sets of input values, $\{1.25\ M_\odot, 3.8, 67.4$ km s^{-1}Mpc$^{-1}\}$ and $\{1.25\ M_\odot, 3.8, 73$ km s^{-1}Mpc$^{-1}\}$. In Table 3, we report the associated marginalized percentage constraints at the 68% confidence level. The input values for H_0 are chosen to match the most recent Planck and local estimates, respectively [31, 32]. For both sets of input parameters, we explore the constraining power of our mock data-set for different kHz sensitivities. We find that a PLS $= 1 \times 10^{-11}$ is the poorest sensitivity for which the data have some constraining power on the three considered parameters. For higher values of the PLS, the posteriors are dominated by the priors and thus become uninformative. At PLS $= 1 \times 10^{-11}$, instead, the astrophysical parameters are retrieved quite well, so as the Hubble parameter. At this sensitivity level, however, it is not possible to distinguish between the two H_0 input values with enough significance. Notice that a precise determination of H_0 is further complicated by the strong degeneracy with α, as both parameters affect the amplitude of the SGWB leaving mostly unvaried its shape (see Figure 42). As expected, the constraining power increases for lower values of the PLS. In particular, with a PLS $= 5 \times 10^{-12}$ (2.5×10^{-12}) it is possible to distinguish the two conflicting values of the Hubble parameter at $1(2)\sigma$.

We also investigate the constraining power of our mock data-set when incorporating the other cosmological parameters, Ω_M and w. In Figure 46, we show the joint constraints (68% and 95% confidence regions) and marginalized posterior distributions on our full set of parameters θ_a and θ_c. We also report

	PLS 1×10^{-11}	PLS 5×10^{-12}	PLS 2.5×10^{-12}
$\mathcal{M}_c$	0.2%	0.1%	0.1%
α	4.2%	2.1%	1.0%
H_0	6.5%	3.2%	1.6%

Table 3: Marginalized percentage constraints at the 68% confidence level on $\mathcal{M}_c$, α and H_0, with input values $\{1.25\,M_\odot, 3.8, 73\,km\,s^{-1}Mpc^{-1}\}$, for the three different kHz sensitivity levels.

	PLS 1×10^{-11}	PLS 5×10^{-12}	PLS 2.5×10^{-12}
$\mathcal{M}_c$	0.4%	0.3%	0.3%
α	8.7%	7.5%	6.2%
H_0	11%	9,7%	8.2%
Ω_M	9.4%	7.1%	6.5%
w	25%	21%	17%

Table 4: Marginalized percentage constraints at 68% confidence level on all the parameters, with input values $\{1.25\,M_\odot$, 3.8, $73\,km\,s^{-1}Mpc^{-1}$, 0.315, $-1.5\}$, for the three different kHz sensitivity levels.

the associated marginalized percentage constraints at the 68% confidence level in Table 4. As expected, including a larger number of parameters in our model leads to broader posterior constraints. The increased complexity of the parameter space results in multimodal posterior distributions with several secondary peaks and introduces a higher level of degeneracy, especially for the parameters α and H_0. Nevertheless, the constraining power of our data-set remains significant, as the posteriors add information with respect to the priors for all parameters and at all kHz sensitivity levels.

5.5 DISCUSSION AND CONCLUSIONS

In this chapter, I studie the constraining capabilities of mock SGWB measurements in the kHz frequency regime. In the high-frequency range, the SGWB energy density shows a distinctive peak that contains most of the physical information. There are several stellar, galactic, and cosmological processes that affect the amplitude and shape of the SGWB. However, within the frequency range explored by ground-based interferometers, the SGWB follows a power-law behavior with a fixed $f^{2/3}$ slope. As a result, SGWB measurements in this region only allow for the determination of the signal's amplitude, leading to considerable degeneracy among the physical factors responsible for its production. In contrast, the frequency band above a few hundred Hz offers a unique

opportunity to probe the distinct peak of the SGWB, allowing us to constrain the astrophysical and cosmological processes that generate the signal.

As a first step, we identified a set of astrophysical and cosmological parameters that effectively characterize the SGWB sources. We focused our analysis on the SGWB generated by coalescing BNSs, instead of BBHs and NSBHs, because they are minimally affected by metallicity and mainly depend the redshift evolution of the galaxy main sequence, which is well constrained. We adopt empirical, data-driven prescriptions for the galactic environment and restrict our selection of astrophysical parameters to the stellar domain. We use only two astrophysical parameters to describe the BNS population, $\theta_a = \{\mathcal{M}_c, \alpha\}$, where $\mathcal{M}_c$ is the chirp mass at which the BNS mass distribution peaks, and α is the common envelope efficiency parameter. On the cosmological side, both amplitude and shape of the SGWB depend on the adopted scenario. Each cosmology is defined by specific parameters, either directly or indirectly influencing the expression for the energy density of the SGWB, as given in Equation (67). Specifically, we work with the parameters $\theta_c = \{H_0, \Omega_M, w\}$, where H_0 is the Hubble parameter, Ω_M the matter density parameter, and w the dark energy equation of state parameter. We first investigated how varying these parameters affects the SGWB energy density. Then, we did an MCMC analysis using a set of mock data covering a frequency range between a few tens of Hz and a few kHz. The main goal was to evaluate the constraining power of these data on our set of astrophysical and cosmological parameters. For the data points in the $\sim$ 10 Hz range, we set the errors to match the PLS of ET. For those in the kHz, instead, we assume progressively lower errors. Restricting the analysis only to the parameters $\{\mathcal{M}_c, \alpha, H_0\}$, we discovered that our mock data had constraining power for PLSs lower than 10^{-11} in the kHz frequency band. With a PLS of 5×10^{-12} and 2.5×10^{-12}, we could retrieve the Hubble parameter with a precision that has the potential to solve the Hubble tension at 1σ and 2σ, respectively. Including also the remaining parameters, Ω_M and w, we observed a decay in the constraining power. The increased complexity of the parameter space leads to the emergence of several secondary peaks in the posterior distributions. Despite this, the data still add valuable information to the priors, offering potential insights into the values of our astrophysical and cosmological parameters.

In conclusion, our science case establishes the relevance of the SGWB generated by BNSs as a robust observational tool within the kHz frequency range. Its characteristic peak contains a significant amount of physical information, enabling effective constraints on many astrophysical and cosmological processes involved in the production of the SGWB. Despite the complex interplay among numerous parameters, this observable remains effective in providing valuable insights, when measured with sufficient precision.

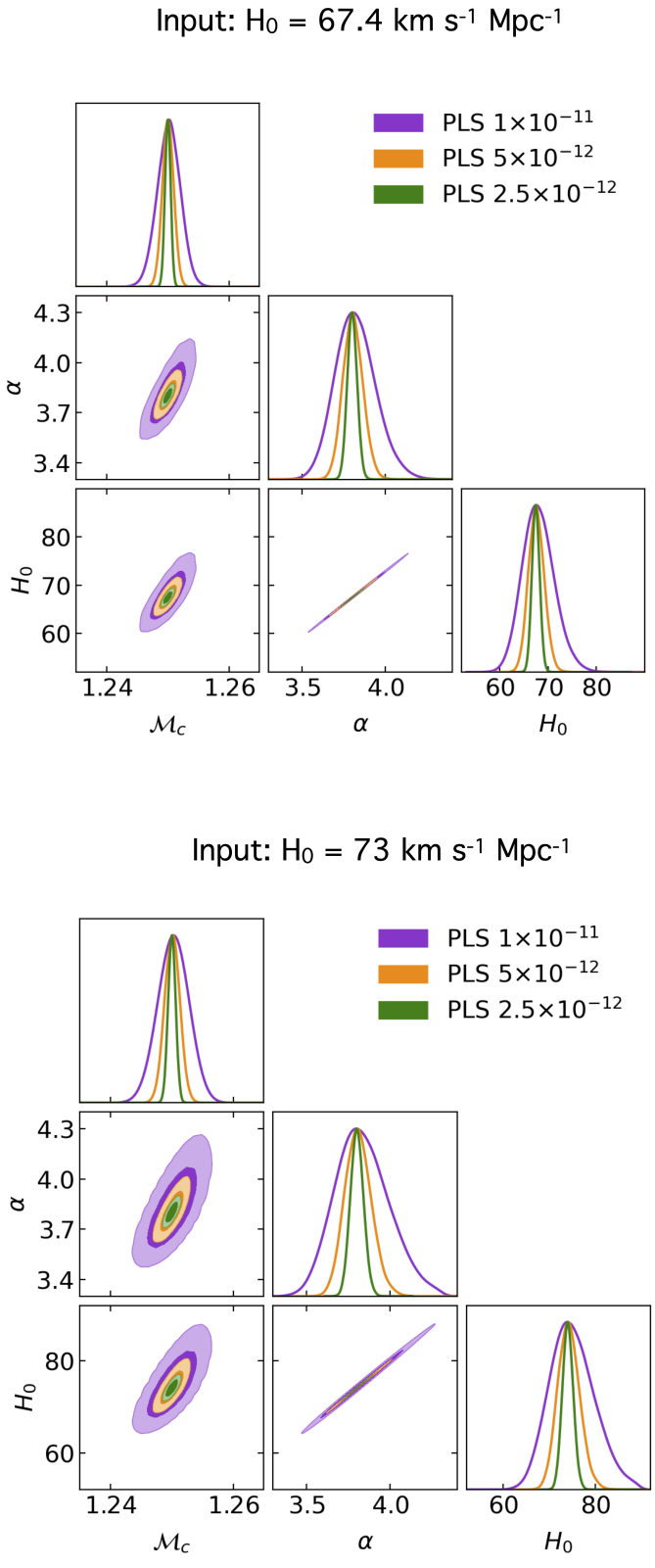

Figure 45: Joint constraints (68% and 95% confidence regions) and marginalized posterior distributions on $\mathcal{M}_c$, α and H_0, for two sets of input values $\{1.25\,M_\odot, 3.8, 67.4\,\mathrm{km\,s^{-1}Mpc^{-1}}\}$ and $\{1.25\,M_\odot, 3.8, 73\,\mathrm{km\,s^{-1}Mpc^{-1}}\}$, and three different sensitivity levels in the kHz range.

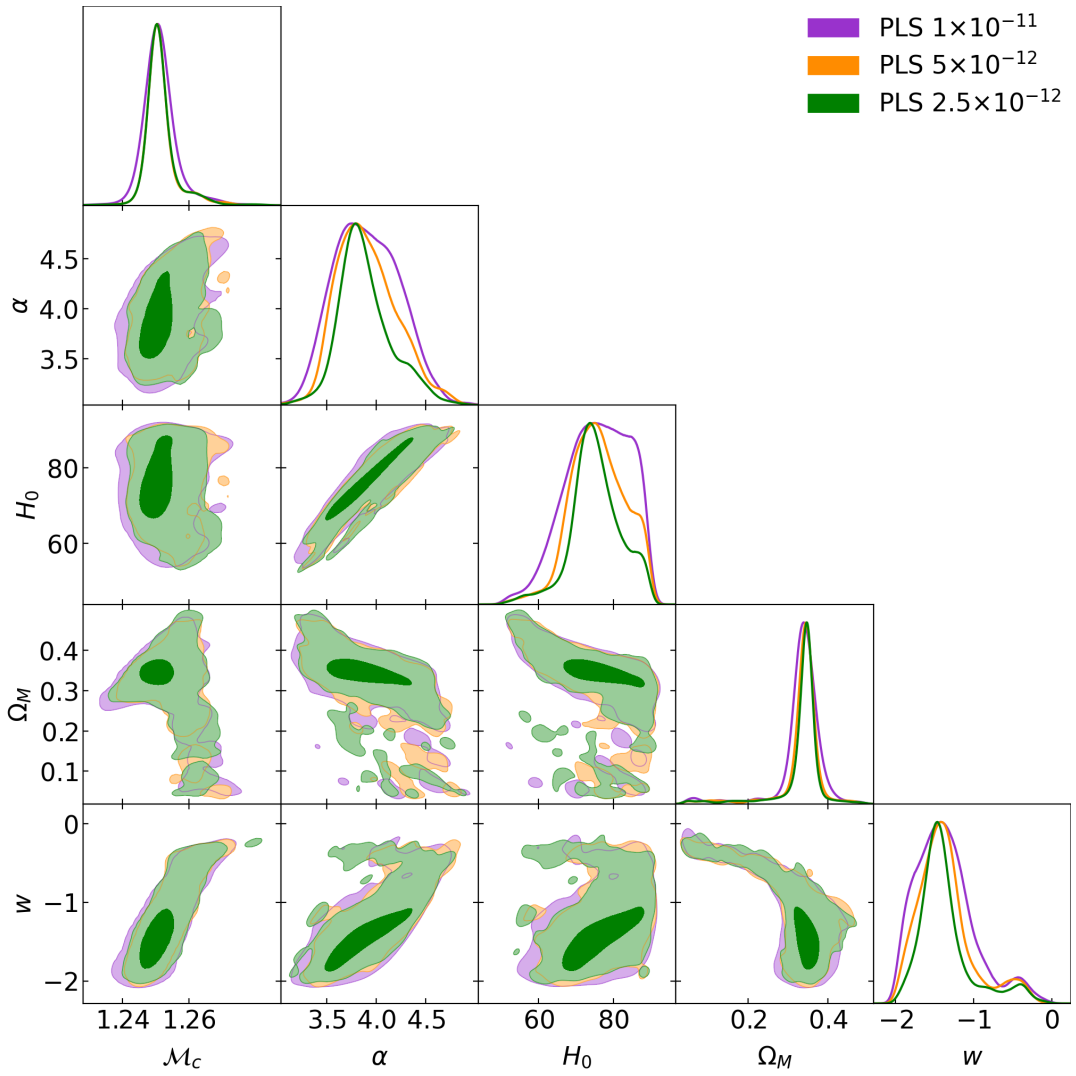

Figure 46: Joint constraints (68% and 95% confidence regions) and marginalized posterior distributions on all the considered parameters, $\mathcal{M}_c$, α, H_0, Ω_M and w, for three different sensitivity levels in the kHz range. The input values for the parameters are $\{1.25\,M_\odot, 3.8, 73\,\mathrm{km\,s^{-1}Mpc^{-1}}, 0.315, -1.5\}$.

6 CONCLUSIONS AND FUTURE PERSPECTIVE

In this Thesis, I have presented the original scientific results obtained during my Ph.D., mainly focusing on the SGWB generated by stellar compact binary coalescences. My work involved the development of a theoretical framework to characterize the intensity and anisotropies of this signal, along with its cross-correlation with other cosmic fields, its detection prospects, and its potential as an observable to constrain the astrophysical and cosmological processes at play. This framework can be applied to different sources of SGWB, each modeled with distinct prescriptions and observed with various GW detectors. Although I explored several specific scenarios during my Ph.D., the established framework stands as an effective starting point for both theoretical and observational studies concerning astrophysical stochastic backgrounds. In this closing chapter, I will summarize the main findings presented in this Thesis. Additionally, I will provide brief descriptions of ongoing projects and outline my research plans for the future.

6.1 MAIN RESULTS

Intensity and anisotropies of the SGWB from stellar compact binary coalescences

In Chapter 2, I introduced the theoretical framework I used to calculate the expected intensity and anisotropies of the SGWB throughout this Thesis. This framework relies on the outputs from the `StarTrack` binary population synthesis code and empirical, data-driven prescriptions for the galactic environment (Section 2.2). Employing these galactic empirical prescriptions, which I have briefly reviewed in Appendix A, allowed me to circumvent the issue of selecting one among various competing astrophysical models. While the used empirical relations come with their observational errors, they establish a robust and well-motivated astrophysical scenario in a field characterized by significant theoretical uncertainties. Using these prescriptions, I evaluated the amplitude of the SGWB as a function of frequency, specifying the contribution of binary black holes (BBH), binary neutron stars (BNS), and neutron star-black hole binaries (NSBH). I considered both the total SGWB, given by the superposition of all GW events, resolved and unresolved, and the residual SGWB, which is obtained subtracting the events whose signal-to-noise ratio is above the detection threshold. I studied the residual SGWB for two different networks of ground-based detectors: the second-generation network composed of LIGO, Virgo and KAGRA (LVK), and the next-generation GW observatory Einstein Telescope (ET). Even at design sensitivity, for LVK the unresolved events will continue to be the vast majority. In contrast, the exceptional sensitivity of ET will enable the detection of the majority of GW events up to extremely high redshifts.

As a consequence, the residual background for ET is anticipated to be significantly lower than the total one, potentially unveiling 'hidden' sub-dominant populations of merging binaries (Section 2.3).

Transitioning to the analysis of anisotropies, my initial focus was characterizing the SGWB as a tracer of the large-scale structure (LSS). This involved computing the redshift distribution, bias, and magnification bias of the SGWB energy density. Crucially, this characterization was possible due to the empirical approach for the galactic environment. By classifying the host galaxies of the GW source based on their star formation rates, I could effectively use this classification to determine the clustering properties of the SGWB, derived from the well-established ones of the host galaxies (Section 2.4). Leveraging this characterization of the SGWB as a tracer of the LSS, I calculated the angular power spectrum of its anisotropies using the Boltzmann solver `CLASS`. I computed the expected angular power spectra for both the total SGWB, allowing comparison with previous studies, and, for the first time to my knowledge, the residual SGWB. Additionally, I performed a tomographic analysis to identify the contributions of GW events located at various redshifts to the SGWB anisotropies across different scales (Section 2.5). Finally, I introduced a novel method to simulate full-sky maps of the SGWB. This method accounts for both clustering properties and the intrinsic Poissonian nature of the signal, originating from the discrete distribution of sources in space and time. This framework was essential for quantifying the impact of the resulting shot noise, characterized by a flat angular power spectrum significantly larger than the anisotropies induced by the LSS (Section 2.6).

Cross-correlation with CMB lensing: theory and detection prospects

Numerous recent studies have shown that using the cross-correlation with other cosmic fields – tracers of the same LSS, such as galaxy number counts, galaxy lensing, and CMB temperature fluctuations – is an effective method to reduce the impact of shot noise. In Chapter 3, I investigated the cross-correlation of the SGWB from stellar binary coalescences with CMB lensing. As a starting point, I characterized the two fields as tracers of the LSS, using a shared notation involving the definition of kernels (Section 3.2). Then, I computed the cross-correlation angular power spectra for BBHs, BNSs, and NSBHs, and for both the total and residual stochastic backgrounds. I considered several detector networks including both present and forthcoming ground-based detectors – namely, LIGO, Virgo, KAGRA, Einstein Telescope and Cosmic Explorer. The results revealed a substantial level of correlation between these two fields. This finding is non-trivial, suggesting that the distribution of merging binaries, as observed through SGWB anisotropies, is meaningfully correlated with the linear structures probed by CMB lensing (Section 3.4). Subsequently, I calculated the signal-to-noise ratio (S/N) for both the SGWB×SGWB auto-correlation and the SGWB×CMB lensing cross-correlation, accounting for shot noise and instrumental noise. This computation was done for a network of GW detectors including all the considered GW instruments, combined with the Simons Ob-

servatory for CMB lensing measurements. The results show that the S/N for the cross-correlation substantially surpasses that of the auto-correlation, proving the efficacy of the cross-correlation with CMB lensing in mitigating the impact of shot noise. Nevertheless, the relatively poor angular resolution of GW detectors remains a significant limitation, hindering the detection of the SGWB anisotropies beyond the first few multipoles.

An important caveat is that, in this analysis, I made the assumption that both the SGWB and CMB lensing were Gaussian fields. This assumption is not always true for the SGWB, particularly in the frequency band explored by ground-based detectors. Properly incorporating the statistical properties of the SGWB, along with the ongoing advancements in data analysis and map-making techniques, would likely enhance the prospects for detection. Nevertheless, my analysis serves as an initial step in evaluating the effectiveness of cross-correlation with CMB lensing in enhancing the intrinsic LSS-induced anisotropies in the SGWB.

Searching for SGWB anisotropies with constellations of space-based detectors

In Chapter 4, as follow-up work, I explored the potential of using a constellation of space-based detectors to measure the anisotropies of the SGWB. This study aimed to address the challenge of limited angular resolution discussed in the previous work. A detector configuration with multiple instruments in orbit around the Sun has a notably increased interferometric baseline of ≈ 1 AU, compared to ≈ 1 Earth radius for ground-based interferometers, resulting in a significantly enhanced angular resolution. The pipeline remains similar to the one for the previous work discussed in Chapter 3, albeit with a focus on space-based interferometers. Specifically, my analysis included a constellation of multiple LISA-like detectors, operating within the mHz frequency band, and the proposed Japanese mission DECIGO, which operates within the deci-Hz band (Section 4.2). Furthermore, in addition to stellar compact binaries, I also studied the SGWB generated by repeated mergers of stellar remnants with massive BH seeds situated at the centers of distant galaxies (Section 4.3). This was done within the context of the recently proposed massive BH seed formation process discussed in Appendix C.

I computed the angular resolution of the considered detector configurations (Section 4.2), the expected amplitude of the SGWB produced by stellar compact binaries and consecutive mergers with massive BH seeds (Section 4.4). Then, I focused specifically on anisotropies, and computed the S/N of both the SGWB×SGWB auto-correlation and the SGWB×CMB lensing cross-correlation, for both the considered SGWB sources and the different constellations of detectors (Sections 4.5 and 4.6). The analysis revealed that a constellation of two LISAs, observing for a decade, can marginally detect the cross-correlation between CMB lensing and the SGWB generated during the formation of massive BH seeds. Specifically, the S/N reaches unity at $\ell_{\rm max} \lesssim 30$. Furthermore, I found that DECIGO can probe the cross-correlation between CMB lensing and the SGWB produced by merging compact binaries. With an observation time

of ten years, the S/N reaches unity at $\ell_{max} \lesssim 10$ for BNSs and $\ell_{max} \lesssim 40$ for BBHs. In summary, this preliminary analysis has shown that employing a constellation of space-based interferometers could enhance angular sensitivity sufficiently enough to investigate the SGWB anisotropies, particularly through cross-correlations with other cosmic fields such as CMB lensing.

Astrophysical and cosmological relevance of the SGWB high-frequency features

In Chapter 5, I studied how to use the high-frequency features of the SGWB to constrain a selection of astrophysical and cosmological parameters. The SGWB energy density is determined by various factors – stellar, galactic, and cosmological. However, for binary coalescences, the low-frequency regime is characterized by a power-law behavior with a fixed slope $\propto f^{2/3}$, resulting in an extreme degeneracy where any modification merely shifts the amplitude of the signal. In contrast, the shape and location of the high-frequency peak are influenced by different factors in different ways. Hence, a series of SGWB measurements within the frequency band where the peak is located would offer valuable insights into the physical processes at play. In this study, I developed a theoretical framework to use the peak of the SGWB from coalescing BNSs to constrain a set of astrophysical and cosmological parameters. I achieve this by performing a Markov Chain Monte Carlo (MCMC) analysis on a collection of simulated SGWB measurements within the kHz band. The choice of focusing on BNSs was motivated by their relatively simple mass distribution, peaking at approximately $\sim 1.3\ M_\odot$, and slight dependence on metallicity. As a consequence, it was possible to describe BNS systems through a limited number of astrophysical parameters, at least at first approximation.

First, I examined how varying the values of astrophysical and cosmological parameters (i.e., the peak of the chirp mass distribution, the common envelope efficiency parameter, the Hubble parameter, the matter content parameter and the dark energy effective equation of state) impacts the morphology of the SGWB (Section 5.2). Then, I defined a mock SGWB data-set and outlined the MCMC procedure in Section 5.3. Based on the prior assumptions on the parameters, it was possible to recover the input values of the chirp mass and common envelope efficiency with percent accuracy. The cosmological expansion history, described by the Hubble constant, matter abundance, and the effective equation of state of dark energy, was also successfully reconstructed (Section 5.4). Moreover, I provided insights into the required sensitivity in the high-frequency regime needed to measure the H_0 parameter with sufficient precision to possibly shed light on the Hubble tension. While there exist various methods to estimate the Hubble constant using GWs, the approach introduced in this work stands as a completely independent method.

Besides the specific results obtained for the parameters considered in this study, I have developed a methodology that can be applied in future research investigating other features of the astrophysical sources generating stochastic backgrounds. I am already planning on employing this method to analyze the SGWB from merging stellar BBHs and revisiting case of BNSs, this time

focusing on the influence of different equations of state for neutron stars. I will delve further into this plan in Section 6.3.

6.2 ONGOING PROJECTS

Cross-correlation with galaxy lensing and ISW

I'm currently working on two projects related to the cross-correlation of the SGWB with other cosmic fields. One project, in collaboration with Dr. Carmelita Carbone (staff researcher at INAF-IASF in Milan), focuses on cross-correlating the SGWB from stellar compact binary coalescences with galaxy lensing and the integrated Sachs-Wolfe effect of the CMB. The expected cross-correlation signal will be computed using a constraint mapping approach to combine my theoretical predictions for the SGWB angular power spectrum (Chapters 2 and 3) with the outcomes of cosmological simulations of galaxy lensing and the integrated Sachs-Wolfe effect. The final goal is to assess the detectability of such signals by combining data from the Euclid mission with SGWB maps from forthcoming GW instruments.

Cross-correlation with galaxy number counts

The second project, in collaboration with Dr. Lumen Boco (postdoc at SISSA), focuses on modeling the cross-correlation between the SGWB and resolved GW events from stellar compact binary coalescences with galaxy number counts. The initial phase of the study involves developing a semi-empirical model to compute the distribution of the stellar content, generated within galaxies at a specific time t_i, among galaxies with different masses at a subsequent time t_f. The aim is to predict the 'GW luminosity' of galaxies, which is related to the rate and properties of the merger events occurring in each galaxy at a time t_f, based on binary systems formed at earlier an time t_i. Identifying the galaxies that host specific GW events is crucial for cross-correlation studies for two reasons. First, assigning a probability of hosting a merger event to galaxies with specific properties allows us to select the most suitable survey to observe galaxies with the highest probability. Second, the selection of those galaxies that most likely host binary mergers is essential for achieving a high correlation level and maximizing the S/N.

Constraining the hierarchical merger scenario with the SGWB

A third ongoing project, on which I am working in collaboration with Prof. Davide Gerosa, Dr. Arianna Renzini, and Dr. Riccardo Buscicchio (University of Milano-Bicocca), aims to explore the possible constraints on the hierarchical merger scenario through the (non-)detection of the SGWB. While the majority of compact binary mergers observed by LIGO and Virgo involves first-generation BHs originating from the collapse of massive stars, a smaller subset may comprise second (or higher) generation black holes resulting from prior

mergers. These hierarchically assembled BBHs possess distinctive features, including greater masses, dimensionless spins clustered around a characteristic value of ≈ 0.7, and a delayed redshift distribution. These unique characteristics significantly influence the GW emission, affecting both individual events and the SGWB. Hierarchical mergers are a unique and relatively clean case where a single astrophysical prediction connects these two qualitatively different observables. The goal of this project is to answer the question: can the current non-detection of the SGWB be used to put constraints on the number of LIGO/Virgo events that have been hierarchically assembled?

6.3 FUTURE PLANS

In the next few months, I plan to wrap up the ongoing projects described in the previous section. Then, I would like to dedicate some of my time to further developing those projects. Furthermore, a research line I am planning on pursuing involves building upon my latest project discussed in Chapter 5. Following this initial science case, my aim is to employ this methodology in more advanced scenarios. For example, I intend to refine the description of BNS systems by integrating the dependence on the neutron star equation of state. Indeed, the equation of state significantly affects the masses of the NSs and the features of the waveforms, both contributing to the overall energy density of the SGWB. I also plan to extend the analysis to BBH systems, which are expected to produce a SGWB with a peak at lower frequencies (a few hundred Hz). As discussed in Chapter 5, the BBH case requires a larger number of parameters to be described because the properties and evolution of such systems heavily depend on the metallicity and various formation channels. Furthermore, since next-generation detectors will resolve the majority of coalescing BBHs, implementing this methodology for such systems will involve considering the residual SGWB, obtained by excluding all resolved events from the energy density computation.

Finally, given the vast volume of data expected from current and future GW observatories, my focus in the upcoming years is to bridge theoretical and observational perspectives and enhance my skills in data interpretation. In the following, I will outline a few specific ideas for achieving these goals within my research background. As a member of ET, one of my focuses for the coming years is to explore the potential of stochastic searches with third-generation ground-based experiments. Since ET will detect a significant portion of BBH events, the SGWB will predominantly originate from BNSs and possibly from sub-populations of BBHs. Moreover, by combining stochastic searches results with resolved events, one can gain insights into important properties related to the source population, such as the star formation history and the initial mass functions. This can be achieved, for example, using empirical, data-driven prescriptions for the galactic environment, thus reverse-engineering these properties from GW data. Finally, I aim to broaden my knowledge of stochastic search techniques to enhance my ability to forecast more refined detection prospects

for physically motivated signals. Concerning SGWB anisotropies, for example, one of my plans is to understand the potential of upcoming instruments, both in space and on Earth. One approach I am excited about involves assessing how these instruments would respond to specific anisotropic signals, such as the simulated SGWB maps presented in Chapter 2, and determining what we can learn about their generation mechanisms.

ELEMENTS OF GALAXY STATISTICS AND EVOLUTION

An innovative aspect of the work presented in this Thesis is the use of empirical, data-driven prescriptions for the galactic environment. This approach was crucial in many ways. Employing empirical prescriptions allows us to circumvent the issue of selecting one among various competing astrophysical models. While the empirical relations we use come with their observational errors, they establish a robust and well-motivated astrophysical scenario in a field characterized by significant theoretical uncertainties. By using the star formation rate (SFR) as a galaxy statistic and the fundamental metallicity relation (FMR) to assign metallicities, we have identified the contributions of galaxies with distinct features (e.g., SFR, metallicity, halo mass) to the total GW emission. This method is crucial in obtaining accurate predictions of the merger rates as functions of redshift and chirp mass, as extensively discussed in Refs. [76, 77]. These refined predictions for the merger rates significantly impact the amplitude and shape of the SGWB. Furthermore, understanding the contributions of galaxies with different SFR to the SGWB was fundamental in calculating the bias of the SGWB energy density. Indeed, this calculation started from the bias of the host galaxies, which was in turn obtained matching the SFR with the mass of the dark matter halo. For all this reasons, I believe it is useful to provide a very basic overview of the elementary concepts of galaxy statistics and evolution that I employed for the work presented in this Thesis.

The galaxy stellar mass function

The galaxy stellar mass function (GSMF) $d^2N/d\log M_\star dV$ is the number of galaxies per unit comoving volume per bin of stellar mass at different redshifts. It is typically built deriving the stellar mass from near-IR observations, dividing the mass range in bins and counting the galaxies in each bin in a given volume. The overall GSMF is usually fitted via a single Schechter function [309]:

$$\frac{d^2N}{d\log M_\star dV} = \Phi_{ref}\left(\frac{M_\star}{M_{ref}}\right)^{\alpha} \exp\left(-\frac{M_\star}{M_{ref}}\right), \tag{72}$$

which is characterized by a power-law behaviour at $M_\star \ll M_{ref}$ and an exponential cut at $M_\star \gg M_{ref}$, which hinders the presence of extremely massive galaxies. This behavior is clearly visible in Figure 47, which shows the redshift evolution of the GSMF as obtained by Davidzon et. al (2017) [306]. The total stellar mass density can be determined by integrating the GSMF multiplied by the stellar mass itself:

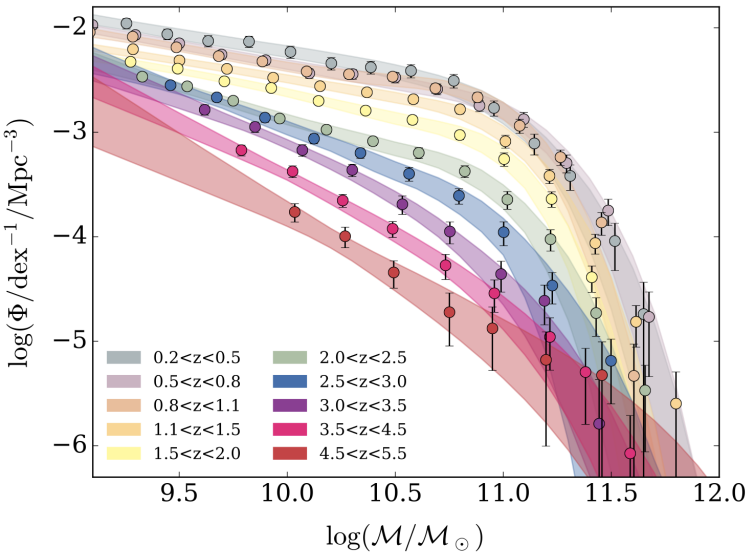

Figure 47: Evolution of the total galaxy stellar mass function between $z = 0.2$ and $z = 5.5$ obtained by Davidzon et. al (2017) [306] for the COSMOS2015 galaxy sample. Credits: Figure 15 of Ref. [306].

$$\rho_\star = \int \mathrm{d}\log M_\star M_\star \frac{\mathrm{d}^2 N}{\mathrm{d}\log M_\star \mathrm{d}V}. \tag{73}$$

The galaxy main sequence

The main sequence (MS) is a well-known relation between the stellar mass and the SFR of star-forming galaxies. This relation has been established both through observational data and theoretical models. Most studies describe it as a power-law relation, whose slope and normalization depend on redshift, with a scatter of $\sigma_{MS} = 0.2 - 0.3$ dex[1]. Figure 48 shows the MS obtained by Speagle et al. (2014) [230] from a compilation of observational studies in the literature. The varying slope of the MS and the two orders of magnitude change in the SFR at fixed mass across different redshifts are clearly visible. The evolution of slope and normalization of the MS is still debated, with relevant differences among various works. Nevertheless, the MS is extremely useful, as it offers a relation between the mass and SFR of star-forming galaxies which can be used for both observational and theoretical purposes. Another point to be highlighted, is that not all galaxies lie on the MS. A family of highly star-forming objects, the so-called starburst galaxies, is found to be $\approx 0.6 - 1$ dex above it. The fraction of starburst galaxies with respect to the total is though to be less than a few

1 The term dex was coined within astrophysics as a convenient unit indicating the order of magnitude of any number or ratio. Specifically, the dex is defined as the number of (possibly fractional) orders of magnitude separating two values. For example, $\log_{10}(5) \approx 0.7$ and $\log_{10}(8) \approx 0.9$, so the ratio of 8 to 5 is ≈ 0.2 dex.

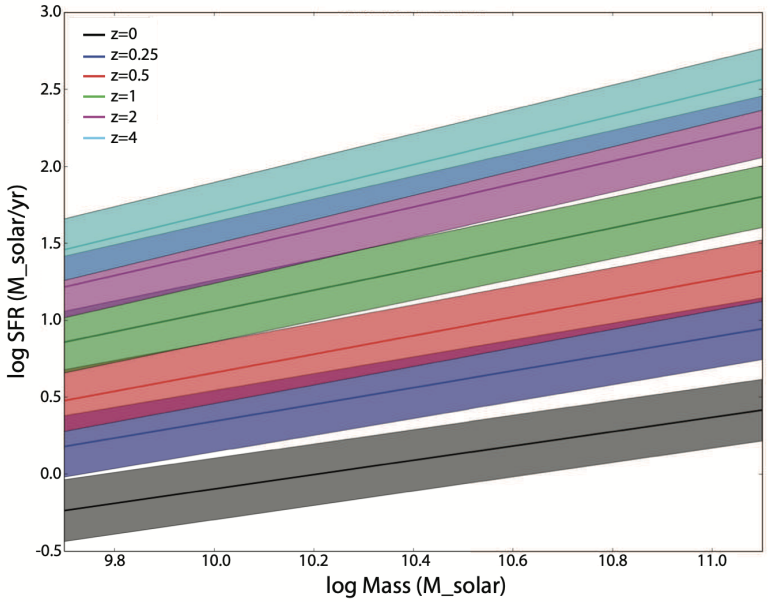

Figure 48: Main sequence (MS) of star-forming galaxies plotted at several redshifts. The widths of the distributions represent the scatters around the best-fit MSs from Speagle et al. (2014) [230]. Credits: Figure 8 of Ref. [230].

percent [227], but since they produce stars at a very high rate, it is important to take into account also their contribution.

The galaxy star formation rate function

The galaxy star formation rate function (SFRF) $d^2N/dV/d\log\psi$ is the number density of galaxies per logarithmic SFR bin. The SFRF is often derived from the UV and IR luminosity functions of galaxies, as luminosity correlates with the SFR [221, 310]. Typically, a galaxy's SFR is linked to its UV luminosity, mainly originating from young, blue stars. However, because dust absorbs UV radiation and re-emits it in the mid/far-IR range, estimating the SFR based solely on UV data can significantly underestimate it. Nonetheless, for galaxies with relatively low SFR ($\psi \lesssim 30-50\,M_\odot/yr$) and minimal dust content, estimating the SFR from UV data alone is still possible using standard UV slope corrections [311]. In contrast, highly star-forming galaxies with $\psi \gtrsim 30-50\,M_\odot/yr$ are much more rich in dust, so that UV corrections tend to fail. Therefore, the estimates of the SFR must be based on far-IR/(sub)mm wide-area surveys [312]. However, given the sensitivity limit of far-IR surveys, the shape of the SFR functions at the bright end becomes progressively more uncertain at $z \gtrsim 3$. Despite these limitations, relevant constraints in the high-redshift regime have been obtained from the combination of deep radio surveys, far-IR/(sub)millimeter stacking and super-deblending techniques, and targeted far-IR/(sub)millimeter observations of significant samples of star-forming galaxies and quasar hosts (see Refs. [76, 77, 307] for a complete review

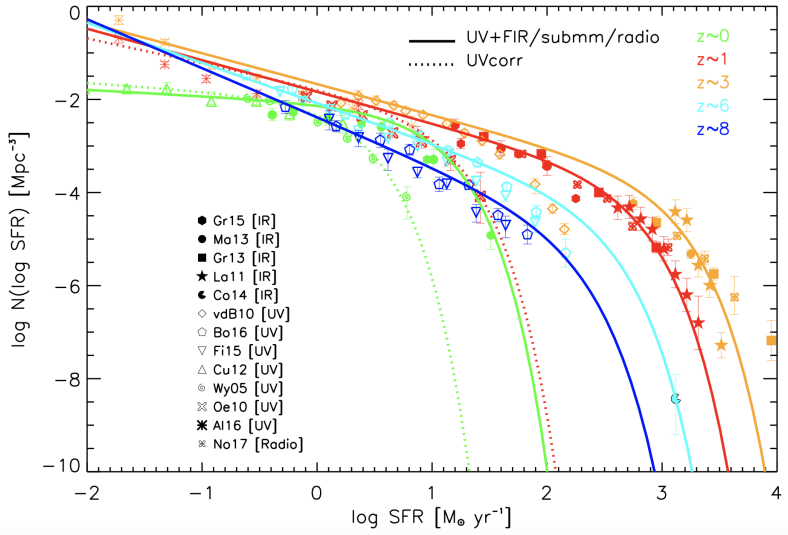

Figure 49: Star formation rate functions (SFRF) at different redshifts computed by Lapi et al. (2017) [307]. Solid lines show the function obtained from UV plus far-IR/(sub)millimeter and radio data, referring to the overall population of galaxies. Dotted lines (only plotted at $z = 0$ and 1) show those from (dust-corrected) UV data, referring to disk galaxies. The data points represent the collection of UV, far-IR/(sub)millimeter, and radio data specified in the caption of the original figure. Credits: Figure 1 of Ref. [307].

of these observations). All these data-sets all well-approximated by a simple Schechter function:

$$\frac{d^2N}{dV\,d\log\psi}(\psi,z) = \mathcal{N}(z)\left(\frac{\psi}{\psi_c(z)}\right)^{1-\alpha_c(z)} \exp\left(-\frac{\psi}{\psi_c(z)}\right), \tag{74}$$

where $\mathcal{N}(z)$, $\psi_c(z)$, and $\alpha_c(z)$ are redshift-dependent fitting parameters [221]. Figure 49, shows the mentioned datasets and the resulting fitted SFRF obtained by Lapi et al. (2017) [307]. Notably, at $z \gtrsim 1$, heavily obscured, highly star-forming galaxies dominate the bright end of the SFRF, representing the progenitors of local massive elliptical galaxies. In contrast, mildly star-forming galaxies populate the faint end, likely evolving into spheroid-like objects with relatively low stellar mass. At $z \lesssim 1$, late-type disk galaxies, with SFRs of a few solar masses per year, are well captured by the UV-inferred SFRF.

Star formation rate density

Another fundamental quantity is the star formation rate density (SFRD), ρ_ψ, which is the stellar mass formed per unit time and volume at a specific redshift. From the SFRF, the cosmic SFR density can be easily estimated as:

$$\rho_\psi(z) = \int d\log\psi\,\psi \frac{d^2N}{d\log\psi\,dV}(\psi,z). \tag{75}$$

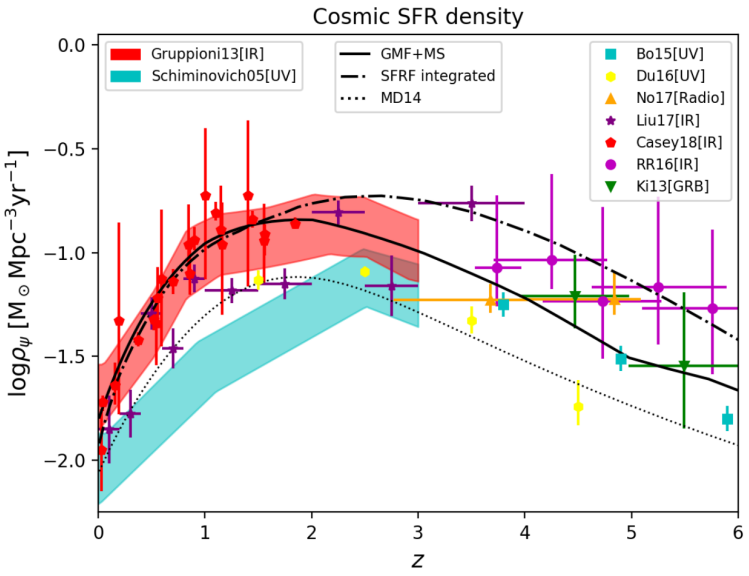

Figure 50: Cosmic star formation rate density as a function of redshift. The black dot-dashed curve is the result of the integration of the measured SFRF. The black solid line shows the result obtained integrating the SFRF reconstructed from the galactic stellar mass functions in combination with the main sequence. For reference, the dotted line shows the determination by Madau & Dickinson [308]. The data points are from the UV, radio, far-IR/(sub)millimeter observations reported in the caption of the original figure. Credits: Figure 2 of Ref. [77].

Another method to estimate the cosmic SFRD is convolving the GSMFs of star forming galaxies at different redshifts with a probability distribution around the MS [215]:

$$\rho_\psi(z) = \int \mathrm{d}\log M_\star \frac{\mathrm{d}^2 N}{\mathrm{d}\log M_\star \mathrm{d}V}(z, M_\star) \frac{\mathrm{d}p}{\mathrm{d}\log\psi}(\psi|z, M_\star) \tag{76}$$

The probability distribution $\mathrm{d}p/\mathrm{d}\log\psi(\psi|z, M_\star)$ simply describes the galaxy distribution in SFR at fixed stellar mass and redshift, according to the observations. For example, in Boco et al. (2021) [77], it is modeled as double Gaussian, one for the galaxies within the MS, and one for starburst galaxies. The cosmic SFRD, as determined from these two methods, is shown in Figure 50. Notably, the SFRD computed using these methods tends to exhibit significantly higher values compared to many previous determinations, including the famous one by Madau & Dickinson [308]. This discrepancy arises from recent discoveries made through IR and far-IR/submm observations with Herschel and ALMA. These observations have unveiled a substantial number of dusty, star-forming galaxies that are strongly attenuated or even invisible in the optical/UV bands. These dusty galaxies, characterized by extremely high levels of star formation ($\sim 50 - 3000 M_\odot/\mathrm{yr}$), have a substantial impact on the overall star formation during the cosmic period between $2 \lesssim z \lesssim 6$ [313, 314].

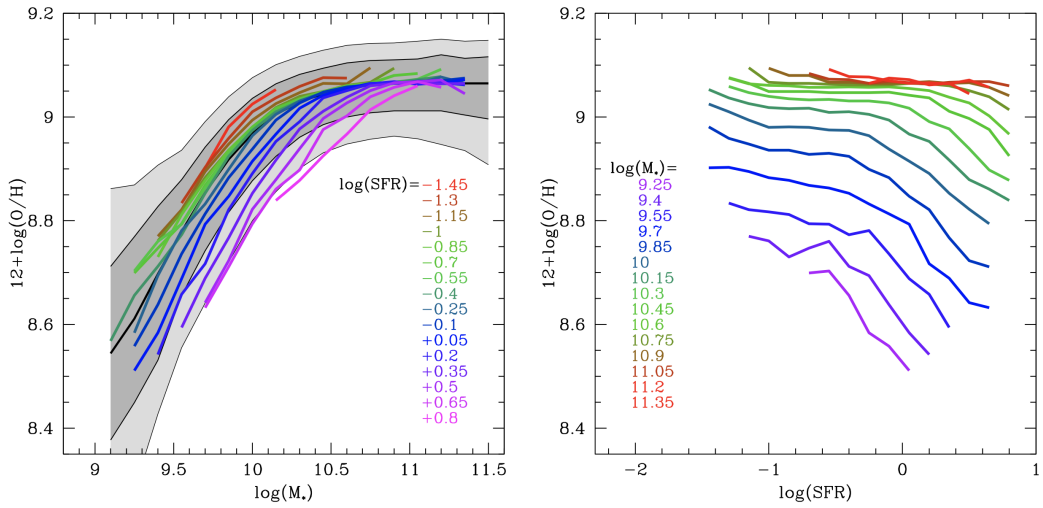

Figure 51: Left panel: mass-metallicity relation of local SDSS galaxies as obtained in Mannucci et al. (2010) [222]. The grey-shaded areas contain 64% and 90% of all SDSS galaxies, with the thick central line showing the median relation. The colored lines show the median metallicity as a function of $M_\star$ of galaxies with different SFR. Right panel: median metallicity as a function of the SFR for galaxies with different $M_\star$. Credits: Figure 1 of Ref. [222].

Chemical evolution and metallicity scaling relations

The gas-phase metallicity significantly impacts the evolution of massive stars, regulating the intensity of stellar winds and hence determining the mass of stellar remnants. Therefore, accurately modeling the metallicity is crucial in calculating the redshift and mass distributions of binary systems. There are several methods to measure the gas-phase metallicity of a galaxy. These methods generally rely on looking for metal recombination emission lines in HII regions [315]. On a global scale, the interplay between the metallicity and other galactic properties, such as the stellar mass and the SFR, is naturally reflected by different scaling relations. These empirical relations carry precious information on the chemical evolution history of galaxies and play a crucial role in determining the the properties of the binary systems that they host.

The mass-metallicity relation (MZR) establishes a correlation between gas-phase metallicity (Z_{gas}), often derived from strong optical oxygen emission lines as 12+log(O/H), and stellar mass ($M_\star$). Empirically observed, the MZR remains valid across objects with stellar masses spanning five orders of magnitude. When considering a fixed stellar mass, the MZR generally suggests a decrease in Z_{gas} at higher redshifts. However, the extent of this redshift-dependent evolution remains the subject of an active debate [316, 317]. The fundamental metallicity relation (FMR) is a three-parameter correlation among $M_\star$, SFR, and Z_{gas}. The inclusion of the SFR accounts for the secondary dependence of metallicity on this quantity. Initially observed by Mannucci et al. (2010) [222] in local SDSS galaxies, this relation suggests that Z_{gas} decreases with increasing SFR at fixed $M_\star$. This observation has been consistently sup-

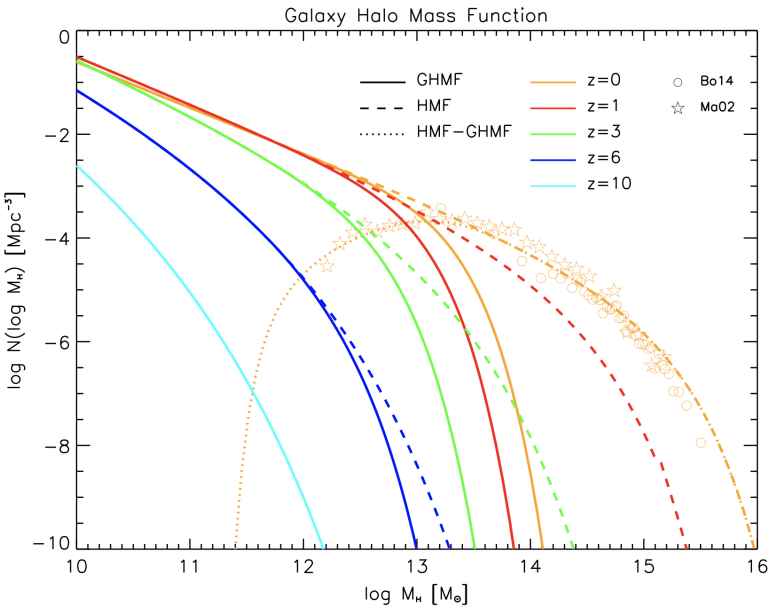

Figure 52: Galaxy halo mass function at various redshifts (solid lines), as obtained by Aversa et al. [241] from the halo mass function (dashed lines) by adding the global subhalo mass function and subtracting the mass function of multiply occupied halos. The dotted line is the resulting group halo mass function at $z = 0$ (obtained subtracting the solid line from the dashed one). The curves are compared with empirical determinations from X-ray and optical observations. Credits: Figure 14 of Ref. [241].

ported by larger data-sets, showing an anti-correlation between Z_{gas} and SFR across galaxies with the same stellar mass and redshift. The FMR is thought to be almost redshift independent, which is supported by observations extending up to $z \sim 3.5$ [223–225]. In the studies presented in this Thesis, I used the FMR to assign metallicities to galaxies with given $M_\star$ and SFR. In Figure 51, I show the FMR for SDSS galaxies, as reported by Mannucci et al. (2010). For a comparison of the binary merger rates computed with the MZR and the FMR, please refer to Boco et. al (2021) [77].

The galaxy halo mass function

Relating the properties of galaxies with those of the associated dark matter halo was fundamental in characterizing the SGWB as a tracer of the LSS. Therefore, I will conclude this Appendix by briefly addressing the galaxy halo mass function (GHMF). The GHMF is the the mass function (i.e., the number density per logarithmic bin of mass) of halos not containing subhalos and possibly hosting only a single galaxy. Indeed, dark matter halos are not standalone entities, but are rather characterized by the presence of many substructures, known as subhalos. Subhalos are smaller and less massive halos orbiting in the potential well of a larger halo and may host small satellite galaxies. In order to characterize the galaxy distribution as a tracer of the underlying dark

matter distribution, it is necessary to identify those halos that are more likely to host only one galaxy. In this Thesis, I used the GHMF computed by Aversa et. al (2015) [241], shown in Figure 52. There, the authors derive the mass function associated with halos hosting one individual galaxy following a computation that includes two steps: (i) accounting for the possibility that a halo contains various subhalos, and (ii) probabilistically excluding halos corresponding to galaxy systems rather than to individual galaxies.

Once we have statistically associated each galaxy with its own dark matter halo (hosting only one galaxy), it is possible to relate the various galactic properties to the halo mass M_h. This is usually done through abundance matching, which is a standard procedure to derive a monotonic relationship between the galaxy and the halo properties by matching the corresponding number densities. For example, in Equation (103) of Chapter 2, I used an abundance matching to link the SFR with M_h. This was necessary for assigning to galaxies with a given SFR a bias $b(z, \psi)$, which crucially enters in the computation of the SGWB bias $b_\Omega(z)$ of Equation (104). Indeed, there are many different prescriptions for evaluating the bias of dark matter halos as a function of their mass M_h. I used the $b(z, M_H)$ prescription from Sheth et al. (1999) [242], approximated as in Lapi&Danese (2014) [243].

REFINED DEFINITION OF DETECTION THRESHOLD AND MAGNIFICATION BIAS

B

In this Appendix, I briefly review the theoretical model for the SGWB developed in Chapter 2 and used throughout all this Thesis. In particular, I report here a slightly improved version which I adopted in Chapters 3 and 4.

As I extensively discussed, a crucial tool for the description of any SGWB is its isotropic energy density $\Omega_{gw}(f)$. This quantity can be computed summing the contributions of all the GW events whose signal-to-noise ratio is below a given detection threshold $\bar{\rho}$. For compact binary coalescences, the expression for $\Omega_{gw}(f)$ is:

$$\Omega_{gw}(f) = \frac{8\pi G f}{3H_0^3 c^2} \int dz \int d\mathcal{M}_c \frac{\mathcal{R}(\mathcal{M}_c, z)}{(1+z)h(z)} \frac{dE}{df}(f_e(z)|\mathcal{M}_c) \times \\ \times \int_0^\infty d\rho \epsilon_{\bar{\rho}}(\rho) P_\rho(\rho|\mathcal{M}_c, z), \tag{77}$$

where $\mathcal{M}_c$ is the chirp mass, $f_e = (1+z)f$ is the frequency at the source frame, $\mathcal{R} = d^2\dot{N}/dVd\mathcal{M}_c$ is the intrinsic merger rate, $h(z) = [\Omega_M(1+z)^3 + 1 - \Omega_M]^{1/2}$, $dE/df(f_e(z)|\mathcal{M}_c)$ is the energy spectrum of the GW signal emitted by a single binary, ρ is the signal-to-noise ratio associated to a certain GW event, $\bar{\rho}$ is the detection threshold, and $P_\rho(\rho|\mathcal{M}_c, z)$ is the sky-averaged distribution of signal-to-noise ratio for a given detector at given chirp mass and redshift. The difference between Equation (77) and the corresponding one in Chapter 2, Equation (92), is in the presence of the function $\epsilon_{\bar{\rho}}(\rho)$. We introduce $\epsilon_{\bar{\rho}}(\rho)$ as an efficiency function that sets the sharpness of the signal-to-noise ratio threshold. In the simplest case, which we adopted in Chapter 2, $\epsilon_{\bar{\rho}}$ is a step function centered around $\bar{\rho}$, so that its effect is to sharply remove all the GW events whose signal-to-noise ratio is greater than $\bar{\rho}$. In the studies presented in Chapters 3 and 4, instead, we opted for a smooth threshold given by an error function with amplitude equal to the square root of the variance of the sky-averaged distribution of ρ.

In order to characterize the SGWB as a tracer of the LSS and evaluate its kernel by means of Equation (42), we need to compute its redshift distribution $d\Omega_{gw}/dz$, its bias b_Ω and its magnification bias s_Ω, whose expressions are reported in Section 2.4. Clearly, the new definition of detection threshold particularly affects the magnification bias, which depends on those events that, due to the lensing magnification, move from below to above the threshold. Moreover, with respect to the original expression of Equation (79), we slightly modify the definition of magnification bias, simply by a numerical factor $4/5$. Both definitions are equally used in the literature and, in this case, it was easier to work with this other definition:

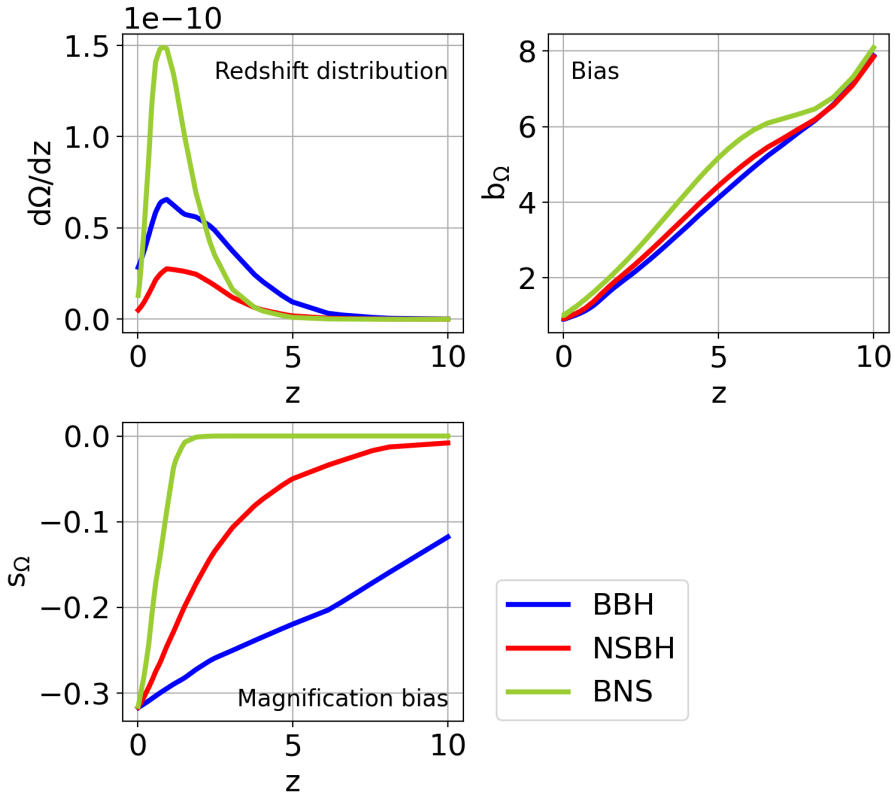

Figure 53: Redshift distribution, bias and magnification bias of the SGWB energy density for BBHs (blue), NSBHs (red) and BNSs (green), for ET at $f_{ref} = 65$ Hz.

$$\frac{d\Omega_{gw}^{lensed}}{dz} \equiv \frac{d\Omega_{gw}}{dz}\left[1 + \kappa(s_\Omega - 1)\right], \tag{78}$$

where κ is the lensing convergence, so that

$$s_{\Omega,\bar{\rho}}(z, f) = -\frac{1}{2}\frac{d\log_{10}\left(\frac{d\Omega_{gw}(f,z,<\rho)}{dz}\right)}{d\log_{10}\rho}\bigg|_{\rho=\bar{\rho}}. \tag{79}$$

Figure 53 shows the redshift distribution, bias and magnification bias of the residual SGWB for ET at $f_{ref} = 65$ Hz, computed with the slightly different prescriptions discussed in this Appendix.

GROWTH OF SUPERMASSIVE BLACK HOLE SEEDS VIA GASEOUS DYNAMICAL FRICTION

C

In this Appendix, I briefly review the supermassive black hole (SMBH) seed growth mechanism recently proposed in Boco et al. (2020, 2021) [277, 278]. This new mechanism envisages the migration of stellar compact remnants – and eventually primordial black holes (PBHs) – via gaseous dynamical friction toward the central high-density regions of the star-forming progenitors of local early-type galaxies (ETGs) at $z \gtrsim 1$. Once in the galactic center, the remnants undergo consecutive mergers giving birth to the SMBH seed.

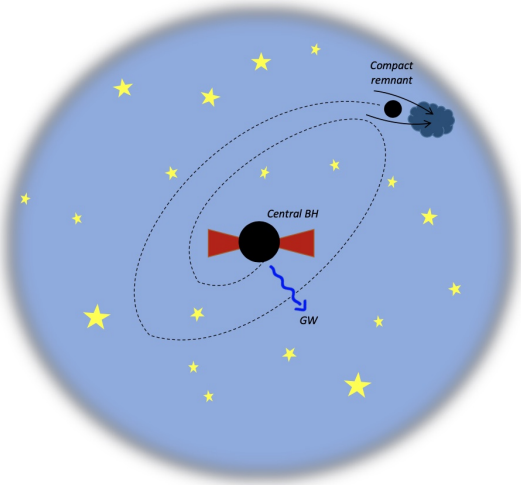

Figure 54: Schematic representation of the SMBH seed formation process involving repeated mergers with stellar remnants sinking into the galactic center due to gaseous dynamical friction. Credits: Figure 1 of Ref. [277].

The recent observations of high redshift quasars ($z \gtrsim 7$), powered by SMBHs with $M \gtrsim 10^9\ M_\odot$, have created tension between the estimated age of the Universe at those redshifts and the typical timescales of SMBH growth [284–287]. Indeed, the age of the Universe at $z \gtrsim 7$ was around $t_{age} \sim 0.7$ Gyr, while the time to grow a SMBH with $M \gtrsim 10^9\ M_\odot$ through standard Eddington accretion is around $t_{acc} \sim 0.7$ Gyr. Possible solutions to this conundrum are divided in two classes: those envisaging a faster super-Eddington accretion, and those proposing a rapid formation of a massive seed that is subsequently further grown through standard Eddington accretion. The mechanisms proposed by Boco et. al (2020,2021) belongs to the second category and exploits the process of gaseous dynamical friction. An object moving in a gaseous environment

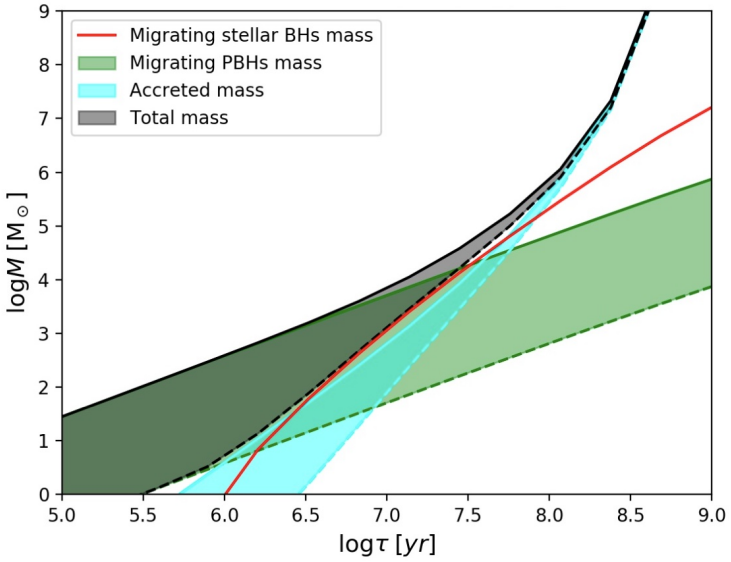

Figure 55: Growth of the central BH mass as a function of the galactic age τ, due to the gaseous dynamical friction process. The red line, and the green, cyan and black shaded areas show the contributions of stellar remnants, PBHs, gas accretion, and the total accretion, respectively. The shaded areas show the effect of varying the PBH-to-DM (dark matter) fraction from 0.01 (dashed edge lines) to 1 (solid edge lines). Credits: Figure 1 of Ref. [278].

feels the dynamical friction force, given by the interaction between the object itself and its gravitationally-induced gas wake [318]:

$$F_{DF} \propto \frac{4\pi G^2 m^2 \rho^2}{v^2}, \tag{80}$$

where m and v are the mass and the velocity of the object, respectively, and ρ is the density of the gaseous environment. This dynamical drag subtracts energy and angular momentum from the moving object, making it sink toward the galactic center. The idea behind the proposed method, schematically depicted in Figure 54, is therefore the following. The central SMBH seed is formed via subsequent mergers of stellar (or primordial) BHs, migrating to the central region of the galaxy via gaseous dynamical friction. In recent years, the radio interferometer ALMA observed a large population of star-forming dust-obscured galaxies at high redshift, featuring a high SFR, $\psi \sim 10^2 - 10^3\, M_\odot/\mathrm{yr}$, a huge gas reservoir, $M_{gas} \sim 10^{10} - 10^{12}\, M_\odot$, and a compact size, $R \sim 1$ kpc. These galaxies have extremely high gas densities and a large number of stars and compact remnant available, which makes them perfect candidates for the dynamical friction-induced growth process to occur.

Running a series of dynamical simulations, the authors of Boco et al. (2020) [277] derived a fitting formula for the dynamical friction migration timescale, τ_{DF}. They then showed that, under reasonable assumptions and initial conditions, this process can build up a central BH of $\sim 10^4 - 10^6\, M_\odot$ within some $10^7 - 10^8$ yr, so effectively providing heavy seeds before standard Eddington

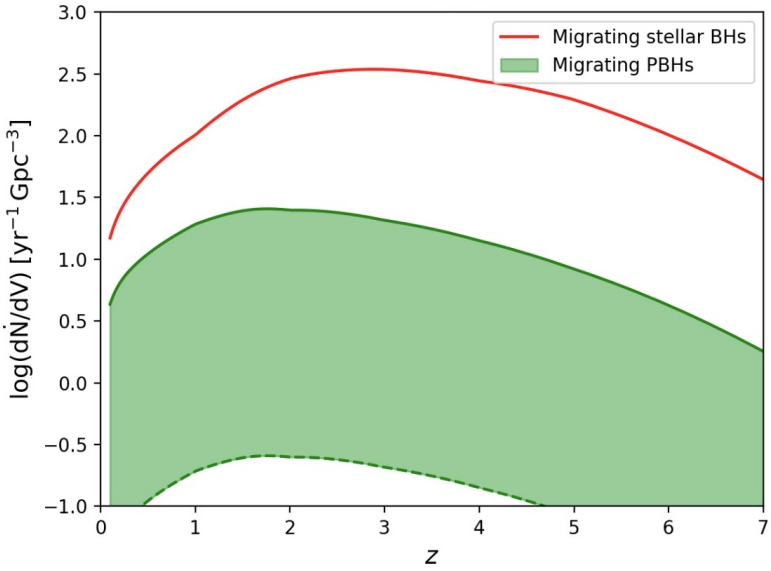

Figure 56: Cosmic merger rate density as a function of redshift, due to the gaseous dynamical friction process. The red solid line refers to migrating stellar compact remnants, the green shaded area to migrating PBHs. Credits: Figure 2 of Ref. [278].

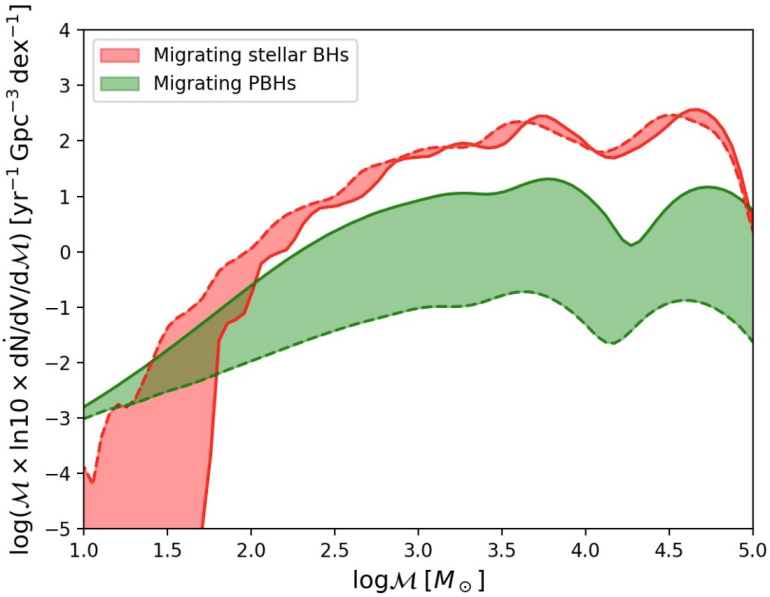

Figure 57: Cosmic chirp mass distribution at $z \sim 2$. The red shaded area refers to migrating stellar compact remnants, while the green one to migrating PBHs. Credits: Figure 3 of Ref. [278].

accretion takes over to become the dominant process for further SMBH growth. The total central BH growth as a function of time is shown in Figure 55, together with the contribution of different accretion processes. The merger rates per unit chirp mass in a galaxy with spatially-integrated SFR ψ at redshift z can be computed arguing that the merger rates of the migrating compact objects

contributing to the growth of the central BH seed at a time τ depend on the birth rates of such objects at a time $\tau - \tau_{DF}$, weighted by the corresponding distributions of initial positions and velocities. The resulting merger rate densities as a function of redshift and chirp mass are shown in Figures 56 and 57. The specific features of the merger rates are commented in Refs. [277, 278], and can be used to compute the GW signals emitted during the entire process. Indeed, the repeated mergers of stellar and primordial BHs with the central growing seed copiously produce GWs, whose detection can be used to test this scenario. In Boco et al. (2020) [277], the authors compute the expected detection rate for individual GW events originating from this mechanism as possibly detected by forthcoming GW interferometers – namely, the ET, the LISA and the DECIGO. Since the typical masses of the binaries involved in this process can be small (stellar, at the beginning of the process) as well as very large (supermassive, at the end of the process), the resulting GW signals span a wide range of frequencies. In Boco et al. (2021) [278], to which I actively contributed, the SGWB produced during this process is also computed. The energy density of such SGWB is plotted as a function of the observed frequency in Figure 34 of Chapter 4, where I discuss the detection prospects for both the intensity and the anisotropies of such signal with constellations of space-based detectors.

BIBLIOGRAPHY

[1] A. Einstein. "Approximative integration of the field equations of gravitation." In: *Sitzungsber. Preuss. Akad. Wiss. Berlin* 1916 (1916), pp. 688–696.

[2] A. Einstein. "About gravitational waves." In: *Sitzungsber. Preuss. Akad. Wiss. Berlin* 1918 (1918), pp. 154–167.

[3] A. Einstein. "The foundation of the general theory of relativity." In: *Annalen Phys.* 49.7 (1916). Ed. by J.-P. Hsu and D. Fine, pp. 769–822. DOI: 10.1002/andp.19163540702.

[4] J. Aasi et al. "Advanced LIGO." In: *Class. Quant. Grav.* 32 (2015), p. 074001. DOI: 10.1088/0264-9381/32/7/074001. arXiv: 1411.4547 [gr-qc].

[5] F. Arcenese et al. "Advanced Virgo: a second-generation interferometric gravitational wave detector." In: *Classical and Quantum Gravity* 32.2 (Jan. 2015), p. 024001. DOI: 10.1088/0264-9381/32/2/024001. arXiv: 1408.3978 [gr-qc].

[6] B. P. Abbott et al. "GW170817: Observation of Gravitational Waves from a Binary Neutron Star Inspiral." In: *Phys. Rev. Lett.* 119.16 (2017). DOI: 10.1103/PhysRevLett.119.161101. arXiv: 1710.05832 [gr-qc].

[7] B. P. Abbott et al. "Multi-messenger Observations of a Binary Neutron Star Merger." In: *Astrophys. Journal Letters* 848.2 (2017), p. L12. DOI: 10.3847/2041-8213/aa91c9. arXiv: 1710.05833 [astro-ph.HE].

[8] The LIGO Scientific Collaboration, the Virgo Collaboration, and the KAGRA Collaboration. "GWTC-3: Compact Binary Coalescences Observed by LIGO and Virgo During the Second Part of the Third Observing Run." In: *arXiv e-prints* (Nov. 2021). DOI: 10.48550/arXiv.2111.03606. arXiv: 2111.03606 [gr-qc].

[9] R. Abbott et al. "Population of Merging Compact Binaries Inferred Using Gravitational Waves through GWTC-3." In: *Phys. Rev. X* 13.1 (2023). DOI: 10.1103/PhysRevX.13.011048. arXiv: 2111.03634 [astro-ph.HE].

[10] K. Somiya. "Detector configuration of KAGRA: The Japanese cryogenic gravitational-wave detector." In: *Class. Quant. Grav.* 29 (2012). Ed. by M. Hannam, P. Sutton, S. Hild, and C. van den Broeck, p. 124007. DOI: 10.1088/0264-9381/29/12/124007. arXiv: 1111.7185 [gr-qc].

[11] R. Abbott et al. "Upper limits on the isotropic gravitational-wave background from Advanced LIGO and Advanced Virgo's third observing run." In: *Phys. Rev. D* 104.2 (2021). DOI: 10.1103/PhysRevD.104.022004. arXiv: 2101.12130 [gr-qc].

[12] R. Abbott et al. "Search for anisotropic gravitational-wave backgrounds using data from Advanced LIGO and Advanced Virgo first three observing runs." In: *Phys. Rev. D* 104.2 (2021). DOI: 10.1103/PhysRevD.104.022005. arXiv: 2103.08520 [gr-qc].

[13] G. Agazie et al. "The NANOGrav 15 yr data set: evidence for a GW background." In: *Astrophys. J. Lett.* 951.1 (2023), p. L8. DOI: 10.3847/2041-8213/acdac6. arXiv: 2306.16213 [astro-ph.HE].

[14] J. Antoniadis et al. "The second data release from the European Pulsar Timing Array III. Search for gravitational wave signals." In: *Astron. Astrophys.* 678 (2023), A50. DOI: 10.1051/0004-6361/202346844. arXiv: 2306.16214 [astro-ph.HE].

[15] D. J. Reardon et al. "Search for an Isotropic Gravitational-wave Background with the Parkes Pulsar Timing Array." In: *Astrophys. J. Lett.* 951.1 (2023), p. L6. DOI: 10.3847/2041-8213/acdd02. arXiv: 2306.16215 [astro-ph.HE].

[16] G. Agazie et al. "The NANOGrav 15 yr data set: constraints on supermassive black hole binaries from the gravitational-wave background." In: *Astrophys. J. Lett.* 952.2 (2023), p. L37. DOI: 10.3847/2041-8213/ace18b. arXiv: 2306.16220 [astro-ph.HE].

[17] B. Allen and A. C. Ottewill. "Detection of anisotropies in the gravitational wave stochastic background." In: *Phys. Rev. D* 56 (1997), pp. 545–563. DOI: 10.1103/PhysRevD.56.545. arXiv: gr-qc/9607068.

[18] C. Conneely, A. H. Jaffe, and C. M. F. Mingarelli. "On the Amplitude and Stokes Parameters of a SGWB." In: *Mon. Not. Roy. Astron. Soc.* 487.1 (2019), pp. 562–579. DOI: 10.1093/mnras/stz1022. arXiv: 1808.05920 [astro-ph.CO].

[19] A. Renzini et al. "Comparison of maximum-likelihood mapping methods for gravitational-wave backgrounds." In: *Phys. Rev. D* 105.2 (2022), p. 023519. DOI: 10.1103/PhysRevD.105.023519. arXiv: 2107.02292 [gr-qc].

[20] B. Allen and J. D. Romano. "Detecting a stochastic background of gravitational radiation: Signal processing strategies and sensitivities." In: *Phys. Rev. D* 59 (1999), p. 102001. DOI: 10.1103/PhysRevD.59.102001. arXiv: gr-qc/9710117.

[21] C. J. Moore, R. H. Cole, and C. P. L. Berry. "Gravitational-wave sensitivity curves." In: *Class. Quant. Grav.* 32.1 (2015), p. 015014. DOI: 10.1088/0264-9381/32/1/015014. arXiv: 1408.0740 [gr-qc].

[22] C. M. F. Mingarelli, S. R. Taylor, B. S. Sathyaprakash, and W. M. Farr. "Understanding $\Omega_{gw}(f)$ in Gravitational Wave Experiments." In: (Nov. 2019). arXiv: 1911.09745 [gr-qc].

[23] J. Romano and N. Cornish. "Detection methods for stochastic GW backgrounds: a unified treatment." In: *Living Rev. Rel.* 20.1 (2017), p. 2. DOI: 10.1007/s41114-017-0004-1. arXiv: 1608.06889 [gr-qc].

[24] S. G. Crowder, R. Namba, V. Mandic, S. Mukohyama, and M. Peloso. "Measurement of Parity Violation in the Early Universe using Gravitational-wave Detectors." In: *Phys. Lett. B* 726 (2013), pp. 66–71. DOI: 10.1016/j.physletb.2013.08.077. arXiv: 1212.4165 [astro-ph.CO].

[25] V. Domcke, J. Garcia-Bellido, M. Peloso, M. Pieroni, A. Ricciardone, L. Sorbo, and G. Tasinato. "Measuring the net circular polarization of the stochastic gravitational wave background with interferometers." In: *JCAP* 05 (2020), p. 028. DOI: 10.1088/1475-7516/2020/05/028. arXiv: 1910.08052 [astro-ph.CO].

[26] G. Orlando, M. Pieroni, and A. Ricciardone. "Measuring Parity Violation in the Stochastic Gravitational Wave Background with the LISA-Taiji network." In: *JCAP* 03 (2021), p. 069. DOI: 10.1088/1475-7516/2021/03/069. arXiv: 2011.07059 [astro-ph.CO].

[27] K. Martinovic, C. Badger, M. Sakellariadou, and V. Mandic. "Searching for parity violation with the LIGO-Virgo-KAGRA network." In: *Phys. Rev. D* 104.8 (2021), p. L081101. DOI: 10.1103/PhysRevD.104.L081101. arXiv: 2103.06718 [gr-qc].

[28] G. Cusin, R. Durrer, and P. G. Ferreira. "Polarization of a stochastic gravitational wave background through diffusion by massive structures." In: *Phys. Rev. D* 99.2 (2019), p. 023534. DOI: 10.1103/PhysRevD.99.023534. arXiv: 1807.10620 [astro-ph.CO].

[29] L. Valbusa Dall'Armi, A. Nishizawa, A. Ricciardone, and S. Matarrese. "Circular Polarization of the Astrophysical Gravitational Wave Background." In: *Phys. Rev. Lett.* 131.4 (2023), p. 041401. DOI: 10.1103/PhysRevLett.131.041401. arXiv: 2301.08205 [astro-ph.CO].

[30] A. G. Riess, S. Casertano, W. Yuan, L. M. Macri, and D. Scolnic. "Large Magellanic Cloud Cepheid Standards Provide a 1% Foundation for the Determination of the Hubble Constant and Stronger Evidence for Physics beyond ΛCDM." In: *Astrophys. J.* 876.1 (2019), p. 85. DOI: 10.3847/1538-4357/ab1422. arXiv: 1903.07603 [astro-ph.CO].

[31] A. G. Riess et al. "A Comprehensive Measurement of the Local Value of the Hubble Constant with 1 km/s/Mpc Uncertainty from the Hubble Space Telescope and the SHoES Team." In: *Astrophys. J. Lett.* 934.1 (2022), p. L7. DOI: 10.3847/2041-8213/ac5c5b. arXiv: 2112.04510 [astro-ph.CO].

[32] Planck Collaboration. "Planck 2018 results. VI. Cosmological parameters." In: *A&A* 641, A6 (Sept. 2020), A6. DOI: 10.1051/0004-6361/201833910. arXiv: 1807.06209 [astro-ph.CO].

[33] E. Di Valentino, O. Mena, S. Pan, L. Visinelli, W. Yang, A. Melchiorri, D. F. Mota, A. G. Riess, and J. Silk. "In the realm of the Hubble tension—a review of solutions." In: *Class. Quant. Grav.* 38.15 (2021). DOI: 10.1088/1361-6382/ac086d. arXiv: 2103.01183 [astro-ph.CO].

[34] L. Pagano, L. Salvati, and A. Melchiorri. "New constraints on primordial gravitational waves from Planck 2015." In: *Phys. Lett. B* 760 (2016), pp. 823–825. DOI: 10.1016/j.physletb.2016.07.078. arXiv: 1508.02393 [astro-ph.CO].

[35] M. Maggiore. "Gravitational wave experiments and early universe cosmology." In: *Phys. Rept.* 331 (2000), pp. 283–367. DOI: 10.1016/S0370-1573(99)00102-7. arXiv: gr-qc/9909001.

[36] R. A. Isaacson. "Gravitational Radiation in the Limit of High Frequency. I. The Linear Approximation and Geometrical Optics." In: *Phys. Rev.* 166 (5 1968), pp. 1263–1271. DOI: 10.1103/PhysRev.166.1263.

[37] T. Regimbau. "The astrophysical GW stochastic background." In: *Research in Astronomy and Astrophysics* 11 (2011), pp. 369–390. DOI: 10.1088/1674-4527/11/4/001. arXiv: 1101.2762 [astro-ph.CO].

[38] N. J. Cornish and J. D. Romano. "When is a gravitational-wave signal stochastic?" In: *Phys. Rev. D* 92.4 (2015), p. 042001. DOI: 10.1103/PhysRevD.92.042001. arXiv: 1505.08084 [gr-qc].

[39] N. Christensen. "Stochastic Gravitational-Wave Backgrounds." In: *Rept. Prog. Phys.* 82.1 (2019), p. 016903. DOI: 10.1088/1361-6633/aae6b5. arXiv: 1811.08797 [gr-qc].

[40] C. Caprini and D. Figueroa. "Cosmological backgrounds of gravitational waves." In: *Class. Quant. Grav.* 35.16 (2018). DOI: 10.1088/1361-6382/aac608. arXiv: 1801.04268 [astro-ph.CO].

[41] A. Renzini et al. "Stochastic Gravitational-Wave Backgrounds: Current Detection Efforts and Future Prospects." In: *Galaxies* 10.1 (2022), p. 34. DOI: 10.3390/galaxies10010034. arXiv: 2202.00178 [gr-qc].

[42] M. C. Guzzetti, N. Bartolo, M. Liguori, and S. Matarrese. "Gravitational waves from inflation." In: *Riv. Nuovo Cim.* 39.9 (2016), pp. 399–495. DOI: 10.1393/ncr/i2016-10127-1. arXiv: 1605.01615 [astro-ph.CO].

[43] M. Tristram et al. "Improved limits on the tensor-to-scalar ratio using BICEP and Planck data." In: *Phys. Rev. D* 105.8 (2022), p. 083524. DOI: 10.1103/PhysRevD.105.083524. arXiv: 2112.07961 [astro-ph.CO].

[44] L. Sorbo. "Parity violation in the Cosmic Microwave Background from a pseudoscalar inflaton." In: *JCAP* 06 (2011), p. 003. DOI: 10.1088/1475-7516/2011/06/003. arXiv: 1101.1525 [astro-ph.CO].

[45] N. Barnaby, J. Moxon, R. Namba, M. Peloso, G. Shiu, and P. Zhou. "Gravity waves and non-Gaussian features from particle production in a sector gravitationally coupled to the inflaton." In: *Phys. Rev. D* 86 (2012), p. 103508. DOI: 10.1103/PhysRevD.86.103508. arXiv: 1206.6117 [astro-ph.CO].

[46] L. Senatore, E. Silverstein, and M. Zaldarriaga. "New Sources of Gravitational Waves during Inflation." In: *JCAP* 08 (2014), p. 016. DOI: 10.1088/1475-7516/2014/08/016. arXiv: 1109.0542 [hep-th].

[47] K. N. Ananda, C. Clarkson, and D. Wands. "The Cosmological gravitational wave background from primordial density perturbations." In: *Phys. Rev. D* 75 (2007), p. 123518. DOI: 10.1103/PhysRevD.75.123518. arXiv: gr-qc/0612013.

[48] S. Clesse, J. García-Bellido, and. Orani. "Detecting the Stochastic Gravitational Wave Background from Primordial Black Hole Formation." In: (Dec. 2018). arXiv: 1812.11011 [astro-ph.CO].

[49] J. Garcia-Bellido, M. Peloso, and C. Unal. "Gravitational Wave signatures of inflationary models from Primordial Black Hole Dark Matter." In: *JCAP* 09 (2017), p. 013. DOI: 10.1088/1475-7516/2017/09/013. arXiv: 1707.02441 [astro-ph.CO].

[50] S. Y. Khlebnikov and I. I. Tkachev. "Classical decay of inflaton." In: *Phys. Rev. Lett.* 77 (1996), pp. 219–222. DOI: 10.1103/PhysRevLett.77.219. arXiv: hep-ph/9603378.

[51] P. Amaro-Seoane et al. "Laser Interferometer Space Antenna." In: *arXiv e-prints* (Feb. 2017). arXiv: 1702.00786 [astro-ph.IM].

[52] N. Bartolo et al. "Science with the space-based interferometer LISA. IV: Probing inflation with gravitational waves." In: *JCAP* 12 (2016). DOI: 10.1088/1475-7516/2016/12/026. arXiv: 1610.06481 [astro-ph.CO].

[53] F. R. Bouchet et al. "COrE (Cosmic Origins Explorer) A White Paper." In: (Feb. 2011). arXiv: 1102.2181 [astro-ph.CO].

[54] T. Matsumura et al. "Mission design of LiteBIRD." In: *J. Low Temp. Phys.* 176 (2014), p. 733. DOI: 10.1007/s10909-013-0996-1. arXiv: 1311.2847 [astro-ph.IM].

[55] P. A. R. Ade et al. "A Measurement of the Cosmic Microwave Background B-Mode Polarization Power Spectrum at Sub - Degree Scales with POLARBEAR." In: *Astrophys. J.* 794.2 (2014). [Erratum: Astrophys.J. 848, 73 (2017)], p. 171. DOI: 10.1088/0004-637X/794/2/171. arXiv: 1403.2369 [astro-ph.CO].

[56] K. N. Abazajian et al. "CMB-S4 Science Book, First Edition." In: (Oct. 2016). arXiv: 1610.02743 [astro-ph.CO].

[57] P. Ade et al. "The Simons Observatory: Science goals and forecasts." In: *JCAP* 02 (2019), p. 056. DOI: 10.1088/1475-7516/2019/02/056. arXiv: 1808.07445 [astro-ph.CO].

[58] A. Kosowsky, M. S. Turner, and R. Watkins. "Gravitational radiation from colliding vacuum bubbles." In: *Phys. Rev. D* 45 (1992), pp. 4514–4535. DOI: 10.1103/PhysRevD.45.4514.

[59] C. Caprini, R. Durrer, and G. Servant. "Gravitational wave generation from bubble collisions in first-order phase transitions: An analytic approach." In: *Phys. Rev. D* 77 (2008). DOI: 10.1103/PhysRevD.77.124015. arXiv: 0711.2593 [astro-ph].

[60] S. J. Huber and T. Konstandin. "Gravitational Wave Production by Collisions: More Bubbles." In: *JCAP* 09 (2008), p. 022. DOI: 10.1088/1475-7516/2008/09/022. arXiv: 0806.1828 [hep-ph].

[61] C. Caprini, R. Durrer, and G. Servant. "The stochastic gravitational wave background from turbulence and magnetic fields generated by a first-order phase transition." In: *JCAP* 12 (2009), p. 024. DOI: 10.1088/1475-7516/2009/12/024. arXiv: 0909.0622 [astro-ph.CO].

[62] C. Caprini and R. Durrer. "Gravitational waves from stochastic relativistic sources: Primordial turbulence and magnetic fields." In: *Phys. Rev. D* 74 (2006), p. 063521. DOI: 10.1103/PhysRevD.74.063521. arXiv: astro-ph/0603476.

[63] M. Hindmarsh, S. J. Huber, K. Rummukainen, and D. J. Weir. "Gravitational waves from the sound of a first order phase transition." In: *Phys. Rev. Lett.* 112 (2014), p. 041301. DOI: 10.1103/PhysRevLett.112.041301. arXiv: 1304.2433 [hep-ph].

[64] M. Hindmarsh, S. J. Huber, K. Rummukainen, and D. J. Weir. "Numerical simulations of acoustically generated gravitational waves at a first order phase transition." In: *Phys. Rev. D* 92.12 (2015), p. 123009. DOI: 10.1103/PhysRevD.92.123009. arXiv: 1504.03291 [astro-ph.CO].

[65] C. Caprini et al. "Science with the space-based interferometer eLISA. II: Gravitational waves from cosmological phase transitions." In: *JCAP* 04 (2016), p. 001. DOI: 10.1088/1475-7516/2016/04/001. arXiv: 1512.06239 [astro-ph.CO].

[66] M. Sakellariadou. "Gravitational waves emitted from infinite strings." In: *Phys. Rev. D* 42 (1990). [Erratum: Phys.Rev.D 43, 4150 (1991)], pp. 354–360. DOI: 10.1103/PhysRevD.42.354.

[67] T. Damour and A. Vilenkin. "Gravitational radiation from cosmic (super)strings: Bursts, stochastic background, and observational windows." In: *Phys. Rev. D* 71 (2005), p. 063510. DOI: 10.1103/PhysRevD.71.063510. arXiv: hep-th/0410222.

[68] X. Siemens, V. Mandic, and J. Creighton. "Gravitational wave stochastic background from cosmic (super)strings." In: *Phys. Rev. Lett.* 98 (2007), p. 111101. DOI: 10.1103/PhysRevLett.98.111101. arXiv: astro-ph/0610920.

[69] P. Auclair et al. "Probing the gravitational wave background from cosmic strings with LISA." In: *JCAP* 04 (2020). DOI: 10.1088/1475-7516/2020/04/034. arXiv: 1909.00819 [astro-ph.CO].

[70] V. Kalogera and G. Baym. "The Maximum Mass of a Neutron Star." In: *The Astrophysical Journal* 470.1 (1996), p. L61. DOI: 10.1086/310296.

[71] F. Özel, D. Psaltis, R. Narayan, and J. E. McClintock. "The Black Hole Mass Distribution in the Galaxy." In: *The Astrophys. J.* 725.2 (Dec. 2010), pp. 1918–1927. DOI: 10.1088/0004-637X/725/2/1918. arXiv: 1006.2834 [astro-ph.GA].

[72] W. M. Farr, N. Sravan, A. Cantrell, L. Kreidberg, C. D. Bailyn, I. Mandel, and V. Kalogera. "The Mass Distribution of Stellar-mass Black Holes." In: *The Astrophys. J.* 741.2, 103 (Nov. 2011), p. 103. DOI: 10.1088/0004-637X/741/2/103. arXiv: 1011.1459 [astro-ph.GA].

[73] A. Gupta et al. "Black holes in the low mass gap: implications for gravitational wave observations." In: *Phys. Rev. D* 101.10 (2020), p. 103036. DOI: 10.1103/PhysRevD.101.103036. arXiv: 1909.05804 [gr-qc].

[74] P. Amaro Seoane et al. "Astrophysics with the Laser Interferometer Space Antenna." In: *Living Rev. Rel.* 26.1 (2023), p. 2. DOI: 10.1007/s41114-022-00041-y. arXiv: 2203.06016 [gr-qc].

[75] T. Callister, M. Fishbach, D. Holz, and W. Farr. "Shouts and murmurs: combining individual gravitational-wave sources with the stochastic background to measure the history of binary black hole mergers." In: *Astrophys. J. Lett.* 896.2 (2020). DOI: 10.3847/2041-8213/ab9743. arXiv: 2003.12152 [astro-ph.HE].

[76] L. Boco, A. Lapi, S. Goswami, F. Perrotta, C. Baccigalupi, and L. Danese. "Merging Rates of Compact Binaries in Galaxies: Perspectives for Gravitational Wave Detections." In: *The Astrophyscal Journal* (July 2019). DOI: 10.3847/1538-4357/ab328e. arXiv: 1907.06841 [astro-ph.GA].

[77] L. Boco, A. Lapi, M. Chruslinska, D. Donevski, A. Sicilia, and L. Danese. "Evolution of Galaxy Star Formation and Metallicity: Impact on Double Compact Objects Mergers." In: *Astrophys. J.* 907.2 (2021), p. 110. DOI: 10.3847/1538-4357/abd3a0. arXiv: 2012.02800 [astro-ph.GA].

[78] V. Ferrari, S. Matarrese, and R. Schneider. "Gravitational wave background from a cosmological population of core collapse supernovae." In: *Mon. Not. Roy. Astron. Soc.* 303 (1999), p. 247. DOI: 10.1046/j.1365-8711.1999.02194.x. arXiv: astro-ph/9804259.

[79] A. Buonanno, G. G. Sigl, G. Raffelt, H. Janka, and E. Muller. "Stochastic gravitational-wave background from cosmological supernovae." In: *Phys. Rev. D* 72 (2005), p. 084001. DOI: 10.1103/PhysRevD.72.084001. arXiv: astro-ph/0412277.

[80] K. Crocker, T. Prestegard, V. Mandic, T. Regimbau, K. Olive, and E. Vangioni. "Systematic study of the stochastic gravitational wave background due to stellar core collapse." In: *Phys. Rev. D* 95.6 (2017). DOI: 10.1103/PhysRevD.95.063015. arXiv: 1701.02638 [astro-ph.CO].

[81] V. Ferrari, S. Matarrese, and R. Schneider. "The stochastic background of gravitational waves generated by a cosmological population of young, rapidly rotating neutron stars." In: *Mon. Not. Roy. Astron. Soc.* 303 (1999), p. 258. DOI: 10.1046/j.1365-8711.1999.02207.x. arXiv: astro-ph/9806357.

[82] S. Marassi, R. Ciolfi, R. Schneider, L. Stella, and V. Ferrari. "Stochastic background of gravitational waves emitted by magnetars." In: *MNRAS* 411 (2011), p. 2549. DOI: 10.1111/j.1365-2966.2010.17861.x. arXiv: 1009.1240 [astro-ph.CO].

[83] E. S. Phinney. "A Practical theorem on gravitational wave backgrounds." In: (July 2001). arXiv: astro-ph/0108028.

[84] B. P. Abbott et al. "GW170817: Implications for the SGWB from Compact Binary Coalescences." In: *Phys. Rev. Lett.* 120.9 (2018), p. 091101. DOI: 10.1103/PhysRevLett.120.091101. arXiv: 1710.05837 [gr-qc].

[85] B. P. Abbott et al. "GW150914: Implications for the stochastic gravitational wave background from binary black holes." In: *Phys. Rev. Lett.* 116.13 (2016). DOI: 10.1103/PhysRevLett.116.131102. arXiv: 1602.03847 [gr-qc].

[86] C. Wu, V. Mandic, and T. Regimbau. "Accessibility of the Gravitational Wave Background due to Binary Coalescences to Second and Third Generation Gravitational-Wave Detectors." In: *Phys. Rev. D* 85 (2012). DOI: 10.1103/PhysRevD.85.104024. arXiv: 1112.1898 [gr-qc].

[87] X. Zhu, E. Howell, D. Blair, and Z. Zhu. "On the gravitational wave background from compact binary coalescences in the band of ground-based interferometers." In: *Mon. Not. Roy. Astron. Soc.* 431.1 (2013). DOI: 10.1093/mnras/stt207. arXiv: 1209.0595 [gr-qc].

[88] X. Zhu, E. Howell, T. Regimbau, D. Blair, and Z. Zhu. "Stochastic Gravitational Wave Background from Coalescing Binary Black Holes." In: *Astrophys. J.* 739 (2011), p. 86. DOI: 10.1088/0004-637X/739/2/86. arXiv: 1104.3565 [gr-qc].

[89] S. Marassi, R. Schneider, G. Corvino, V. Ferrari, and S. Portegies Zwart. "Imprint of the merger and ring-down on the GW background from BH binaries coalescence." In: *Phys. Rev. D* 84 (2011). DOI: 10.1103/PhysRevD.84.124037. arXiv: 1111.6125 [astro-ph.CO].

[90] P. Rosado. "Gravitational wave background from binary systems." In: *Phys. Rev. D* 84 (2011). DOI: 10.1103/PhysRevD.84.084004. arXiv: 1106.5795 [gr-qc].

[91] C. Contaldi. "Anisotropies of gravitational wave backgrounds: a line of sight approach." In: *Phys. Lett. B* 771 (2017), pp. 9–12. DOI: 10.1016/j.physletb.2017.05.020. arXiv: 1609.08168 [astro-ph.CO].

[92] G. Cusin and G. Tasinato. "Doppler boosting the stochastic gravitational wave background." In: *JCAP* 08.08 (2022), p. 036. DOI: 10.1088/1475-7516/2022/08/036. arXiv: 2201.10464 [astro-ph.CO].

[93] A. Jenkins and M. Sakellariadou. "Anisotropies in the SGWB: Formalism and the cosmic string case." In: *Phys. Rev. D* 98.6 (2018), p. 063509. DOI: 10.1103/PhysRevD.98.063509. arXiv: 1802.06046 [astro-ph.CO].

[94] R. K. Sachs and A. M. Wolfe. "Perturbations of a cosmological model and angular variations of the microwave background." In: *Astrophys. J.* 147 (1967), pp. 73–90. DOI: 10.1007/s10714-007-0448-9.

[95] A. Jenkins et al. "Anisotropies in the astrophysical GW background: the impact of BH distributions." In: *Phys. Rev. Lett.* 122.11 (2019). DOI: 10.1103/PhysRevLett.122.111101. arXiv: 1810.13435 [astro-ph.CO].

[96] G. Cusin, I. Dvorkin, C. Pitrou, and J. Uzan. "First predictions of the angular power spectrum of the astrophysical gravitational wave background." In: *Phys. Rev. Lett.* 120 (2018). DOI: 10.1103/PhysRevLett.120.231101. arXiv: 1803.03236 [astro-ph.CO].

[97] N. Bartolo, D. Bertacca, S. Matarrese, M. Peloso, A. Ricciardone, A. Riotto, and G. Tasinato. "Anisotropies and non Gaussianity of the Cosmological Gravitational Wave Background." In: *Phys. Rev. D* 100.12 (2019), p. 121501. DOI: 10.1103/PhysRevD.100.121501. arXiv: 1908.00527 [astro-ph.CO].

[98] N. Bartolo, D. Bertacca, S. Matarrese, M. Peloso, A. Ricciardone, A. Riotto, and G. Tasinato. "Characterizing the cosmological gravitational wave background: Anisotropies and non-Gaussianity." In: *Phys. Rev. D* 102.2 (2020), p. 023527. DOI: 10.1103/PhysRevD.102.023527. arXiv: 1912.09433 [astro-ph.CO].

[99] N. Bartolo et al. "Gravitational wave anisotropies from primordial black holes." In: *JCAP* 02 (2020), p. 028. DOI: 10.1088/1475-7516/2020/02/028. arXiv: 1909.12619 [astro-ph.CO].

[100] L. Valbusa Dall'Armi, A. Ricciardone, N. Bartolo, D. Bertacca, and S. Matarrese. "Imprint of relativistic particles on the anisotropies of the stochastic gravitational wave background." In: *Phys. Rev. D* 103.2 (2021). DOI: 10.1103/PhysRevD.103.023522. arXiv: 2007.01215 [astro-ph.CO].

[101] F. Schulze, L. Valbusa Dall'Armi, J. Lesgourgues, A. Ricciardone, N. Bartolo, D. Bertacca, C. Fidler, and S. Matarrese. "GW_CLASS: Cosmological Gravitational Wave Background in the cosmic linear anisotropy solving system." In: *JCAP* 10 (2023), p. 025. DOI: 10.1088/1475-7516/2023/10/025. arXiv: 2305.01602 [gr-qc].

[102] G. Cusin, C. Pitrou, and J. Uzan. "Anisotropy of the astrophysical gravitational wave background: Analytic expression of the angular power spectrum and correlation with cosmological observations." In: *Phys. Rev. D* 96.10 (2017), p. 103019. DOI: 10.1103/PhysRevD.96.103019. arXiv: 1704.06184 [astro-ph.CO].

[103] G. Cusin, C. Pitrou, and J. Uzan. "The signal of the gravitational wave background and the angular correlation of its energy density." In: *Phys. Rev. D* 97.12 (2018), p. 123527. DOI: 10.1103/PhysRevD.97.123527. arXiv: 1711.11345 [astro-ph.CO].

[104] G. Cusin, I. Dvorkin, C. Pitrou, and J. Uzan. "Properties of the stochastic astrophysical gravitational wave background: astrophysical sources dependencies." In: *Phys. Rev. D* 100.6 (2019), p. 063004. DOI: 10.1103/PhysRevD.100.063004. arXiv: 1904.07797 [astro-ph.CO].

[105] G. Cusin, I. Dvorkin, C. Pitrou, and J. Uzan. "Stochastic gravitational wave background anisotropies in the mHz band: astrophysical dependencies." In: *MNRAS* (Apr. 2019). DOI: 10.1093/mnrasl/slz182. arXiv: 1904.07757 [astro-ph.CO].

[106] A. Jenkins et al. "Anisotropies in the astrophysical GW background: Predictions for the detection of compact binaries by LIGO and Virgo." In: *Phys. Rev. D* 98.6 (2018). DOI: 10.1103/PhysRevD.98.063501. arXiv: 1806.01718 [astro-ph.CO].

[107] V. Springel et al. "Simulations of the formation, evolution and clustering of galaxies and quasars." In: *Nature* 435.7042 (June 2005), pp. 629–636. DOI: 10.1038/nature03597. arXiv: astro-ph/0504097.

[108] G. Cusin, I. Dvorkin, C. Pitrou, and J. Uzan. "Comment on the article "Anisotropies in the astrophysical GW background: The impact of black hole distributions" by A.C. Jenkins and others [arXiv:1810.13435]." In: (Nov. 2018). arXiv: 1811.03582 [astro-ph.CO].

[109] A. Jenkins et al. "Response to Cusin et al's comment on arXiv: 1810.13435." In: (Jan. 2019). arXiv: 1901.01078 [astro-ph.CO].

[110] D. Bertacca, A. Ricciardone, N. Bellomo, A. Jenkins, S Matarrese, A. Raccanelli, T. Regimbau, and M. Sakellariadou. "Projection effects on the observed angular spectrum of the astrophysical stochastic gravitational wave background." In: *Phys. Rev. D* 101.10 (2020), p. 103513. DOI: 10.1103/PhysRevD.101.103513. arXiv: 1909.11627 [astro-ph.CO].

[111] N. Bellomo, D. Bertacca, A. Jenkins, S. Matarrese, A. Raccanelli, T. Regimbau, A. Ricciardone, and M. Sakellariadou. "CLASS_GWB: robust modeling of the astrophysical GW background anisotropies." In: *JCAP* 06.06 (2022), p. 030. DOI: 10.1088/1475-7516/2022/06/030. arXiv: 2110.15059 [gr-qc].

[112] C. Pitrou, G. Cusin, and J. Uzan. "Unified view of anisotropies in the astrophysical gravitational-wave background." In: *Phys. Rev. D* 101.8 (2020), p. 081301. DOI: 10.1103/PhysRevD.101.081301. arXiv: 1910.04645 [astro-ph.CO].

[113] A. C. Jenkins and M. Sakellariadou. "Shot noise in the astrophysical gravitational-wave background." In: *Phys. Rev. D* 100.6 (2019), p. 063508. DOI: 10.1103/PhysRevD.100.063508. arXiv: 1902.07719 [astro-ph.CO].

[114] A. Jenkins, J. D. Romano, and M. Sakellariadou. "Estimating the angular power spectrum of the gravitational-wave background in the presence of shot noise." In: *Phys. Rev. D* 100.8 (2019), p. 083501. DOI: 10.1103/PhysRevD.100.083501. arXiv: 1907.06642 [astro-ph.CO].

[115] D. Alonso, G. Cusin, P. Ferreira, and C. Pitrou. "Detecting the anisotropic astrophysical GW background in the presence of shot noise through cross-correlations." In: *Phys. Rev. D* 102.2 (2020), p. 023002. DOI: 10.1103/PhysRevD.102.023002. arXiv: 2002.02888 [astro-ph.CO].

[116] G. Capurri, A. Lapi, C. Baccigalupi, L. Boco, G. Scelfo, and T. Ronconi. "Intensity and anisotropies of the stochastic gravitational wave background from merging compact binaries in galaxies." In: *JCAP* 2021.11 (Nov. 2021), p. 032. DOI: 10.1088/1475-7516/2021/11/032. arXiv: 2103.12037 [gr-qc].

[117] A. Malhotra, E. Dimastrogiovanni, M. Fasiello, and M. Shiraishi. "Cross-correlations as a Diagnostic Tool for Primordial Gravitational Waves." In: *JCAP* 03 (2021), p. 088. DOI: 10.1088/1475-7516/2021/03/088. arXiv: 2012.03498 [astro-ph.CO].

[118] A. Ricciardone et al. "Cross-Correlating Astrophysical and Cosmological GW Backgrounds with the Cosmic Microwave Background." In: *PRL* 127.27 (2021). DOI: 10.1103/PhysRevLett.127.271301. arXiv: 2106.02591 [astro-ph.CO].

[119] M. Braglia and S. Kuroyanagi. "Probing prerecombination physics by the cross-correlation of stochastic GWs and CMB anisotropies." In: *Phys. Rev. D* 104.12 (2021), p. 123547. DOI: 10.1103/PhysRevD.104.123547. arXiv: 2106.03786 [astro-ph.CO].

[120] E. Dimastrogiovanni, M. Fasiello, A. Malhotra, P. D. Meerburg, and G. Orlando. "Testing the early universe with anisotropies of the gravitational wave background." In: *JCAP* 02.02 (2022), p. 040. DOI: 10.1088/1475-7516/2022/02/040. arXiv: 2109.03077 [astro-ph.CO].

[121] G. Perna et al. "Non-Gaussianity from the cross-correlation of the astrophysical gravitational wave background and the cosmic microwave background." In: *JCAP* 10 (2023), p. 014. DOI: 10.1088/1475-7516/2023/10/014. arXiv: 2302.08429 [astro-ph.CO].

[122] D. Alonso, C. Contaldi, G. Cusin, P. Ferreira, and A. Renzini. "Noise angular power spectrum of gravitational wave background experiments." In: *PRD* 101.12 (2020). DOI: 10.1103/PhysRevD.101.124048. arXiv: 2005.03001 [astro-ph.CO].

[123] N. Aghanim et al. "Planck 2018 results. I. Overview and the cosmological legacy of Planck." In: *Astron. Astrophys.* 641 (2020), A1. DOI: 10.1051/0004-6361/201833880. arXiv: 1807.06205 [astro-ph.CO].

[124] N. J. Secrest, S. von Hausegger, M. Rameez, R. Mohayaee, S. Sarkar, and J. Colin. "A Test of the Cosmological Principle with Quasars." In: *Astrophys. J. Lett.* 908.2 (2021), p. L51. DOI: 10.3847/2041-8213/abdd40. arXiv: 2009.14826 [astro-ph.CO].

[125] C. Dalang and C. Bonvin. "On the kinematic cosmic dipole tension." In: *Mon. Not. Roy. Astron. Soc.* 512.3 (2022), pp. 3895–3905. DOI: 10.1093/mnras/stac726. arXiv: 2111.03616 [astro-ph.CO].

[126] L. Valbusa Dall'Armi, A. Ricciardone, and D. Bertacca. "The dipole of the astrophysical gravitational-wave background." In: *JCAP* 11 (2022), p. 040. DOI: 10.1088/1475-7516/2022/11/040. arXiv: 2206.02747 [astro-ph.CO].

[127] A. K.-W. Chung, A. C. Jenkins, J. D. Romano, and M. Sakellariadou. "Targeted search for the kinematic dipole of the gravitational-wave background." In: *Phys. Rev. D* 106.8 (2022), p. 082005. DOI: 10.1103/PhysRevD.106.082005. arXiv: 2208.01330 [gr-qc].

[128] D. Chowdhury, G. Tasinato, and I. Zavala. "Response of the Einstein Telescope to Doppler anisotropies." In: *Phys. Rev. D* 107.8 (2023). DOI: 10.1103/PhysRevD.107.083516. arXiv: 2209.05770 [gr-qc].

[129] S. Mastrogiovanni, C. Bonvin, G. Cusin, and S. Foffa. "Detection and estimation of the cosmic dipole with the einstein telescope and cosmic explorer." In: *Mon. Not. Roy. Astron. Soc.* 521.1 (2023), pp. 984–994. DOI: 10.1093/mnras/stad430. arXiv: 2209.11658 [astro-ph.CO].

[130] N. Bartolo et al. "Probing anisotropies of the Stochastic Gravitational Wave Background with LISA." In: *JCAP* 11 (2022), p. 009. DOI: 10.1088/1475-7516/2022/11/009. arXiv: 2201.08782 [astro-ph.CO].

[131] C. Affeldt et al. "Advanced techniques in GEO 600." In: *Class. Quant. Grav.* 31.22 (2014), p. 224002. DOI: 10.1088/0264-9381/31/22/224002.

[132] M. Saleem et al. "The science case for LIGO-India." In: *Class. Quant. Grav.* 39.2 (2022), p. 025004. DOI: 10.1088/1361-6382/ac3b99. arXiv: 2105.01716 [gr-qc].

[133] M. Punturo et al. "The Einstein Telescope: a third-generation GW observatory." In: *Class. Quant. Grav.* 27 (2010). DOI: 10.1088/0264-9381/27/19/194002.

[134] M. Maggiore et al. "Science Case for the Einstein Telescope." In: *JCAP* 03 (2020), p. 050. DOI: 10.1088/1475-7516/2020/03/050. arXiv: 1912.02622 [astro-ph.CO].

[135] M. Branchesi et al. "Science with the Einstein Telescope: a comparison of different designs." In: *JCAP* 07 (2023), p. 068. DOI: 10.1088/1475-7516/2023/07/068. arXiv: 2303.15923 [gr-qc].

[136] D. Reitze et al. "Cosmic Explorer: The U.S. contribution to GW astronomy beyond LIGO." In: *Bull. Am. Astron. Soc.* 51.7 (2019), p. 035. arXiv: 1907.04833 [astro-ph.IM].

[137] M. Evans et al. "A Horizon Study for Cosmic Explorer: Science, Observatories, and Community." In: *arXiv preprint* (Sept. 2021). arXiv: 2109.09882 [astro-ph.IM].

[138] A. Sesana. "Prospects for Multiband Gravitational-Wave Astronomy after GW150914." In: *Physical Review Letters* 116.23 (June 2016), p. 231102. DOI: 10.1103/PhysRevLett.116.231102. arXiv: 1602.06951.

[139] M. Armano et al. "Sub-Femto- g Free Fall for Space-Based Gravitational Wave Observatories: LISA Pathfinder Results." In: *Phys. Rev. Lett.* 116.23 (2016), p. 231101. DOI: 10.1103/PhysRevLett.116.231101.

[140] G. Harry, P. Fritschel, D. Shaddock, W. Folkner, and E. Phinney. "Laser interferometry for the big bang observer." In: *Class. Quant. Grav.* 23 (2006), pp. 4887–4894. DOI: 10.1088/0264-9381/23/15/008.

[141] S. Kawamura et al. "Current status of space gravitational wave antenna DECIGO and B-DECIGO." In: *PTEP* 2021.5 (May 2021), 05A105. DOI: 10.1093/ptep/ptab019. arXiv: 2006.13545.

[142] S. Detweiler. "Pulsar timing measurements and the search for gravitational waves." In: *Astrophys. J.* 234 (Dec. 1979), pp. 1100–1104. DOI: 10.1086/157593.

[143] R. W. Hellings and G. S. Downs. "Upper limits on the isotropic gravitational radiation background from pulsar timing analysis." In: *Astrophys. J. Lett.* 265 (Feb. 1983), pp. L39–L42. DOI: 10.1086/183954.

[144] M. A. McLaughlin. "The North American Nanohertz Observatory for Gravitational Waves." In: *Class. Quant. Grav.* 30 (2013), p. 224008. DOI: 10.1088/0264-9381/30/22/224008. arXiv: 1310.0758 [astro-ph.IM].

[145] R. Manchester et al. "The Parkes Pulsar Timing Array Project." In: *Publications of the Astronomical Society of Australia* 30 (Jan. 2013). DOI: 10.1017/pasa.2012.017. arXiv: 1210.6130.

[146] M. Kramer and D. J. Champion. "The European Pulsar Timing Array and the Large European Array for Pulsars." In: *Classical and Quantum Gravity* 30.22 (Nov. 2013).

[147] G. Hobbs et al. "The International Pulsar Timing Array project: using pulsars as a gravitational wave detector." In: *Classical and Quantum Gravity* 27.8 (Apr. 2010), p. 084013. DOI: 10.1088/0264-9381/27/8/084013. arXiv: 0911.5206 [astro-ph.SR].

[148] J. P. W. Verbiest et al. "The International Pulsar Timing Array: First data release." In: *MNRAS* 458.2 (May 2016), pp. 1267–1288. DOI: 10.1093/mnras/stw347. arXiv: 1602.03640.

[149] M. Kamionkowski, A. Kosowsky, and A. Stebbins. "Statistics of cosmic microwave background polarization." In: *Phys. Rev. D* 55 (1997), pp. 7368–7388. DOI: 10.1103/PhysRevD.55.7368. arXiv: astro-ph/9611125.

[150] W. Hu and M. J. White. "CMB anisotropies: Total angular momentum method." In: *Phys. Rev. D* 56 (1997), pp. 596–615. DOI: 10.1103/PhysRevD.56.596. arXiv: astro-ph/9702170.

[151] P. Ade et al. "The latest constraints on inflationary B-modes from the BICEP/Keck telescopes." In: *56th Rencontres de Moriond on Cosmology*. Mar. 2022. arXiv: 2203.16556 [astro-ph.CO].

[152] A. Suzuki et al. "The POLARBEAR-2 and the Simons Array Experiment." In: *J. Low Temp. Phys.* 184.3-4 (2016). Ed. by P. Camus, A. Juillard, and A. Monfardini, pp. 805–810. DOI: 10.1007/s10909-015-1425-4. arXiv: 1512.07299 [astro-ph.IM].

[153] S. Adachi et al. "Improved Upper Limit on Degree-scale CMB B-mode Polarization Power from the 670 Square-degree POLARBEAR Survey." In: *Astrophys. J.* 931.2 (2022), p. 101. DOI: 10.3847/1538-4357/ac6809. arXiv: 2203.02495 [astro-ph.CO].

[154] T. Louis et al. "The Atacama Cosmology Telescope: Two-Season ACTPol Spectra and Parameters." In: *JCAP* 06 (2017), p. 031. DOI: 10.1088/1475-7516/2017/06/031. arXiv: 1610.02360 [astro-ph.CO].

[155] D. Hanson et al. "Detection of B-mode Polarization in the Cosmic Microwave Background with Data from the South Pole Telescope." In: *PRL.* 111.14 (2013). DOI: 10.1103/PhysRevLett.111.141301. arXiv: 1307.5830 [astro-ph.CO].

[156] K. Abazajian et al. "CMB-S4: Forecasting Constraints on Primordial Gravitational Waves." In: *Astrophys. J.* 926.1 (2022), p. 54. DOI: 10.3847/1538-4357/ac1596. arXiv: 2008.12619 [astro-ph.CO].

[157] E. Allys et al. "Probing Cosmic Inflation with the LiteBIRD Cosmic Microwave Background Polarization Survey." In: *PTEP* 2023.4 (2023), 042F01. DOI: 10.1093/ptep/ptac150. arXiv: 2202.02773 [astro-ph.IM].

[158] P. A. R. Ade et al. "Detection of B-Mode Polarization at Degree Angular Scales by BICEP2." In: *Phys. Rev. Lett.* 112.24 (2014), p. 241101. DOI: 10.1103/PhysRevLett.112.241101. arXiv: 1403.3985 [astro-ph.CO].

[159] R. Flauger, J. C. Hill, and D. N. Spergel. "Toward an Understanding of Foreground Emission in the BICEP2 Region." In: *JCAP* 08 (2014), p. 039. DOI: 10.1088/1475-7516/2014/08/039. arXiv: 1405.7351 [astro-ph.CO].

[160] M. J. Mortonson and U. Seljak. "A joint analysis of Planck and BICEP2 B modes including dust polarization uncertainty." In: *JCAP* 10 (2014), p. 035. DOI: 10.1088/1475-7516/2014/10/035. arXiv: 1405.5857 [astro-ph.CO].

[161] P. Campeti, E. Komatsu, D. Poletti, and C. Baccigalupi. "Measuring the spectrum of primordial gravitational waves with CMB, PTA and Laser Interferometers." In: *JCAP* 01 (2021), p. 012. DOI: 10.1088/1475-7516/2021/01/012. arXiv: 2007.04241.

[162] N. Christensen. "Measuring the stochastic gravitational radiation background with laser interferometric antennas." In: *Phys. Rev. D* 46 (12 1992), pp. 5250–5266. DOI: 10.1103/PhysRevD.46.5250.

[163] B. Abbott et al. "Upper limits on the stochastic gravitational-wave background from advanced LIGO's first observing run." In: *Phys. Rev. Lett.* 118.12 (2017). DOI: 10.1103/PhysRevLett.118.121101. arXiv: 1612.02029 [gr-qc].

[164] B. Abbott et al. "Search for the isotropic stochastic background using data from Advanced LIGO's second observing run." In: *Phys. Rev. D* 100.6 (2019), p. 061101. DOI: 10.1103/PhysRevD.100.061101. arXiv: 1903.02886 [gr-qc].

[165] S. Ballmer. "A radiometer for stochastic gravitational waves." In: *Class. Quant. Grav.* 23 (2006). Ed. by N. Mio, S179–S186. DOI: 10.1088/0264-9381/23/8/S23. arXiv: gr-qc/0510096.

[166] S. Mitra, S. Dhurandhar, T. Souradeep, A. Lazzarini, V. Mandic, S. Bose, and S. Ballmer. "Gravitational wave radiometry: Mapping a stochastic gravitational wave background." In: *Phys. Rev. D* 77 (2008), p. 042002. DOI: 10.1103/PhysRevD.77.042002. arXiv: 0708.2728 [gr-qc].

[167] E. Thrane, S. Ballmer, J. D. Romano, S. Mitra, D. Talukder, S. Bose, and V. Mandic. "Probing the anisotropies of a stochastic gravitational-wave background using a network of ground-based laser interferometers." In: *Phys. Rev. Let.* 80.12, 122002 (Dec. 2009), p. 122002. DOI: 10.1103/PhysRevD.80.122002. arXiv: 0910.0858.

[168] A. I. Renzini and C. R. Contaldi. "Mapping Incoherent Gravitational Wave Backgrounds." In: *Mon. Not. Roy. Astron. Soc.* 481.4 (2018). DOI: 10.1093/mnras/sty2546. arXiv: 1806.11360 [astro-ph.IM].

[169] C. M. F. Mingarelli, T. Sidery, I. Mandel, and A. Vecchio. "Characterizing gravitational wave stochastic background anisotropy with pulsar timing arrays." In: *Phys. Rev. D* 88.6 (2013). DOI: 10.1103/PhysRevD.88.062005. arXiv: 1306.5394 [astro-ph.HE].

[170] S. R. Taylor and J. R. Gair. "Searching for anisotropic gravitational wave backgrounds using pulsar timing arrays." In: *Phys. Rev. D* 88 (2013). DOI: 10.1103/PhysRevD.88.084001. arXiv: 1306.5395 [gr-qc].

[171] J. Gair, J. Romano, S. Taylor, and C. Mingarelli. "Mapping gravitational wave backgrounds using methods from CMB analysis: Application to pulsar timing arrays." In: *Phys. Rev. D* 90.8 (2014). DOI: 10.1103/PhysRevD.90.082001. arXiv: 1406.4664 [gr-qc].

[172] N. J. Cornish and R. van Haasteren. "Mapping the nano-Hertz gravitational wave sky." In: (June 2014). arXiv: 1406.4511 [gr-qc].

[173] J. Romano, S. Taylor, N. Cornish, J. Gair, C. Mingarelli, and R. van Haasteren. "Phase-coherent mapping of GW backgrounds using ground-based laser interferometers." In: *Phys. Rev. D* 92.4 (2015). DOI: 10.1103/PhysRevD.92.042003. arXiv: 1505.07179 [gr-qc].

[174] E. Thrane and J. Romano. "Sensitivity curves for searches for GW backgrounds." In: *Phys. Rev. D* 88.12 (2013). DOI: 10.1103/PhysRevD.88.124032. arXiv: 1310.5300 [astro-ph.IM].

[175] S. Marassi et al. "Gravitational wave backgrounds and the cosmic transition from Population III to Population II stars." In: *Mon. Not. Roy. Astron. Soc.* 398 (2009), p. 293. DOI: 10.1111/j.1365-2966.2009.15120.x. arXiv: 0906.0461 [astro-ph.CO].

[176] E. Vangioni, K. A. Olive, T. Prestegard, J. Silk, P. Petitjean, and V. Mandic. "The Impact of Star Formation and Gamma-Ray Burst Rates at High Redshift on Cosmic Chemical Evolution and Reionization." In: *Mon. Not. Roy. Astron. Soc.* 447 (2015), p. 2575. DOI: 10.1093/mnras/stu2600. arXiv: 1409.2462 [astro-ph.GA].

[177] B. Abbott et al. "Upper limit map of a background of gravitational waves." In: *Phys. Rev. D* 76 (2007), p. 082003. DOI: 10.1103/PhysRevD.76.082003. arXiv: astro-ph/0703234.

[178] R. van Haasteren, Y. Levin, P. McDonald, and T. Lu. "On measuring the gravitational-wave background using Pulsar Timing Arrays." In: *Mon. Not. Roy. Astron. Soc.* 395 (2009), p. 1005. DOI: 10.1111/j.1365-2966.2009.14590.x. arXiv: 0809.0791 [astro-ph].

[179] Z. Arzoumanian et al. "The NANOGrav 12.5 yr data set: search for an isotropic stochastic gravitational wave background." In: *Astrophys. J. Lett.* 905.2 (2020), p. L34. DOI: 10.3847/2041-8213/abd401. arXiv: 2009.04496 [astro-ph.HE].

[180] B. Goncharov et al. "On the Evidence for a Common-spectrum Process in the Search for the Nanohertz Gravitational-wave Background with the Parkes Pulsar Timing Array." In: *Astrophys. J. Lett.* 917.2 (2021). DOI: 10.3847/2041-8213/ac17f4. arXiv: 2107.12112 [astro-ph.HE].

[181] S. Chen et al. "Common-red-signal analysis with 24-yr high-precision timing of the European Pulsar Timing Array: inferences in the stochastic gravitational-wave background search." In: *Mon. Not. Roy. Astron. Soc.* 508.4 (2021), pp. 4970–4993. DOI: 10.1093/mnras/stab2833. arXiv: 2110.13184 [astro-ph.HE].

[182] J. Antoniadis et al. "The International Pulsar Timing Array second data release: Search for an isotropic gravitational wave background." In: *MNRAS* 510.4 (2022), pp. 4873–4887. DOI: 10.1093/mnras/stab3418. arXiv: 2201.03980 [astro-ph.HE].

[183] S. Vitale, W. M. Farr, K. Ng, and C. L. Rodriguez. "Measuring the star formation rate with gravitational waves from binary black holes." In: *Astrophys. J. Lett.* 886.1 (2019), p. L1. DOI: 10.3847/2041-8213/ab50c0. arXiv: 1808.00901 [astro-ph.HE].

[184] T. Regimbau et al. "Digging deeper: observing primordial gravitational waves below the binary black hole produced stochastic background." In: *Phys. Rev. Lett.* 118.15 (2017). DOI: 10.1103/PhysRevLett.118.151105. arXiv: 1611.08943 [astro-ph.CO].

[185] S. Bavera, G. Franciolini, G. Cusin, A. Riotto, M. Zevin, and T. Fragos. "Stochastic gravitational-wave background as a tool for investigating multi-channel astrophysical and primordial black-hole mergers." In: *Astron. Astrophys.* 660 (2022), A26. DOI: 10.1051/0004-6361/202142208. arXiv: 2109.05836 [astro-ph.CO].

[186] V. Bromm and R. Larson. "The First stars." In: *Ann. Rev. Astron. Astrophys.* 42 (2004), pp. 79–118. DOI: 10.1146/annurev.astro.42.053102.134034. arXiv: astro-ph/0311019.

[187] C. Périgois, C. Belczynski, T. Bulik, and T. Regimbau. "StarTrack predictions of the stochastic gravitational-wave background from compact binary mergers." In: *Phys. Rev. D* 103.4 (2021). DOI: 10.1103/PhysRevD.103.043002. arXiv: 2008.04890 [astro-ph.CO].

[188] C. Périgois, F. Santoliquido, Y. Bouffanais, U. Di Carlo, N. Giacobbo, S. Rastello, M. Mapelli, and T. Regimbau. "Gravitational background from dynamical binaries and detectability with 2G detectors." In: *Phys. Rev. D* 105.10 (2022). DOI: 10.1103/PhysRevD.105.103032. arXiv: 2112.01119 [astro-ph.CO].

[189] K. Martinovic, C. Perigois, T. Regimbau, and M. Sakellariadou. "Footprints of Population III Stars in the Gravitational-wave Background." In: *Astrophys. J.* 940.1 (2022), p. 29. DOI: 10.3847/1538-4357/ac9840. arXiv: 2109.09779 [astro-ph.SR].

[190] K. Belczynski, T. Ryu, R. Perna, E. Berti, T. L. Tanaka, and T. Bulik. "On the likelihood of detecting gravitational waves from Population III compact object binaries." In: *Mon. Not. Roy. Astron. Soc.* 471.4 (2017). DOI: 10.1093/mnras/stx1759. arXiv: 1612.01524 [astro-ph.HE].

[191] T. Hartwig, M. Volonteri, V. Bromm, R. S. Klessen, E. Barausse, M. Magg, and A. Stacy. "Gravitational Waves from the Remnants of the First Stars." In: *Mon. Not. Roy. Astron. Soc.* 460.1 (2016), pp. L74–L78. DOI: 10.1093/mnrasl/slw074. arXiv: 1603.05655 [astro-ph.GA].

[192] M. Raidal, C. Spethmann, V. Vaskonen, and H. Veermäe. "Formation and Evolution of Primordial Black Hole Binaries in the Early Universe." In: *JCAP* 02 (2019), p. 018. DOI: 10.1088/1475-7516/2019/02/018. arXiv: 1812.01930 [astro-ph.CO].

[193] G. Mentasti and M. Peloso. "ET sensitivity to the anisotropic Stochastic Gravitational Wave Background." In: *JCAP* 03 (2021), p. 080. DOI: 10.1088/1475-7516/2021/03/080. arXiv: 2010.00486 [astro-ph.CO].

[194] D. Agarwal, J. Suresh, S. Mitra, and A. Ain. "Angular power spectra of the anisotropic SGWB: developing statistical methods and analyzing data from ground-based detectors." In: *PRD* 108.2 (2023). DOI: 10.1103/PhysRevD.108.023011. arXiv: 2302.12516 [gr-qc].

[195] G. Mentasti, C. R. Contaldi, and M. Peloso. "Intrinsic limits on the detection of the anisotropies of the Stochastic Gravitational Wave Background." In: (2023). arXiv: 2301.08074 [gr-qc].

[196] G. Mentasti, C. R. Contaldi, and M. Peloso. "Prospects for detecting anisotropies and polarization of the stochastic gravitational wave background with ground-based detectors." In: *JCAP* 08 (2023), p. 053. DOI: 10.1088/1475-7516/2023/08/053. arXiv: 2304.06640 [gr-qc].

[197] F. Estabrook, M. Tinto, and J. Armstrong. "Time-delay analysis of LISA gravitational wave data: Elimination of spacecraft motion effects." In: *Phys. Rev. D* 62 (4 2000).

[198] T. A. Prince, M. Tinto, S. L. Larson, and J. W. Armstrong. "The LISA optimal sensitivity." In: *Phys. Rev. D* 66 (2002), p. 122002. DOI: 10.1103/PhysRevD.66.122002. arXiv: gr-qc/0209039.

[199] M. Tinto, J. Armstrong, and F. Estabrook. "Discriminating a gravitational wave background from instrumental noise in the LISA detector." In: *Phys. Rev. D* 63 (2001), p. 021101. DOI: 10.1103/PhysRevD.63.021101.

[200] T. Robson, N. J. Cornish, and C. Liu. "The construction and use of LISA sensitivity curves." In: *Class. Quant. Grav.* 36.10 (2019), p. 105011. DOI: 10.1088/1361-6382/ab1101. arXiv: 1803.01944 [astro-ph.HE].

[201] T. Smith and R. Caldwell. "LISA for cosmologists: calculating the signal-to-noise ratio for stochastic and deterministic sources." In: *Phys. Rev. D* 100.10 (2019). [Erratum: Phys.Rev.D 105, 029902 (2022)]. DOI: 10.1103/PhysRevD.100.104055. arXiv: 1908.00546 [astro-ph.CO].

[202] J. Crowder and N. J. Cornish. "LISA source confusion." In: *Phys. Rev. D* 70 (2004), p. 082004. DOI: 10.1103/PhysRevD.70.082004. arXiv: gr-qc/0404129.

[203] A. Lamberts, S. Blunt, T. B. Littenberg, S. Garrison-Kimmel, T. Kupfer, and R. E. Sanderson. "Predicting the LISA white dwarf binary population in the Milky Way with cosmological simulations." In: *Mon. Not. Roy. Astron. Soc.* 490.4 (2019), pp. 5888–5903. DOI: 10.1093/mnras/stz2834. arXiv: 1907.00014 [astro-ph.HE].

[204] S. Babak, C. Caprini, D. G. Figueroa, N. Karnesis, P. Marcoccia, G. Nardini, M. Pieroni, A. Ricciardone, A. Sesana, and J. Torrado. "Stochastic gravitational wave background from stellar origin binary black holes in LISA." In: *JCAP* 08 (2023), p. 034. DOI: 10.1088/1475-7516/2023/08/034. arXiv: 2304.06368 [astro-ph.CO].

[205] A. Mangiagli, C. Caprini, M. Volonteri, S. Marsat, S. Vergani, N. Tamanini, and H. Inchauspé. "Massive black hole binaries in LISA: Multimessenger prospects and electromagnetic counterparts." In: *Phys. Rev. D* 106.10 (2022), p. 103017. DOI: 10.1103/PhysRevD.106.103017. arXiv: 2207.10678 [astro-ph.HE].

[206] A. Klein et al. "Science with the space-based interferometer eLISA: Supermassive black hole binaries." In: *Phys. Rev. D* 93.2 (2016), p. 024003. DOI: 10.1103/PhysRevD.93.024003. arXiv: 1511.05581 [gr-qc].

[207] S. Babak, J. Gair, A. Sesana, E. Barausse, C. F. Sopuerta, C. P. L. Berry, E. Berti, P. Amaro-Seoane, A. Petiteau, and A. Klein. "Science with the space-based interferometer LISA. V: Extreme mass-ratio inspirals." In: *Phys. Rev. D* 95.10 (2017), p. 103012. DOI: 10.1103/PhysRevD.95.103012. arXiv: 1703.09722 [gr-qc].

[208] C. R. Contaldi, M. Pieroni, A. I. Renzini, G. Cusin, N. Karnesis, M. Peloso, A. Ricciardone, and G. Tasinato. "Maximum likelihood map-making with the Laser Interferometer Space Antenna." In: *Phys. Rev. D* 102.4 (2020), p. 043502. DOI: 10.1103/PhysRevD.102.043502. arXiv: 2006.03313 [astro-ph.CO].

[209] S. Banagiri, A. Criswell, T. Kuan, V. Mandic, J. D. Romano, and S. R. Taylor. "Mapping the gravitational-wave sky with LISA: a Bayesian spherical harmonic approach." In: *MNRAS* 507.4 (Nov. 2021), pp. 5451–5462. DOI: 10.1093/mnras/stab2479. arXiv: 2103.00826 [astro-ph.IM].

[210] J. Lesgourgues. "The Cosmic Linear Anisotropy Solving System (CLASS). Part I: Overview." In: *Preprint* (2011). arXiv: 1104.2932 [astro-ph.IM].

[211] D. Blas, J. Lesgourgues, and T. Tram. "The Cosmic Linear Anisotropy Solving System (CLASS). Part II: Approximation schemes." In: *JCAP* 2011.07 (2011), 034–034. ISSN: 1475-7516. DOI: 10.1088/1475-7516/2011/07/034.

[212] J. Barrett, S. Gaebel, C. Neijssel, A. Vigna-Gómez, S. Stevenson, C. P. Berry, W. Farr, and I. Mandel. "Accuracy of inference on the physics of binary evolution from gravitational-wave observations." In: *MRAS* 477.4 (2018), pp. 4685–4695. DOI: 10.1093/mnras/sty908. arXiv: 1711.06287 [astro-ph.HE].

[213] C. J. Neijssel, A. Vigna-Gómez, S. Stevenson, J. W. Barrett, S. M. Gaebel, F. S. Broekgaarden, S. E. de Mink, D. Szécsi, S. Vinciguerra, and I. Mandel. "The effect of the metallicity-specific star formation history on double compact object mergers." In: *MNRAS* 490.3 (2019), 3740–3759. DOI: 10.1093/mnras/stz2840.

[214] M. Chruslinska, K. Belczynski, J. Klencki, and M. Benacquista. "Double neutron stars: merger rates revisited." In: *Mon. Not. Roy. Astron. Soc.* 474.3 (2018), pp. 2937–2958. DOI: 10.1093/mnras/stx2923. arXiv: 1708.07885 [astro-ph.HE].

[215] M. Chruslinska, G. Nelemans, and K. Belczynski. "The influence of the distribution of cosmic star formation at different metallicities on the properties of merging double compact objects." In: *Mon. Not. Roy. Astron. Soc.* 482.4 (2019), pp. 5012–5017. DOI: 10.1093/mnras/sty3087. arXiv: 1811.03565 [astro-ph.HE].

[216] M. Dominik, K. Belczynski, C. Fryer, D. E. Holz, E. Berti, T. Bulik, I. Mandel, and R. O'Shaughnessy. "Double Compact Objects. I. The Significance of the Common Envelope on Merger Rates." In: *The Astrophysical Journal* 759.1 (2012), p. 52. DOI: 10.1088/0004-637X/759/1/52. arXiv: 1202.4901.

[217] N. Giacobbo and M. Mapelli. "The progenitors of compact-object binaries: impact of metallicity, common envelope and natal kicks." In: *Mon. Not. Roy. Astron. Soc.* 480.2 (2018), pp. 2011–2030. DOI: 10.1093/mnras/sty1999. arXiv: 1806.00001 [astro-ph.HE].

[218] D. Maoz, F. Mannucci, and G. Nelemans. "Observational clues to the progenitors of Type-Ia supernovae." In: *Ann. Rev. Astron. Astrophys.* 52 (2014), pp. 107–170. DOI: 10.1146/annurev-astro-082812-141031. arXiv: 1312.0628 [astro-ph.CO].

[219] R. Abbott et al. "Population Properties of Compact Objects from the Second LIGO-Virgo Gravitational-Wave Transient Catalog." In: *Astrophys. J. Lett.* 913.1 (2021), p. L7. DOI: 10.3847/2041-8213/abe949. arXiv: 2010.14533 [astro-ph.HE].

[220] R. Abbott et al. "Observation of gravitational waves from two neutron star-black hole coalescences." In: *Astrophys. J. Lett.* 915 (2021), p. L5. DOI: 10.3847/2041-8213/ac082e. arXiv: 2106.15163 [astro-ph.HE].

[221] C. Mancuso, A. Lapi, J. Shi, J. Gonzalez-Nuevo, R. Aversa, and L. Danese. "The Quest for Dusty Star-forming Galaxies at High Redshift $z \gtrsim 4$." In: *Astrophys. J.* 823.2 (2016), p. 128. DOI: 10.3847/0004-637X/823/2/128. arXiv: 1604.02507 [astro-ph.GA].

[222] F. Mannucci, G. Cresci, R. Maiolino, A. Marconi, and A. Gnerucci. "A fundamental relation between mass, star formation rate and metallicity in local and high-redshift galaxies." In: *MRAS* 408.4 (2010), 2115–2127. ISSN: 0035-8711. DOI: 10.1111/j.1365-2966.2010.17291.x.

[223] F. Mannucci, R. Salvaterra, and M. A. Campisi. "The metallicity of the long GRB hosts and the fundamental metallicity relation of low-mass galaxies." In: *MNRAS* 414.2 (2011), 1263–1268. DOI: 10.1111/j.1365-2966.2011.18459.x.

[224] L. Hunt, P. Dayal, L. Magrini, and A. Ferrara. "Coevolution of metallicity and star formation in galaxies to $z \simeq 3.7$ – II. A theoretical model." In: *MNRAS* 463.2 (2016), 2020–2031. DOI: 10.1093/mnras/stw2091.

[225] M. Curti, F. Mannucci, G. Cresci, and R. Maiolino. "The mass–metallicity and the fundamental metallicity relation revisited on a fully Te-based abundance scale for galaxies." In: *MNRAS* 491.1 (2019), 944–964. DOI: 10.1093/mnras/stz2910.

[226] E. Daddi et al. "Multiwavelength Study of Massive Galaxies at $z\sim2$. II. Widespread Compton-thick Active Galactic Nuclei and the Concurrent Growth of Black Holes and Bulges." In: *The Astrophysical Journal* 670.1 (Nov. 2007). DOI: 10.1086/521820. arXiv: 0705.2832 [astro-ph].

[227] G. Rodighiero et al. "The Lesser Role of Starbursts in Star Formation at z = 2." In: *ApJ Letter* 739.2, L40 (Oct. 2011), p. L40. DOI: 10.1088/2041-8205/739/2/L40. arXiv: 1108.0933 [astro-ph.CO].

[228] G. Rodighiero et al. "Relationship between Star Formation Rate and Black Hole Accretion At Z = 2: the Different Contributions in Quiescent, Normal, and Starburst Galaxies." In: *ApJ Letter* 800.1, L10 (Feb. 2015), p. L10. DOI: 10.1088/2041-8205/800/1/L10. arXiv: 1501.04634 [astro-ph.GA].

[229] K. E. Whitaker et al. "Constraining the Low-mass Slope of the Star Formation Sequence at 0.5 < z < 2.5." In: *The Astrophysical Journal* 795.2, 104 (Nov. 2014), p. 104. DOI: 10.1088/0004-637X/795/2/104. arXiv: 1407.1843 [astro-ph.GA].

[230] J. S. Speagle, C. L. Steinhardt, P. L. Capak, and J. D. Silverman. "A Highly Consistent Framework for the Evolution of the Star-Forming "Main Sequence" from z~0-6." In: *Astrophys. J. Suppl.* 214.2 (2014), p. 15. DOI: 10.1088/0067-0049/214/2/15. arXiv: 1405.2041 [astro-ph.GA].

[231] C. Schreiber et al. "The Herschel view of the dominant mode of galaxy growth from z = 4 to the present day." In: *Astronomy and Astrophysics* 575, A74 (Mar. 2015), A74. DOI: 10.1051/0004-6361/201425017. arXiv: 1409.5433 [astro-ph.GA].

[232] J. S. Dunlop et al. "A deep ALMA image of the Hubble Ultra Deep Field." In: *MNRAS* 466.1 (Apr. 2017), pp. 861–883. DOI: 10.1093/mnras/stw3088. arXiv: 1606.00227 [astro-ph.GA].

[233] F. Calore, A. Cuoco, T. Regimbau, S. Sachdev, and P. D. Serpico. "Cross-correlating galaxy catalogs and gravitational waves: a tomographic approach." In: *Phys. Rev. Res.* 2 (2020). DOI: 10.1103/PhysRevResearch.2.023314. arXiv: 2002.02466 [astro-ph.CO].

[234] L. Cao, Y. Lu, and Y. Zhao. "Host galaxy properties of mergers of stellar binary black holes and their implications for advanced LIGO gravitational wave sources." In: *MNRAS* 474.4 (2017). DOI: 10.1093/mnras/stx3087.

[235] S.-S. Li, S. Mao, Y. Zhao, and Y. Lu. "Gravitational lensing of gravitational waves: A statistical perspective." In: *Mon. Not. Roy. Astron. Soc.* 476.2 (2018), pp. 2220–2229. DOI: 10.1093/mnras/sty411. arXiv: 1802.05089 [astro-ph.CO].

[236] A. Sicilia, A. Lapi, L. Boco, M. Spera, U. N. Di Carlo, M. Mapelli, F. Shankar, D. M. Alexander, A. Bressan, and L. Danese. "The Black Hole Mass Function Across Cosmic Times. I. Stellar Black Holes and Light Seed Distribution." In: *Astrophys. J.* 924.2 (2022), p. 56. DOI: 10.3847/1538-4357/ac34fb. arXiv: 2110.15607 [astro-ph.GA].

[237] L. S. Finn. "Binary inspiral, gravitational radiation, and cosmology." In: *Phys. Rev. D* 53 (1996), pp. 2878–2894. DOI: 10.1103/PhysRevD.53.2878. arXiv: gr-qc/9601048.

[238] S. R. Taylor and J. R. Gair. "Cosmology with the lights off: standard sirens in the Einstein Telescope era." In: *Phys. Rev. D* 86 (2012), p. 023502. DOI: 10.1103/PhysRevD.86.023502. arXiv: 1204.6739 [astro-ph.CO].

[239] P. Ajith et al. "A Template bank for gravitational waveforms from coalescing binary black holes. I. Non-spinning binaries." In: *Phys. Rev. D* 77 (2008). [Erratum: Phys.Rev.D 79, 12990 (2009)]. DOI: 10.1103/PhysRevD.77.104017. arXiv: 0710.2335 [gr-qc].

[240] Kowalska-Leszczynska, I., Regimbau, T., Bulik, T., Dominik, M., and Belczynski, K. "Effect of metallicity on the gravitational-wave signal from the cosmological population of compact binary coalescences." In: *A&A* 574 (2015), A58. DOI: 10.1051/0004-6361/201424417.

[241] R. Aversa, A. Lapi, G. de Zotti, F. Shankar, and L. Danese. "Black hole and galaxy coevolution from continuity equation and abundance matching." In: *Astrophys. J.* 810.1 (2015), p. 74. DOI: 10.1088/0004-637X/810/1/74. arXiv: 1507.07318 [astro-ph.GA].

[242] R. K. Sheth, H. Mo, and G. Tormen. "Ellipsoidal collapse and an improved model for the number and spatial distribution of dark matter haloes." In: *Mon. Not. Roy. Astron. Soc.* 323 (2001), p. 1. DOI: 10.1046/j.1365-8711.2001.04006.x. arXiv: astro-ph/9907024.

[243] A. Lapi and L. Danese. "Statistics of Dark Matter Halos in the Excursion Set Peak Framework." In: *JCAP* 07 (2014), p. 044. DOI: 10.1088/1475-7516/2014/07/044. arXiv: 1407.1137 [astro-ph.CO].

[244] L. Hui, E. Gaztañaga, and M. LoVerde. "Anisotropic magnification distortion of the 3D galaxy correlation. I. Real space." In: *Physical Review D* 76.10 (Nov. 2007). DOI: 10.1103/physrevd.76.103502.

[245] G. Scelfo, N. Bellomo, A. Raccanelli, S. Matarrese, and L. Verde. "GW×LSS: chasing the progenitors of merging binary black holes." In: *JCAP* 09 (2018), p. 039. DOI: 10.1088/1475-7516/2018/09/039. arXiv: 1809.03528 [astro-ph.CO].

[246] G. Scelfo, L. Boco, A. Lapi, and M. Viel. "Exploring galaxies-gravitational waves cross-correlations as an astrophysical probe." In: *JCAP* (July 2020). arXiv: 2007.08534 [astro-ph.CO].

[247] E. Di Dio, F. Montanari, J. Lesgourgues, and R. Durrer. "The CLASSgal code for Relativistic Cosmological Large Scale Structure." In: *JCAP* 11 (2013), p. 044. DOI: 10.1088/1475-7516/2013/11/044. arXiv: 1307.1459 [astro-ph.CO].

[248] C. Bonvin and R. Durrer. "What galaxy surveys really measure." In: *Physical Review D* 84.6 (Sept. 2011). ISSN: 1550-2368. DOI: 10.1103/physrevd.84.063505.

[249] A. Challinor and A. Lewis. "Linear power spectrum of observed source number counts." In: *Physical Review D* 84.4 (Aug. 2011). DOI: 10.1103/physrevd.84.043516.

[250] J. Gonzalez-Nuevo, L. Toffolatti, and F. Argueso. "Predictions of the angular power spectrum of clustered extragalactic point sources at CMB frequencies from flat and all-sky two-dimensional simulations." In: *The Astrophysical Journal* 621.1 (Mar. 2005), pp. 1–14. DOI: 10.1086/427425.

[251] A. Zonca, L. Singer, D. Lenz, M. Reinecke, C. Rosset, E. Hivon, and K. Gorski. "healpy: equal area pixelization and spherical harmonics transforms for data on the sphere in Python." In: *Journal of Open Source Software* 4.35 (Mar. 2019), p. 1298. DOI: 10.21105/joss.01298.

[252] K. Gorski, E. Hivon, A. Banday, B. Wandelt, F. Hansen, M. Reinecke, and M. Bartelmann. "HEALPix: A Framework for High-Resolution Discretization and Fast Analysis of Data Distributed on the Sphere." In: *ApJ* 622 (Apr. 2005), pp. 759–771. DOI: 10.1086/427976. eprint: arXiv:astro-ph/0409513.

[253] S. Mukherjee and J. Silk. "Time-dependence of the astrophysical stochastic gravitational wave background." In: *Mon. Not. Roy. Astron. Soc.* 491.4 (2020), pp. 4690–4701. DOI: 10.1093/mnras/stz3226. arXiv: 1912.07657 [gr-qc].

[254] G. Cañas Herrera, O. Contigiani, and V. Vardanyan. "Cross- correlation of the astrophysical gravitational-wave background with galaxy clustering." In: *Phys. Rev. D* 102.4 (2020). DOI: 10.1103/PhysRevD.102.043513. arXiv: 1910.08353 [astro-ph.CO].

[255] B. P. Abbott et al. "Directional limits on persistent gravitational waves using data from Advanced LIGO's first two observing runs." In: *Phys. Rev. D* 100.6 (2019), p. 062001. DOI: 10.1103/PhysRevD.100.062001. arXiv: 1903.08844 [gr-qc].

[256] B. P. Abbott et al. "Directional Limits on Persistent Gravitational Waves from Advanced LIGO's First Observing Run." In: *Phys. Rev. Lett.* 118.12 (2017), p. 121102. DOI: 10.1103/PhysRevLett.118.121102. arXiv: 1612.02030 [gr-qc].

[257] A. I. Renzini and C. R. Contaldi. "Gravitational Wave Background Sky Maps from Advanced LIGO O1 Data." In: *Phys. Rev. Lett.* 122.8 (2019), p. 081102. DOI: 10.1103/PhysRevLett.122.081102. arXiv: 1811.12922 [astro-ph.CO].

[258] A. Renzini and C. Contaldi. "Improved limits on a stochastic SGWB and its anisotropies from Advanced LIGO O1 and O2 runs." In: *Phys. Rev. D* 100.6 (2019), p. 063527. DOI: 10.1103/PhysRevD.100.063527. arXiv: 1907.10329 [gr-qc].

[259] A. Ain, J. Suresh, and S. Mitra. "Very fast stochastic gravitational wave background map making using folded data." In: *Phys. Rev. D* 98.2 (2018), p. 024001. DOI: 10.1103/PhysRevD.98.024001. arXiv: 1803.08285 [gr-qc].

[260] S. Hotinli, M. Kamionkowski, and A. Jaffe. "The search for anisotropy in the gravitational-wave background with pulsar-timing arrays." In: *Open J. Astrophys.* 2.1 (2019), p. 8. DOI: 10.21105/astro.1904.05348. arXiv: 1904.05348 [astro-ph.CO].

[261] K. Yang, V. Mandic, C. Scarlata, and S. Banagiri. "Searching for Cross-Correlation Between SGWB and Galaxy Number Counts." In: *Mon. Not. Roy. Astron. Soc.* 500.2 (2020). DOI: 10.1093/mnras/staa3159. arXiv: 2007.10456 [astro-ph.CO].

[262] S. Mukherjee, B. D. Wandelt, and J. Silk. "Multimessenger tests of gravity with weakly lensed GWs." In: *Phys. Rev. D* 101.10 (2020). DOI: 10.1103/PhysRevD.101.103509. arXiv: 1908.08950 [astro-ph.CO].

[263] S. Mukherjee, B. D. Wandelt, and J. Silk. "Probing the theory of gravity with gravitational lensing of gravitational waves and galaxy surveys." In: *MNRAS* 494.2 (2020). DOI: 10.1093/mnras/staa827. arXiv: 1908.08951 [astro-ph.CO].

[264] B. Sathyaprakash et al. "Scientific Objectives of Einstein Telescope." In: *Class. Quant. Grav.* 29 (2012). DOI: 10.1088/0264-9381/29/12/124013. arXiv: 1206.0331 [gr-qc].

[265] T. Namikawa et al. "Simons Observatory: Constraining inflationary gravitational waves with multitracer B-mode delensing." In: *Phys. Rev. D* 105.2 (2022), p. 023511. DOI: 10.1103/PhysRevD.105.023511. arXiv: 2110.09730 [astro-ph.CO].

[266] F. Bianchini et al. "Cross-correlation between the CMB lensing potential measured by Planck and high-z submillimeter galaxies detected by the Herschel-atlas survey." In: *Astrophysical Journal* 802 (1 Mar. 2015). ISSN: 15384357. DOI: 10.1088/0004-637X/802/1/64.

[267] F. Bianchini et al. "Toward a tomographic analysis of the cross-correlation between Planck CMB lensing and H-ATLAS galaxies." In: *The Astrophysical Journal* 825 (1 June 2016), p. 24. ISSN: 1538-4357. DOI: 10.3847/0004-637x/825/1/24.

[268] A. Lewis and A. Challinor. "Weak gravitational lensing of the CMB." In: *Phys. Rept.* 429 (2006), pp. 1–65. DOI: 10.1016/j.physrep.2006.03.002. arXiv: astro-ph/0601594.

[269] M. Bartelmann and P. Schneider. "Weak gravitational lensing." In: *Phys. Rept.* 340 (2001), pp. 291–472. DOI: 10.1016/S0370-1573(00)00082-X. arXiv: astro-ph/9912508.

[270] D. N. Limber. "The Analysis of Counts of the Extragalactic Nebulae in Terms of a Fluctuating Density Field. II." In: *Astrophys. J.* 119 (1954), p. 655. DOI: 10.1086/145870.

[271] R. E. Smith, J. A. Peacock, A. Jenkins, S. D. M. White, C. S. Frenk, F. R. Pearce, P. A. Thomas, G. Efstathiou, and H. M. P. Couchmann. "Stable clustering, the halo model and nonlinear cosmological power spectra." In: *Mon. Not. Roy. Astron. Soc.* 341 (2003), p. 1311. DOI: 10.1046/j.1365-8711.2003.06503.x. arXiv: astro-ph/0207664.

[272] G. Capurri, A. Lapi, and C. Baccigalupi. "Detectability of the Cross-Correlation between CMB Lensing and Stochastic GW Background from Compact Object Mergers." In: *Universe* 8.3 (Mar. 2022), p. 160. DOI: 10.3390/universe8030160. arXiv: 2111.04757 [astro-ph.CO].

[273] P. Amaro Seoane et al. "The effect of mission duration on LISA science objectives." In: *General Relativity and Gravitation* 54.1, 3 (Jan. 2022), p. 3. DOI: 10.1007/s10714-021-02889-x. arXiv: 2107.09665 [astro-ph.IM].

[274] eLISA Consortium et al. "The Gravitational Universe." In: *arXiv e-prints* (May 2013). arXiv: 1305.5720 [astro-ph.CO].

[275] S. Sato et al. "The status of DECIGO." In: *Journal of Physics Conference Series*. Vol. 840. Journal of Physics Conference Series. May 2017, 012010, p. 012010. DOI: 10.1088/1742-6596/840/1/012010.

[276] S. Kawamura et al. "The Japanese space gravitational wave antenna: DECIGO." In: *Classical and Quantum Gravity* 28.9, 094011 (May 2011), p. 094011. DOI: 10.1088/0264-9381/28/9/094011.

[277] L. Boco, A. Lapi, and L. Danese. "Growth of Supermassive Black Hole Seeds in ETG Star-forming Progenitors: Multiple Merging of Stellar Compact Remnants via Gaseous Dynamical Friction and Gravitational-wave Emission." In: *Astrophys. J.* 891.1, 94 (Mar. 2020), p. 94. DOI: 10.3847/1538-4357/ab7446. arXiv: 2002.03645 [astro-ph.GA].

[278] L. Boco, A. Lapi, A. Sicilia, G. Capurri, C. Baccigalupi, and L. Danese. "Growth of massive black hole seeds by migration of stellar and primordial black holes: gravitational waves and stochastic background." In: *JCAP* 2021.10, 035 (Oct. 2021), p. 035. DOI: 10.1088/1475-7516/2021/10/035. arXiv: 2104.07682 [astro-ph.CO].

[279] M. Armano et al. "Beyond the Required LISA Free-Fall Performance: New LISA Pathfinder Results down to 20 μ Hz." In: *PRL* 120.6, 061101 (Feb. 2018), p. 061101. DOI: 10.1103/PhysRevLett.120.061101.

[280] J. Baker et al. "High angular resolution gravitational wave astronomy." In: *arXiv e-prints*, arXiv:1908.11410 (Aug. 2019), arXiv:1908.11410. arXiv: 1908.11410 [astro-ph.HE].

[281] S. Wang, V. Vardanyan, and K. Kohri. "Probing primordial black holes with anisotropies in stochastic gravitational-wave background." In: *Phys. Rev. D* 106.12 (2022). DOI: 10.1103/PhysRevD.106.123511. arXiv: 2107.01935 [gr-qc].

[282] T. Ishikawa et al. "Improvement of the Target Sensitivity in DECIGO by Optimizing its Parameters for Quantum Noise Including the Effect of Diffraction Loss." In: *Galaxies* 9.1 (Feb. 2021), p. 14. DOI: 10.3390/galaxies9010014. arXiv: 2012.11859 [gr-qc].

[283] Y. Kawasaki, R. Shimizu, T. Ishikawa, K. Nagano, S. Iwaguchi, I. Watanabe, B. Wu, S. Yokoyama, and S. Kawamura. "Optimization of Design Parameters for GW Detector DECIGO Including Fundamental Noises." In: *Galaxies* 10.1 (Feb. 2022), p. 25. DOI: 10.3390/galaxies10010025. arXiv: 2202.04253 [gr-qc].

[284] X. Fan et al. "A Survey of z>5.7 Quasars in the Sloan Digital Sky Survey. IV. Discovery of Seven Additional Quasars." In: *AJ* 131.3 (Mar. 2006), pp. 1203–1209. DOI: 10.1086/500296. arXiv: astro-ph/0512080 [astro-ph].

[285] D. J. Mortlock et al. "A luminous quasar at a redshift of z = 7.085." In: *Nature* 474.7353 (June 2011), pp. 616–619. DOI: 10.1038/nature10159. arXiv: 1106.6088 [astro-ph.CO].

[286] B. P. Venemans et al. "Copious Amounts of Dust and Gas in a z = 7.5 Quasar Host Galaxy." In: *Astrophys. J. Lett.* 851.1, L8 (Dec. 2017), p. L8. DOI: 10.3847/2041-8213/aa943a. arXiv: 1712.01886 [astro-ph.GA].

[287] B. P. Venemans, M. Neeleman, F. Walter, M. Novak, R. Decarli, J. F. Hennawi, and H.-W. Rix. "400 pc Imaging of a Massive Quasar Host Galaxy at a Redshift of 6.6." In: *Astrophys. J. Lett.* 874.2, L30 (Apr. 2019), p. L30. DOI: 10.3847/2041-8213/ab11cc. arXiv: 1903.09202 [astro-ph.GA].

[288] D. Blas and A. C. Jenkins. "Bridging the μ Hz Gap in the Gravitational-Wave Landscape with Binary Resonances." In: *PRL* 128.10, 101103 (Mar. 2022), p. 101103. DOI: 10.1103/PhysRevLett.128.101103. arXiv: 2107.04601 [astro-ph.CO].

[289] D. Blas and A. Jenkins. "Detecting stochastic gravitational waves with binary resonance." In: *PRD* 105.6, 064021 (Mar. 2022), p. 064021. DOI: 10.1103/PhysRevD.105.064021. arXiv: 2107.04063 [gr-qc].

[290] K. Abazajian et al. "CMB-S4 Science Case, Reference Design, and Project Plan." In: *arXiv e-prints*, arXiv:1907.04473 (July 2019), arXiv:1907.04473. arXiv: 1907.04473 [astro-ph.IM].

[291] K. Abazajian et al. "Snowmass 2021 CMB-S4 White Paper." In: *arXiv e-prints*, arXiv:2203.08024 (Mar. 2022), arXiv:2203.08024. arXiv: 2203.08024 [astro-ph.CO].

[292] R. Abbott et al. "Constraints on the Cosmic Expansion History from GWTC–3." In: *Astrophys. J.* 949.2 (2023), p. 76. DOI: 10.3847/1538-4357/ac74bb. arXiv: 2111.03604 [astro-ph.CO].

[293] T. Regimbau and V. Mandic. "Astrophysical sources of SGWB." In: *Class. Quant. Grav.* 25 (2008). Ed. by S. Hughes and E. Katsavounidis, p. 184018. DOI: 10.1088/0264-9381/25/18/184018. arXiv: 0806.2794 [astro-ph].

[294] F. Santoliquido, M. Mapelli, Y. Bouffanais, N. Giacobbo, U. N. Di Carlo, S. Rastello, M. C. Artale, and A. Ballone. "The cosmic merger rate density evolution of compact binaries formed in young star clusters and in isolated binaries." In: *Astrophys. J.* 898.2 (2020), p. 152. DOI: 10.3847/1538-4357/ab9b78. arXiv: 2004.09533 [astro-ph.HE].

[295] F. Santoliquido, M. Mapelli, N. Giacobbo, Y. Bouffanais, and M. C. Artale. "The cosmic merger rate density of compact objects: impact of star formation, metallicity, initial mass function and binary evolution." In: *Mon. Not. Roy. Astron. Soc.* 502.4 (2021), pp. 4877–4889. DOI: 10.1093/mnras/stab280. arXiv: 2009.03911 [astro-ph.HE].

[296] F. Santoliquido, M. Mapelli, M. C. Artale, and L. Boco. "Modelling the host galaxies of binary compact object mergers with observational scaling relations." In: *Mon. Not. Roy. Astron. Soc.* 516.3 (2022), pp. 3297–3317. DOI: 10.1093/mnras/stac2384. arXiv: 2205.05099 [astro-ph.HE].

[297] P. Popesso, A. Concas, G. Cresci, S. Belli, G. Rodighiero, H. Inami, M. Dickinson, O. Ilbert, M. Pannella, and D. Elbaz. "The main sequence of star-forming galaxies across cosmic times." In: *Monthly Notices of the Royal Astronomical Society* 519.1 (Feb. 2023), pp. 1526–1544. DOI: 10.1093/mnras/stac3214. arXiv: 2203.10487 [astro-ph.GA].

[298] N. Farrow, X.-J. Zhu, and E. Thrane. "The mass distribution of Galactic double neutron stars." In: *Astrophys. J.* 876.1 (2019), p. 18. DOI: 10.3847/1538-4357/ab12e3. arXiv: 1902.03300 [astro-ph.HE].

[299] P. Landry and J. S. Read. "The Mass Distribution of Neutron Stars in Gravitational-wave Binaries." In: *Astrophys. J. Lett.* 921.2 (2021), p. L25. DOI: 10.3847/2041-8213/ac2f3e. arXiv: 2107.04559 [astro-ph.HE].

[300] T. Fragos, J. Andrews, E. Ramirez-Ruiz, G. Meynet, V. Kalogera, R. Taam, and A. Zezas. "The complete evolution of a neutron-star binary through a common envelope phase using 1D hydrodynamic simulations." In: *Astrophys. J. Lett.* 883.2 (2019). DOI: 10.3847/2041-8213/ab40d1. arXiv: 1907.12573 [astro-ph.HE].

[301] D. Foreman-Mackey, D. W. Hogg, D. Lang, and J. Goodman. "emcee: The MCMC Hammer." In: *Publications of the Astronomical Society of the Pacific* 125.925 (2013), pp. 306–312. DOI: 10.1086/670067.

[302] N. Giacobbo and M. Mapelli. "The impact of electron-capture supernovae on merging double neutron stars." In: *Mon. Not. Roy. Astron. Soc.* 482.2 (2019), pp. 2234–2243. DOI: 10.1093/mnras/sty2848. arXiv: 1805.11100 [astro-ph.SR].

[303] D. Laghi, N. Tamanini, W. Del Pozzo, A. Sesana, J. Gair, S. Babak, and D. Izquierdo-Villalba. "Gravitational-wave cosmology with extreme mass-ratio inspirals." In: *Mon. Not. Roy. Astron. Soc.* 508.3 (2021), pp. 4512–4531. DOI: 10.1093/mnras/stab2741. arXiv: 2102.01708 [astro-ph.CO].

[304] P. A. R. Ade et al. "Planck 2013 results. XVI. Cosmological parameters." In: *Astron. Astrophys.* 571 (2014), A16. DOI: 10.1051/0004-6361/201321591. arXiv: 1303.5076 [astro-ph.CO].

[305] P. A. R. Ade et al. "Planck 2015 results. XIII. Cosmological parameters." In: *Astron. Astrophys.* 594 (2016), A13. DOI: 10.1051/0004-6361/201525830. arXiv: 1502.01589 [astro-ph.CO].

[306] I. Davidzon et al. "The COSMOS2015 galaxy stellar mass function . Thirteen billion years of stellar mass assembly in ten snapshots." In: *A&A* 605, A70 (Sept. 2017), A70. DOI: 10.1051/0004-6361/201730419. arXiv: 1701.02734 [astro-ph.GA].

[307] A. Lapi, C. Mancuso, A. Bressan, and L. Danese. "Stellar Mass Function of Active and Quiescent Galaxies via the Continuity Equation." In: *Astrophys. J.* 847.1 (2017), p. 13. DOI: 10.3847/1538-4357/aa88c9. arXiv: 1708.07643 [astro-ph.GA].

[308] P. Madau and M. Dickinson. "Cosmic Star Formation History." In: *Ann. Rev. Astron. Astrophys.* 52 (2014), pp. 415–486. DOI: 10.1146/annurev-astro-081811-125615. arXiv: 1403.0007 [astro-ph.CO].

[309] P. Schechter. "An analytic expression for the luminosity function for galaxies." In: *Astrophys. J.* 203 (Jan. 1976), pp. 297–306. DOI: 10.1086/154079.

[310] R. C. Kennicutt and N. J. Evans. "Star Formation in the Milky Way and Nearby Galaxies." In: *ARA&A* 50 (Sept. 2012), pp. 531–608. DOI: 10.1146/annurev-astro-081811-125610. arXiv: 1204.3552 [astro-ph.GA].

[311] R. J. Bouwens et al. "UV Luminosity Functions at Redshifts z ~ 4 to z ~ 10: 10,000 Galaxies from HST Legacy Fields." In: *Astrophys. J.* 803.1, 34 (Apr. 2015), p. 34. DOI: 10.1088/0004-637X/803/1/34. arXiv: 1403.4295 [astro-ph.CO].

[312] A. Lapi et al. "Herschel-ATLAS Galaxy Counts and High-redshift Luminosity Functions: The Formation of Massive Early-type Galaxies." In: *Astrophys. J.* 742.1, 24 (Nov. 2011), p. 24. DOI: 10.1088/0004-637X/742/1/24. arXiv: 1108.3911 [astro-ph.CO].

[313] T. Wang et al. "A dominant population of optically invisible massive galaxies in the early Universe." In: *Nature* 572.7768 (2019), pp. 211–214. DOI: 10.1038/s41586-019-1452-4. arXiv: 1908.02372 [astro-ph.GA].

[314] C. Gruppioni et al. "The ALPINE-ALMA [CII] survey. The nature, luminosity function, and star formation history of dusty galaxies up to z ≈ 6." In: *A&A* 643, A8 (Nov. 2020), A8. DOI: 10.1051/0004-6361/202038487. arXiv: 2006.04974 [astro-ph.GA].

[315] R. Maiolino and F. Mannucci. "De re metallica: the cosmic chemical evolution of galaxies." In: *A&A Rev.* 27.1, 3 (Feb. 2019), p. 3. DOI: 10.1007/s00159-018-0112-2. arXiv: 1811.09642 [astro-ph.GA].

[316] L. J. Kewley and S. L. Ellison. "Metallicity Calibrations and the Mass-Metallicity Relation for Star-forming Galaxies." In: *Astrophys. J.* 681.2 (July 2008), pp. 1183–1204. DOI: 10.1086/587500. arXiv: 0801.1849 [astro-ph].

[317] R. Maiolino et al. "AMAZE. I. The evolution of the mass-metallicity relation at z>3." In: *Astron. Astrophys.* 488 (2008), pp. 463–479. DOI: 10.1051/0004-6361:200809678. arXiv: 0806.2410 [astro-ph].

[318] E. C. Ostriker. "Dynamical friction in a gaseous medium." In: *Astrophys. J.* 513 (1999), p. 252. DOI: 10.1086/306858. arXiv: astro-ph/9810324.